PORTUGALIAE PHYSICA

PORTUGALIAE PHYSICA

117

SINGULARITIES ON FIXED CYCLE UNDIRECTED ANIMALS

A FEW ADDITIONAL ANALYSES

M. Conceição Pires de Carvalho and J. A. M. S. Duarte

Laboratório de Física — Faculdade de Ciências do Porto, 4000 Porto, Portugal

ABSTRACT — The cycle animal values on the triangular and square site problems (extended by one more term) and the honeycomb bond cycle 1 animals are studied for their leading and confluent singularities as well as their multiplicities.

INTRODUCTION AND SUMMARY

In this presentation we aim at a consistent revision of results on the singularity location and exponent values for fixed cycle undirected animals. A classification of such undirected site animals according to their cyclomatic index for two-dimensional lattices was published by Duarte in 1981 [1]. Trees — or zero cycle animals — were much debated around the period following the field theoretic predictions of Lubensky and coworkers [2]. Duarte and Ruskin [3] proved that the leading singularity estimates for trees overlapped with those for the complete animals, as predicted in [2], and a significant advance followed in ref. [4], where 2 and 3-dimensional data for most usual lattices were found to back a graph-theoretical prediction for bond animals (i.e. pertaining to weak embeddings) that the singularity alteration for c-cycle

Portgal. Phys. — Vol. 16, fasc. 1-2, pp. 1-7, 1985

1

animals is reduced to a change in the exponent (leading exponent here) according to the law

$$\Theta_c = \Theta_0 - c \tag{1}$$

As can be seen, singularities get progressively stronger. Also, the multiplicity for trees remains unaltered for all c-cycle values. This requires a shift of multiplicity on summing all cycle values to obtain the complete number of undirected animals: a significant difference in structure from the percolation perimeter partition, which is well known to be characterized by a variable multiplicity [1]. The data in Whittington, Torrie and Gaunt [3] for cycle values 2,1 in 2 dimensions are complemented in Duarte [1] to the order presently available for trees (and also for the honeycomb site animals). We have added here the 1-cycle honeycomb bond animals (for trees, see [3]) in table I and repeat the analyses for the additional evidence.

TABLE I

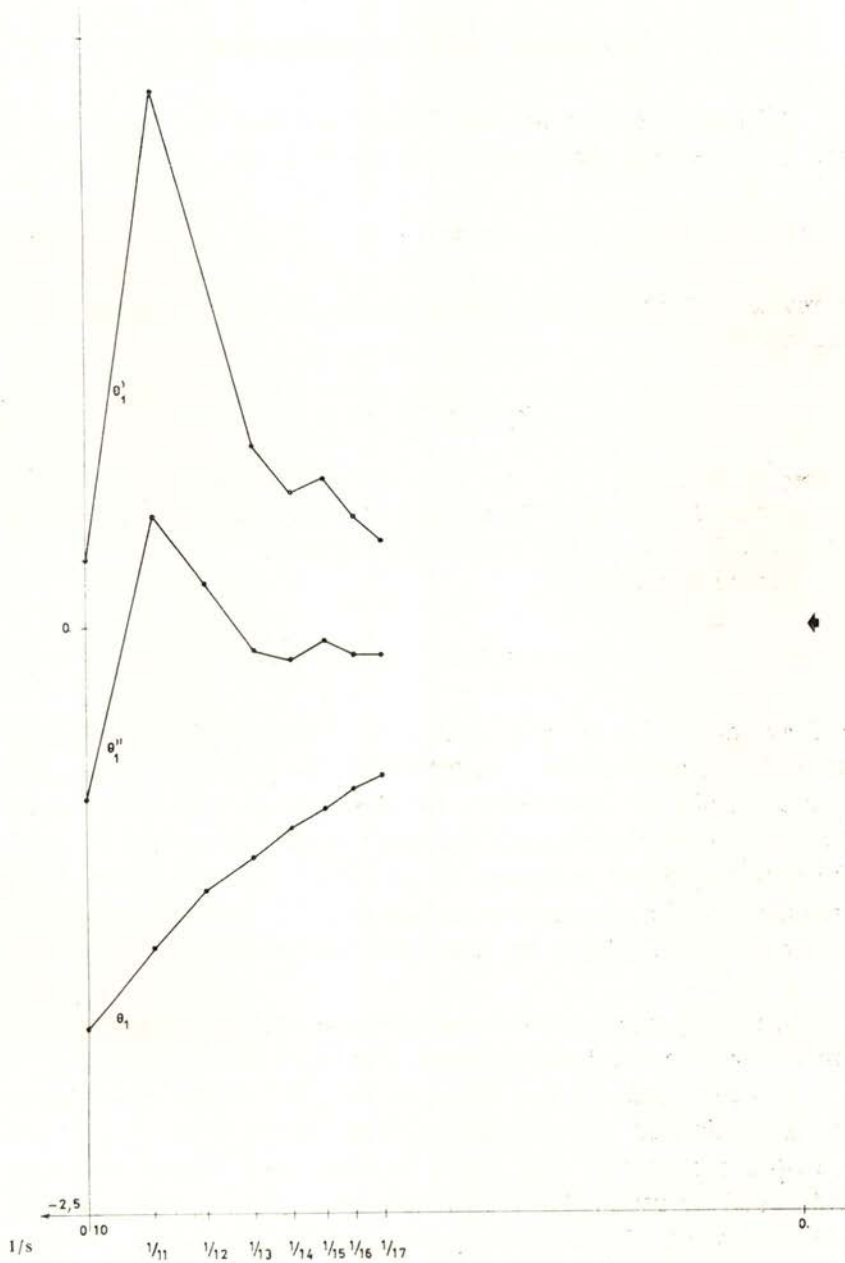| s	g_{s1}
6	1.
7	6.
8	27.
9	110.
10	432.
11	1,626.
12	5,956.
13	21,450.
14	76,296.
15	268,634.
16	938,667.
17	3,260,496.

2

Portgal. Phys. — Vol. 16, fasc. 1-2, pp. 1-7, 1985

Fig. 1 — Θ_1 sequences for the honeycomb bond 1-cycle animals: Θ_1, biassed estimates, Θ_1' linear intercepts on them, Θ_1'', averages of the Θ_1 and Θ_1' sequences.

Portgal. Phys. — Vol. 16, fasc. 1-2, pp. 1-7, 1985

3

ANALYSES AND CONCLUSIONS

All sequences are for two-dimensional lattices. According to eq. 1, the leading singularity is therefore known to vary as

$$\Theta_c = 1 - c \tag{2}$$

a result that should be approached by the usual extrapolating sequences

$$\Theta_c(s) = s \ (1 - R_s/\lambda_o) \tag{3}$$

where $R_s = g_{s,\,c}/g_{s-1,\,c}$ is the ratio of successive c-cycle number of animals, λ_0 a good estimate of the multiplicity (in the present case, usually the central estimate for trees).

Linear extrapolants

$$\Theta'_c(s) = s \ \Theta_c(s) - (s-1) \ \Theta_c(s-1) \tag{4}$$

and averages of $\Theta_c(s)$ and $\Theta'_c(s)$ (here called $\Theta''_c(s)$) may also be used for assessing the evolution of the exponent sequences (Fig. 2): while the extra terms for the triangular site and square site sequences bring no great alteration in the pattern for Θ_1 or Θ_2, the new sequences according to eq. 3 for the honeycomb bond animals are of a comparable quality (Fig. 1), hovering somewhat below the $\Theta_1 = 0$ limit, as found for the other two lattices [4].

We also present graphical evidence on the λ_0 value estimates for the honeycomb bond problem (Fig. 3).

1 — cycle animals and trees are the most useful cycle values for estimation of the multiplicity. The combination $\Theta_1 = 0$ and $\Theta_0 = + 1$ means that the ratios R_s and their linear intercepts under- and overestimate the λ_0 value, respectively. Their averages evolve closer to the multiplicity limit (cf. Fig. 3) and one expects to compare them with the tree estimates biassed with $\Theta_0 = 1$

$$\lambda_b(s) = s \ R_s/(s-\Theta_0) \tag{5}$$

4

Portgal. Phys. — Vol. 16, fasc. 1-2, pp. 1-7, 1985

This comparison helped halving the uncertainty for λ_0 in triangular site animals in [4] and trim it slightly here

$$\lambda_0 = 4.19 \pm 0.015 \ ; \ 4.196 \pm 0.007 \ ; \ 4.195 \pm 0.005 \qquad (6)$$
$$[3] \qquad\qquad [4] \qquad\qquad \text{this work}$$

while the extra term for the square site animals warrants no alteration of the value in ref. [4]

$$\lambda_0 = 3.795 \pm 0.007 \qquad (7)$$

Fig. 2 — Comparison of site 1-cycle animal exponents for the triangular (B), square (C) and honeycomb site (A) cases. The overall estimate is $\theta_1 = -0.1 \pm 0.2$.

The results for λ_0 relative to fixed cycle honeycomb bond animals given in Fig. 3 bring no revision of the estimate given in [3]

$$\lambda_0 = 3.35 \pm 0.01 \qquad (8)$$

An interesting question arises with the possibility of a direct evaluation of the confluent singularities for fixed cycle animals.

Portgal. Phys. — Vol. 16, fasc. 1-2, pp. 1-7, 1985

5

Confluent singularities of an algebraic type have been referred by a number of authors and analysed for the total numbers of animals [5]. The asymptotic form of the tree values, for example, is then given by

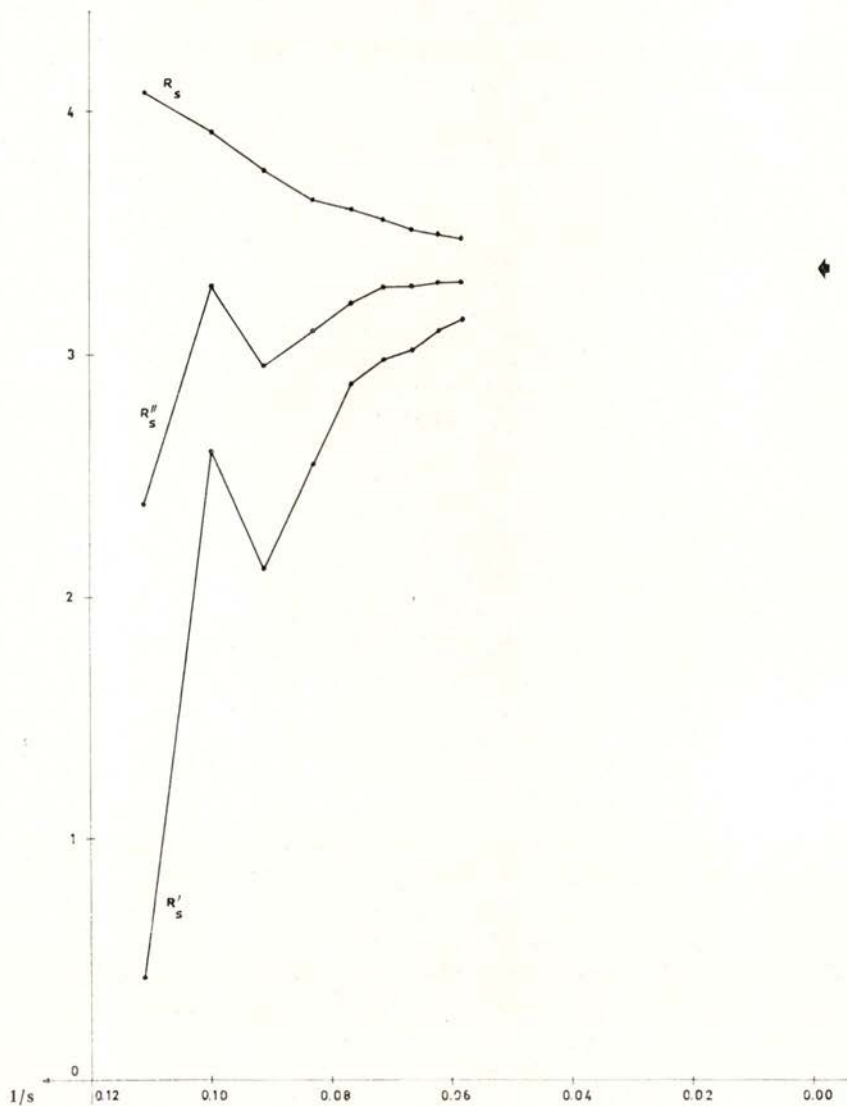$$g_{s,0} \sim \lambda_0^s \, s^{-1} \, (1 + E \, s^{-w} + \dots) \tag{9}$$

Fig. 3 — Multiplicity estimates for the honeycomb bond 1-cycle animals: R_s ratios, R'_s, linear intercepts on them, R''_s, averages of the previous sequences.

with w the confluent correction. An independent estimate of w, not sensitive to the λ_0 variation, can be obtained from the second log difference

$$\text{Log} \left[\left(s^2 - 1 \right)/s^2 \cdot g_{s+1,0} \, g_{s-1,0}/\left(g_{s,0} \right)^2 \right] \sim s^{-(w+2)} \tag{10}$$

and the best results were obtained for the triangular bond trees (to $s < 11$ in [4]) and square matching trees (to $s < 11$ in [3]). All the others, including square site and bond trees, triangular site and both honeycomb trees were virtually of no pratical use. Even for the two best examples mentioned above, it is impossible to go beyond saying that the data are not incompatible with the w estimate for lattice animals [5]

$$w = 0.86 \pm 0.05 \tag{11}$$

but an independent estimate is out of question for such comparatively short series.

In conclusion, the extended evidence confirms and marginally improves the multiplicity estimates, whereas the rather incipient evidence on the confluent singularity is not in disagreement with the animal value (11).

This paper contains the results of a communication to the Conferência Nacional de Física, Évora 1984.

REFERENCES

[1] DUARTE, J. A. M. S., *Portgal Phys.*, 12, 99 (1981).

[2] LUBENSKY, T., ISAACSON, J., *Phys. Rev.*, **A20**, 2130 (1979).

[3] DUARTE, J. A. M. S., RUSKIN, H., *J. Physique* (Paris), 42, 1585 (1981).

[4] WHITTINGTON, S. G., TORRE, G. M., GAUNT, D. S., *J. Phys.*, **A16**, 1695 (1983).

[5] GUTTMANN, A. J., *J. Phys.*, **A15**, 1987 (1982).

VARIATIONAL DERIVATION OF MEAN FIELD THEORIES WITH MIXED STATES

J. da Providência and C. Fiolhais

Departamento de Física, Universidade de Coimbra, 3000 Coimbra, Portugal

ABSTRACT — A variational approach to the dynamics of many-fermion systems appropriate to physical situations requiring a description in terms of mixed states has been developed. The formalism presented here leads in a straightforward way to a mean field theory for mixed states. In this framework, the well-known Hartree-Fock and RPA results for pure states are generalized to the case of mixtures.

1 – INTRODUCTION

D. Brink has suggested in 1955 that one could build collective excitations on top of any stationary state of the nucleus, not necessarily its ground state [1].

In this vein, one may consider collective excitations, which have as "ground state" a mixture of pure states, chosen such as to make the energy of the system stationary. This conjecture has received strong support in 1981, with the experimental discovery at Berkeley of resonances in heavy ion collisions, which could be explained in terms of a dipole displacement of protons against neutrons in compound nuclei [2]. Indeed, γ-ray spectra from deexcitation of compound nuclei with excitation energies of ~ 50 MeV, have been measured and could be fitted by a bump superimposed on a statistical background. The same research group has been able to study the spectra of γ-rays associated with products of deep-inelastic reactions, concluding that the giant dipole resonance strength function is temperature dependent [3]. The experiment indicates that the collective frequency decreases

Portgal. Phys. — Vol. 16, fasc. 1-2, pp. 9-26, 1985

9

with the increase of excitation energy, while the resonance width becomes larger.

Such studies have added a new dimension to our knowledge of nuclear structure. It is then important to know how the theoretical nuclear response function can be formulated for excited systems, and how does it compare with experimental results.

These calculations, which begun only recently, are expected to provide a guide for future observations in the field [4, 5, 6]. For example it is not excluded that other resonance multipolarities may be found in hot nuclei, although the techniques involved should be more sophisticated. In this context one may recall that the experimental discovery of the normal giant dipole mode preceded by 25 years the detection of the quadrupole resonance.

Within the range of theoretical methods available to tackle the problem of nuclear collective motion at zero excitation, the variational approaches distinguish themselves because of their wide flexibility [7]. They provide an unified frame for a lot of approximation schemes, which are established according to the intuitive view one may have of the physical situation.

In this paper we present a variational approach to collective excitations in hot nuclei, putting the emphasis on the derivation of mean-field theories appropriate to that kind of situations.

As we have already presented the method in another publication [8] — where we have also applied it to a schematic two-level model — we limit ourselves here to present in detail the calculations which lead, in the independent-particle approximation, to the self-consistent mean field picture of stationary and quasi-stationary states.

The Hartree-Fock mean-field so obtained differs from the result with pure states (Slater determinants) through the introduction of occupation numbers of the single-particle levels. We call special attention to the fact that this occupation parameters must not be prescribed by the usual assumptions of the grand canonical ensemble. We stress this point, because it is not sure that there is always complete thermalization of the nuclear systems occuring in heavy ion reactions. This is in contrast with the case of matter inside massive stars, where statistical equilibrium is reached during its late evolutive stage.

Small oscillation of the mean-field due to an external perturbation are accounted for, leading to the response function of

the excited system (Random Phase Approximation (RPA) for mixed states).

Specializing the results to mixed states corresponding to thermal equilibrium, the occupation numbers are given by the Fermi-Dirac distribution and the thermal Hartree-Fock and RPA formulae are readily obtained.

The paper is organized as follows. In section 2 we sketch the method. This is based on the density matrix formalism, which is the natural tool to deal with mixed states. In section 3 the response function for mixed states is discussed. In section 4 the features of thermal equilibrium are presented. In section 5 we introduce the notation needed within the independent particle approximation. The static Hartree-Fock theory for mixed states is derived in section 6, while the corresponding RPA is derived in section 7. The conclusions, which are formulated in section 8, contain some perspectives of further work in the field.

2 — GENERAL FORMALISM

Let H denote the hamiltonian of a general N particle system. According to the principles of quantum mechanics, an arbitrary mixed state of the system is described by a density matrix D whose trace is unity

$$\text{Tr } D = 1 \,. \tag{2.1}$$

The density matrix D_0 describing a stationary mixed state satisfies the condition

$$[\, H \,, \, D_0 \,] = 0 \,. \tag{2.2}$$

This condition may be formulated variationally. For this purpose we consider the set of all density matrices having a fixed spectrum of eigenvalues given a priori. If D_0 belongs to that set, so does the matrix

$$D = U \, D_0 \, U^+ = e^{-iF} \, D_0 \, e^{iF} \,, \tag{2.3}$$

where F is an arbitrary hermitean operator. The stationarity

condition for the energy, which is necessary to assure minimum energy,

$$\delta \ \mathrm{Tr} \ (DH) = \delta \ \mathrm{Tr} \ (e^{-iF} \ D_0 \ e^{iF} \ H) = 0 \qquad (2.4)$$

leads to

$$\mathrm{Tr} \ ([D_0 , \ \delta F] \ H) = \mathrm{Tr} \ ([H , \ D_0] \ \delta F) = 0 \qquad (2.5)$$

Since this equation must hold for all variations δF one obtains finally eq. (2.2).

We will discuss now the time evolution of D. According to the rules of quantum-dynamics the operator D should satisfy the Liouville-von Neumann equation

$$\dot{D} = i \ [D , \ H] \qquad (2.6)$$

which is equivalent to

$$D (t) = e^{-iHt} \ D (0) \ e^{iHt} . \qquad (2.7)$$

We see that the eigenvalue spectrum of D remains unchanged with the time. Our aim is to obtain a variational formulation of (2.6) which could be used as a source of reliable approximation schemes to the exact dynamical equation. We begin with writing the time-dependent density matrix in terms of the stationary density matrix which satisfies eq. (2.2):

$$D (t) = U (t) \ D_0 \ U^{+} (t) , \qquad (2.8)$$

where $U (t)$ is a variational unitary operator (the unitarity of U assures the time-invariance of the eigenvalue spectrum of D).

Let us consider the action integral

$$I = \int_{t_1}^{t_2} L \ dt , \qquad (2.9)$$

where the lagrangian is given by

$$L = i \, \mathrm{Tr} \, (U \, D_0 \, \dot{U}^+) + \mathrm{Tr} \, (U \, D_0 \, U^+ H) \,. \qquad (2.10)$$

The least action principle $\delta I = 0$ with L given by (2.10) does lead to the correct equation of motion (2.6) as we shall prove in the following.

We denote now by δF an infinitesimal hermitean time-dependent operator which satisfies

$$U + \delta U = U \, e^{-i \, \delta F} \,. \qquad (2.11)$$

We have therefore

$$\delta U = - i \, U \, \delta F \,, \qquad (2.12)$$

$$U^+ \delta U = - \delta U^+ U = - i \, \delta F \,. \qquad (2.13)$$

The following boundary condition may be imposed on δF :

$$\mathrm{Tr} \, [\, D_0 \, \delta F (t_1) \,] = \mathrm{Tr} \, [\, D_0 \, \delta F (t_2) \,] = 0 \,. \qquad (2.14)$$

The variation of the action integral may be written

$$\delta I = \int_{t_1}^{t_2} dt \, [\, i \, \mathrm{Tr} \, (\, \delta U \, D_0 \, \dot{U}^+ + U D_0 \, \delta \dot{U}^+) +$$

$$+ \, \mathrm{Tr} \, (\, \delta U \, D_0 \, U^+ H + U D_0 \, \delta U^+ H) \,] = i \, \mathrm{Tr} \, (\, D_0 \, \delta U^+ U) \, \Big|_{t_1}^{t_2} +$$

$$+ \int_{t_1}^{t_2} dt \, \mathrm{Tr} \, \{ \, \delta U \, U^+ \, [\, i \, (U D_0 \, \dot{U}^+ + \dot{U} D_0 \, U^+) +$$

$$+ \, (U D_0 \, U^+ H - H U D_0 \, U^+) \,] \, \}$$

$$= - \, \mathrm{Tr} \, (\, \delta F \, D_0) \, \Big|_{t_1}^{t_2} + i \int_{t_1}^{t_2} dt \, \mathrm{Tr} \, \{ \, U \, \delta F \, U^+ \, (- i \, \dot{D} - [\, D \,, \, H \,]) \, \}$$

$$= \int_{t_1}^{t_2} dt \, \mathrm{Tr} \, \{ \, U \, \delta F \, U^+ \, (\dot{D} - i \, [\, D \,, \, H \,]) \, \} = 0 \,, \qquad (2.15)$$

Portgal. Phys. — Vol. 16, fasc. 1-2, pp. 9-26, 1985

13

where use has been made of (2.13) and of the boundary condition (2.14). Since the variation δF is arbitrary for $t_1 < t < t_2$ one gains indeed the Liouville-von Neumann equation (2.6) from the action principle.

3 – THE LINEAR RESPONSE FUNCTION
FOR MIXED STATES

If a quantal system stays in a stationary state described by the time-independent density matrix D_0 and at some later occasion is slightly perturbed, the density matrix of the perturbed system may be written

$$D(t) = e^{-iF(t)} D_0 e^{iF(t)} \tag{3.1}$$

where $F(t)$ is a hermitean infinitesimal operator. Since F is infinitesimal the lagrangian (2.10) may be replaced by its leading order terms. The following quadratic lagrangian is obtained (the linear terms give no contribution):

$$L^{(2)} = (-i/2) \, \text{Tr} \, (D_0 [F, \dot{F}]) + 1/2 \, \text{Tr} \, (D_0 [F, [H, F]]) . \tag{3.2}$$

The principle of least action will then lead to linear equations of motion which are the small amplitude limit of the Liouville-von Neumann equation. From the variation

$$\delta \int L^{(2)} \, dt = 0 \tag{3.3}$$

we obtain

$$i \, \text{Tr} \, (D_0 [\delta F, \dot{F}]) - \text{Tr} \, (D_0 [\delta F, [H, F]]) = 0 , \tag{3.4}$$

so that

$$i \, \text{Tr} \{ \delta F ([\dot{F}, D_0] + i [[H, F], D_0]) \} = 0 , \tag{3.5}$$

or, since δF is arbitrary,

$$[\dot{F}, D_0] = -i [H, [F, D_0]] \tag{3.6}$$

14

Portgal. Phys. — Vol. 16, fasc. 1-2, pp. 9-26, 1985

Here the Jacobi identity for double commutators has been used together with the equilibrium condition (2.2).

We consider now the eigenmode solutions of (3.6). We insert the appropriate ansatz

$$F_r(t) = e^{-i\omega_r t} \Theta_r^+ + e^{i\omega_r t} \Theta_r \tag{3.7}$$

and obtain

$$\omega_r [\Theta_r^+, D_0] = [H, [\Theta_r^+, D_0]]$$

$$-\omega_r [\Theta_r, D_0] = [H, [\Theta_r, D_0]] \tag{3.8}$$

where we can consider $\omega_r > 0$. The following normalization condition for the operators Θ_r and Θ_s^+ may be imposed:

$$\text{Tr} (D_0 [\Theta_r, \Theta_s^+]) = \delta_{rs} \tag{3.9}$$

$$\text{Tr} (D_0 [\Theta_r, \Theta_s]) = \text{Tr} (D_0 [\Theta_r^+, \Theta_s^+]) = 0.$$

The general solution of eq. (3.6) can be written as

$$F(t) = \sum_r (f_r e^{-i\omega_r t} \Theta_r^+ + f_r^* e^{i\omega_r t} \Theta_r). \tag{3.10}$$

The normalization (3.9) leads to the following expression for the mixed state transition amplitudes

$$f_r = \text{Tr} (D_0 [\Theta_r, F(0)])$$

$$f_r^* = \text{Tr} (D_0 [F(0), \Theta_r^+]). \tag{3.11}$$

The energy-weighted sum-rule for these transition amplitudes may now be derived. Indeed from eq. (3.4) with F instead of δF we conclude that

$$i \text{Tr} (D_0 [F, \dot{F}]) = \text{Tr} (D_0 [F, [H \quad F]]) \tag{3.12}$$

It may be easily checked that $i \operatorname{Tr}(D_0 [F, \dot{F}]) = 2 \sum_r \omega_r |f_r|^2$. Therefore

$$\sum_r \omega_r |f_r|^2 = 1/2 \ \operatorname{Tr}(D_0 [F, [H, F]]) . \qquad (3.13)$$

We emphasize that this sum-rule is exact and not restricted to the RPA, in which $\log D_0$ and F are one-body operators.

Since the operators H and D_0 commute they may be simultaneously diagonalized. Denoting by $\{ |m> \}$ a set of common eigenvalues

$$H | m> = E_m | m>$$

$$D_0 | m> = P_m | m> \qquad (3.14)$$

the solutions of the equations of motion (3.8) are given by

$$\omega_r = E_m - E_n$$

$$\Theta_r^+ = (P_n - P_m)^{-1/2} | m> <n| \qquad (3.15)$$

with $E_m > E_n$ and $P_n > P_m$. The index r labels the pair (m, n).

4 – THERMAL EQUILIBRIUM

The stationarity condition (2.2) should not be confused with the condition for statistical equilibrium.

It is well-known that thermal equilibrium occurs when the entropy

$$S = -\operatorname{Tr}(D \log D) \qquad (4.1)$$

is maximal for a given value of the energy $E = \operatorname{Tr}(DH)$. In order to determine the states of thermal equilibrium the function

$$W = \beta \ \operatorname{Tr}(DH) + \operatorname{Tr}(D \log D) \qquad (4.2)$$

16

Portgal. Phys. — Vol. 16, fasc. 1-2, pp. 9-26, 1985

should, therefore, be minimized with respect to variations of D satisfying the normalization condition (2.1). The parameter β is a Lagrange multiplier which fixes the energy and should be interpreted as the inverse of the temperature. The function W is proportional to the well-known Helmholtz function.

The minimization of (4.2) may be viewed as consisting of two steps:

i) Minimization with respect to D for a fixed eigenvalue spectrum. This stage is identical to the time-independent variational procedure formulated in section 2 because the entropy is not affected by canonical transformations. We determine, within the class of all density matrices with a given spectrum, the density matrix D_0 which minimizes the energy and commutes with the hamiltonian H, so that it may be simultaneously diagonalized with H (see eqs. (3.14)). In this first stage we obtain the eigenvectors $|m>$ of H and D_0 and the corresponding eigen-energies E_m.

ii) Minimization with respect to the eigenvalues of D, the set of eigenvectors being kept fixed. We determine the eigenvalues P_m of D_0 which are suitable to describe thermal equilibrium. The function (4.2) may be written

$$W = \beta \sum_m P_m E_m + \sum_m P_m \log P_m \qquad (4.3)$$

and the normalization condition (2.1) reads as

$$\sum_m P_m = 1 \qquad (4.4)$$

Minimization of W with respect to the eigenvalue spectrum P_m is now easily performed leading to

$$P_m = Z^{-1} e^{-\beta E_m} \quad , \quad Z = \sum_m e^{-\beta E_m} \qquad (4.5)$$

Finally we arrive at the following inequality

$$-\log (\sum_m e^{-\beta E_m}) < \beta \, \text{Tr} \, (DH) + \text{Tr} \, (D \log D)$$

which is precisely the well known Peierls variational principle for the free energy.

We observe that the equilibrium condition (2.2) is a necessary but not sufficient condition for statistical equilibrium. That condition may be interpreted as indicating short-term equilibrium around which the system may oscillate due to a small external perturbation. On the other hand thermal equilibrium should be understood as long-term equilibrium. The composition of the mixed state is in this case specified by (4.5).

5 – INDEPENDENT PARTICLE APPROXIMATION FOR MIXED STATES : NOTATION

In the independent particle approximation we assume that the density-matrix has the following form

$$D = C \, e^{K} ; \qquad (5.1)$$

here K is a one-body hermitean operator and C is a normalization constant.

As this approximation is most conveniently discussed for a variable number of particles in the formalism of second quantization we represent the hamiltonian as

$$H = T + V$$

$$T = \sum_{\mu\nu} t_{\mu\nu} \, a_{\mu}^{+} \, a_{\nu}$$

$$V = 1/2 \sum_{\mu\nu\rho\sigma} v_{\mu\nu\rho\sigma} \, a_{\mu}^{+} \, a_{\nu}^{+} \, a_{\sigma} \, a_{\rho} \qquad (5.2)$$

where a_i^+, a_j are respectively creation and annihilation fermion operators corresponding to an orthonormal set of single particle states.

If the number of particles is kept fixed we can write

$$T = \sum_{i=1}^{N} t_i$$

(5.3)

$$V = 1/2 \sum_{i \neq j=1}^{N} v_{ij}$$

where the operators t_i and v_{ij} act respectively on functions of the coordinates of the particle i and of the particles i and j. The symbols t and v denote therefore, respectively, the restriction of T and V to one-body and two-body Hilbert spaces.

The expectation values of T and V in the mixed state described by an independent-particle density matrix D may be written

$$< T > = Tr \, (DT) = \sum_{\mu\nu} \rho_{\mu\nu} \, t_{\nu\mu} = tr \, (\rho t)$$

(5.4)

$$< V > = Tr \, (DV) = 1/2 \sum_{\mu\nu\rho\sigma} \rho_{\mu\nu} \, \rho_{\rho o} v^{A}_{\nu\sigma, \, \mu\rho} = 1/2 \, tr_1 \, tr_2 \, (\rho_1 \, \rho_2 \, v^{A}_{12})$$

where $\rho_{\mu\nu}$ are the elements of the one-body density matrix

$$\rho_{\mu\nu} = < \mu | \rho | \nu > = Tr \, (D \, a_{\nu}^{+} \, a_{\mu})$$

(5.5)

and v^A is the antisymmetrized interaction defined through

$$v^{A}_{\mu\nu, \, \rho\sigma} = v_{\mu\nu, \, \rho\sigma} - v_{\mu\nu, \, \sigma\rho}$$

(5.6)

We should call attention to the distinction between "Tr" and "tr". "Tr" denotes trace in the Hilbert space of state vectors corresponding to an arbitrary number of particles (which is the direct sum of Hilbert spaces of state vectors corresponding to definite numbers of particles). On the other hand "tr" means trace in the Hilbert space of single-particle state vectors.

Portgal. Phys. — Vol. 16, fasc. 1-2, pp. 9-26, 1985

19

The relationship between D and ρ indicated by (5.5) can be made more explicit. If k is the restriction of K to the one-body Hilbert space then

$$\rho = e^k / (1 + e^k) \qquad (5.7)$$

The average number of particles, which must be kept fixed in all the calculations, is

$$N = \mathrm{Tr} \, (D \, \sum_\mu a_\mu^+ \, a_\mu) = \mathrm{tr} \, \rho \qquad (5.8)$$

6 — HARTREE-FOCK APPROXIMATION FOR MIXED STATES

The Hartree-Fock approximation for mixed states requires that the variational space in (2.4) only includes independent-particle density matrices. Therefore $\log D_0$ should be a one-body hermitian operator while F is an arbitrary hermitian one-body operator.

The variational equation (2.5) with δF a one-body operator determines the independent-particle density matrix D_0 which commutes as nearly as possible with H. Let us start with

$$\mathrm{Tr} \, (D_0 \, [H, F]) = 0 \qquad (6.1)$$

which can be obtained from (2.5) using the cyclic property of the trace and replacing δF by F. For fixed N the hamiltonian is given by (5.3) and we have

$$F = \sum_{i=1}^N f_i \qquad (6.2)$$

Then elementary algebraic manipulations lead to

$$[H, F] = \sum_{i=1}^N [t_i , f_i] + 1/2 \sum_{i \neq j=1}^N [v_{ij} , f_i + f_j] \qquad (6.3)$$

so that

$$\text{Tr} (D_0 [H, F]) = \text{tr}_1 (\rho_{0,1} [t_1, f_1]) +$$

$$+ 1/2 \, \text{tr}_1 \, \text{tr}_2 (\rho_{0,1} \, \rho_{0,2} [\overset{A}{v_{12}}, f_1 + f_2]) = 0 \tag{6.4}$$

where ρ_0 is related to D_0 as in (5.5). From (6.4) we obtain further

$$\text{Tr} (D_0 [H, F] = \text{tr}_1 (f_1 [\rho_{0,1}, h_1]) = 0 \tag{6.5}$$

where

$$h_1 = t_1 + \text{tr}_2 (\overset{A}{v_{12}} \rho_{0,2}) \tag{6.6}$$

Since f_1 is arbitrary (6.5) implies finally

$$[h, \rho_0] = 0 \tag{6.7}$$

These are the Hartree-Fock equations for mixed states. Let us consider now a representation in which h and ρ_0 are simultaneously diagonal:

$$h \, | \mu > \; = \; \varepsilon_\mu | \mu >$$

$$\rho_0 | \mu > \; = \; n_\mu | \mu > \tag{6.8}$$

Then the Hartree-Fock equations may be written in the matricial form

$$t_{\mu\nu} + \sum_k n_k \overset{A}{v}_{\mu k, \nu k} = \varepsilon_\mu \, \delta_{\mu\nu} \tag{6.9}$$

The occupation numbers n_ν are easily determined in the case of statistical equilibrium through the minimization of the function

$$W' = \beta E - S - \beta\mu \, N \tag{6.10}$$

The last term appears because a constraint in the mean number of particles must be included when using a formalism with a

Portgal. Phys. — Vol. 16, fasc. 1-2, pp. 9-26, 1985

21

variable number of particles. The function (6.10) is clearly proportional to the grand canonical potential. Following the arguments given at section 4 and using (5.1) and (5.7) it is straightforward to arrive at

$$n_\nu = [\, 1 + e^{\beta \,(\, \varepsilon_\nu - \mu \,)} \,]^{-1} \qquad (6.11)$$

which is just the Fermi-Dirac distribution function. Our general mixed-state formalism provides a rigorous justification to the introduction of Fermi-Dirac occupation numbers in the Hartree-Fock equations (6.9), which are then called thermal Hartree-Fock equations. We emphasize however that the occupation numbers which appear in (6.9) may be given by some other prescription when situations of non-thermal equilibrium are under consideration. The occupation numbers $n_\nu = 1$, $\nu \leqslant N$ and $n_\nu = 0$, $\nu > N$, correspond to the $T = 0$ situation.

7 – RANDOM PHASE APPROXIMATION FOR MIXED STATES

Let us consider again the lagrangian (3.2), but we are now going to assume that both log D_0 and F are one-body operators.

For a fixed number of particles we have the following values for the commutators involved in $L^{(2)}$:

$$[\, F, \dot{F} \,] = \sum_{i=1}^{N} [\, f_i, \dot{f}_i \,] \qquad (7.1)$$

$$
[\, F, [\, H, F \,]\,] = \sum_{i=1}^{N} [\, f_i, [\, t_i, f_i \,]\,] +
$$
$$
+ \; 1/2 \sum_{i \neq j=1}^{N} [\, f_i + f_j, [\, \overset{A}{v_{ij}}, f_i + f_j \,]\,]
\qquad (7.2)
$$

so that

$$L^{(2)} = (-i/2)\ tr_1\ (\rho_{0,1}\ [\ f_1\ ,\ \dot{f}_1\ ]) + 1/2\ tr_1\ (\rho_{0,1}\ [\ f_1\ ,\ [\ t_1\ ,\ f_1\ ]\ ]) \tag{7.3}$$

$$+ 1/4\ tr_1\ tr_2\ (\rho_{0,1}\ \rho_{0,2}\ [\ f_1 + f_2\ ,\ [\ v_{12}^A\ ,\ f_1 + f_2\ ]\ ])$$

The condition of least action leads now to

$$i\ tr_1\ (\rho_{0,1}\ [\ \delta f_1\ ,\ f_1\ ]) - tr_1\ (\rho_{0,1}\ [\ \delta f_1\ ,\ [\ t_1\ ,\ f_1\ ]\ ]) \tag{7.4}$$

$$- tr_1\ tr_2\ (\rho_{0,1}\ \rho_{0,2}\ [\ \delta f_1\ ,\ [\ v_{12}^A\ ,\ f_1 + f_2\ ]\ ]) = 0$$

After some straightforward algebraic manipulations we obtain

$$i\ [\ \dot{f}_1\ ,\ \rho_{0,1}\ ] - [\ [\ h\ ,\ f_1\ ]\ ,\ \rho_{0,1}\ ] - [\ tr_2\ (\rho_{0,2}\ [\ v_{12}^A\ ,\ f_2\ ])\ ,\ \rho_{0,1}\ ] = 0 \tag{7.5}$$

Finally in the representation in which ρ_0 and h are both diagonal

$$i\ \dot{f}_{\mu\nu}\ (n_\nu - n_\mu) - (\varepsilon_\mu - \varepsilon_\nu)\ f_{\mu\nu}\ (n_\nu - n_\mu) - \underset{\rho\sigma}{\Sigma}\ (n_\rho - n_\sigma) \tag{7.6}$$

$$(n_\nu - n_\mu)\ v_{\mu\rho,\ \nu\sigma}^A\ f_{\sigma\rho} = 0$$

The solutions for the normal modes are obtained Fourier-analysing F. The one-body approximation of (3.7) is

$$f_r\ (t) = e^{-i\omega_r t}\ \theta_r^+ + e^{i\omega_r t}\ \theta_r \tag{7.7}$$

which inserted in (7.6) provides the following RPA equations for mixed states

$$\omega_r\ \theta_{r,\ kl}^+\ (n_l - n_k) - (\varepsilon_k - \varepsilon_l)\ \theta_{r,\ kl}^+\ (n_l - n_k) \tag{7.8}$$

$$- \underset{ij}{\Sigma}\ (n_i - n_j)\ (n_l - n_k)\ v_{ki,\ lj}^A\ \theta_{r,\ ji}^+ = 0$$

Portgal. Phys. — Vol. 16, fasc. 1-2, pp. 9-26, 1985

23

These equations can still be written in matricial form

$$\omega_r \begin{pmatrix} X_r \\ Y_r \end{pmatrix} = \begin{pmatrix} A & B \\ -B^* & -A^* \end{pmatrix} \begin{pmatrix} X_r \\ Y_r \end{pmatrix} \qquad (7.9)$$

with

$$X_{r,\mu\nu} = \theta^+_{r,\mu\nu} (n_\nu - n_\mu) \quad , \quad n_\nu > n_\mu$$

$$Y_{r,\mu\nu} = \theta^+_{r,\mu\nu} (n_\nu - n_\mu) \quad , \quad n_\mu > n_\nu$$

$$A_{\mu\nu,\rho\sigma} = (\varepsilon_\mu - \varepsilon_\nu) \, \delta_{\nu\sigma} \, \delta_{\mu\rho} + \overset{A}{v}_{\mu\rho,\nu\sigma} (n_\rho - n_\sigma) \quad , \quad n_\nu > n_\mu, \ n_\rho > n_\sigma$$

$$B_{\mu\nu,\rho\sigma} = \overset{A}{v}_{\mu\rho,\nu\sigma} (n_\rho - n_\sigma) \qquad , \ n_\nu > n_\mu, \ n_\sigma > n_\rho$$

In analogy with (3.9) the following normalization condition may be imposed:

$$\mathrm{tr} \, (\rho_0 \, [\theta_r, \, \theta^+_s \,]) = \delta_{rs}$$

$$\qquad (7.10)$$

$$\mathrm{tr} \, (\rho_0 \, [\theta_r, \, \theta_s \,]) = \mathrm{tr} \, (\rho_0 \, [\theta^+_r, \, \theta^+_s \,]) = 0$$

The general solution of eq. (7.6) is

$$f = \sum_r (f_r \, e^{-i\omega_r t} \, \theta^+_r + f^*_r \, e^{i\omega_r t} \, \theta_r) \qquad (7.11)$$

where the mixed-state transition amplitudes are given by

$$f_r = \mathrm{tr} \, (\rho_0 \, [\theta_r, \, f\,(0)\,])$$

$$f^*_r = \mathrm{tr} \, (\rho_0 \, [f\,(0), \, \theta^+_r \,]) \qquad (7.12)$$

We observe finally that the RPA preserves the energy-weighted sum-rule

$$\sum_r \omega_r |f_r|^2 = 1/2 \, \mathrm{Tr} \, (D_0 \, [F, \, [H, \, F]\,]) \qquad (7.13)$$

where the right-hand side can be evaluated with the aid of (7.2).

If ρ_0 is the independent-particle mixed state determined by conventional equilibrium statistical mechanics then its eigenvalues n are the Fermi-Dirac occupation numbers (6.11) and eqs. (7.8) are known under the name of thermal RPA equations.

8 – CONCLUSIONS

We have developed a variational approach appropriate to physical situations requiring a description in terms of mixed states. The formalism presented leads in a straightforward way to a mean field theory for mixed states. In this framework, the well-known Hartree-Fock and RPA results for pure states are generalized to the case of mixtures.

As extensions of this work, which are presently being carried out, we would like to refer the following:

1 – The description of correlations not included in a mean-field by boson expansions adequate for mixed states. We can establish a temperature dependent Holstein-Primakoff expansion, for magnetically ordered systems, which is useful in the study of the interaction between spin waves [9].

2 – The translation of the quantal mean-field formulae into classical terms. We obtain in this way a thermal Thomas-Fermi theory, for the ground-state of a statistical system, and a fluid dynamical representation of small oscillations around it [10].

3 – The application to heavy ion collisions, such as those described in the introduction. In a realistic model, a constraint on the angular momentum must be introduced and the singe-particle states must be replaced by the single quasi-particle states of the Hartree-Fock-Bogolyubov approach.

REFERENCES

[1] D. M. BRINK, *D. Phil. Thesis*, University of Oxford, 1959 (unpublished).

[2] J. O. NEWTON et al., *Phys. Rev. Lett.*, **46** (1981), 1383.

[3] J. E. DRAPER et al., *Phys. Rev. Lett.*, **49** (1982),434

[4] H. M. SOMMERMAN, *Ann. of Phys.*, **151** (1983), 163.

[5]   D. Vautherin and N. Vinh-Mau, *Nucl. Phys.*, **A422** (1984), 140.

[6]   O. Civitarese et al., *Ann. of Phys.*, **156** (1984), 142.

[7]   P. Ring and P. Schuck, *"The nuclear many-body problem"*, Springer, 1980.

[8]   J. da Providência and C. Fiolhais, *Nucl. Phys.*, **A435** (1985), 190.

[9]   J. da Providência and C. Fiolhais, contribution to the "VIII Workshop on Condensed Matter Theories" Granada, 1984 (to be published).

[10] J. da Providência and C. Fiolhais, "Variational formulation of classical mean field theories for finite temperatures" (to be published).

THE FIRST TOWNSEND COEFFICIENT FOR
ARGON-ISOBUTANE MIXTURES

E. P. de Lima, R. Ferreira Marques, M. A. F. Alves
and A. J. P. L. Policarpo

Departamento de Física, Universidade de Coimbra, 3000 Coimbra, Portugal

ABSTRACT — Using the Korff approximation for the first Townsend coefficient and the evolution of the charge with the anode voltage for a proportional counter geometry, effective molecular parameters were calculated for argon-isobutane mixtures with the following isobutane concentrations: 32, 39, 44, 48, 51, 56 and 60 percent.

1 — INTRODUCTION

Data are available on the first Townsend coefficient α, the mean number of ion-pairs produced per unit length of drift, for noble gases, hydrocarbon gases and a wide variety of mixtures [1].

Argon-isobutane mixtures have been widely used in detectors, an important characteristic of isobutane being its low optical transmission cut-off at ~ 7.3 eV [2], helping to prevent spurious effects due to photon feedback. Together with its widespread use in multiwire proportional chambers, multiwire drift chambers and more recently, time projection chambers, a reasonable knowledge of the basic mechanisms is now available, useful from the point of view of gaseous electronics and of better understanding and predicting the detectors intrinsic properties. Most theoretical interpretations rely on the Boltzman transport equations and are directed towards the transport coefficients, both with and without magnetic fields, computing drift velocities ω and diffusion

Portgal. Phys. — Vol. 16, fasc. 1-2, pp. 27-34, 1985

27

coefficients D. The interpretation of these parameters corresponds essentially, from an instrumental point of view, to the problem of positioning by drift techniques. Using experimental data on D and ω from [3] for mixtures of argon and isobutane (from 7 % up to 38 % isobutane) good fits have been obtained [4] that enabled to guess the behaviour of the total and excitation cross-sections of isobutane with energy [5].

Recently, research in a new mode of charge multiplication in gaseous detectors is being pursued: the formation of narrow streamers ~ 150 μm wide, orthogonally to thick anode wires, that quench themselves under a continuously applied high voltage. Large currents, approaching 1 mA are produced in less than ~ 100 ns, allowing for good localization properties with simple electronics. Again, and essentially for the optical transmission properties of isobutane, argon-isobutane mixtures are being used in the self-quenching streamer mode, SQS [6 , 7], and efforts are being made towards understanding the basic mechanisms involved. It is known that the process is strongly photon mediated and space charge conditioned [8] and based on a mechanism of self-breeding by photoelectrons of the avalanche; quantitative estimations have been made of the photon flux as a function of its wavelength [9]. The first Townsend coefficient is a determinant parameter both for itself and for the calculation of the photon fluxes, essential to a quantitative interpretation of the SQS mode, and in this work experimental data for α over a wide range of isobutane concentrations (large concentrations are a necessary condition to obtain good efficiency plateaux) is presented.

2 — EXPERIMENTAL TECHNIQUE

The experimental system used in this work is essentially the one described in [7]. The gaseous mixture, argon-isobutane, in different proportions, flows through a cylindrical proportional detector under a continuous flow regimen at atmospheric pressure. For the determination of the gaseous composition, calibration curves of the flowmeters were obtained for both gases used. The

detector has an aluminium cathode 13 cm long and 14 mm internal diameter. The anode is a nichrome wire 60 μm thick stretched along the detector axis.

The measurements of the charge characteristics of the chamber were made using a conventional charge amplifier electronic system and multichannel analyzer. The calibration of this system was made by using a Si-semiconductor detector. The bombarding radiation, X-rays from a ^{55}Fe source, enters the detector through an aluminium (0.025 mg/cm^2) window.

3 — EXPERIMENTAL RESULTS AND DATA ANALYSIS

The experimental data obtained in this work are displayed in Fig. 1. The behaviour of the results is similar to that observed in multiwire chambers for the same mixtures [1] and proportional counters used for SQS filled with argon-methane and methylal [10]. It reflects the general behaviour of the first Townsend coefficient in mixtures of noble gases and polyatomic gases namely that, for increasing concentrations of this last component, higher fields are needed to obtain the same α.

Data analysis must consider carefully space-charge distortion of the field, otherwise the molecular properties of the gas are obscured. Provided that this effect is taken into account determination of α for such different techniques as sparking potentials and conduction measurements [11] lead to the same results for the same regions of E/p.

Space-charge effects are well defined in Fig. 1 for charges $\geq$ 1.5 pC. This detector was provided with better insulators (^{1}) than a counter used previously for SQS studies [7]; the spread of pulse-heights for higher voltages was small so that reliable data, with clear space-charge effects, could be collected. These data were used for the analysis reported in this work.

The usual Korff approximation [12] $\alpha = $ pA exp ($-$ B p/E) was used, where A and B are constants for a certain mixture, p is the pressure and E the electric field. From the field confi-

---

(^{1}) Kindly made for us by Dr. Rob Hollander, of IRI-ISO group, Delft Technical University, Holland.

guration, the charge gain of the counter is given, with a very good approximation, by

$$Q(V) = (E_{RX} \, e/W) \, \exp \, [\, AV' \, / \, B \, \exp \, (-Ba \, / \, V') \,]$$

where E_{RX} is the X-ray energy, e the electron charge, W the energy needed to produce an ion pair and $V' = V/\ln(b/a)$, V being the applied voltage, b and a the cathode and anode radius
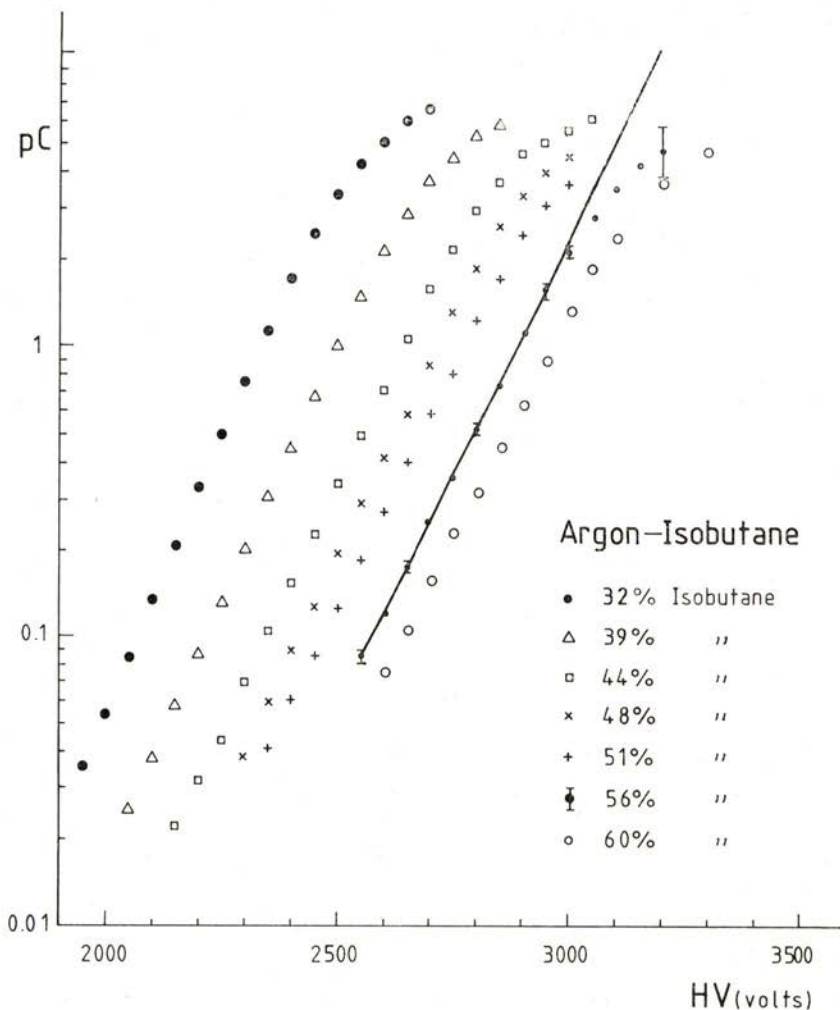
Fig. 1 — The average measured charge against applied anode voltage for different argon-isobutane mixtures. The isobutane concentration is quoted for each mixture. A least squares fit is shown.

respectively. The number of primary ion pairs was calculated using the formula given in [13]. Weighted non-linear least square fits to the experimental data, using the expression above for the gain, were made for the several concentrations of isobutane. As an example Fig. 2 shows the evolution of x^2, by varying the number of experimental data points used (successively supressing data corresponding to higher anode voltages) with the highest charge, Q_{max}, included in the fit. The same Fig. 2 shows also a detected correlation between A and B, that was taken into account,
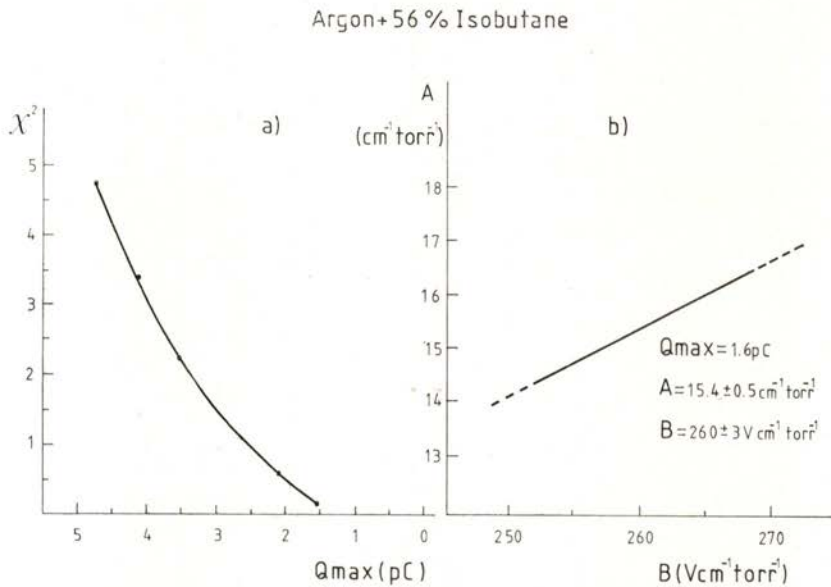
Argon + 56 % Isobutane

Fig. 2 — a) The evolution of the x^2 as a function of maximum charge included in the fit (Q_{max}); b) The detected correlation between parameters A and B for the argon + 56 % isobutane mixture; full line corresponds to good fits.

at this stage, simply by the uncertainties quoted for A and B. As an example, a best fit for the argon + 56 % isobutane is shown in Fig. 1, deviations at large charges being attributed to space-charge effects, although the question of the validity of the expression used for α should not be completely disregarded. The data obtained are summarized in Table I. Uncertainties in A are $\sigma_A \simeq 0.5$, and in B, $\sigma_B \simeq 3$.

TABLE I — Derived molecular constants according to $\alpha = pA \exp(-Bp/E)$

% isobutane	32	39	44	48	51	56	60
A (cm^{-1} $torr^{-1}$)	13.1	14.6	15.8	16.6	15.5	15.4	17.9
B (V cm^{-1} $torr^{-1}$)	195	220	240	255	251	260	286
E/p max (V cm^{-1} $torr^{-1}$)	185	205	213	221	225	237	241

The corresponding effective mean free path length at atmospheric pressure $\lambda_{mo} = 1/A$ (λ_m at pressure p is given by λ_{mo}/p) and the effective ionization potential $V_i = B \lambda_{mo}$ [14], are presented in Table II.

TABLE II — Effective molecular parameters

% isobutane	32	39	44	48	51	56	60
λ_{mo} (μm)	1.00	0.90	0.83	0.79	0.85	0.85	0.74
V_i (eV)	14.87	15.08	15.23	15.37	16.14	16.91	15.98

4 – DISCUSSION

The main source of uncertainty associated with the data obtained in this work may be related to space-charge effects: positive ions produced in the early avalanches give rise to modifications of the local electric field and therefore reduce the gain

32

Portgal. Phys. — Vol. 16, fasc. 1-2, pp. 27-34, 1985

associated to electrons, from the same track, arriving later to the high field region.

Experimental data available now for this effect concern both proportional counter and multiwire chambers [15, 16, 17] and the space charge reduction is of course dependent on the track geometry and diffusion. Data using X-rays leading to energy deposits varying by an order of magnitude (Mn K and Mn L) show space-charge gain effects starting at about 1 pC (0.3 pC from [16] and 2.4 pC from [15]) if the criterion of negligible field distortion for the lower energy deposit is used. Although the main experimental parameters used by these authors that can affect the space-charge are similar to those of this work (X-ray energy, diffusion, wire thickness) another relevant one, the spatial distribution of the avalanche, is unknown. Nevertheless the threshold for field distortion obtained in this work by the use of Korff's approximation can be considered quite reasonable implying the validity of that approximation for the argon-isobutane mixtures studied, up to the E/p values quoted.

The value of the effective ionization potential V_i is also natural: indeed the thresholds for ionization for argon and isobutane are respectively 15.77 eV and 10.57 eV, and the mean energy to make an ion-pair is about 25 eV. No considerations can be made concerning λ_{mo} due to lack of information on cross-section for ionization: for processes induced by electron impact there is data up to 8 eV only.

In the same way that experimental data on drift velocities and diffusion parameters allowed the determination of total and excitations cross-sections for mixtures of argon and isobutane, the data presented here may lead to the calculation of ionization cross-sections.

As a general indication and to be compared with the data of this work effective molecular parameters for several hydrocarbons are calculated from [11] and shown in Table III.

TABLE III — Effective molecular parameters [11]

Hydrocarbon	Methane	Ethane	Ethylene	Acetylene
λ_{mo}	1.8	1.3	1.4	0.88
(μm)	1.5	1.1	1.2	0.87
V_i	27.1	23.2	32.0	22.2
(eV)	23.8	19.4	29.4	22.5
E/p range (V cm^{-1} torr^{-1})	33-165	50-190	43-154	47-285

REFERENCES

[1] F. SAULI, *Principles of Operation of Multiwire Proportional Drift Chambers*, CERN 77-09, Geneve, 1977.

[2] E. BARRELET, T. EKELÖF, B. LUND-JENSEN, J. SEGUINOT, J. TOCQUEVILLE, M. URBAN, T. YPSILANTIS, *Nucl. Instr. and Meth.* **200** (1982) 219.

[3] G. CHARPAK, F. SAULI and W. DUINKER, *Nucl. Instr. and Meth.* **108** (1973) 413.

[4] V. PALLADINO and B. SADOULET, *Nucl. Instr. and Meth.* **128** (1975) 323.

[5] G. SCHULTZ and J. GRESSER, *Nucl. Instr. and Meth.* **151** (1978) 413.

[6] G. BATTISTONI, E. IAROCCI, M. M. MASSAI, G. NICOLETTI and L. TRASATTI, *Nucl. Instr. and Meth.* **164** (1979) 57.

[7] E. P. DE LIMA, M. SALETE S. C. P. LEITE, A. J. P. L. POLICARPO and M. A. F. ALVES, *IEEE Trans. Nucl. Sci.* **NS-30** (1983) 90.

[8] M. ATAC, A. V. TOLLESTRUP and D. POTTER, *Nucl. Instr. and Meth.* **200** (1982) 345

[9] E. P. DE LIMA, A. J. P. L. POLICARPO, M. SALETE S. C. P. LEITE and JOAQUIM DE JESUS, *IEEE Trans. Nucl. Sci.* **NS-32** (1985) 510.

[10] G. D. ALEKSEEV, N. A. KALININA, V. V. KARPUKHIN, D. M. KHAZINS and V. V. KRUGLOV, *Nucl. Instr. and Meth.* **177** (1980) 385.

[11] A. E. D. HEYLEN, *J. Chem. Phys.* **38** (1963) 765.

[12] S. A. KORFF, *Electron and Nuclear Counters*, Van Nostrand, New York (1946).

[13] C. E. MELTON, G. S. HURST and T. E. BORTNER, *Phys. Rev.* **96** (1954) 643.

[14] A. VON ENGEL, *Ionized Gases*, Clarendon Press, Oxford (1965); T. WATANABE, C. MORI, and T. AOYAMA, *Nucl. Instr. and Meth.* **178** (1980) 121.

[15] C. MORI and T. WATANABE, *Nucl. Instr. and Meth.* **204** (1982) 149.

[16] C. MORI, M. UNO and T. WATANABE, *Nucl. Instr. and Meth.* **196** (1982) 49.

[17] H. WALENTA, *Proc. of the Isabelle Summer Workshop* (1977), BNL 50721, (1977) 41; H. FRESH, F. LAPIQUE, M. PANTHER and F. PIUZ, *Nucl. Instr. and Meth.* **156** (1978) 87.

EXCITED STATES OF THE «H3» CENTRE
IN DIAMOND

Maria Helena Nazaré and Gordon Davies (¹)

Departamento de Física e Centro de Física (INIC)
Universidade de Aveiro, 3800 Aveiro, Portugal

ABSTRACT — We report the effects of uniaxial stress perturbations on the H13 absorption lines in diamond. These lines are transitions to higher excited states of the well-known H3 optical centre. We show that, in common with other centres in diamond, the symmetry of the H3 centre is the same in each of its electronic states. However, there are large differences in responses of the different states to stresses. This suggests that each of the electronic states at the H3 centre is highly localised at the centre. The vibronic interactions between these spatially localised states produce significant effects on the optical spectra, even for states of very different energies.

1 — INTRODUCTION

When different experimental techniques are used to probe a defect in a crystal, they often produce data on different electronic states (including different charge states) of the defect. Because the equilibrium atomic configuration of the defect depends on the electron distribution, the defect may be observed with very different structures by the different experimental techniques. For example, recent work on a carbon-carbon defect in silicon has shown that the two carbon atoms occupy equivalent sites

---

(¹) Department of Physics, King's College, Strand, London WC2R 2LS.

in the lattice when the defect is examined using optically detected magnetic resonance [1], but the two C atoms are grossly inequivalent when the defect is investigated by electron paramagnetic resonance [2].

Structural changes like these are of interest in themselves. They also cause practical problems. For example, they make it difficult to be certain whether the same defect is being observed in different experiments.

In diamond there are only a few published sets of optical studies made on significantly different states of centres. These studies are of:

a) *The neutral vacancy.* The lowest energy optical transition (zero-phonon line at 1.673 eV) has been studied in detail, particularly, e. g. [3], by the technique of uniaxial stresses which will concern us throughout this paper. A series of higher transitions nearer 3 eV has also been investigated by uniaxial stresses [4]. In all the electronic states the neutral vacancy has the same point group symmetry: tetrahedral.

b) *The negative vacancy.* An optical transition at 3.150 eV ascribed to the negative vacancy [5] has been investigated by uniaxial stresses [6]. The symmetry of the centre is again tetrahedral: evidently changing the charge state of the vacancy in diamond from neutral to singly negative does not change its symmetry. This contrasts strongly with the different symmetries observed for different charge states of the vacancy in silicon [7].

c) *The 594 nm centre.* This centre is known to produce both the 2.086 eV (594 nm) and the 2.917 eV zero-phonon lines [8]. In both cases uniaxial stress measurements have shown the centres to be trigonal [8, 9]. In addition, paramagnetic resonance measurements on optically excited states (e. g. data on the nitrogen-vacancy centre, by J. A. van Wyk, private communication 1984) also show the same symmetries as those deduced from the optical studies.

Present evidence suggests then that defects in diamond probably have the same symmetry, regardless of electronic state.

36

Portgal. Phys. — Vol. 16, fasc. 1-2, pp. 35-50, 1985

The purpose of this paper is to examine another optical centre, the well-known "H3" centre with its main zero-phonon line at 2.463 eV. The centre is believed to be formed from two substitutional nitrogen atoms and one vacancy [10]. Recently [11] Collins has shown that the "H13" absorption line at 3.361 eV most probably also occurs at the H3 centre. This result is intriguing for the 2.463 eV transition has been shown [12] to occur at a rhombic I centre (point group C_{2v}), while the 3.361 eV line has been shown [13] to occur at a trigonal centre (point group C_{3v}, D_3 or D_{3d}). In this paper we present new data on the effects of uniaxial stresses on the 3.361 eV transition (and neighbouring lines). In § 3 we show that the 3.361 eV line does occur at a rhombic I centre, as for the 2.463 eV line: again the point group of a centre is the same for different excited states. We show that there are significant differences in the effects of stress on each excited state. In § 4 we suggest that these differences can produce interesting vibronic effects, and we show that unusual features in the absorption spectra of the H3 centre may be explained.

2 – EXPERIMENTAL DATA

Natural diamonds were used throughout. The samples were cut to cuboids with linear dimensions of 1 to 2 mm, and were oriented so that stresses could be applied along the main crystallographic axes. The crystals were irradiated with about 5×10^{21} m^{-2} 2 MeV electrons and annealed at about 1100 K for two hours.

The 3.361 eV line is relatively weak. Throughout this work measurements were therefore made using the luminescence excitation technique with the samples at liquid nitrogen temperature. The specimen was excited by light from a 1 kW Xenon arc, focussed through a 3/4 m grating monochromator. Luminescence from the sample was detected in a direction perpendicular to the exciting beam. Fig. 1 shows the zero-stress luminescence excitation spectrum recorded with all the visible luminescence being detected from the diamond at photon energies $h\nu < 2.5$ eV. This luminescence occurs from the H3 band (i.e. the 2.463 eV zero-phonon line and all its phonon sidebands [11]). This is confirmed

by the broken line on Fig. 1 which shows the luminescence excitation spectrum recorded at the *same* resolution but using a second monochromator to select only H3 luminescence (defined as the difference between the luminescence intensity at the peak of the H3 one-phonon sideband and the intensity at the minimum

159 meV

3·2   3·3   3·4   3·5   3·6

Photon energy eV
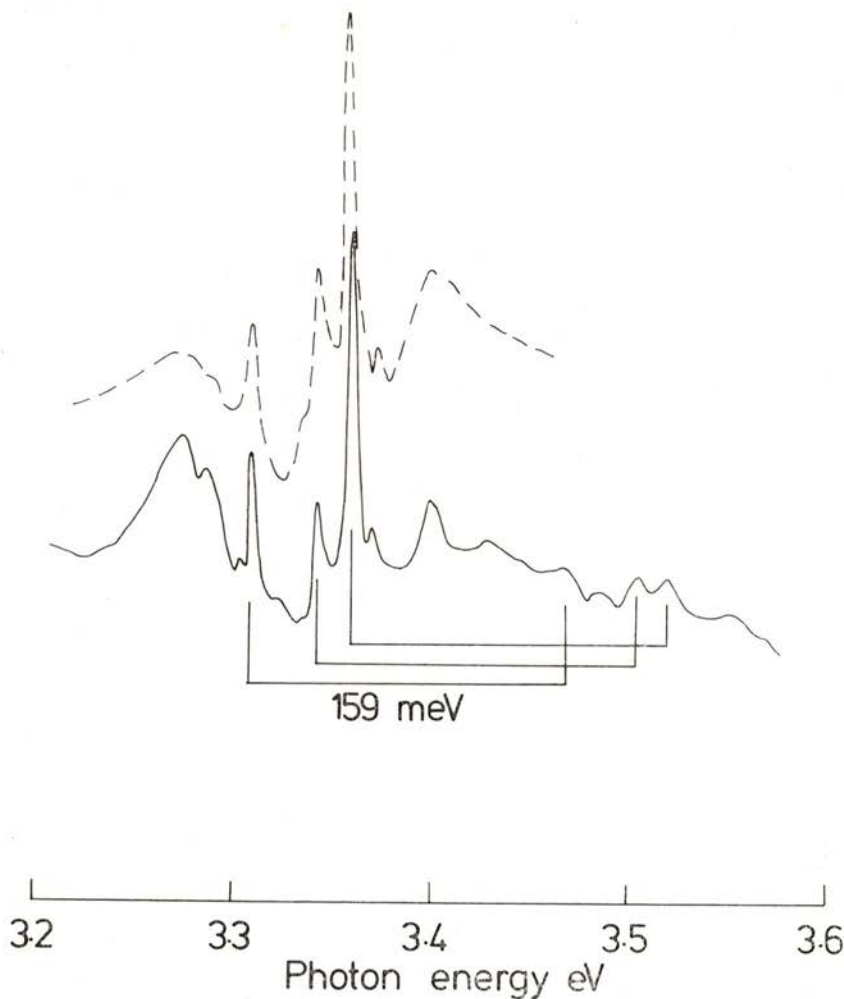
Fig. 1 — Luminescence excitation spectrum of the «H13» region at liquid nitrogen temperature. The solid line shows the spectrum recorded when all the emission in the H3 region is detected. The broken line shows the spectrum detected when a second monochromator was used to select only H3 emission, and is a higher resolution version of the spectrum given in reference [11].

between the first and second H3 phonon sidebands). The total luminescence excitation spectrum evidently arises predominantly from the H3 band. In the stress experiments the total emission with $h\nu < 2.5$ eV was detected.

Fig. 2 shows the spectra recorded under uniaxial compressions along the $<001>$, $<111>$ and $<110>$ axes. The energies of the stress-split components are shown as functions of the applied stress in Fig. 3. When detecting the luminescence from a resonantly excited defect, the observed stress-splitting pattern should depend on the experimental geometry [18]. However, in these experiments using small specimens it was not feasible to mask the crystals so as to closely define the optical geometry without seriously decreasing the already small signal. The polarisation of the spectra we recorded were very similar to those reported in the earlier absorption measurements [13].

3 – ANALYSIS OF THE EXPERIMENTAL DATA

The exact form of the spectrum near 3.3 eV is sample dependent. In particular, the broad line near 3.32 eV shown in the sample for $<001>$ and $<110>$ stresses (figure 2) is independent of the H3 centre: it is associated with the similar «H4» centre [14]. Allowing for these independent lines there are still many transitions in figure 1 occurring at the same centre. The 3.344 eV line has been correlated with the 3.361 eV line [13]. Other transitions at 3.310 and 3.373 eV, and the doublet at 3.403 eV always appeared in our samples in very similar strengths relative to the 3.361 eV line. Further evidence that the 3.310, 3.344, 3.361 and 3.403 eV lines occur at the same centre comes from what appear to be their one-phonon sidebands, all involving a well-defined phonon peak energy 159 ± 0.7 meV. The assigned one-phonon (and in some cases two-phonon) sidebands are linked to their zero-phonon lines in figure 1. The different intensities of the one-phonon sidebands relative to the zero-phonon lines will be discussed in § 4.

The presence of all these closely spaced transitions creates problems in interpreting the uniaxial stress data. Stress induced interactions must be expected to occur producing shifts that are non-linear functions of the applied stress. In addition some of the
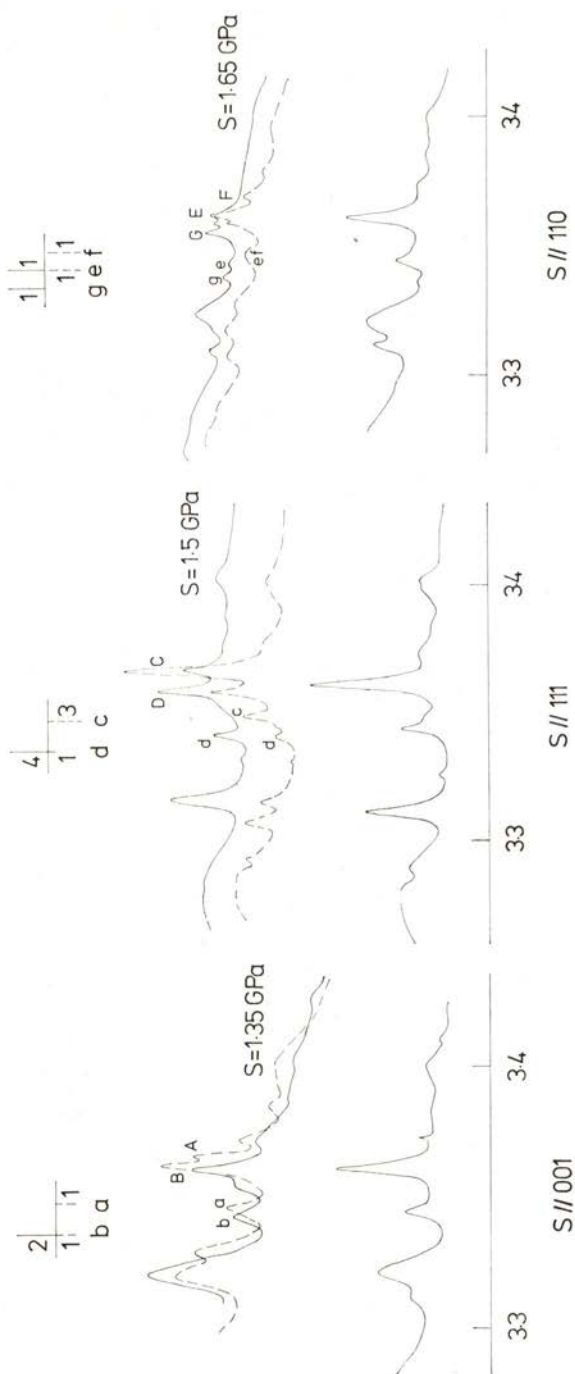
Fig. 2 — Effect of uniaxial stresses on the luminescence excitation spectrum in the H13 region. For each stress axis, the bottom spectum was recorded at zero stress. The two upper spectra were recorded at the indicated stresses — the solid line is for the exciting light polarised parallel to the stress axis and the broken line is for exciting light polarised perpendicular to the stress axis. For [110] stress the perpendicular polarisation has its electric vector parallel to [1$\bar{1}$0]. All spectra were recorded at liquid nitrogen temperature. The spike spectra show the predicted splitting patterns for the transition at a rhombic I centre, as discussed in § 3.
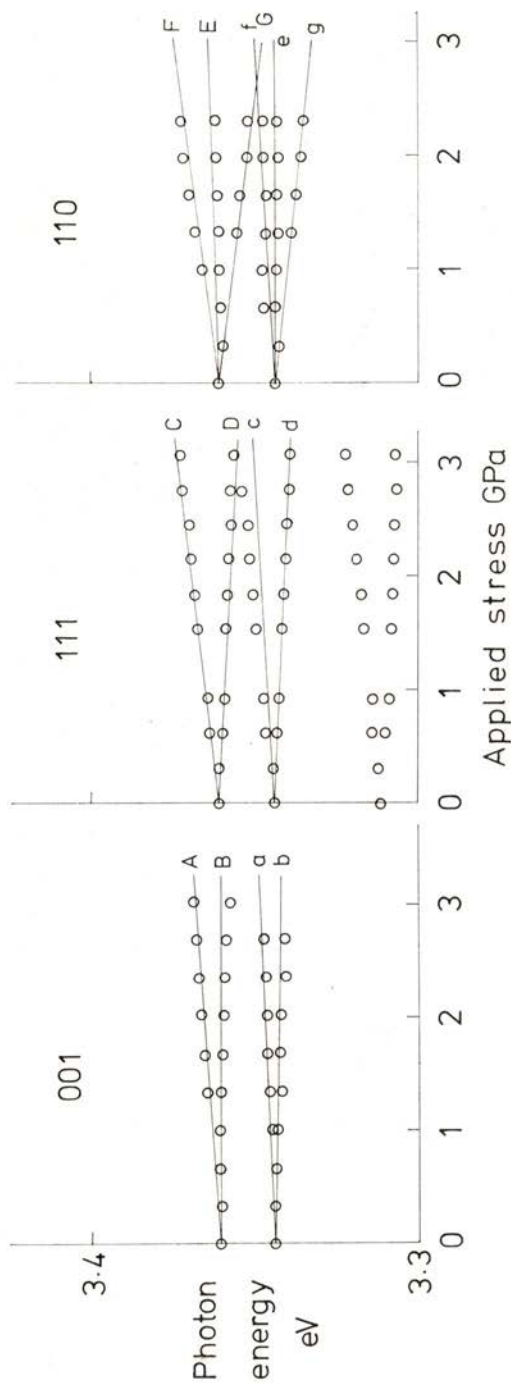
Fig. 3 — The energies of the stress-split components from the 3.344 and 3.361 eV lines as a function of stress. The points are experimental data recorded at liquid nitrogen temperature. The solid lines are calculated as in § 3 using first order theory only. The 3.310 eV H3-associated line is only clearly resolved in our data for [111] stress: in this case the shift rates appear to be similar to those of the 3.344 and 3.361 eV lines.

(non-interacting) components become superimposed with increasing stress (e. g. components C and D on figure 2). The widths of the lines (~ 4 meV at zero stress and low temperature) are sufficiently large compared to some of the large separations of the lines that a fully detailed analysis is not feasible.

The effects of stresses in all three stress directions are clearest for the 3.344 eV line. This splits into the number of components with the polarisations and relative intensities only as expected for a transition at a C_{2v} centre (see insets to figure 2 and reference [15]) or an A to E transition at a tetragonal centre [16, 17]. The latter assignment requires the E state not to split under stress; the simplest assignment is that the 3.344 eV line occurs in the same C_{2v} symetry as the 2.463 eV line of the centre.

Under uniaxial stress, a transition at a C_{2v} centre oriented with its C_2 axis along the [001] crystal axis is perturbed *to first order* in the stress tensor components by [15]:

$$\Delta (h\nu) = A_1 s_{zz} + A_2 (s_{xx} + s_{yy}) + A_3 s_{xy} \qquad (1)$$

where the s_{ij} are defined with respect to the crystal axes x, y, z . By "first order perturbation" we mean that the stress is sufficiently small that there is negligible stress-induced mixing of the states involved in the transition with any other state of the centre.

Under <001>, <111> and <110> the energy dependence of each stress-split component is given in terms of the unknown "stress parameters" A_1, A_2 and A_3 as shown in Table 1. The unweighted least squares fit of the theoretical shift rates to the observed shift rates (denoted *a* for line *a* etc.) is obtained when A_1 and A_2 satisfy

$$25A_1 + 149A_2 = 36b + 24 (c+d) + 36 (f+g) + 18e$$

and

$$53A_1 + 25A_2 = 36a + 12 (c+d) + 18e ,$$

and when

$$26A_3 = 6 (d-c) + 9 (g-f) .$$

The least squares fit is shown by the lines on figure 3, using the parameters listed in Table 1. The fit appears to be plausible.

TABLE 1

a) Comparison of the experimental and theoretical
shift rates for the 3.344 and 3.361 eV lines.

| Stress axis | Linear shift rates | Shift rates (meV / GPa) | | | | | |
| | | 3.344 eV | | | 3.361 eV | | |
		Compt	Expt	Fit	Compt	Expt	Fit
001	A_1	a	1.1	1.4	A	2.7	2.5
	A_2	b	−1.2	−0.7	B	−0.8	0.1
111	$1/3 (A_1 + 2A_2 - 2A_3)$	c	3.6	2.1	C	4.0	4.1
	$1/3 (A_1 + 2A_2 + 2A_3)$	d	−1.6	−2.0	D	−1.5	−2.2
110	$1/2 (A_1 + A_2)$	e	−0.2	0.4	E	0.6	1.3
	$A_2 - A_3$	f	1.8	2.4	F	5.6	4.9
	$A_2 + A_3$	g	−3.6	−3.7	G	−4.4	−4.6

Typical uncertainties are ± 0.3 meV / GPa .

b) Stress parameters used in the fit (meV / GPa).

Line (eV)	A_1	A_2	A_3
3.344	1.5	−3.1	−0.7
3.361	2.5	−4.7	0.1
2.463 (H3)	−8.7	6.9	6.7

The uncertainties in the parameters for the 3.344 and 3.361 eV lines are
~ ±0.2 meV / GPa. This large uncertainty is caused by the relatively small
perturbations of the closely spaced lines.

From the polarisation of the stress-split components, the
3.344 eV line occurs from a ground state whose irreducible
representation in the C_{2v} point group is A_1 to the excited B_1
state, or any other transition which can occur under a $<110>$

electric dipole moment. (A complete tabulation of equivalent transitions is given in reference [12]). Since the 3.344 eV transition occurs from the same ground state as the 2.463 eV line, which we will assume for definiteness is an A_1 state, there are only two possibilities for the excited state of the 3.344 eV line, B_1 or B_2, which are consistent with our stress data.

The 3.361 eV line behaves in a similar way to the 3.344 eV line (figures 2 and 3). The main difference is that the stress-split components of the 3.361 eV line are not polarised as fully as expected for an isolated A_1 to B_1 transition. For example, under $<111>$ stress component C is not fully polarised with its electric vector perpendicular to the stress axis. Possibly this is an effect of the nearby 3.373 eV line, whose stress-split components overlap (and probably interact with) those of the 3.361 eV line. We cannot separate these effects in the experimental data. However, in the limit of large stress, similar states which interact weakly with each other split with shift rates equal to the non-interacting states. We have therefore fitted the theory of equation (1) to the 3.361 eV line. The shift rates are shown in figure 3. There is a plausible fit to the experimental data using the stress parameters listed in table 1. These parameters are very similar to those of the 3.344 eV line, also listed in the table. In the most clearly resolved spectra, taken under $<111>$ stress, the H3-related line near 3.31 eV also appears to split with a similar shift rate to the 3.344 and 3.361 eV lines (figure 3).

We have shown that the 3.344 and 3.361 eV transitions occur at a C_{2v} symmetry, the same as for the lower energy 2.463 eV line. The earlier assignment of the 3.344 and 3.361 eV lines to a trigonal centre [13] arose through misinterpreting the complex experimental data resulting from the many, nearly degenerate, excited states of the centre.

4 — VIBRONIC COUPLING

We have shown that the symmetry of the «H3» defect is the same in the «H13» excited states (near 3.36 eV) as in the «H3» excited states (at 2.463 eV). However, the stress parameters show that substantial relaxations occur between the H3 and H13 states. The stress parameters of table 1 only give the

difference in perturbation of the excited and ground zero-phonon states (equation 1). The differences between H13 and H3 are of the same order as the H3 parameters (last line, table 1). Evidently the electronic orbitals in the 2.463 eV and 3.361 eV excited states are both still sufficiently localised that the electron-lattice coupling is strongly dependent on the electronic state. It follows that these compact electronic orbitals may interact with each other vibronically as the atoms of the defect vibrate.

As an example of the vibronic coupling we consider the 3.344, 3.361 eV pair of zero-phonon lines. These lines are observed in the intensity ratio (figure 1):

$$I_{3.344} / I_{3.361} \simeq 0.2 \ .$$

Their one phonon sidebands involving the 159 meV phonons are very weak, but are almost equal in intensity. This difference does not arise from different electron-lattice interaction of the two electronic states, for their stress parameters are closely similar (table 1). A more likely cause is that the 3.344 and 3.361 eV states are interacting vibronically, the interaction transferring intensity from the 3.361 eV zero-phonon line to the one-phonon sideband of the 3.344 eV line. The amount of the intensity transferred is about 0.1 of the intensity of the 3.361 eV line, assuming that in the absence of the interaction the one-phonon sidebands of the 3.344 and 3.361 eV lines would have had intensities in proportion to the zero-phonon lines.

For a quantitative discussion we denote the electronic excited state of the 3.344 eV line by $\phi_1 (r)$, and that of the 3.361 eV line by $\phi_2 (r)$, where r represents all the electronic co-ordinates. The harmonic oscillator wave-functions for the nth quantum level of the 159 meV mode is denoted $\chi_n (Q)$, where Q is the mode's coordinate. Since the 3.344 and 3.361 eV lines have similar stress parameters (table 1) we will assume that the equilibrium values of Q for these two states are the same. Then, in the absence of any vibronic interaction, the vibronic wavefunctions and energies for the two states are simply

$$\psi_{1,n} (r, Q) = \phi_1 (r) \chi_n (Q) , \ E = W_1 + (n + 1/2) \hbar \omega$$
$$\psi_{2,n} (r, Q) = \phi_2 (r) \chi_n (Q) , \ E = W_2 + (n + 1/2) \hbar \omega$$

where W_1 and W_2 are the energies of the two electronic states.

We now introduce a vibronic coupling perturbation energy

$$C = c\,Q\,. \tag{2}$$

Here c is an electronic operator with a matrix element

$$C = \int dr\ \phi_1(r)\,c\,\phi_2(r) \tag{3}$$

between the two states. This perturbation couples vibronic states differing by one in the quantum number:

$$\int dr\, dQ\ \psi_{1,n}\ c\, Q\ \psi_{2,n+1} = C\ (\hbar/m_\omega)^{1/2}\ \sqrt{(n+1)/2}$$

$$\int dr\, dQ\ \psi_{1,n-1}\ c\, Q\ \psi_{2,n} = C\ (\hbar/m_\omega)^{1/2}\ \sqrt{n/2} \tag{4}$$

This coupling mixes the $\psi_{1,n}$ and $\psi_{2,n}$ to form new vibronic states

$$\psi_p(r,Q) = \sum_n a_{pn}\,\psi_{1,n}(r,Q) + \sum_n b_{pn}\,\psi_{2,n}(r,Q)$$

The coefficients a_{np}, b_{pn} are given by the secular matrix whose elements are as given in equation (4), in terms of the unknown $C\,(\hbar/m_\omega)^{1/2}$ and

$$W_2 - W_1 \simeq 17\,\text{meV}\,.$$

From the coefficients the transition probability to the pth vibronic level is

$$T_p = (t_1\,a_{po} + t_2\,b_{po})^2 \tag{5}$$

where from the measured zero phonon intensities

$$(t_1/t_2)^2 = 0.2\,.$$

Numerical diagonalisation shows that 0.1 of the 3.361 eV absorption would be transferred to the one-phonon sideband of the 3.344 eV line when

$$C\,(\hbar/m_\omega)^{1/2} \simeq 50\,\text{meV} \tag{6}$$

with about a $\pm\,20\,\%$ uncertainty.

46

Portgal. Phys. — Vol. 16, fasc. 1-2, pp. 35-50, 1985

To give this interaction energy some physical meaning we can compare it to the stress parameters of table 1. From equations (2) and (3), C is the interaction energy between ϕ_1 and ϕ_2 for a unit displacement in Q. Multiplying C by a bond length in diamond, $a_0 = 0.154$ nm, gives the interaction energy per unit strain in the crystal. Division by an appropriate elastic constant e for diamond then gives an interaction energy per unit stress. The choice of elastic constant depends on the mode of vibration (e. g. whether it is a shearing mode or produces compressions on any particular axis). The type of mode is not known. We will use a simple mean of the elastic constants C_{11}, C_{12} and C_{44} with the value $e \simeq 600$ GPa per unit strain. Using the mass of one carbon atom for m and $\hbar\omega = 159$ meV, from equation (6) the interaction energy per unit stress is

$$C_s = Ca_0 / e \simeq 2.7 \text{ meV} / \text{GPa} .$$

This is within the range of the stress parameters for the H3 centre (table 1). The interaction will lead to stress-induced mixing of the 3.344 and 3.361 eV lines in the stress experiments. On figure 3 the stress-split components of the 3.344 eV line move almost parallel to the components of the 3.361 eV line they are interacting with, reducing the effects of the interaction. At 2 GPa, two states 17 meV apart interacting through C_s would have their energies changed by ~ 1.6 meV as a result of their mutual repulsion: an effect less than the width of the 3.344 and 3.361 eV lines. The repulsion would be primarily seen as an apparent change of slope of the stress-split components and probably accounts for some of the deviations between experiment and theory on figure 3.

The same idea of vibronic coupling can be used to explain the unusual peak at 3.28 eV in figure 1, which is associated with the H3 centre [11]. The 3.28 eV line has an integrated intensity of the order of 10^{-2} of the intensity of the H3 vibronic band. The 3.28 eV line is very wide, 43 meV at low temperature, over ten times wider than typical zero-phonon lines in diamond. We suggest that it is the one-phonon sideband of a forbidden transition at the H3 centre; the line is observed through vibronic mixing with the H3 band. We assume (and we will support this below) that the phonon mode has again $\hbar\omega = 159$ meV. The energy of

the forbidden zero-phonon line producing the 3.28 eV line is therefore ~ 3.12 eV, ~ 470 meV higher than the centroid of the H3 band. Repeating the vibronic calculations with

$$W_2 - W_1 = 470 \text{ meV},$$

and with the transition probabilities $t_1 = 1$, $t_2 = 0$ in equation (5), we find that 10^{-2} of the absorption would be transferred to the 3.28 eV line when the vibronic interaction term

$$C \ (\hbar/m\omega)^{1/2} \simeq 160 \ \text{meV}$$

(see figure 4). The resulting stress parameter $C_s \simeq 8.6 \text{ meV} / \text{GPa}$ is still within the range observed at the H3 centre (table 1).
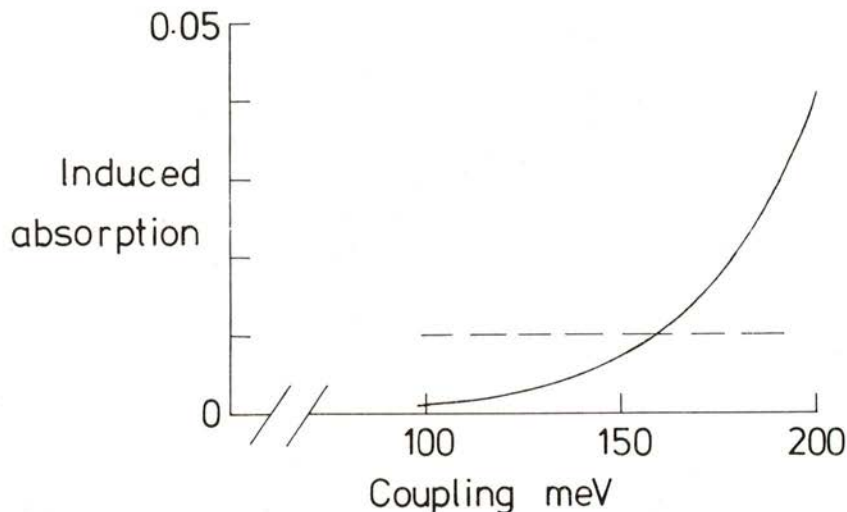
Fig. 4 — The solid line shows the calculated fraction of the absorption transferred from an allowed to a forbidden transition when the excited states of the allowed and forbidden lines are separated by 470 eV. The broken line shows the experimental value for the 3.28 eV H3-associated line relative to the H3 band; this value is obtained at a vibronic coupling (defined in § 4) of 160 meV, equivalent to a typical stress parameter for the H3 centre.

The same mechanism can explain the 3.32 eV H4 associated line seen on figure 2. This line again is 10^{-2} of the H4 band, and

again its electronic state lies ~ 460 meV above the centroid of the allowed (H4) band. In this case a further peak, ~ 150 meV above the 3.32 eV line, can be resolved in favourable samples [14]; this is interpreted as the two-phonon sideband of the forbidden line, giving direct evidence for a mode quantum $\hbar\omega$ ~ 150 to 160 meV.

Paul Spear (private communication 1983) has shown that the 3.32 eV line is a transition at a monoclinic I centre, the same symmetry as the H4 centre, as would be expected in this model.

Vibronic interactions between states separated by considerable energies are clearly possible in diamond, producing the features like the 3.28 eV line. Vibronic interactions like these can occur essentially because the amplitudes of the vibrations are equivalent to considerable strains. For example, a 159 meV mode involving one vibrating carbon atom has a root mean square amplitude in its zero-point (n=0) motion of

$$[<Q^2>]^{1/2} = (\hbar \ / \ m\omega)^{1/2} = 3.3 \times 10^{-12} \, m$$

This is equivalent to a 2 % strain of a 0.154 nm bond length, very large compared with the 0.3 % strains typical in uniaxial stress experiments.

5 – SUMMARY

We have shown that the excited states of the H3 centre, giving transitions near 3.35 eV, occur at a C_{2v} centre, the same symmetry as the basic 2.463 eV H3 transition. Nevertheless substantial differences occur in the response to stresses of the different excited states of the H3 centre. These lead to vibronic coupling, modifying the form of the optical spectra. In particular, isolated broad lines may occur, as observed in the experimental spectra, as a result of the vibronic coupling. Measurable bands may be induced even when the forbidden line is several hundred meV distant from the allowed line. We have suggested that this is the origin of the broad 3.28 eV line associated with the H3 centre. With this assignment, a phenomenological explanation has

now been given for all the H3-associated lines observed in the visible and ultra-violet spectra of irradiated and annealed diamond.

REFERENCES

[1] K. P. O'DONNELL, K. M. LEE and G. D. WATKINS, *Physica,* **116B**, 258 (1983).

[2] K. L. BROWER, *Phys. Rev.,* **B9**, 2607 (1974).

[3] G. DAVIES and C. FOY, *J. Phys.,* **C13**, 2203 (1980).

[4] C. FOY and G. DAVIES, *J. Phys.,* **C13**, L25 (1980).

[5] G. DAVIES, *Nature,* **269**, 498 (1977).

[6] G. DAVIES and E. C. LIGHTOWLERS, *J. Phys.,* **C3**, 638 (1970).

[7] G. D. WATKINS, «Lattice defects in semiconductors 1974». Inst. Phys. Conf. Ser., **23**, ed. F. A. Huntley, (Bristol: Institute of Physics), pp. 1-22.

[8] G. DAVIES and M. H. NAZARE, *J. Phys.,* **C13**, 4127 (1980).

[9] G. DAVIES, *J. Phys.,* **C12**, 2551 (1979).

[10] G. DAVIES, *J. Phys.,* **C9**, L537 (1976).

[11] A. T. COLLINS, *J. Phys.,* **C16**, 6691 (1983).

[12] G. DAVIES, M. H. NAZARE and M. F. HAMER, *Proc. R. Soc. London,* **A351**, 245 (1976).

[13] M. H. NAZARE and J. P. CASQUILHO, *Portugal. Phys.,* **12**, 229 (1981).

[14] A. T. COLLINS, M. F. THOMAZ and M. I. B. JORGE, *J. Phys.,* **C16**, 5417 (1983).

[15] A. A. KAPLYANSKII, *Opt. Spectros.,* **16**, 329 (1964).

[16] A. A. KAPLYANSKII, *Opt. Spectros.,* **16**, 557 (1964).

[17] A. E. HUGHES and W. A. RUNCIMAN, *Proc. Phys. Soc.,* **90**, 827 (1967).

[18] K. MOHAMMED, G. DAVIES and A. T. COLLINS, *J. Phys.,* **C15**, 2779 (1982).

RECENTLY FORMED STARS: OBSERVATIONS AND MODELS (*)

M. T. V. T. Lago and C. C. Sá

Grupo de Matemática Aplicada, Universidade do Porto, 4000 Porto, Portugal

ABSTRACT — The impact of the recent observational achievements of Space Astronomy together with new developments in the theories of star formation, stellar evolution and the origin of the Solar System led to a burst in research work on recently formed stars.

This paper, a compilation of our own ongoing research in this topic is divided in three sections: 1 — The Introduction, where the properties characteristic of young stars, specially T Tauri stars, are summarized; section 2 — containing a brief description of our spectroscopic data (both in the UV and in the visual wavelength region) and of the resulting physical parameterization of the atmosphere of the star inferred from the analysis of these data, and section 3 — a brief reference to models we developed constrained by the observational results refered in the previous section.

Since the paper aims at a compilation more than a presentation of detailed work no effort has been made to explain, either techniques and methods used or how the results were obtained. References to those are occasionally given and we direct the interested reader to them.

1 – INTRODUCTION

While refering to young stars we will concentrate on the so called class of T Tauri stars. Without entering in the details of how a particular star will be classified as belonging to this class we will point out some of the peculiar characteristics of such class:

— T Tauri stars are low mass stars (1 to 3 solar mass),

— they exhibit a peculiar continuum energy distribution when compared to «normal» stars belonging to the same spectral class,

---

(*) Communication presented at «4.ª Conferência Nacional de Física», Évora, Abril de 1984.

i. e., as displayed on Fig. 1, their spectra show an excess emission all the way from the UV to the infrared wavelengths,

— although being cool stars (effective temperature in the range 3000 to 6000 K) they show an emission line spectrum overlapping the continuum. (The number and intensity of the emission lines present in the spectra varies from star to star; as a rule, there are always emission lines present to some degree),

— they are irregular variables.

Different lines of argument point to T Tauri stars as being young (< 10^6 years) stars still in the phase of gravitational contraction towards the main sequence [2]. These stars are located near dense molecular clouds to which they are observed to be dynamically associated [3]. These molecular clouds are known to be places of ongoing star formation.

For further reading we refer to a large number of recent articles on T Tauri stars scattered through the literature. Two review articles on T Tauri stars have also recently appeared; one [4], essentially dealing with the observations at different wavelengths, the other [5], describing theoretical modelling, although strongly biased towards the protostellar collapse phase. A more wide review of the T Tauri stars, including a critical analysis of models and mechanisms and their relations with the observations, however strongly needed, is yet to come.

2 – THE DATA

In this section we will present some of our spectroscopic data on T Tauri stars. We will concentrate on a particular T Tauri star, RU Lupi. For this star we have the most complete set of observations and the data analysis is at a more advanced stage.

2.1 – *The visual wavelength range*

Our data includes:

— several intermediate dispersion spectra (20 Å mm^{-1}) obtained at the Anglo-Australian Telescope. These spectra have been used for line identification and immediate analysis, such as the assessment of values of density and temperature for the
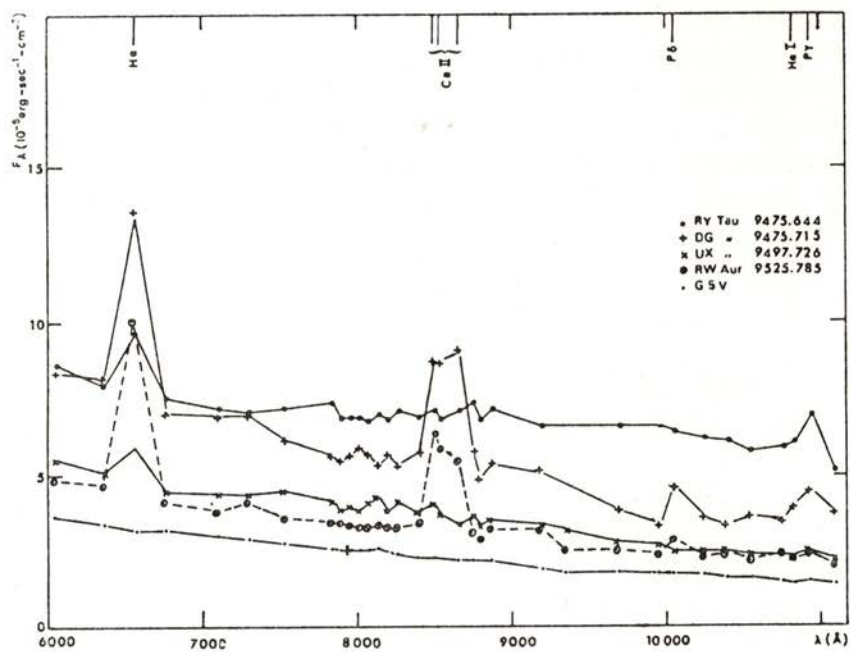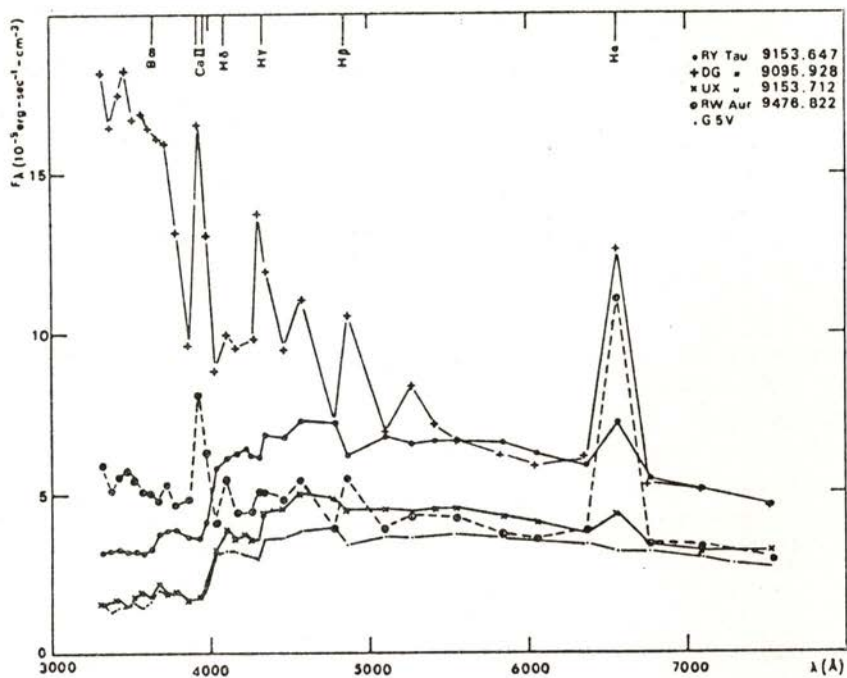
Fig. 1 — The spectral energy distribution of T Tauri stars classified as dG5. The lowest curve is for a standard G5V star (arbitrary vertical scale [1]).

different layers in the stellar atmosphere producing the emission lines [6]. The conclusions are compiled in Table 1 while Fig. 2 displays one of such spectra;
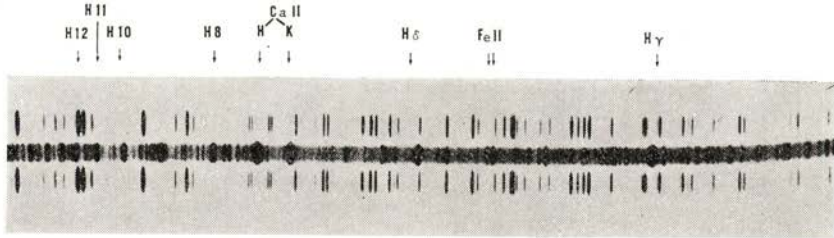
Fig. 2 — An intermediate dispersion spectrum of RU Lupi in the wavelength range [3600, 4580] Å . The spectrum was obtained with the Anglo-Australian Telescope and the Royal Greenwich Observatory spectrograph.

— high resolution spectra (at inverse dispersion 5 to 10 Å mm⁻¹) also obtained at the Anglo-Australian Telescope. This high quality data allows, through the detailed line profile analysis to conclude on the presence of suprathermal motions in the stellar atmosphere (from the line widths) and even of a strong stellar wind (from the line profile shape) [6]; furthermore we were able to get a velocity distance relationship (from the profile assymetry) [7]. These results are also included in Table 1a (the last line).

TABLE 1a — Summary of observational constraints of the wind of RU Lupi suggested by the optical data analysis.

	Fe I, Ti II	Fe II	Ca II, H I	He I
density (cm⁻³)	$N_p < 10^{12}$ $N_H = 10^{14}$ $N_e < 10^{12}$	$N_e > 10^9$		$N_e > 10^{11}$
temperature (K)	5800		10^4	10^5
velocity (Km s⁻¹)	170		240	

2.2 – *The ultraviolet data*

Over the last five years a wealth of information on every field in Astronomy has resulted from the activity of the International Ultraviolet Explorer (NASA-ESA). T Tauri stars are no exception and a large amount of data on such stars is now available in the data bank. Our own observations include:

— low resolution spectra (Fig. 3) that has led to conclude on the presence in the T Tauri stars of a transition region, similar to the Sun, with temperatures up to 10^5 K ;

FLUX IS IN ERGS/CM/CM/S/A ×10××-16
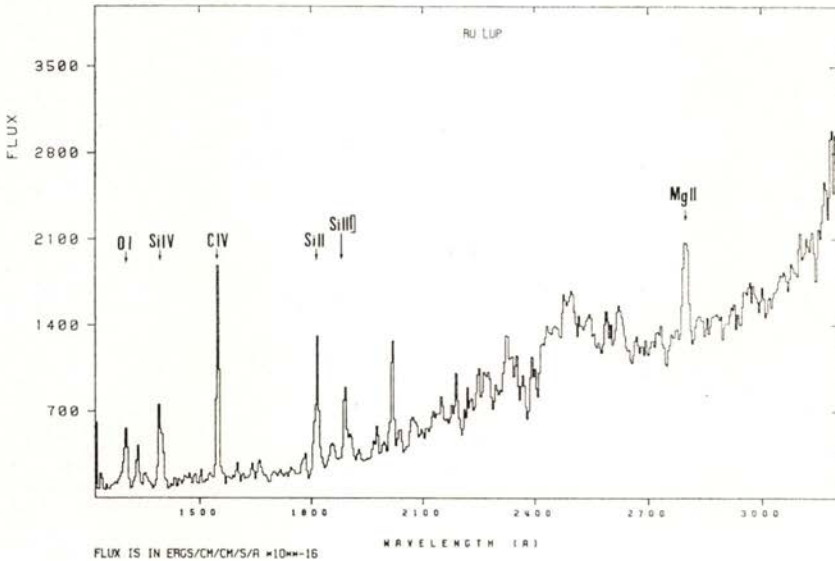
Fig. 3 — Low resolution UV spectrum of RU Lupi in the wavelength range [1200, 3200] Å . The spectrum shown results from the merging of two spectra both obtained with the International Ultraviolet Explorer (ESA-NASA).

— high resolution spectra (Fig. 4) that confirmed the presence of a (strong) stellar wind and have been used to constrain the models developed for this star.
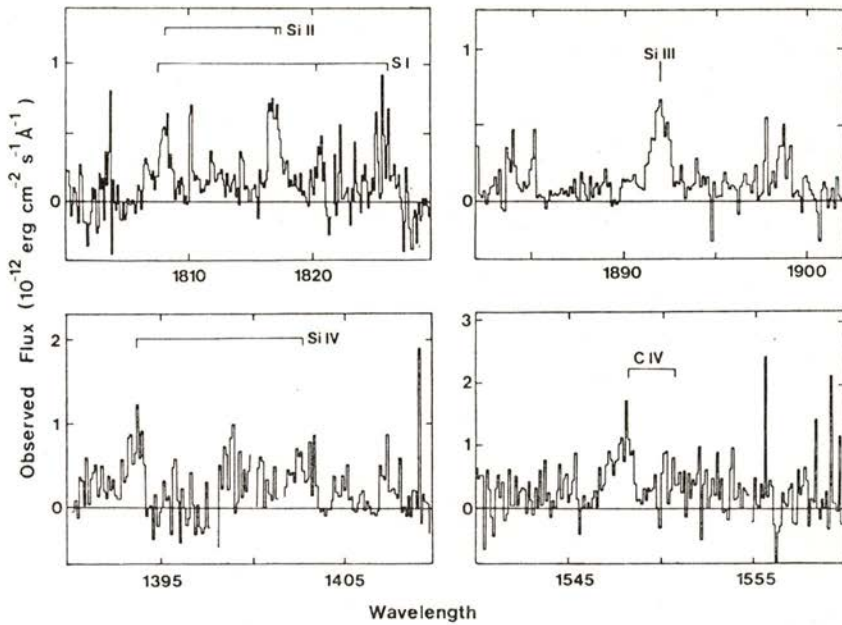
Fig. 4 — High resolution UV data of RU Lupi obtained with the satellite International Ultraviolet Erplorer (ESA-NASA) [8].

From the analysis of the UV observations further information on the atmosphere of RU Lupi is obtained. These results are summarized in Table 1b.

TABLE 1b — Summary of observational constraints of the wind of RU Lupi resulting from the UV data analysis.

	Mg II, Si II	Si III], C III], Si IV, C IV
density (cm^{-3})		10^{10}
temperature (K)	10^4	5.10^4 - 10^5
velocity (Km s^{-1})	240	150 - 170

3 — A MODEL FOR RU LUPI

From the analysis of all the available data the following picture of RU Lupi emerges:

a central star of mass ~ 1 $M_\odot$, radius ~ 1.6 $R_\odot$ and effective temperature 4400 K, surrounded by a spherically symmetric envelope where the observed emission lines originate; this (geometrically narrow) envelope is not isothermal and can be divided in a chromospheric layer and a higher temperature layer similar to the solar transition region. However the amount of flux coming out of these two regions is highly enhanced relatively to the Sun - RU Lupi emits both in the chromosphere and transition region approximately 10^4 times more energy than the sun. This seems to be a common characteristic for T Tauri stars, however with a variable degree of intensity from star to star.

Therefore, the next logic question to be asked is: do T Tauri stars have such strong coronae as well? The observations one can use to investigate this problem are out of the range of IUE. Therefore one uses both optical observations, searching for the coronal lines of [FeX] and [FeXIV] that are observed in the solar corona, and X-ray emission. These observations would indicate the presence in T Tauri stars of emitting regions of temperature up to 10^7 K. Several searches were done both in the optical ([9], [10]) and in the X-ray using the Einstein satellite [11]. In the case of RU Lupi no detections were made and in more general terms the existence of a corona in T Tauri stars is still a puzzle. Fig. 5 summarizes the result of work done on such topic, not just for RU Lupi but also for other two T Tauri stars previously detected as X-ray sources with the Einstein satellite [12].

Several explanations for the observational results have been proposed, namely,

— the variability of coronal line and/or X-ray emission (may be flare-like outbursts);

— the X-ray mechanism being non-thermal, perhaphs associated with some particle acceleration mechanism-magnetic field lines reconnection, for example.

Meanwhile theoretical modelling has also been attempted. 'In the model the presence of a magnetic field and linearly

Portgal. Phys. — Vol. 16, fasc. 1-2, pp. 51-59, 1985

57

polarized Alfvén waves propagating outwards constitute the primary mechanism for driving the wind. Both theory and observations constrain the wind solutions and the overall picture is as follows [13]:
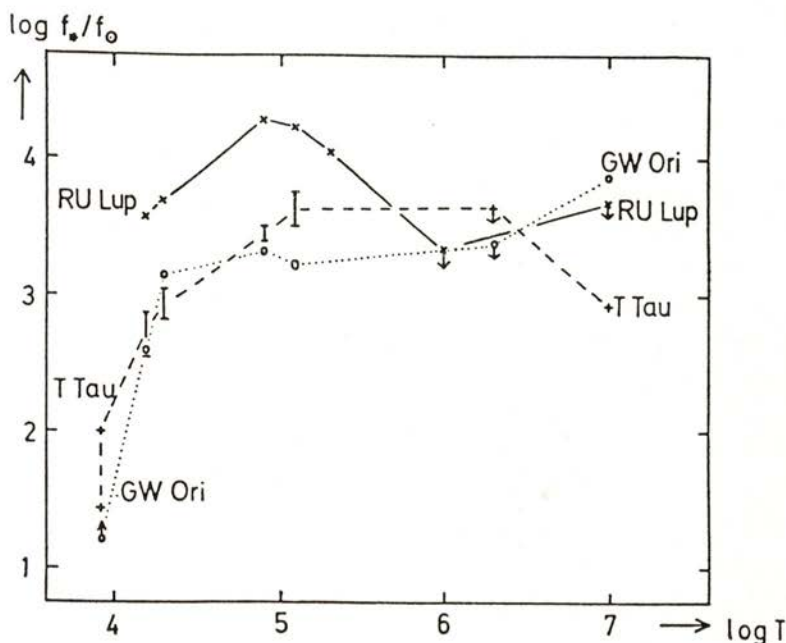
Fig. 5 — Plots of the ratio of stellar to solar fluxes in 3 T-Tauri stars as a function of temperature [8]. This figure shows firstly that the distribution of material with temperature in the outer regions of these stars is different from that in the Sun (i. e. the ratios are not constant with temperature).

— the wind velocity starts with very low values near the base of the chromosphere but (due to the presence of the waves) accelerates very fast reaching velocities of the order of 240 Kms^{-1} quite close to the stellar surface. In order to explain the observed stratification in the widths of the lines dissipation of the waves is assumed to occur before the flow velocity reaches the escape velocity [14]. Therefore the wind will decelerate afterwards due to the gravitational forces. The higher excitation lines would be produced in the decelerating region. The IUE high resolution observations have confirmed such expectations since CIV, SiIV,

SiIII] and CIII] are observed to be narrower than the strong MgII, CaII and Balmer lines [8].

This model is able to reproduce the velocity-distance relationship suggested by the optical line profiles and also the rather restricted density requirements imposed by the observations. It seems able to reproduce as well the line profiles observed for the hydrogen lines used to test the model. Furthermore, it suggests a possible explanation for the variation of the temperature through the line emitting region: the heating occurs as a result of the wave energy dissipation (over a short range of distances from the star surface) due to the density gradient. Further theoretical and observational work is being done, respectively the inclusion of a realistic dissipation mechanism while considering the energy problem in the stellar atmosphere and the study of variability. Through the study of variability, simultaneously in the chromosphere and transition region, we will be able to understand what causes the variations (changes in opacity or/and physical changes in the stellar atmosphere). Furthermore the time scales involved will probably provide a very severe constraint to the candidate mechanisms for wind driving and heating.

REFERENCES

[1] Kuhi, L. V., 1974, *Astron. Astrophys. Suppl.*, **15**, 47.
[2] Herbig, G. H., 1983, NATO-ASI «Birth and Infancy of stars», Les Houches.
[3] Jones, B. F. & Herbig, G. H., 1979, *Astron. J.*, **84**, 1872.
[4] Cohen, M., 1984, *Physics Reports*, **116**, 173.
[5] Bertout, C., 1984, *Rep. Prog. Phys.*, **47**, 111.
[6] Lago, M. T. V. T. & Penston, M. V., 1982, *Mon. Not. R. astron. Soc.*, **198**, 429.
[7] Lago, M. T. V. T., 1982, *Mon. Not. R. astron. Soc.*, **198**, 445.
[8] Lago, M. T. V. T., Penston, M. V. & Johnstone, R., 1984, Proceedings of «Fourth European IUE Conference», ESA SP-218, 233.
[9] Gahm, G. F., Lago, M. T. V. T. & Penston, M. V., 1981, *Mon. Not. R. astron. Soc.*, **195**, 59P.
[10] Lago, M. T. V. T., Penston, M. V. & Johnstone, R. M., 1985, *Mon Not. R. astron. Soc.*, **212**, 151.
[11] Gahm, G. F., 1980, *Astrophys. J. Lett*, **242**, L163.
[12] Feigelson, E. D. & Decampli, W. M., 1981, *Astrophys. J. Lett.*, **243**, L89.
[13] Lago, M. T. V. T., 1984, *Mon. Not. R. astron. Soc.*, **210**, 323.
[14] Lago, M. T. V. T., 1979, DPhil. thesis, University of Sussex.
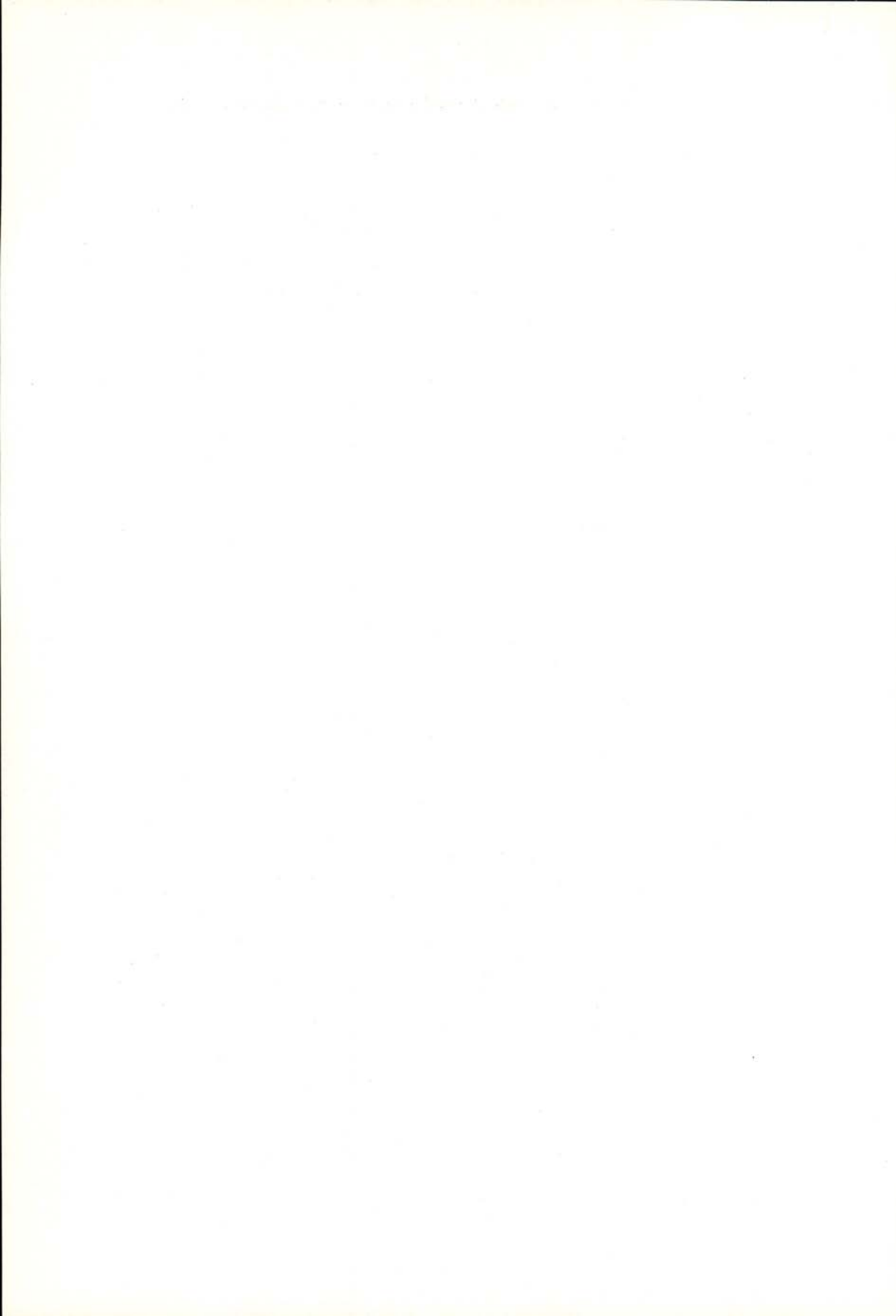
RESONANT ABSORPTION OF GRAVITATIONAL WAVES IN THE PAST OF THE UNIVERSE

P. G. MACEDO

Dep. de Matemática, Univ. de Coimbra, 3000 Coimbra, Portugal

P. M. DE CARVALHO

Dep. de Matemática Aplicada, Univ. do Porto, 4000 Porto, Portugal

ABSTRACT — The way the cyclotron absorption of gravitational waves varies with the cosmological red shift is analised.

One concludes that waves in the proto interstellar and interstellar medium with frequency near the double of the electron Larmor frequency $2 \omega_L$ were never significantly absorbed in the period between the epoch when the reaction $\gamma \rightarrow e + \bar{e}$ ceased to occur spontaneously and the present epoch.

It has recently been shown [1] that in a non-collisional magnetized plasma, there is a weak cyclotron damping of gravitational waves propagating parallel to the magnetic field which permeates the plasma. For a weak collisional regime this effect has been shown to increase with collisions [2].

The existence of an electromagnetic microwave background with temperature of 3 K has been known for many years [3]. This effect is due to the recombination of hydrogen when the temperature of the Universe was 4000 K.

We therefore address ourselves the question: Was there an epoch in the past, when the Universe was not transparent to gravitational radiation in the resonant band near $2 \omega_L$ (ω_L being the electron Larmor frequency for the interstellar medium and the media which in the past gave rise to it) due to this phenomenon?

If the answer to this question were affirmative this could be a mechanism to contribute for a fossil gravitational wave background.

However, we conclude by this study that the answer is negative. For the sake of simplicity, we assume that from the

Portgal. Phys. — Vol. 16, fasc. 1-2, pp. 61-64, 1985

61

epoch of galaxy formation until now galaxies did not have a significant evolution as far as the values of density, temperature and magnetic field are concerned. The interstellar medium is therefore assumed to be a fossil which dates from that epoch.

We also assume a frozen-in magnetic field which permeated the pre-galactic medium along its evolution.

We assume that the typical values for the collisional frequency (ω_c), electron Larmor frequency (ω_L), temperature (T) and number density (n) for the interstellar medium at the time of galaxy formation where identical to the present ones, i. e.,

$$\omega_{c_G} \sim 6 \times 10^{-4} \text{ Hz} , \; \omega_{L_G} \sim 20 \text{ Hz} , \; T_G \sim 10^4 \text{ K} , \; n_G \sim 10^4 \text{ cm}^{-3} \; (*),$$

The previous evolution of ω_c, ω_L and n, until such epoch, were given (using the standard Friedman model) [3] as a function of the temperature T by:

$$
\begin{aligned}
\omega_c &\simeq 6 \times 10^{-10} & T^{3/2} & \quad \text{Hz} \\
\omega_L &\simeq 2 \times 10^{-7} & T^2 & \quad \text{Hz} \\
n &\simeq 10^{-8} & T^3 & \quad \text{cm}^{-3}
\end{aligned}
\tag{1}
$$

From this, one can see that in the past $\omega_c \ll \omega_L$ and therefore, one is justified in using a non-collisional model like the one due to Macedo & Nelson [1]. This model does not take into account the electron-positron pair production (Vlasov's equation does not include terms which are due to it) and therefore, this analysis is restricted by the condition that the temperature of the Universe be lower than $T_{e-\bar{e}}$ given by

$$k T_{e-\bar{e}} \sim 2 m_e c^2 \tag{2}$$

where m_e is the electron rest mass. This condition amounts to $T < 10^{10}$ K.

In Macedo & Nelson's model, the frequency of gravitational waves propagating in a magnetized plasma of density n has a real part ω_r and an imaginary part ω_i (which is responsible for the wave damping), which is given by [2]:

$$\omega_i \sim 10^{-5} \, n \, T^{1/2} \, m_e^{3/2} \, \omega_L^{-1} \, \exp\left[-m_e \lambda^2 (\omega_r - 2 \omega_L)^2 / k T \right], \tag{3}$$

(*) The subscript G means — at the time of galaxy formation.

where λ is the wavelength; in the vicinity of $2\,\omega_L$, where the exponential approaches 1, (3) reduces to

$$\omega_i \sim 10^{-5}\ n\ T^{1/2}\ m_e^{3/2}\ \omega_L^{-1} \tag{4}$$

Using (1) in (4) one gets the behaviour of this imaginary frequency with the temperature of the Universe in the period between the ceasing of $e + \bar{e}$ pair production and the period of galaxy formation

$$\omega_i \sim 10^{-47}\ T^{3/2} \tag{5}$$

If we define the damping frequency ω_d as the inverse of the time t_d it takes for the intensity of the waves to reduce to half its value, one has

$$\omega_d \simeq 1.4 \times 10^{-47}\ T^{3/2} \tag{6}$$

We define a typical frequency ω_τ as the inverse of the time a graviton takes to cross a typical scale distance d_τ which at the time of galaxy formation is of the size of a galaxy ($\sim 10^{23}$ cm).

$$\omega_{\tau_G} = c/d_{\tau_G} \tag{7}$$

Using a Friedman standard model, this distance scale in the past of the Universe (before galaxy formation) evolved as

$$d_\tau = d_{\tau_G}\ T_G\ T^{-1}\ , \tag{8}$$

or

$$d_\tau \sim 10^{27}\ T^{-1} \tag{9}$$

This means that

$$\omega_\tau \sim 3 \times 10^{-13}\ T \tag{10}$$

Comparing ω_τ given by (10) with ω_d given by (6), one notices that, for $T < 10^{10}$ K, $\omega_d \ll \omega_\tau$.

One therefore concludes that, in the frequency band near the resonant frequency $2\,\omega_L$ there is no significant cyclotron absorption of gravitational waves in the Universe in epochs later

Portgal. Phys. — Vol. 16, fasc. 1-2, pp. 61-64, 1985

63

than the epoch when e - e pairs ceased to be spontaneously produced (*).

In this period, we therefore conclude that the Universe was transparent in this frequency band and the cyclotron absorption did not contribute to the gravitational radiation background.

We would like to thank Dr. A. H. Nelson for suggesting the problem and for useful discussions with one of the authors (P. G. Macedo) during his stay in Cardiff.

REFERENCES

[1] P. G. MACEDO & A. H. NELSON, *Phys. Rev.*, **D28**, 2382 (1983).

[2] P. G. MACEDO, Gravitational waves in a weakly collisional magnetized plasma, presented in the GR 10 Conference (Pádua), 1983.

[3] S. WEINBERG, Gravitation and Cosmology, Wiley, New York, 1972.

(*) Note that for $T = 10^{10}$ K one has $\omega_d \sim 10^{-32}$ Hz and $\omega_\tau \sim 10^{-3}$ Hz. In fact this differs by only one order of magnitude from the value of the Hubble parameter at $T = 10^{10}$ K which was $(\dot{R}/R)_{T = 10^{10} \text{ K}} \sim 10^{-2}$ Hz, supposing that $H_0 \sim 50$ Kms^{-1} Mpsc^{-1} and $q_0 \sim 0.002$ [3].

OZONE AND UV SOLAR RADIATION TIME
VARIATIONS AT LISBON

M. F. FIGUEIRA ([1]) and C. A. GONÇALVES ([2])

Instituto Nacional de Meteoroiogia e Geofísica
Rua C do Aeroporto de Lisboa 1700 Lisboa, Portugal

ABSTRACT — Observations of atmospheric ozone, including total and layered from the Dobson No. 13 spectrophotometer and direct sondings with the Brewer-Mast Ozonesonde are being made at Lisbon (38° 46' N; 09° 09' W; 105 m m.s.l.) covering almost three decades. In addition, as from December 1982 observations of the UV solar radiation at surface started at the same location, including the UV-B spectrum between 290 nm and 330 nm with the Berger's Sunburning Ultraviolet Meter, as a contribution to radiation and ozone studies.

Analysis of both total and layered ozone and UV radiation will be presented aiming mainly to show their annual cycle and the local time correlations between both parameters. The maximum of the daily mean UV-B of 15.0 SU (Sunburn Unit) was observed in June, and the minimum of 1.4 SU was observed in December. These values compare well with the results of other observers in places of similar latitudes.

1 — INTRODUCTION

The concern of the scientific community as regards the environmental impact of ozone field variations in relation to UV-B (290 nm to 330 nm) solar radiation increases in the biosphere has been stressed mainly in the second half of this century and is well illustrated by [5, 10, 11] and in other papers presented in the Meeting of Experts on the Ozone Layer, organized by UNEP in Washington DC, 1-9 March 1977. On the light of observations, it was possible to indicate [5, 9, 11] that 10 % reduction in total

---

([1])   Chief, Division of Air Protection; Associate Professor, Department of Physics, Faculty of Sciences, Lisbon; in charge of Research Project I2.

([2])   Chief, Aeronomyc Division; in charge of Research Project I2 «Meteorological Research at INMG for Support of the Environment Protection».

ozone leads to increases of UV-B radiation at near surface air that may be almost twice the percent ozone reduction. In addition, analysis of Aspendale data [1] on both erythemally effective ultraviolet radiation and total ozone pointed towards a higher percent UV-B increase near ground than a simultaneous percent total ozone change in the mean, although the dispersion of individual cases is large.

Being aware of this problem and taking advantage of the ozone observations available in Lisbon, a preliminary analysis of UV-B and ozone variations was undertaken and the results will be reported here, but it is understood that the interpretation of the results is subject to severe limitations, which was not the case of other larger networks [2, 4].

2 – THE DATA AND THEIR ANALYSIS

The results of the observations used in this paper include total and layered ozone both obtained with the Dobson ozone spectrophotometer No. 13 of the IOC located in Lisbon and operated by the Portuguese National Institute for Meteorology and Geophysics, the vertical distribution of ozone being derived from the Umkher method on C wavelength. In addition, in December 1982 a program of observations of solar UV-B radiation was initiated in the same location using the Berger's Sunburning Ultraviolet Meter [3] which allows the detection of the solar spectrum between 290 nm and 330 nm by means of the Sunburn Effect. This implies, as it is well known, that the results may not be expressed as absolute energy, the reason why the computed parameter was the power of the radiation, that is, Sunburn Units per hour. On the time when the relative air mass $\mu = 2.5$ on clear sky without mist, fog, smoke or dust, leading to conditions of very good horizontal visibility, simultaneous special total ozone observations were made and a set of 70 observation pairs was selected for analysis.

The analysis of the UV-B data aiming to compare observation and theory is given in Fig. 1, which shows the annual cycle of this parameter for 1983, with the maximum in June and the minimum in December, as it should be for the Northern Hemisphere when the daily mean is computed from all times of any day.

Therefore, it may be accepted that the data set has internal consistency. In the same figure it is included the annual cycle of the total ozone for the years 1973 and 1983 at the same location, just to illustrate the mainly positive correlation of both parameters, which is not supported by theory on the grounds of absorption laws. This behaviour only stresses that the search for correlations
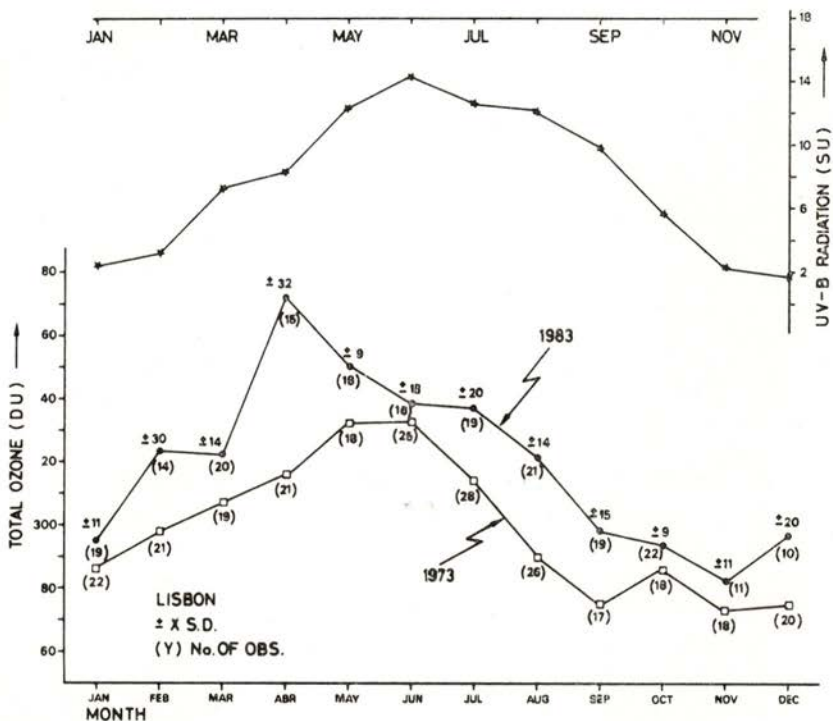
Fig. 1 — Monthly means of total ozone for 1973 and 1983 (lower) and daily means of UV-B solar radiation for 1983 (upper) at Lisbon.

needs to filter, as far as possible, the effect on UV-B variations not due to ozone variations. Before going to this, the reader can see in Fig. 2 how the mean yearly cycle of the UV-B at Lisbon compares with the yearly cycles at other locations on the Northern Hemisphere and conclude that a reasonably spacial consistency of the data exists, taking into account the differences in the length of the samples.

In order to examine the relation between the time variations of UV-B radiation at surface air and the total ozone it must be kept in mind that the ozone time and space variations arise from a complex action of mechanisms either on the basis of radiation
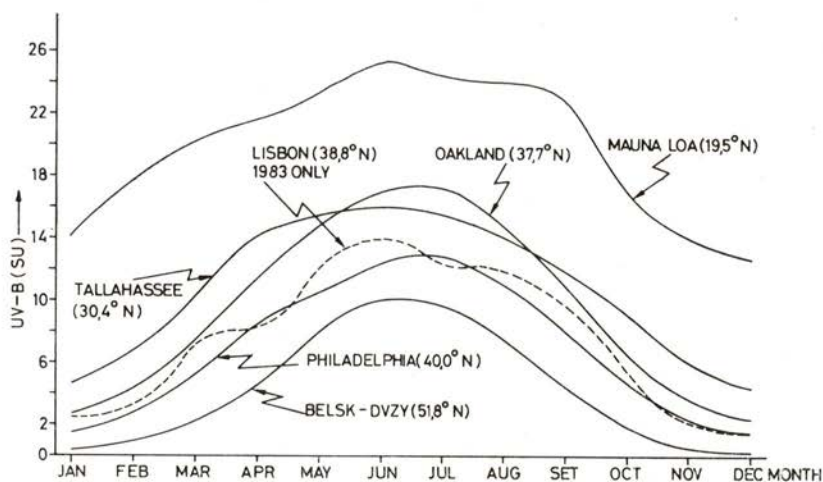
Fig. 2 — Daily mean (six years) of UV-B solar radiation for the indicated locations.

laws or of atmospheric dynamics, which has been dealt with by many authors and illustrated for the Lisbon station results in [6, 7, 8] both for the total and the layered ozone. Fig. 3 shows the effect of the tropospheric jet related circulations on the total ozone variations, which gives rise to ozone concentration gradients across and along the jet axis [6], with highest ozone contents to the left of jets looking downstream. Such large scale ozone transfer process originates significant vertical ozone redistribution mainly in the lower and middle stratosphere and upper troposphere with implications on solar radiation absorption mainly in the UV band of the spectrum. Within this context, the analysis made in Fig. 4 shows that the partial pressure of ozone over Lisbon for the same period of analysis of the UV-B contained in Fig. 1 and 2 was almost constant all over the year above about the 15 hPa level, which agrees with the observed distribution from ozonesondings at the

same location in 1973; but the ozone maximum was, however, of the order of 18 mPa at 50 hPa level in February.
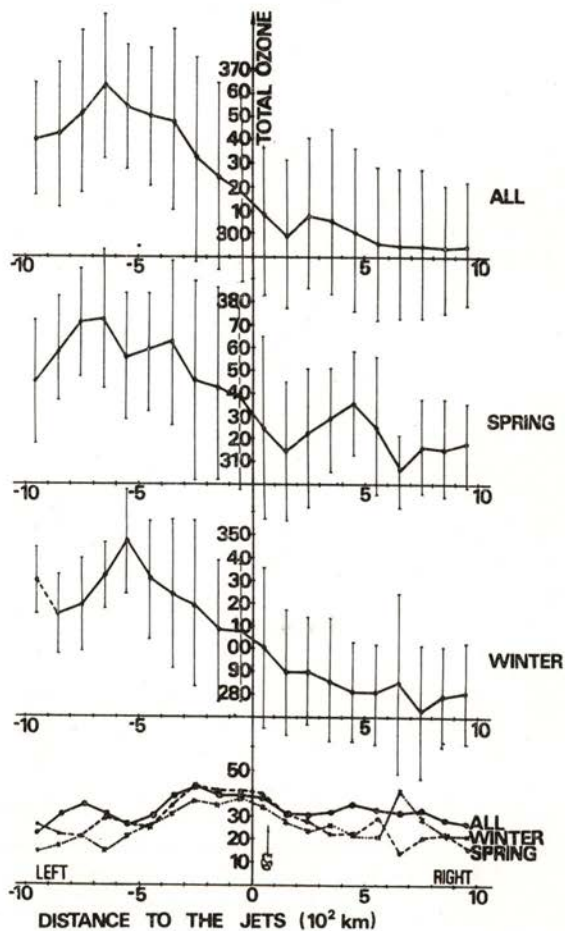
Fig. 3 — Ozone total, Ω, in relation to the jet axis position (Winter and Spring, 1968-1971) for Lisbon, with the standard deviations, σ_Ω, and their variations. (From Figueira, 1973).

The aforementioned significant differences in ozone contents must be the main source of time variations of near ground UV-B solar radiation on occasions of clear skies, but the search for such

correlations requires the existence of sets of simultaneous ozone and UV-B observations at the same relative air mass values as referred to above. To this aim, $\mu = 2.5$ was selected and pairs
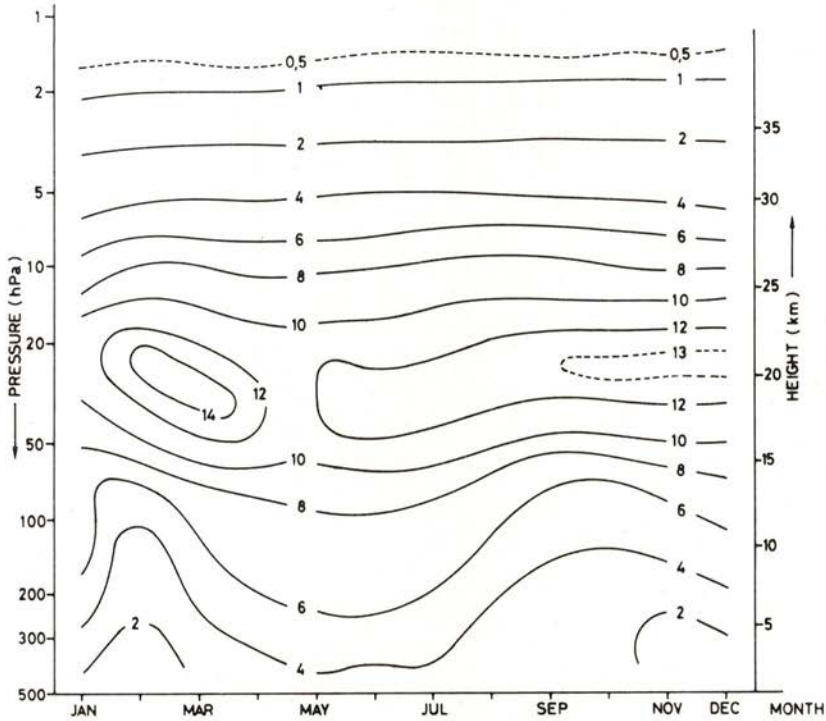
Fig. 4 — Mean time series of the vertical distribution of ozone over Lisbon for 1983, in mPa, from umkehr observations.

of observations were taken, separated in 7 groups of 10 values in chronological order; computed the mean value for the whole sample and for samples of 10 values, the percent deviations, $d\overline{O}_3$ (and $d\overline{UV\text{-}B}$)

$$d\overline{O}_3 = \left\{ \left[(\overline{O}_3)_{10} - (\overline{O}_3)_{70} \right] / (\overline{O}_3)_{70} \right\} . 100$$

where plotted in Fig. 5.

It may be seen from Fig. 5 a clear anticorrelation of the parameters in analysis as expected on theoretical basis, but there is little sign of a double increase of near ground UV-B relative to total ozone decrease as reported by some but not all other authors.
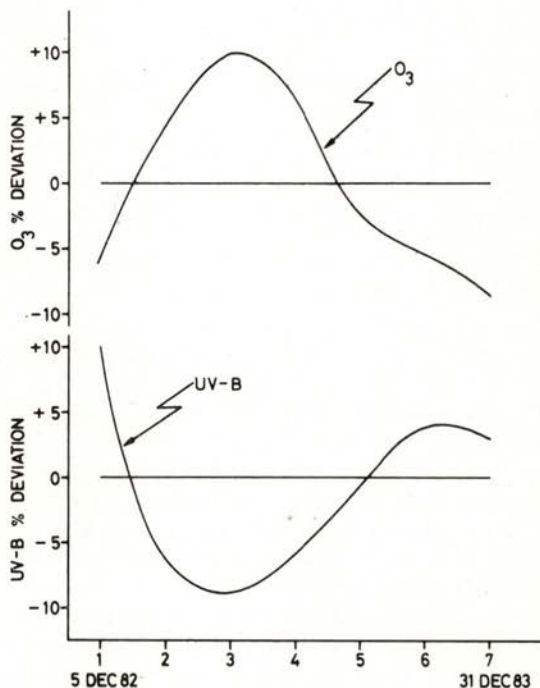
Fig. 5 — Time variations of total ozone and UV-B solar radiation at Lisbon for the indicated period.

3 – CONCLUSIONS

The preliminary study of the relations of total ozone and near ground UV-B solar radiation presented in this paper gives reasonable support that the methods of observation of the second parameter needs to be improved to obtain absolute values, but also that the equipment used so far is certainly very useful for this and other studies. In addition, the authors are aware of the

need to extend the period of simultaneous observations and to improve the method of analysis of the time variations of both parameters with the aim of their better understanding.

REFERENCES

[1] Barton, I. J. and Robertson, D. F., 1975, Measurements of erythemally effective ultraviolet radiation and total ozone content. *Nature,* Vol. 258, No. 5530, Nov. 1975.

[2] Barton, I. J., 1983, The Australian UV-B Monitoring Network CSIRO, Paper No. 46, Australia.

[3] Berger, D. S., 1976, Sunburn Ultraviolet Meter: Design and Performance, *Photochemistry and Photobiology,* Vol. 24, 587-593.

[4] Berger, D. S., and Urbach, F., 1982, A climatology of sunburning ultraviolet radiation, *Photochemistry and Photobiology,* Vol. 35, 187-192.

[5] Boville, B. W., 1979, Environmental Aspects of Stratospheric Ozone Depletion, The Ozone Layer, Environmental Sciences and Applications, Vol. 4. UNEP, Pergamon Press.

[6] Figueira, M. F., 1973, Atmospheric Ozone and Flow Field Variations over Lisbon, PAGEOPH, Vol. 106-108 (1973/V-VII), 1586-1599.

[7] Figueira, M. F., 1978, Ten year observations of total and layered ozone over Lisbon and their trends, W. M. O. No. 511, p. 115-119, 1978.

[8] Figueira, M. F., 1980, Surges of total ozone over Lisbon, Quadrennial Int. Oz. Symp., Boulder, Co.

[9] Machta, L., Cotton, G., Hass, W. and Komhyer, W., 1975, CIAP measurements of solar ultraviolet radiation. Final Report, DOT-AS-20082.

[10] Schulze, R., 1974, Increase of carcinogenic ultraviolet radiation due to reduction in ozone concentration in the atmosphere. Proc. Int. Conf. on struct., compos. and general circ. of the upper and lower atm. and possible antrop. perturb., Vol. I: 479-493.

[11] Urbach, F. et al., 1979, Effects of Ultra-violet Radiation on Human Health, The Ozone Layer, Environmental Sciences and Applications, Vol. 4, UNEP, Pergamon Press.

RESONANT DEGENERATE FOUR-WAVE MIXING
IN A RUBY CRYSTAL

Luís M. Bernardo

Laboratório de Física, Faculdade de Ciências, Universidade do Porto, 4000 Porto, Portugal

ABSTRACT — We study degenerate four-wave mixing (DFWM) in a ruby crystal, theoretically and experimentally, in isotropic and anisotropic configurations. We show that thermal DFWM is negligible when compared with resonant DFWM and this one is not affected by self-focusing. Finally we present phase conjugate reconstruction of a microscopic object as an application of DFWM.

1 — FOUR-WAVE MIXING (FWM)

FWM refers to the interaction of four waves in a non-linear medium. The term "Degenerate Four-Wave Mixing" (DFWM) is used when the waves have all the same frequency. The geometrical configuration for the interaction, where two counter-propagating pump waves are used with a probe beam at some angle ϕ, is sometimes called "backward DFWM" interaction (see Fig. 1). In
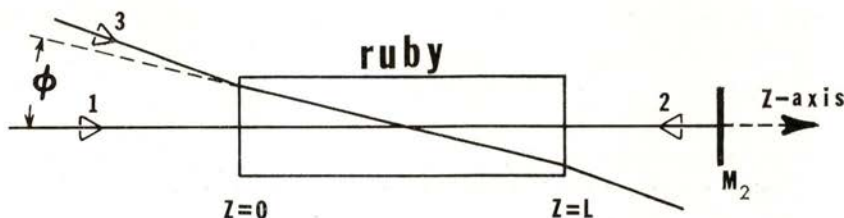
Fig. 1 — Relative positions of the pump beams 1, 2 and the probe beam 3. The angle ϕ is the angle between 1 and 3, inside the crystal. The z-axis has the same direction as beam 1. M_2 is the mirror where beam 1 is reflected to generate beam 2.

this way, the process can be distinguished from the forward DFWM [1], where only one pump with a probe generate a forward phase conjugate signal. This interaction corresponds to 3-wave mixing; but, as the pump acts as if it is formed by two forward pumps (or equivalently, two pump photons take part in the reaction), it can be considered a FWM process. We use "DFWM" instead of "backward DFWM" for simplicity during the exposition, since this is the only configuration we consider in this paper.

The non-linear nature of DFWM implies that the response of the optical medium to the light fields is not linear, i.e. the polarization $\mathbf{P}(\mathbf{r}, t)$ of the medium has terms which are non-linear functions of the electric field $\mathbf{E}(\mathbf{r}, t)$. Because four waves are involved, the first important term of the non-linear polarization, when expanded in powers of $\mathbf{E}(\mathbf{r}, t)$, is of third order [2]

$$\mathbf{P}^{\mathrm{NL}}(\mathbf{r}, t) = \chi^{(3)} : \mathbf{E} \, \mathbf{E} \, \mathbf{E} \tag{1}$$

where $\chi^{(3)}$ is the third order tensor susceptibility and

$$\mathbf{E} = \Sigma_j \, \mathbf{E}_j(\omega) \quad (j = 1, 2, 3, 4) \tag{2}$$

is the field.

For isotropic media and when only the polarization of frequency ω is considered, the condensed expression (1) reduces [3] to

$$\mathbf{P}^{\mathrm{NL}} = \alpha \, (\mathbf{E} \cdot \mathbf{E}^*) \, \mathbf{E} + \gamma \, (\mathbf{E} \cdot \mathbf{E}) \, \mathbf{E}^* \tag{3}$$

The first term leads to the holographic analogy [4, 5], where each pump acts as the reading beam, generating the phase conjugate beam. The second term describes the oscillation at frequency 2ω of the non-linear index of refraction which scatters one of the waves to generate the fourth [6] (parametric interaction). The coefficients α and γ can be made large by choosing the right non-linear medium: one-photon resonant medium for large α, two-photon resonant medium for large γ. Ruby behaves like a one-photon resonant medium and therefore a larger α is expected.

If multi-photon processes are important, odd terms of the polarization higher than the third power of $\mathbf{E}$ have to be considered, since their coefficients cannot be neglected.

The above considerations and general expressions for $\mathbf{P}^{\mathrm{NL}}$ are valid for any non-linear medium. The expressions for the

74

Portgal. Phys. — Vol. 16, fasc. 1-2, pp. 73-98, 1985

susceptibility χ and for the parameters α and γ, however, result from the particular non-linear mechanism involved. In our medium, ruby, the mechanism is resonant absorption and the expressions that will be obtained are valid in general for those media. Therefore, although the theory in this paper refers specifically to a ruby crystal, it can be applied to any resonant absorber, after evaluating the corrections caused by different valued parameters.

2 – RUBY CRYSTAL DESCRIPTION

A ruby crystal is a crystal of sapphire (Al_2O_3) where a certain percentage of Al^{3+} ions has been replaced by chromium ions Cr^{3+}, which cause the pink color of the otherwise colorless sapphire crystal. The Cr_2O_3 doping percentage in our crystal is 0.05 wt.%, i.e. the concentration of Cr^{3+} ions is 1.58×10^{19} ions. cm^{-3}.

In the free Cr atom ($Z = 24$), the shells from 1s through 3p are completely filled; shell 3d has five electrons ($3d^5$) and shell 4s has one electron ($4s^1$). When the Cr atoms are introduced into the host crystal of sapphire, they share, in the bonding, three electrons with O^{2-}, becoming Cr^{3+}. One of those electrons comes from the 4s shell and the other two from the 3d shell. The 3d shell, which can be occupied with 10 electrons, is then only partially filled with two electrons. The possible arrangements of these two electrons in the 3d shell leads to the energy levels of the Cr^{3+} ions in the Al_2O_3 host crystal [7]. When those ions form a solid like the ruby crystal, the energy levels for the crystal will be much more complicated than the ones for an isolated Cr^{3+} ion.

In Fig. 2 we show a detailed energy level diagram of ruby [8] that has been obtained experimentally. For the optical frequency we used (the blue/green light of the Ar laser), the diagram of Fig. 2 can be simplified for that of Fig. 3. The Ar laser light excites the ions from ground state 1 to the excited level 3. From level 3 they decay non radiatively and very fast (< 1 ns) [9] to level 2. The decay time from level 2 to level 1 is comparatively slow, $\tau \simeq 3$ ms at 300 K and 4.3 ms at 77 K [10]. Absorption coefficients for ruby when it is in the excited level 2 have been measured [11]. Those results show that transitions from level 2 to

higher levels (dashed lines in Fig. 2) may take place. However the effect of the excited states' absorption is usually small [9]. Nevertheless, we will consider its effect in the latter calculations of the induced polarization.
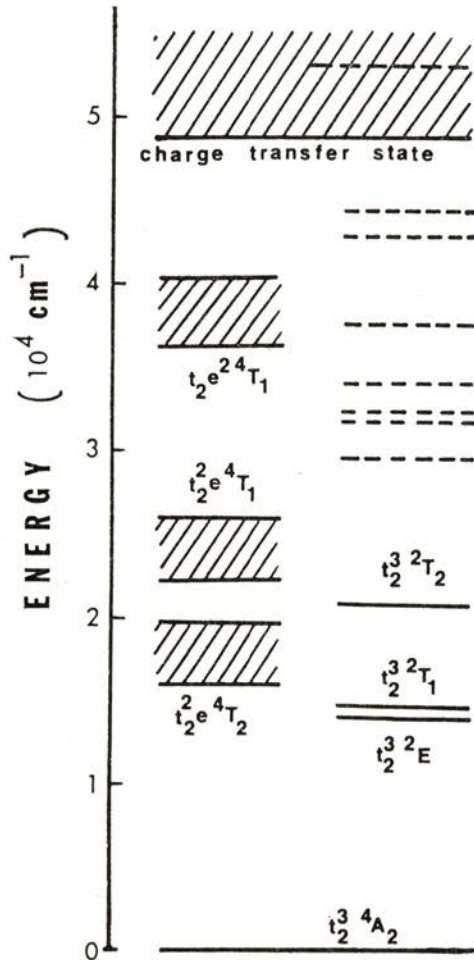
Fig. 2 — Energy level diagram of ruby [8].

The ruby crystal geometry is shown in Fig. 4. Its nonpolished 5×11 mm² surfaces make a 60° angle with the c-axis. Both pairs

76

Portgal. Phys. — Vol. 16, fasc. 1-2, pp. 73-98, 1985

of polished surfaces 5×11 mm^2 and 5×5 mm^2 can be used for the entrance of the beams.
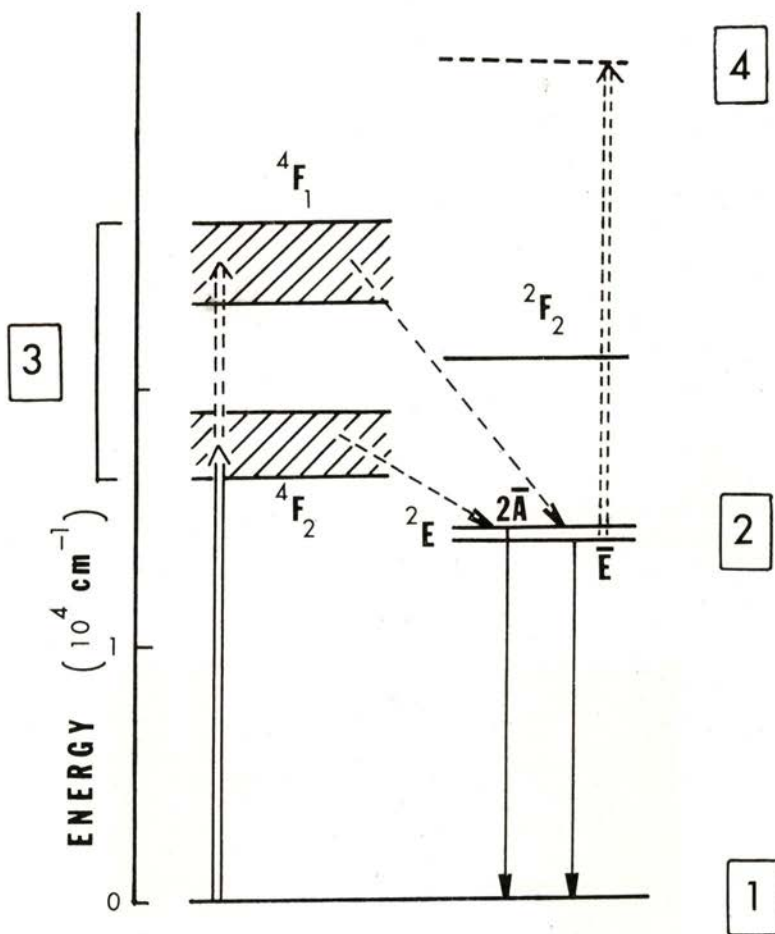
Fig. 3 — Energy level diagram of ruby used for calculations on induced polarization.

The position of the c-axis has been determined by analysis of bi-refringence patterns caused by a convergent beam, incident on the crystal and observed through a polarizer [12]. Figs. 5 and 6 show those patterns for two different orientations of the crystal.

Fig. 5 refers to the transversal orientation, where the laser beam is incident on 5×11 mm² polished surfaces. Fig. 6 refers to the
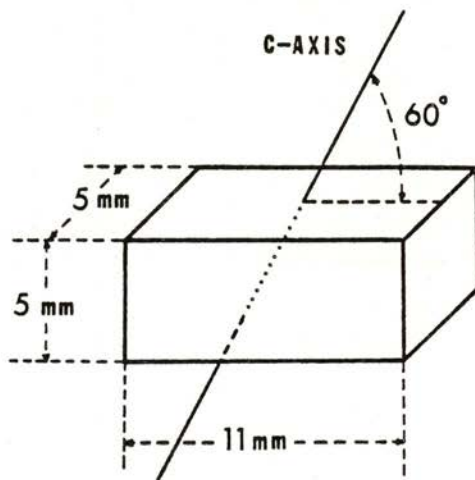
Fig. 4 — Ruby crystal geometry. The c-axis makes a 60° angle with the non-polished surface 5×11 mm² and it is parallel to the polished surfaces 5×11 mm².
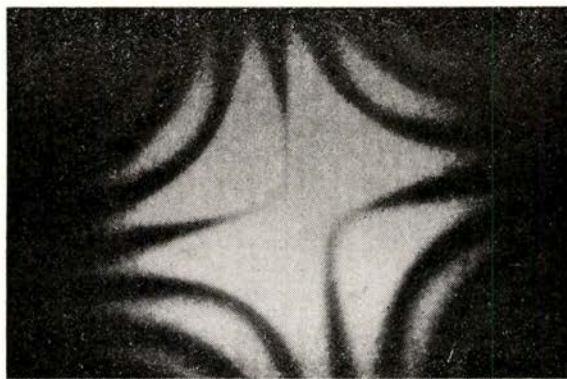
Fig. 5 — Birefringence pattern for the transversal orientation of the crystal.

longitudinal orientation where the beam is incident on the 5×5 mm² polished faces of the crystal.
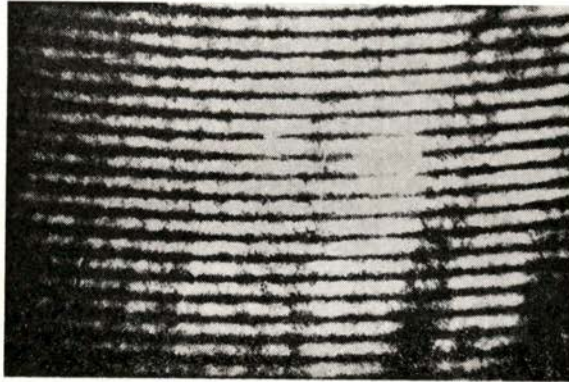
Fig. 6 — Biefringence pattern for the longitudinal orientation of the crystal.

3 – SEMICLASSICAL THEORY OF RESONANT DFWM

In this paper we study the case where the system in Fig. 3 can be decomposed in two independent subsystems 1, 2, 3 and 2, 4; the transition $3 \to 2$ is nonradiative and the exciting field is in resonance only with the transitions $1 \to 3$ and $2 \to 4$.

This approach implies that pumping from level 2 to level 4 is negligible for the calculations carried on the subsystem 1, 2, 3. In other words, the absorption from the excited level 2 is small enough not to change significantly the population of level 2.

We study first the subsystem 1, 2, 3 and then the subsystem 2, 4 as a particular case of it. Finally we get the expressions for the whole system.

We use the semiclassical theory of interaction in the electric dipole approximation [13], with the Hermitian density operator ρ [14]. After neglecting thermal excitation, the equations of motion (Bloch equations) for the density matrix elements ρ_{ij} can be written, introducing relaxation terms [15] as

$$\dot{\rho}_{11} = -(i/\hbar)(V_{13}\rho_{31} - \rho_{13}V_{31}) + \rho_{22}/\tau_{21} + \rho_{33}/\tau_{31} \tag{4a}$$

$$\dot{\rho}_{22} = -\rho_{22}/\tau_{21} + \rho_{33}/\tau_{32} \tag{4b}$$

$$\dot{\rho}_{33} = -(i/\hbar)(V_{31}\rho_{13} - \rho_{31}V_{13}) - \rho_{33}(1/\tau_{31} + 1/\tau_{32}) \tag{4c}$$

$$\dot{\rho}_{13} = -i\omega_{13}\rho_{13} - (i/\hbar)V_{13}(\rho_{33} - \rho_{11}) - \rho_{13}/T \tag{4d}$$

where V_{ij} is the matrix element of the energy of interaction

79

$V = - \mu \cdot E$ with μ as the electric dipole operator and $E = \Sigma_m (A_m / 2) \exp [i (\omega t - k_m \cdot r)] + $ c.c. is the exciting electric field; τ_{ij} is the lifetime of the excited level i before decaying to level j; T is the transverse relaxation time and ω_{ij} is the frequency associated to the energy difference of levels i and j.

From eq. (4d) it is seen that nondriven ($E = 0$) behaviour of ρ_{13} is given by

$$\rho_{13} = \rho_{13} (0) \exp [- (i \omega_{13} + 1 / T) t] = \lambda_{13} (t) \exp (i \omega_{31} t) \tag{5}$$

where $\lambda_{13} (t) = \rho_{13} (0) \exp (- t / T)$ is a time varying slow function, $T^{-1} \ll \omega_{31} = - \omega_{13}$ [16].

When terms in $\exp (\pm 2 i \omega t)$ are ignored and after using the probability conservation equation, we can write eq. 4, in the steady state regime, as:

$$\rho_{11} + \rho_{22} + \rho_{33} = 1 \tag{6a}$$

$$\rho_{22} = (\tau_{21} / \tau_{32}) \rho_{33} \tag{6b}$$

$$\hbar^{-1} (1 + \delta^2)^{-1} | \mu_{13} |^2 (\rho_{11} - \rho_{33}) \sum_{lm} 1/2 \, A_l \cdot A_m^*$$
$$\exp [- i (k_l - k_m) \cdot r] - \rho_{33} (\tau_{31}^{-1} + \tau_{32}^{-1}) = 0 \tag{6c}$$

$$\lambda_{13} = - (i + \delta) (i + \delta^2)^{-1} \mu_{13} (\rho_{11} - \rho_{33}) \sum_m 1/2 \, A_m \exp (- i k_m \cdot r) \tag{6d}$$

where $\delta \equiv (\omega - \omega_{31}) T$ is the normalized detuning of the field from the line center. The solutions of eq 6 are:

$$\rho_{11} = (1 + \alpha I / I_{SAT}) / (1 + \beta I / I_{SAT}) \tag{7a}$$

$$\rho_{22} = (I / I_{SAT}) / (1 + \beta I / I_{SAT}) \tag{7b}$$

$$\rho_{33} = (\alpha I / I_{SAT}) / (1 + \beta I / I_{SAT}) \tag{7c}$$

$$\rho_{13} = - \mu_{13} T \hbar^{-1} (i + \delta) (1 + \delta^2)^{-1} (1 + \beta I / I_{SAT})^{-1}$$
$$\sum_m 1/2 \, A_m \exp [i (\omega t - k_m \cdot r)] \tag{7d}$$

where $\alpha = \tau_{32} / \tau_{21}$, $\beta = 2 \alpha + 1$, $Q = (1 + \tau_{32} / \tau_{31})^{-1}$

$I_{SAT} = \hbar^2 (1 + \delta^2) / (| \mu_{13} |^2 T \tau_{21} Q)$,

$I = 1/2 \sum_{l,m} A_l \cdot A_m^* \, e^{-i (k_l - k_m) \cdot r} + $ c.c.

The magnitude of the induced real polarization is

$$P = N < \mu > = N \, (\mu_{31} \, \rho_{13} + \mu_{13} \, \rho_{31}) \qquad (8)$$

where N is the number density of the absorption centers (Cr^{3+} ions). The real polarization associated with the subsystem 1, 2, 3 is then:

$$P = - \frac{\varepsilon_o \, \alpha_o}{k \, (1 + \delta^2)} \; \frac{\sum\limits_m \mathbf{A}_m \, [\, \delta \cos (\omega t - \mathbf{k}_m \cdot \mathbf{r}) - \sin (\omega t - \mathbf{k}_m \cdot \mathbf{r}) \,]}{1 + \beta \, I \, / \, I_{SAT}} \qquad (9)$$

where ε_o is the permittivity; $k = | \mathbf{k}_m |$ the wave vector and $\alpha_o \equiv (\omega / \hbar) \; N \; | \mu_{13} |^2 \, T$ the line-center ($\delta = 0$) small signal field attenuation coefficient.

Using eq. 7b we can get similarly the polarization associated with the subsystem 2, 4 and write:

$$P' = - \frac{\varepsilon_o \, \alpha_o'}{k \, (1 + \delta'^2)} \; \frac{I \, / \, I_{SAT}}{1 + \beta \, I \, / \, I_{SAT}}$$

$$\frac{\sum\limits_m \mathbf{A}_m \, [\, \delta' \cos (\omega t - \mathbf{k}_m \cdot \mathbf{r}) - \sin (\omega t - \mathbf{k}_m \cdot \mathbf{r}) \,]}{1 + I \, / \, I'_{SAT}} \qquad (10)$$

where $\alpha_o' \equiv (\omega / \hbar) \; N \; | \mu_{24} |^2 \, T'$, $\delta' = (\omega - \omega_{42}) \, T'$ and

$$I'_{SAT} = \hbar^2 \, (1 + \delta'^2) \, / \, (| \mu_{24} |^2 \, T' \, \tau_{24})$$

The total polarization P_t of the whole system is then

$$P_t = \frac{\varepsilon_o \, \alpha_o}{k \, (1 + \delta^2)} \; \{ \sum\limits_m \mathbf{A}_m \, [\, \delta \, (1 + f (I)) \cos (\omega t - \mathbf{k}_m \cdot \mathbf{r}) -$$

$$(1 + g (I)) \sin (\omega t - \mathbf{k}_m \cdot \mathbf{r}) \,] \, \} \, (1 + \beta \, I \, / \, I_{SAT})^{-1} \qquad (11)$$

where

$$g \, (I) = (\alpha_o' / \alpha_o) \; (1 + \delta^2) \; (1 + \delta'^2)^{-1} \, I / I_{SAT} \, (1 + I / I'_{SAT})^{-1} \qquad (12)$$

$$f \, (I) = (\delta' / \delta) \; g \, (I) \qquad (13)$$

Portgal. Phys. — Vol. 16, fasc. 1-2, pp. 73-98, 1985

81

From the following relation

$$P_t = \varepsilon_o \sum_m A_m \left[\chi' \cos(\omega t - k_m \cdot r) - \chi'' \sin(\omega t - k_m \cdot r) \right] \qquad (14)$$

where $\chi = \chi' + i\chi''$ is the susceptibility, we get using eq. (11)

$$\chi = - \frac{\alpha_o}{k(1+\delta^2)} \; \frac{\delta[1+f(I)]+i[1+g(I)]}{1+\beta I / I_{SAT}} \qquad (15)$$

Fig. 7 — Plot of χ_R (I_s) for different values of the parameter I_{SAT}/I'_{SAT}: Curves a, b, c, d, e correspond to $I_{SAT}/I'_{SAT} = 10^{-3}, 10^{-2}, 10^{-1}, 1, 10$; we have taken $\beta = \alpha'_o / \alpha_o = \delta' = \delta = 1$.

In Figs. 7 and 8 we show plots of the susceptibility given by the above equation, with different quantities as parameters and where

$$\tilde{\chi} = \tilde{\chi}_R + \tilde{\chi}_I = - \chi \, k(1+\delta^2)/\alpha_o \qquad (16)$$

and

$$I_S = I / I_{SAT} \qquad (17)$$

In the approximation of neglecting level 4, $f(I)$, $g(I) \ll 1$ and with $\beta \simeq 1$ the complex susceptibility is, as shown in ref. [17],

$$\chi = -(\alpha_0 / k)(1 + \delta^2)^{-1} \frac{\delta + i}{1 + I / I_{SAT}} \tag{18}$$

The non-linear nature of χ and consequently of $\mathbf{P} = \varepsilon_0 \chi \mathbf{E}$ complicates the solution of the wave equation, describing the light wave propagation inside the medium:

$$\nabla^2 \mathbf{E} - \mu\varepsilon_0 \, \partial^2 \mathbf{E} / \partial t^2 = \mu \partial^2 \mathbf{P} / \partial t^2 \tag{19}$$

where $\mathbf{E}(\mathbf{r}, t)$ is a superposition of plane waves. A similar equation also describes the propagation of each component $\mathbf{E}_j$ coupled to the others by the polarization $\mathbf{P}$. In FWM, those components refer to the pumps, probe and FWM signal. For $\mathbf{E}_j$ we can write:

$$\nabla^2 \mathbf{E}_j - \mu\varepsilon_0 \, \partial^2 \mathbf{E}_j / \partial t^2 = \mu \partial^2 \mathbf{P} / \partial t^2 |_j \,, \tag{20}$$
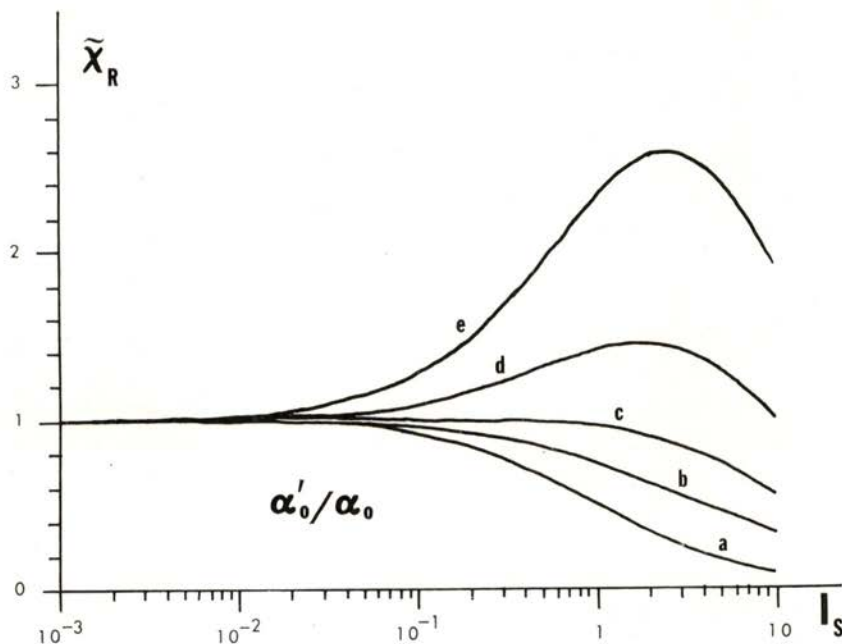
Fig. 8 — Plot of $\chi_R (I_s)$ for different values of the parameter α_0' / α_0 : Curves a, b, c, d, e correspond to $\alpha_0' / \alpha_0 = 0$, 0.25, 1, 2, 4 ; $\beta = \delta' = \delta = 1$; $I_{SAT} / I'_{SAT} = 0.1$.

where the last term represents the component which matches the phase of the first member of the equation.

We consider A_j a slowly varying function of η_j only, where η_j is the direction of propagation of beam j. Using the adiabatic or Born approximation we can get from (20) a system of coupled differential equations for each amplitude A_j. For $j = 4$ we write:

$$\partial A_4 / \partial z = (\tilde{\alpha} / 2) (A_4 - A_1 A_3^* A_2 / I_{SAT}) \tag{21}$$

where $\tilde{\alpha} = \alpha_0 (1 - i \delta) / (1 + \delta^2)$.

To write eq. 21 we have considered $\phi \simeq 0$ and only the beams 1 and 3 interfering to form an hologram which is read by beam 2.

In general, no analytical solutions are possible for those coupled differential equations. However if $A_{3,4} < A_{1,2}$ such solution is possible either when $I < I_{SAT}$ or $I \geq I_{SAT}$. The solution for the first condition is simpler to get and turns out to be a particular case of that of second one [12].

The expression for the intensity of the phase conjugate signal $I_4(0)$ is [12]:

$$I_4(0) = 2 (1 + \delta^2) R T^6 I_1(0)^2 I_3(0) e^{-2\tilde{\alpha}'L} (1 - e^{\tilde{\alpha}'L})^2 / I_{SAT}^2 \tag{22}$$

where,

$$I_{SAT} = \hbar \omega / (Q \sigma \tau_{21}) = 6.6 \times 10^{-21} / (\lambda \sigma) \tag{23}$$

$$\sigma = \tilde{\alpha}' / N_0 , \quad \tilde{\alpha}' = \alpha_0 / (1 + \delta^2) \tag{24}$$

R e T are the reflectance and transmittance of the crystal and $Q = 1$.

So far we have considered the non-linear medium as isotropic. However, the ruby crystal is uniaxial and it seems that an anisotropic theory should be needed. The geometry of interaction (propagation direction of the beams, field polarization and c-axis orientation) conditions the validity of application of those theories.

Figs. 9 and 10 show two possible orientations of the crystal, corresponding to propagation of ordinary waves only. However when the crystal is rotated around $\hat{n}$ by an angle Θ, ordinary and extraordinary waves propagate in the crystal and the developed isotropic theory is no longer valid. We can apply it however separately to each of the waves, treating them as inde-

pendent of each other. As it will be shown, the relative weights or ordinary and extraordinary waves in the measured FWM signal are dependent on the angle of rotation and the characteristic
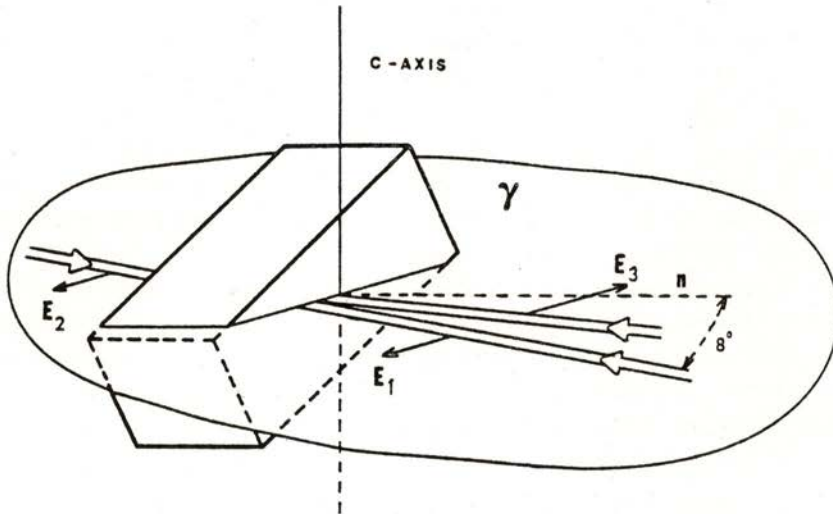
Fig. 9 — Isotropic configuration, with the transversally oriented crystal; the c-axis is normal to plane γ containing the direction of propagation of beams 1, 2 and 3; n is the normal to 5×11 mm² surface of the crystal.
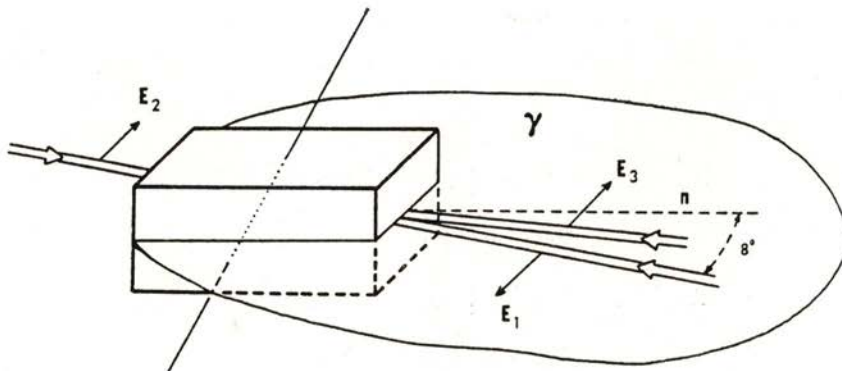
Fig. 10 — Another possible configuration showing the beams 1 and 3 incident on surface 5×5 mm². This is the most efficient configuration, because of the largest interaction length.

parameters associated with those waves. In the holographic interpretation of FWM it means that we have two distinct holograms: one called ordinary and the other extraordinary, which do not interact with each other.

With the two configurations shown in Figs. 9 and 10 we can check experimentally the validity of this theory. At the same time we will show different physical behaviour for those configurations. Geometrically the essential difference between transversal and longitudinal orientation of the crystal is that, during crystal rotation, the c-axis remains approximately normal to the propagation direction of the beams in the first case and makes a 60° angle in the second one.

The quantities appearing in eq. 22 that are different for ordinary and extraordinary waves are $\tilde{\alpha}'$ and I_{SAT}. For light propagating in ordinary and extraordinary modes a net absorption coefficient can be defined for transversal and longitudinal configurations, as function of rotation angle Θ :

$$\tilde{\alpha}'_T = \tilde{\alpha}'_o \cos^2 \Theta + \tilde{\alpha}'_e \sin^2 \Theta \tag{25}$$

$$\tilde{\alpha}'_L = \tilde{\alpha}'_o \, (\cos^2 \Theta + \cos^2 \beta \, \sin^2 \Theta) + \tilde{\alpha}'_e \sin^2 \beta \, \sin^2 \Theta \tag{26}$$

where β, the angle between $\hat{n}$ and c-axis, is 60°.

Fig. 11 shows the theoretical curves given by eqs. 25 and 26 and the experimental data for $\tilde{\alpha}'_T$ and $\tilde{\alpha}'_L$ as functions of Θ .

In analogy with eq. 21, the differential equations for A^o_4 and A^e_4 (the indices o and e stand for "ordinary" and "extraordinary") can be written as:

$$\partial A^o_4 / \partial z = 1/2 \, \tilde{\alpha}_o \, \{ A^o_4 - [\, (A^o_1 \cdot A^{o*}_3) \, / \, I^o_{SAT} +$$
$$(A^e_1 \cdot A^{e*}_3) \, / \, I^e_{SAT}] \, A^o_2 \, \} \tag{27a}$$

$$\partial A^e_4 / \partial z = 1/2 \, \tilde{\alpha}_e \, \{ A^e_4 - [\, (A^o_1 \cdot A^{o*}_3) \, / \, I^o_{SAT} +$$
$$(A^e_1 \cdot A^{e*}_3) \, / \, I^e_{SAT}] \, A^e_2 \, \} \tag{27b}$$

The physical interpretation of the above equation is that the ordinary (extraordinary) component of beam 2 is scattered by both ordinary and extraordinary gratings. However this may not

be the case if the Bragg condition is not satisfied for both waves. In this case, A_2^o (A_2^e) will be scattered only by the ordinary (extraordinary) grating. The equations 27a, b will become:

$$\partial A_4^o / \partial z = 1/2 \, \tilde{\alpha}_o \, [\, A_4^o - (\, A_1^o \cdot A_3^{o\,*} \,) \, A_2^o / I_{SAT}^o \,] \tag{28a}$$

$$\partial A_4^e / \partial z = 1/2 \, \tilde{\alpha}_e \, [\, A_4^e - (\, A_1^e \cdot A_3^{e\,*} \,) \, A_2^e / I_{SAT}^e \,] \tag{28b}$$
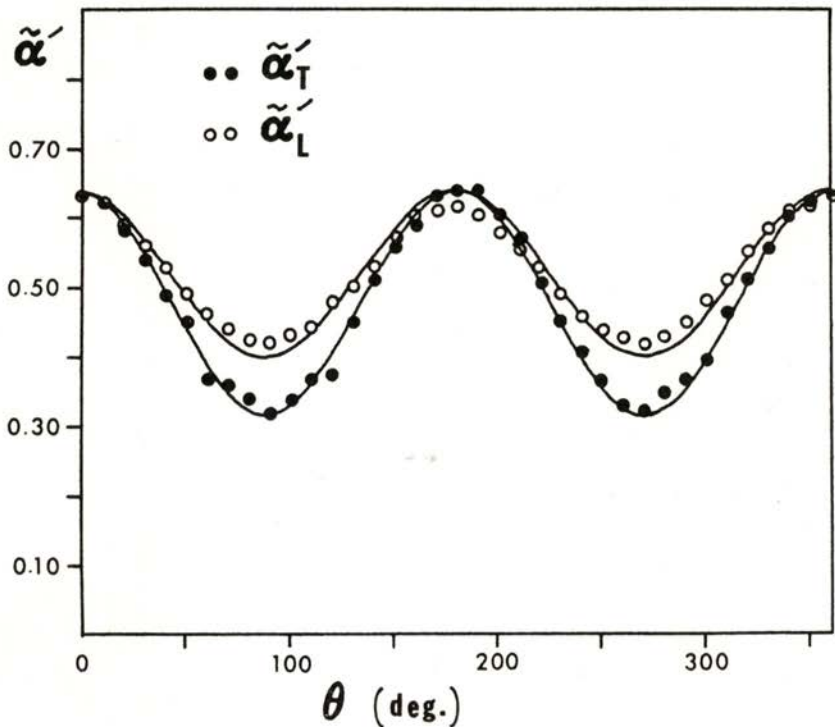
Fig. 11 — Experimental data points and theoretical curves for $\tilde{\alpha}_T'$ and $\tilde{\alpha}_L'$ as a function of rotation angle Θ, for transversal (Fig. 9) and longitudinal (Fig. 10) orientation of the crystal.

The expressions for the intensity $I_4 = I_4^o + I_4^e$ (with $I = A \cdot A^* / 2$) which correspond to those physical situations are [18]

$$I_4(0) = 1/8 \, (\, |B_o|^2 \, \cos^2 \Theta + |B_e|^2 \, \sin^2 \Theta \,)$$
$$(\, C_o \, \cos^2 \Theta + C_e \, \sin^2 \Theta \,)^2 \tag{29}$$
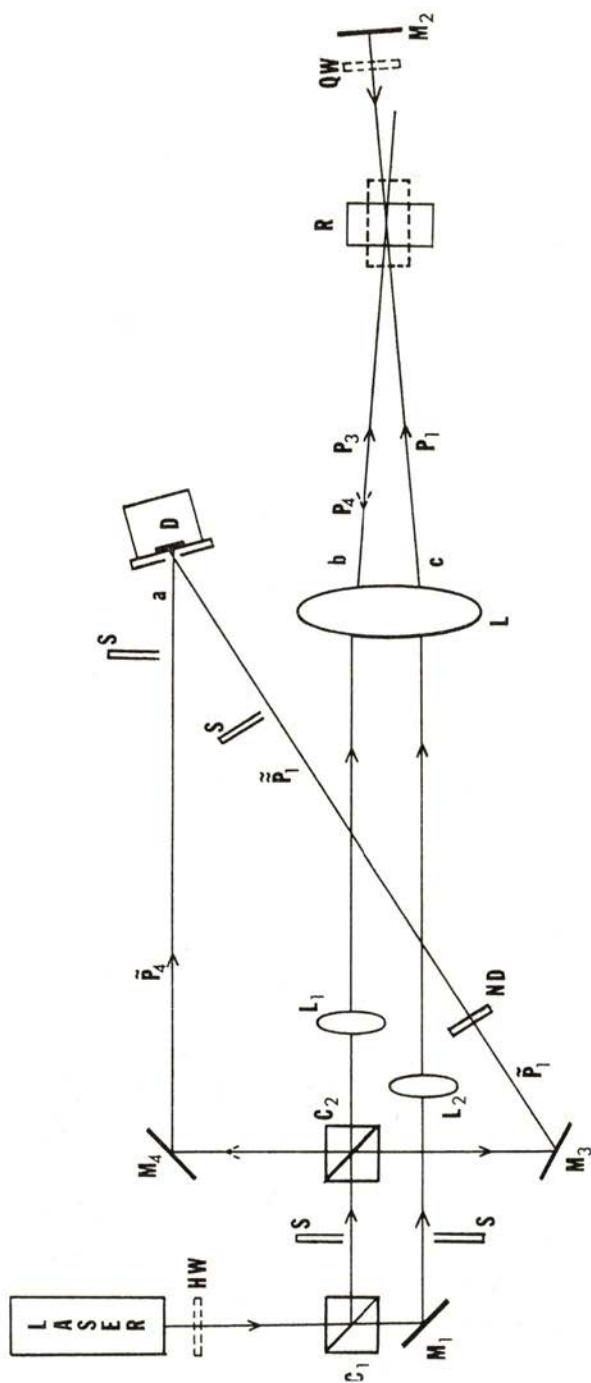
Fig. 12 — Set-up used for DFWM experiments. D is the photodetector; ND a neutral density filter; S are stops. HW and QW are halfwave and quarterwave plates; C_1, C_2 are cube beam splitters; M_1, M_2, M_3 and M_4 are mirrors; L, L_1 and L_2 are lenses, with focal distances $F = 39$ cm, $F_1 = 33.6$ cm; $F_2 = 50$ cm; R is the ruby crystal.

from eq. 27, and

$$I_4^B(0) = 1/8 \left(|B_o|^2 \, C_o^2 \, \cos^6 \Theta + |B_e|^2 \, C_e^2 \, \sin^6 \Theta \right) \qquad (30)$$

from eq. 28, where

$$B_o \equiv B(\tilde{\alpha}_o/2) \exp(-\tilde{\alpha}_o L) \; , \qquad (31a)$$

$$B_e \equiv B(\tilde{\alpha}_e/2) \exp(-\tilde{\alpha}_e L) \; , \qquad (31b)$$

$$B \equiv A_1^2(0) \, A_3^*(0)\sqrt{R} \; , \qquad (32)$$

$$C_o \equiv [\exp(-\tilde{\alpha}_o'L) - 1]/\tilde{\alpha}_o' \, I_{SAT}^o \; , \qquad (33a)$$

$$C_e \equiv [\exp(-\tilde{\alpha}_e'L) - 1]/\tilde{\alpha}_e' \, I_{SAT}^e \; ; \qquad (33b)$$

4 – EXPERIMENTAL RESULTS

The experiments have been performed in order to check the validity of eq. 22 for the isotropic configuration and eqs. 29 and 30 for the anisotropic one. Fig. 12 shows the set-up used to measure the DFWM signal.

A — Isotropic configuration

The orientation of the crystal used for testing eq. 22, is shown in Fig. 9. In this way, only ordinary waves propagate in the crystal. Since the quantity we measured was the power of the 4 different beams, the expression given by eq. 22 had to be modified. The beams have been considered to have Gaussian shapes and their radii have been measured or calculated. Written in terms of measured powers $\tilde{P}_4$ and $\tilde{\tilde{P}}_1$ eq. 22 becomes:

$$\tilde{P}_4 = C(1 + \delta^2) \, \tilde{\tilde{P}}_1^3 \qquad (\mu W, \; cm) \qquad (34)$$

where C depends on the beams' diameters and all the parameters affecting I_4 in eq. 22.

Fig. 13 shows the theoretical curves for different wavelengths of the Ar laser, when $\delta = 0$. In Fig. 14 we show experimental
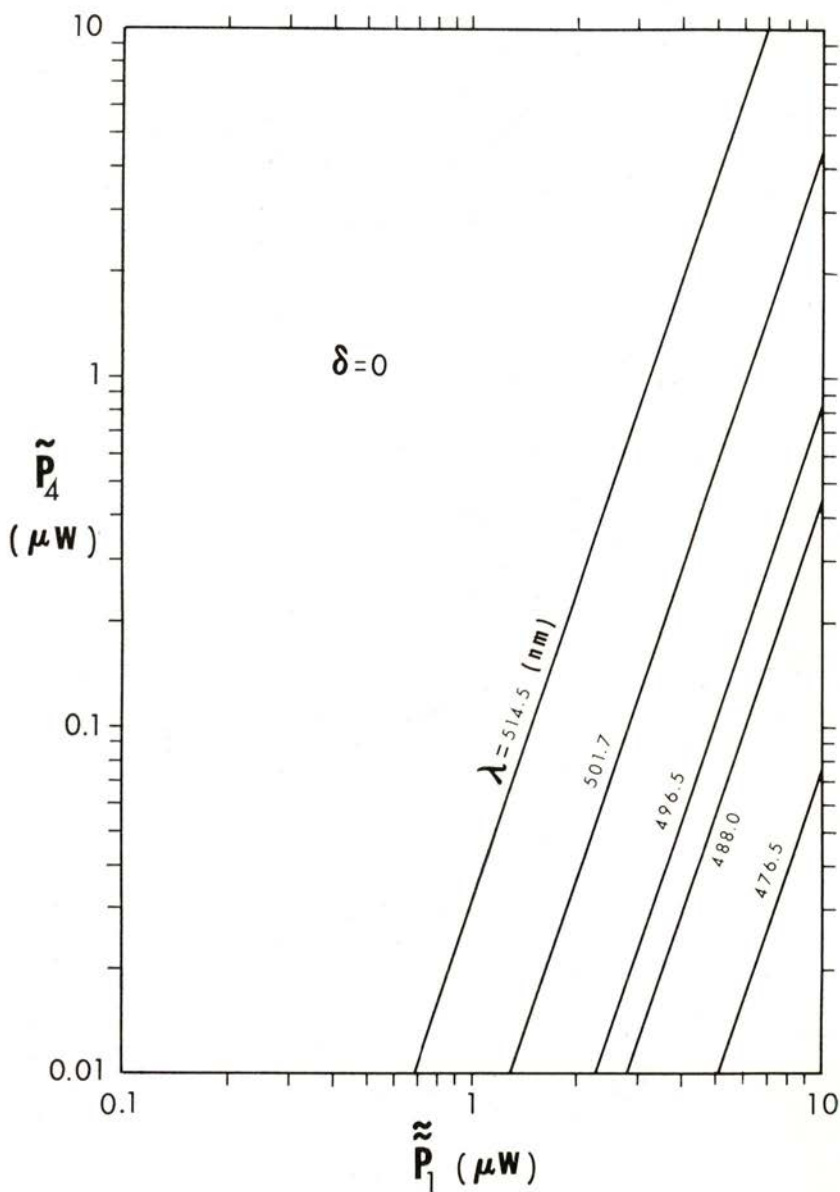
Fig. 13 — Theoretical curves for $\delta = 0$ predicted by eq. 34. Each line corresponds to a different wavelength λ of the Ar laser.

90

Portgal. Phys. — Vol. 16, fasc. 1-2, pp. 73-98, 1985
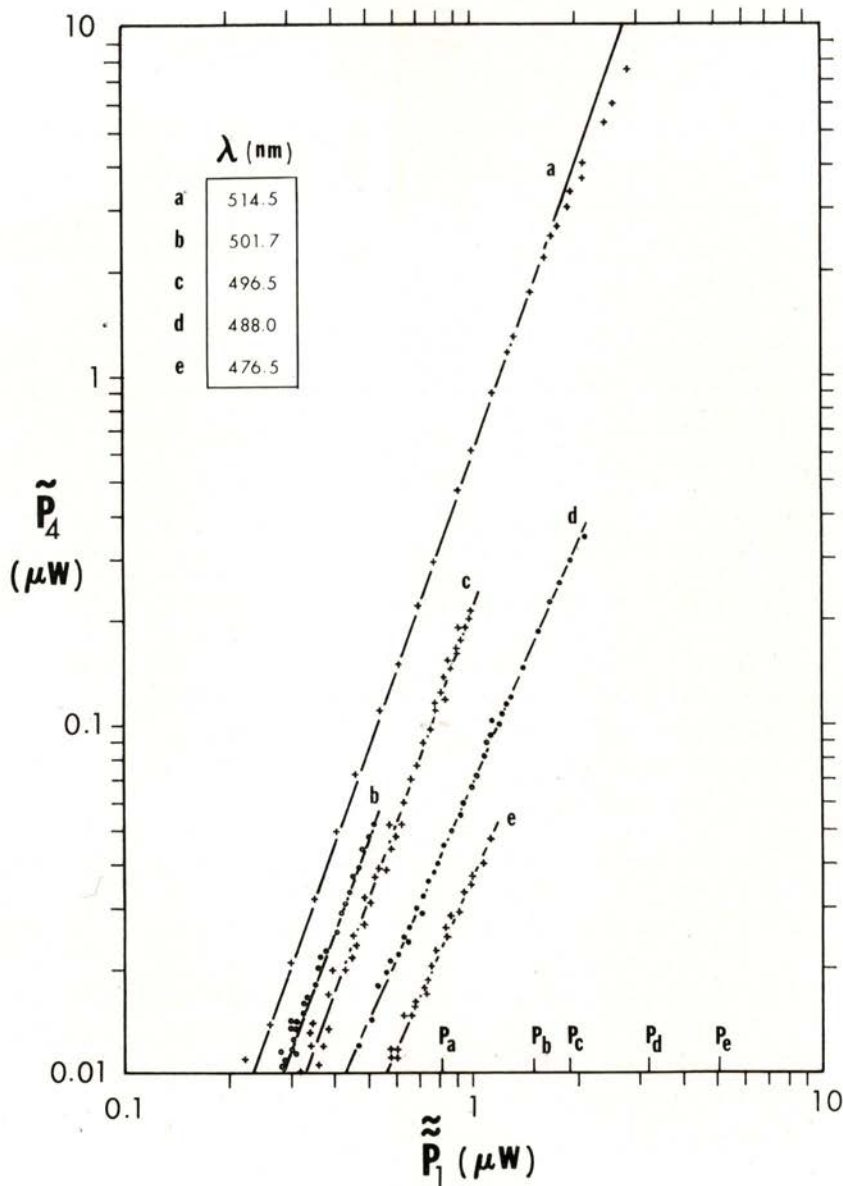
Fig. 14 — Experimental points for $\tilde{P}_4$ as function of $\tilde{\tilde{P}}_1$, with wavelength λ as a parameter. The lines are the best linear fitting.

data for the same wavelengths and where $\tilde{\tilde{P}}_x = 10^{-2} \tilde{\tilde{P}}_{SAT}$ for $\lambda = \lambda_x$ and $x = a, b, c, d, e$.

When we try to fit the experimental data with the theoretical curves we get the following conclusions [12]:

a) δ (unknown independently) depends on the wavelength.

b) Curves a, b, c show a slope close to 2; however d and e deviate from that slope.

c) For large $\tilde{\tilde{P}}_1$, curve a starts deviating from linear behaviour.

The behaviour of curves d and e has been attributed to the increase of beams' diameters with the electric current in the laser.

The non-linearity of curve a for large enough valumes of $\tilde{\tilde{P}}_1$ is due to the proximity of $\tilde{\tilde{P}}_{SAT}$.

B — *Anisotropic configuration*

i) *Transversal orientation for the crystal*

With the crystal orientation shown in Fig. 9, we rotate the crystal by an angle Θ around the direction of propagation k_1.

The theoretical expressions for P_4 derived from eqs. 29 and 30, after substituting for the values of the parameters in eqs. 31, 32 and 33, are respectively:

$$P_4(0) \propto (\cos^2 \Theta + 0.34 \sin^2 \Theta)(\cos^2 \Theta + 0.54 \sin^2 \Theta)^2 \quad (35)$$

$$P_4^B(0) \propto \cos^6 \Theta + 0.1 \sin^6 \Theta \quad (36)$$

The theoretical curves and the experimental data are shown in Fig. 15. The full-line corresponds to eq. 35 and the dashed-line to eq. 36. The best fitting is obtained with eq. 35, showing that the ordinary and extraordinary components of reading beam 2 are diffracted by both ordinary and extraordinary gratings.

ii) *Longitudinal orientation for the crystal*

The crystal has been positioned as in Fig. 10 and rotated around $\hat{k}$, as in i). The experimental expressions for P_4 derived

from eqs. 29 and 30 are, after substituting for the numerical values of the parameters, respectively:

$$P_4(0) \propto (\cos^2\Theta + 0.7 \sin^2\Theta)(\cos^2\Theta + 0.74 \sin^2\Theta)^2 \qquad (37)$$

$$P_4^{B}(0) \propto \cos^6\Theta + 0.4 \sin^6\Theta \qquad (38)$$
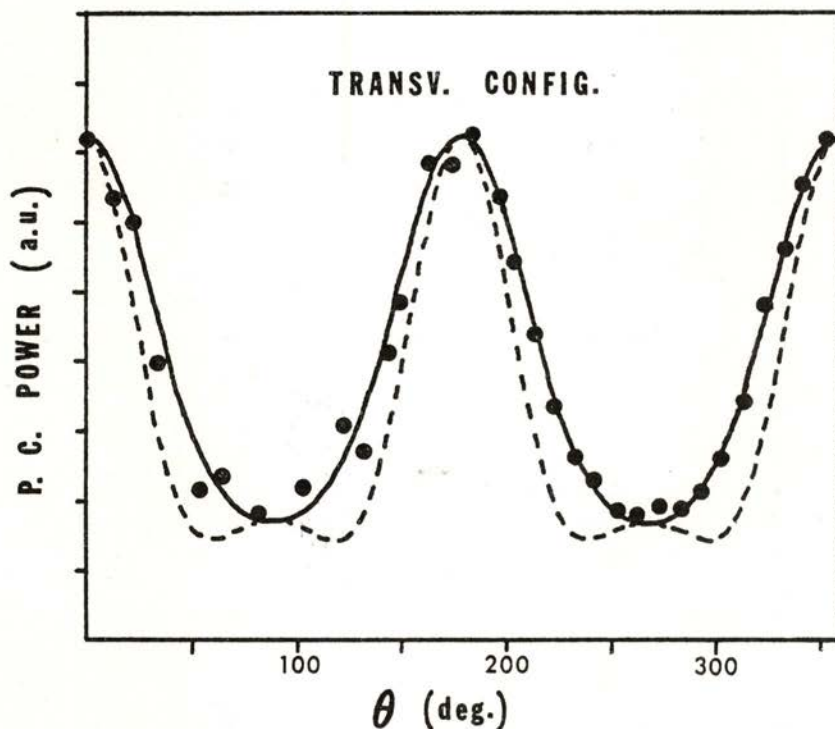
Fig. 15 — Experimental data points and theoretical curves for FWM signal (P. C. Power) as a function of the rotation angle in the transversal configuration. Full line corresponds to eq. 35 and dashed line to eq. 36. The power units are arbitrary (a. u.).

The theoretical curves and the experimental data are shown in Fig. 16. The best fitting (full-line) corresponds to eq. 38.

From the above results we can conclude that, in the longitudinal orientation, the ordinary (extraordinary) beam 2 does

not satisfy the Bragg condition for the extraordinary (ordinary) grating.
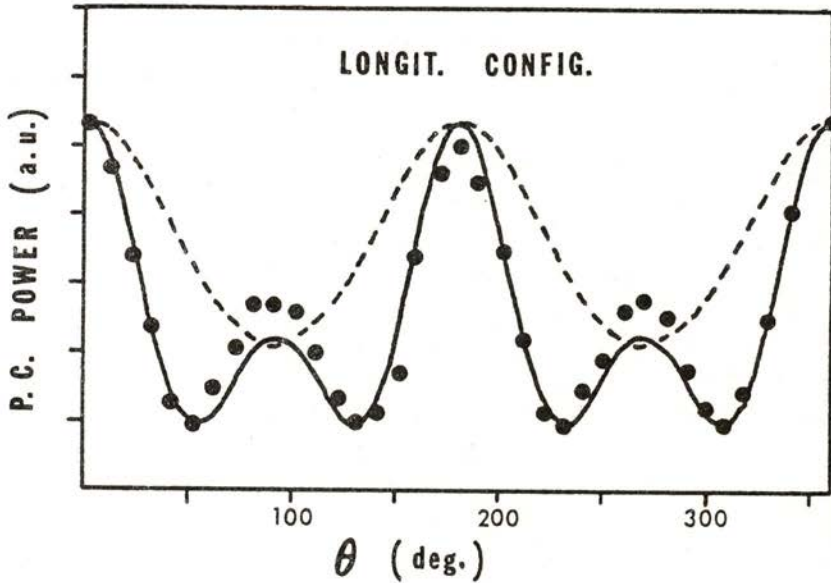
Fig. 16 — Experimental data points and theoretical curves for FWM signal (P. C. Power) as a function of the rotation angle in the longitudinal configuration. Full line corresponds to eq. 38 and dashed line to eq. 37. The power units are arbitrary (a. u.).

5 – THERMAL DFWM

Because of the nonradiative decay from level 3 to level 2 (see fig. 3), a thermal grating is also formed in the crystal. Since the index of refraction changes with temperature ($dn/dT = 12.6 \times 10^{-6}$ K^{-1}) a phase grating due to temperature will result.

The expression for the FWM signal intensity $I_4^{th}(0)$ due to this effect is [12]:

$$I_4^{th}(0) = R\, T^6\, (4\pi \cdot 10^{-13}/\lambda)^2\, e^{-3\tilde{\alpha}' L}\, (1 - e^{-\alpha' L})^2\, I_1^2(0)\, I_3(0)\,, \qquad (39)$$

which when compared with $I_4(0)$ given by eq. 22 turns out to be $\sim 10^{-10}$ smaller! This is the consequence of the high thermal

conductivity ($\lambda = 0.42$ W cm^{-1} K^{-1}) of ruby causing the wash out of the thermal grating very effectively and rapidly (decay time ~ 10^{-8} s).

6 – SELF-FOCUSING

Self-focusing gives rise to a deformation of a beam profile with non-uniform intensity and results from non-uniform changes in the optical properties of the medium, caused by the beam itself. Wavefront deformations of the beams used in FWM may, therefore, exist due to self-focusing. Such deformations can somehow affect the measured phase conjugate signal, as suggested in ref. 19.

Two mechanisms can be responsible for self-focusing: non-uniform distribution of temperature and of energy level excitation.

Theoretically, for the typical powers used in our experiment, the phase delay $\Delta\phi$ between the center and the edge of the Gaussian beam are $\Delta\phi_1 = 0.2$ rad and $\Delta\phi_2 = 0.15$ rad respectively [12]. The radii of curvature have been calculated to be $R_1 = 23$ m and $R_2 = 66$ m. Those values are small when compared with the intrinsic laser beam divergence.

Experimentally we have used both Moiré and double exposure holographic interferometry techniques [12]. We did not observe any curvature effect with $\Delta\phi > \pi$, the maximum sensitivity of the used techniques.

Such results lead us to conclude that for the power levels we used in our c.w. DFWM experiments the self-focusing effects can be neglected.

7 – PHASE CONJUGATION – AN APPLICATION OF FWM

Phase conjugation refers to any process in which a wave

$$E_4(r,t) = \text{Re} \left[A_4(r) \, e^{i\omega t} \right] \tag{40}$$

is generated from an incident wave

$$E_3(r,t) = \text{Re} \left[A_3(r) \, e^{i\omega t} \right] \tag{41}$$

and the relation between their amplitudes is

$$A_4(r) = R \, A_3^*(r) , \tag{42}$$

where R is a constant; Re stands for "real part of" and * for "complex conjugate".

For simplicity we consider the case of 'plane waves'. If we write

$$A_3 = \psi(\mathbf{r}) \, e^{-ikz} \tag{43}$$

and because of the identity

$$E_4(\mathbf{r}, t) = \mathrm{Re}[R\psi^*(\mathbf{r}) \, e^{ikz} \, e^{i\omega t}] = \mathrm{Re}[R\psi^*(\mathbf{r}) \, e^{ikz} \, e^{i\omega t}]^* \tag{44}$$

$$= \mathrm{Re}[R\psi(\mathbf{r}) \, e^{-ikz} \, e^{-i\omega t}] = \mathrm{Re}[R\mathbf{A}_3(\mathbf{r}) \, e^{-i\omega t}],$$

we can say that E_4 is the time reversal of $R E_3$, i. e. E_4 is equal to $R E_3$ after t becomes -t. Phase conjugation and time reversal are therefore often used with the same meaning. The above discussion is also valid for non-plane waves if the superposition principle applies.

The solution of eq. 21 shows that A_4 is proportional to A_3^* i. e. the FWM signal 4 is the phase conjugate of probe 3.

To show the phase conjugate imaging properties of FWM we introduce a resolution chart in our set-up as shown in Fig. 17. The orientation of the crystal is that shown in Fig. 10, which corresponds to maximum efficiency because of the larger inter-action length L.
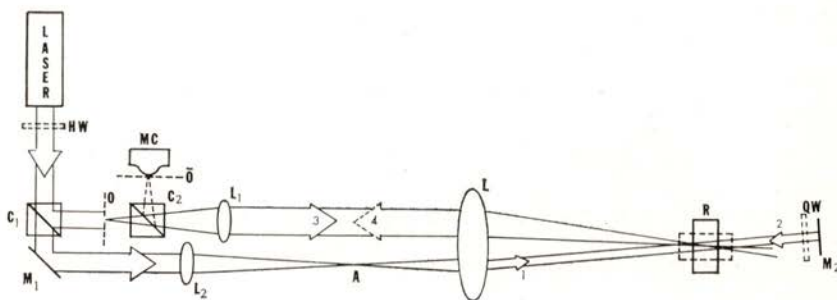
Fig. 17 — Schematic of the experimental set-up (the same as in Fig. 12) for the phase conjugate reconstruction of a microscopic object. 0 and $\bar{0}$ are the object and the phase conjugate object planes. MC is a microscope with a photographic camera.

The input and the phase conjugate image are shown in Fig. 18a, b. A speckle averaging technique has been used [20], to improve the image quality. It consists in moving the crystal

A   B
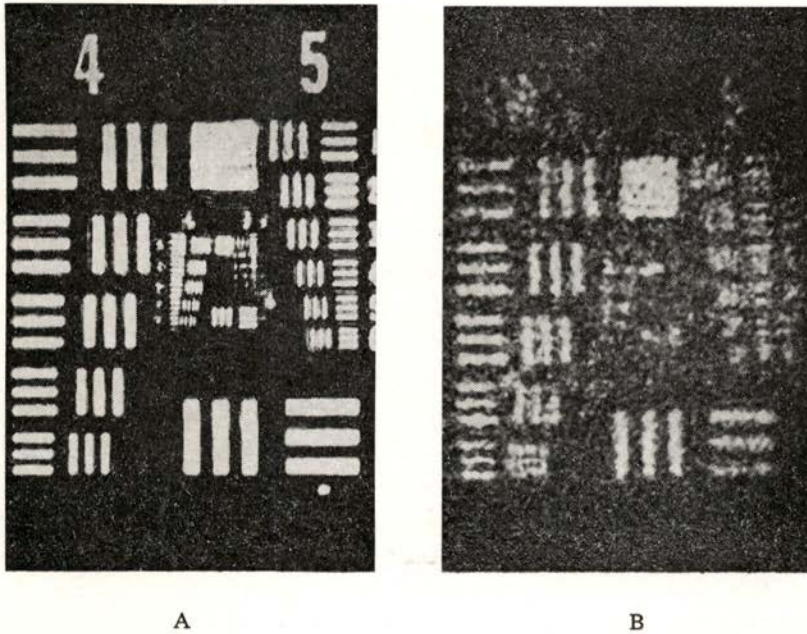
Fig. 18 — (a) Input object in plane 0 (b) phase conjugate reconstructed object after speckle averaging: multiple (15) exposure 15 × 1/125 sec. The spatial frequency of 5-1 group is ~30 line pairs/mm.

continuously during exposure or by steps with multiple exposure. This can be also accomplished by phase modulation of one of the beams which causes in addition, by averaging the grating contrast, a more uniform intensity of the image.

REFERENCES

[1] C. V. Heer and N. C. Griffen, *Opt. Lett.*, 4, 239 (1978). A. Maruani, *IEEE J. Quantum Electron.*, QE-16, 558 (1980). A. L. Smirl, T. F. Boggess and F. A. Hopf, *Opt. Comm.*, 34, 463 (1980).

[2] N. Bloembergen, *Nonlinear Optics* (W. A. Benjamin, Inc., New York, 1965).

[3] P. D. Maker and R. W. Terhune, *Phys. Rev.*, A137, 801 (1965).

[4] A. Yariv, *IEEE J. Quantum Electron.*, QE-14, 650 (1978); *Opt. Comm.*, 25, 23 (1978).

[5] B. I. Stepanov, E. V. Ivakin, A. S. Rubanov, *Sov. Phys. Dokl.*, 16, 44 (1971).

[6] D. G. Steel and J. F. Lam, *Phys. Rev. Lett.*, 43, 1588 (1979).

[7] A. E. Siegman, *An Introduction to Lasers and Masers* (McGraw-Hill Book Company, New York, 1971).

[8] T. Kushida, *J. Phys. Soc. Japan*, 21, 1331 (1966).

[9] M. J. Weber, *Methods of Experimental Physics*, vol. 15-A: Quantum Electronics, ed. C. L. Tang (Academic Press, New York, 1979).

[10] T. H. Mainman, R. H. Hoskins, I. J. D'Haenes, C. K. Asawa and V. Evtuhov, *Phys. Rev.*, 123, 1151 (1961).

[11] W. M. Fairbank, Jr., G. K. Klauminzer and A. L. Schawlow, *Phys. Rev.*, B11, 60 (1975).

[12] L. M. Bernardo, Ph. D. Thesis, Virginia Polytechnic Institute and State University, Blacksburg, Virginia 24061 (1983).

[13] Th. Hansch and P. Toschek, *Z Physik*, 236, 213 (1970).

[14] U. Fano, *Rev. Mod. Phys.*, 29, 74 (1957).

[15] G. Orriols, *Il Nuovo Cimento*, 53B, 1 (1979).

[16] E. I. Shtyrkov, *Opt. Spectrosc.*, 45, 339 (1979).

[17] R. L. Abrams, R. C. Lind, *Opt. Lett.*, 2, 94 (1978).

[18] L. M. Bernardo, S. P. Almeida, *Opt. Comm.*, 48, 389 (1984).

[19] P. F. Liao, D. M. Bloom, *Opt. Lett.*, 3, 4 (1978).

[20] L. M. Bernardo, S. P. Almeida, *Appl. Opt.*, 22, 3926 (1983).

ELECTRONIC CIRCUITS FOR VARIABLE BIT LENGTH, HIGH-SPEED, CLOCKLESS, BINARY ANALOG-TO-DIGITAL AND DIGITAL-TO-ANALOG CONVERTERS

C. A. N. Conde

Physics Department, University of Coimbra, 3000 Coimbra, Portugal

ABSTRACT — It is shown that a simple circuit made of just an operational amplifier, a comparator with precision saturated output and two identical resistors can be used as the basic unit for fast, clockless, variable bit length ADC's. An inexpensive version of this circuit is discussed. It is also shown how a modified circuit can be used as the basic unit for DAC's.

The commercially available analog-to-digital converters [1] are generally of one of the following types: ramp-comparator, integrating and successive approximations. Cascade-encoder type ADC's [2, 3] while very fast have not yet lent themselves to integrated or monolithic circuit units perhaps due to the complexity of the design.

In the present work we describe a very simple circuit that can be used as the basic unit for a variable bit length ADC of the cascade-encoder type. It requires no linear gates nor clocks and lends itself to integration. The only precision components required are two identical resistors (per bit), that can be externally trimmed.

The basic circuit is indicated in Fig. 1.

If we assume that the saturated output of the comparator C is equal to E_0 (logical 1) if $V_i > E_0 / 2$, and equal to zero

(logical 0) if $V_i < E_0 / 2$; the output of the operational amplifier A, is (*)

$$V_0 = \begin{cases} 2\,V_i & \text{if} \quad V_i < E_0 / 2 \\ 2\,V_i - V_0 & \text{if} \quad V_i > E_0 / 2 \end{cases}$$

This means that to obtain the linear output V_0 we multiply the ratio V_i / E_0 by two and then multiply the fractional part of the number thus obtained by E_0 (it is assumed that the input voltages V_i are within the 0 to E_0 Volts range). The integer part is available as a logic signal, B, which is actually equal to the most significant bit of that number. If V_0 is fed to the input
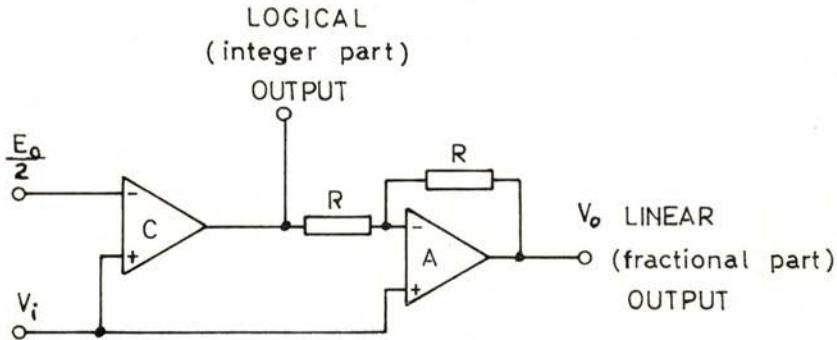
Fig. 1 — The basic circuit for building ADC's of the cascade-encoder type.

of another circuit identical to the one described, the second most significant bit can be obtained at its logical output, etc. Thus, an *n*-bit binary analog-to-digital converter can be built just by connecting in cascade *n* circuits identical to that of Fig. 1, as shown in Fig. 2.

The speed of this ADC is limited mainly by the slew rate and the settling time of the operational amplifiers and the response time of the comparators, and can thus be very fast. As soon as the first circuit processes the input signal V_i and feeds V_0 into

(*) If we consider the operational amplifier with finite gain A, common mode rejection ratio CMRR and input offset voltage e_0, V_0 will be given by $V_0 = [2\,V_i\,(1 + CMRR^{-1}) + 2\,e_0 - E_0\,\delta]\,(1 + 2/A)^{-1}$ where $\delta = 1$ if $V_i > E_0 / 2$ and $\delta = 0$ if $V_i < E_0 / 2$.

the second one it is ready to start processing another input signal. Thus the different circuits in the cascade can process simultaneously successive signals. This will introduce no errors provided the logical outputs are conveniently delayed so that the digital data B_1, B_2, ... B_n corresponding to a same signal V_i arrive at the outputs at the same time. Therefore the limiting speed of this ADC is determined by that of a single stage.
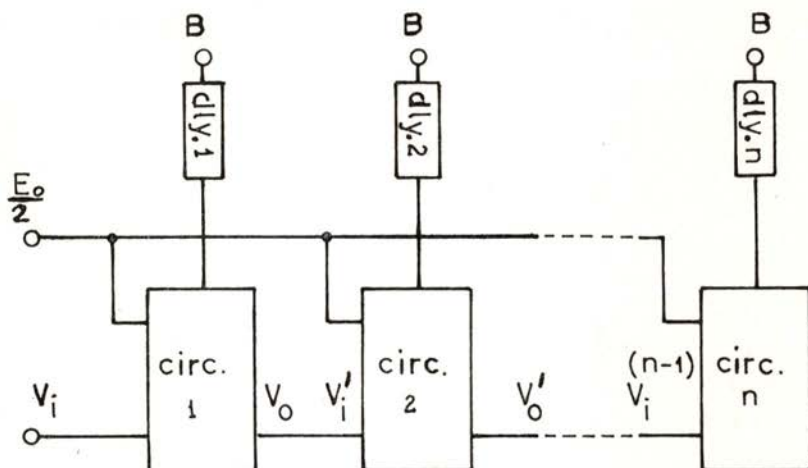
Fig. 2 — An *n* bit ADC.

The response of the basic circuit (Fig. 1) for $V_i \approx E_0 / 2$ was not discussed. For these cases the comparator works in the linear rather than in the saturated region and its output is somewhere between 0 and E_0. Under these circunstances the circuit does not process correctly the input V_i and gives a wrong output V_0. These cases correspond to the region of width ΔV around $E_0 / 2$ shown in Fig. 3. Although ΔV can be very small (of the order of 0.1 mV for a precision comparator) the errors arising in the processing are large and in general cannot be tolerated. This difficulty can be easily solved using a comparator with positive feedback (with very little backlash) or feeding the output of the comparator into a positive feedback circuit like a Schmitt trigger. Then the response of the circuit is of the type shown in Fig. 4. If the backlash ΔV_B is rather smaller than the least significant bit no appreciable errors will arise.

An experimental and inexpensive circuit of the type of that of Fig. 1 was built using a 311 comparator and a 741 operational amplifier. However as this comparator does not give a precision saturated output, it was used in a gating system to connect, through two COS / MOS bilateral switches (CD 4016), the input resistor R (10 kOhm) to a +10 Volts (E_0) supply when the comparator output was a logical one, and to the ground potential when the comparator output was a logical zero. The experimental results show that, with no adjustments, the response function of
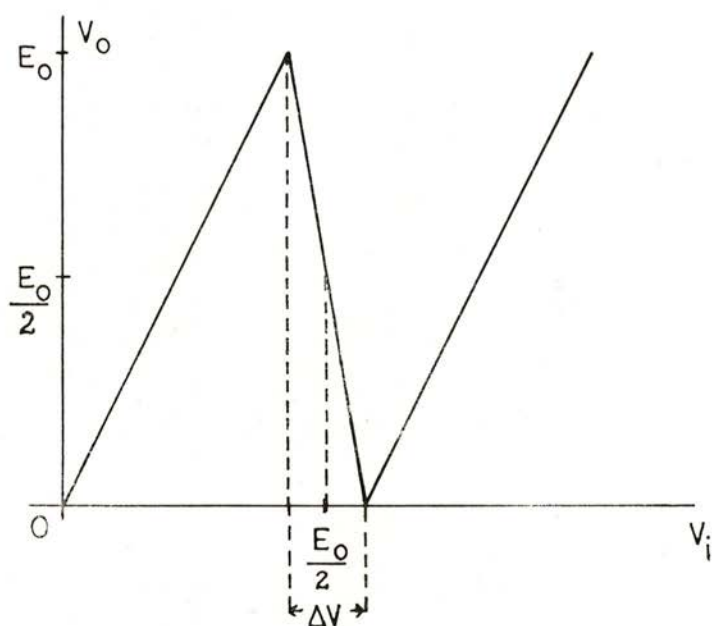
Fig. 3 — Response curve for the circuit of Fig. 1.

the circuit deviates from the theoretical function (Figs. 3 and 4) by about 2 % at the output, V_0, or by about 1 % when referred to the input. This means that ADC's with an accuracy of about 7 bits can be made with no other adjustment than the matching, in pairs, of the resistors R. The main source of error seems to arise from imperfections of the operational amplifier due to the common mode voltage applied to its positive input.

These experimental results show that it should be possible to implement in a single integrated circuit chip one or more circuits of the type of Fig. 1 using COS/MOS and MOS technologies.
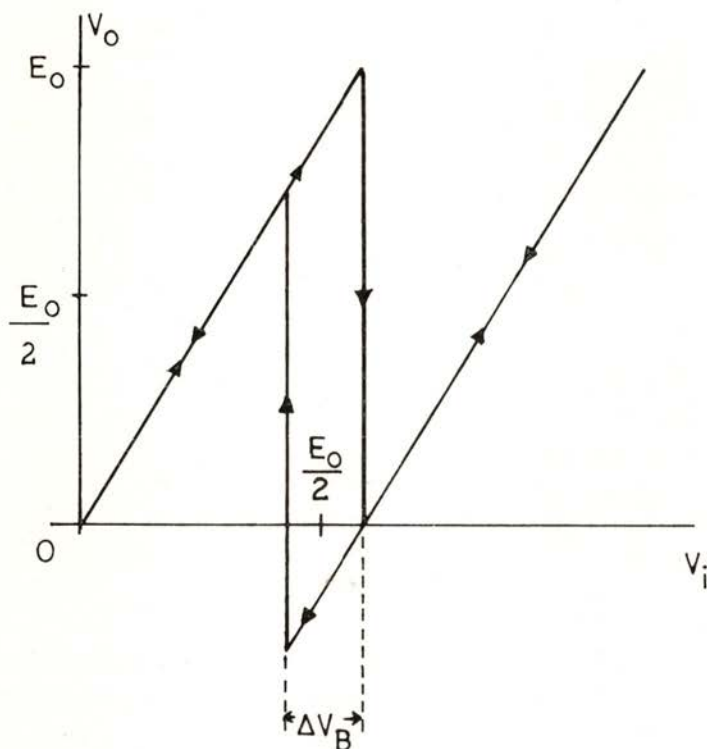
Fig. 4 — Response curve for the circuit of Fig. 1 with hysteresis.

A circuit similar to that of Fig. 1 can also be developed for digital-to-analog conversion. It is shown in Fig. 5. The amplifier with precision saturation I gives a voltage $E_1 = 0$ if bit B is zero and $E_1 = -KE_0$, where K is a scaling factor, if bit B is one. If we have various circuits like this one in cascade, short circuit to ground the input V_i of the first one, and the successive n bits of a binary number are fed at the bit inputs, B's, the linear output at the last stage is given by:

$$V_0 = (2^n B_1 + 2^{n-1} B_2 + \ldots + 2 B_n) \, K E_0$$

which is the analog conversion of the binary number. To avoid saturation of the operational amplifiers, K should be made small: for an 8 bit conversion it should be of the order of 0.001 to keep the output voltage within the 0 to E_0 range.
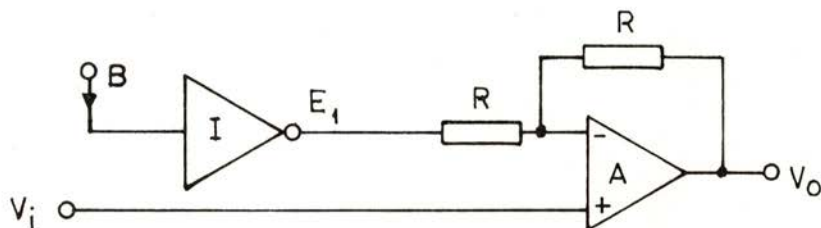
Fig. 5 — Basic circuit for building DAC's.

It is possible to have a circuit that combines the functions of the circuits of Fig. 1 and Fig. 2. With straightforward logic and with an analog switch that connects either a E_0 or a $E_1 = -K E_0$ supply, it is possible, that by the use of just a single logic signal, to have such a circuit executing either ADC or DAC functions. This circuit will not be much more complicated than that of Fig. 1 and will be thus more versatile.

REFERENCES

[1] E. R. HNATEK, «A user's handbook of D/A and A/D converters», John Wiley & Sons, Inc., New York, 1976.

[2] A. SAVITT, «A high-speed analog-to-digital converter», *IRE Trans. Elec. Comp.*, vol. EC-8, 31 (March 1959).

[3] J. V. WAIT, L. P. HUELSMAN and G. A. KORN, «Introduction to operational amplifier theory and applications», McGraw-Hill, Inc., New York, 1975.

104

Portgal. Phys. — Vol. 16, fasc. 1-2, pp. 99-104, 1985

PORTUGALIAE PHYSICA publishes articles or research notes with original results in theoretical, experimental or applied physics; invited review articles may also be included.

Manuscripts, with an abstract, may be written in English or French; they should be typewritten with two spaces and in duplicate. Figures or photographs must be presented in separate sheets and be suitable for reproduction with eventual reduction in size; captions should make the figures intelligible without reference to the text. Authors are requested to comply with the accepted codes concerning references.

There is no page charge. Author(s) will get 50 free reprints (without covers); these are to be shared among all the authors of the article. Authors interested in more reprints should say so when sending their manuscripts; quotations shall be sent with the proofs.

Subscription rates for volume 15:

<div align="center">

4.200 Escudos (US$24) — individuals

10.500 Escudos (US$60) — libraries

</div>

PORTUGALIAE PHYSICA may also be sent on an exchange basis; we wellcome all suggestions to such effect.

All mail to be addressed to

PORTUGALIAE PHYSICA

C/O LABORATÓRIO DE FISICA, FACULDADE DE CIÊNCIAS
PRAÇA GOMES TEIXEIRA
4000 PORTO PORTUGAL

PORTUGALIAE PHYSICA

CONTENTS

PORTUGALIAE PHYSICA

PORTUGALIAE
PHYSICA

AN APPROXIMATE METHOD TO CALCULATE
ENERGY LEVELS

J. Dias de Deus and A. B. Henriques

Centro de Física da Matéria Condensada/INIC, Av. Prof. Gama Pinto 2, 1699 Lisboa Codex, Portugal

ABSTRACT — An approximate method, to calculate energy levels of quantum systems bound by a potential, is introduced which uses the virial theorem and an independent minimization procedure at each energy level. Results obtained are presented and discussed.

I – INTRODUCTION

Recently, an approximate method to calculate energy levels of quantum systems bound by a large class of potentials was introduced by Gersch and Braden [1]. One of its most appealing features is the use of the Heisenberg uncertainty principle, one of the basic principles expressing the physical content of quantum mechanics. The careful and criterious application of approximate methods to deal with the Schrödinger equation is always wellcome, as such methods may help to develop an intuitive understanding of the behaviour of microscopic systems and of how such behaviour is affected by changes in the parameters defining the system.

The variation method is amongst the most powerful approximate methods and highly sophisticated generalizations of Ritz technique have been devised to calculate energy levels beyond the ground-state E_0. These calculations may, for example, start with a linear combination of functions, $\psi_{\text{trial}} = \Sigma_k c_k \chi_k$, not necessarily orthogonal among them, and, by a convenient minimization procedure with respect to the c_k's, successive approximate eigenvalues are then found. The closer these functions are to exact wave-functions, the closer to the exact eigenvalues are the successive E_i's [2].

Our purpose with this note is mainly pedagogical. We shall be dealing with a simple, non-orthodox, application of the variation method which we believe has some connection with the work of ref. [1]. We will enforce the virial theorem (as well as the Hellmann-Feynman theorem), by performing, at each level separately, an independent minimization procedure with respect to a convenient trial wavefunction and a variation parameter β

$$\partial E / \partial \beta = 0, \tag{1}$$

dropping the constraint of orthogonality among the trial wavefunctions corresponding to different levels. We, nevertheless, find that the calculated levels are in very good agreement with the exact ones. An effort is made to understand why this happens.

The great advantage of the technique is to give simple analytical expressions for the energies, in terms of the parameters of the system under study. Even when more than one term is taken in the potential, a simple pocket calculator can easily handle such expressions. The method can thus hopefully play a useful role, both at the pedagogical level and at the level of research, in estimates of energy levels of models under investigation (for example, in elementary particle spectroscopy). We only use knowledge that a student, having followed a basic course in Quantum Mechanics, should have.

In section II we introduce the method and apply it to some important types of potentials. In section III we put together and complete our arguments and draw conclusions.

II — THE METHOD AND APPLICATIONS

With straightforward dimensional arguments one can easily show how condition (1) fulfills the virial theorem as well as the Hellman-Feynman theorem [3]. (See the Appendix for a more general proof).

Consider a potential

$$V(x) \sim x^p \tag{2}$$

and a trial wavefunction depending on the minimization parameter β, $\psi(x, \beta)$, such that

$$\psi(x, \beta) = \sqrt{\beta} \ \phi(\xi) \quad (*) \tag{3a}$$

with

$$\xi \equiv \beta x \tag{3b}$$

and

$$\int \bar{\psi}(x) \ \psi(x) \ dx = \int \bar{\phi}(\xi) \ \phi(\xi) \ d\xi = 1 \tag{3c}$$

The variable ξ is here a convenient dimensionless quantity. The energy eigenvalue, for any level, can be written as

$$<E>_{\nu} = \frac{1}{\mu} < \frac{1}{2} \frac{d^2}{dx^2} >_{\nu} + <V>_{\nu} = <T>_{\nu} + <V>_{\nu}, \tag{4}$$

ν designating the order of the level and μ the reduced mass.

With (2) and (3) the energy $<E>_{\nu}$ is a function of μ and β, $E = E(\mu, \beta)$, β itself being, through the Schrödinger equation, a function of μ.

We have

$$<T>_{\nu} \sim \beta^2 / \mu \quad \text{and} \quad <V>_{\nu} \sim 1 / \beta^p, \tag{5}$$

the dimensionless numerical constants of proportionality in (5) being obtained from integrals over ξ.

The minimization condition (1), then becomes, with the help of expressions (5),

$$\partial <E>_{\nu} / \partial \beta = 2 \ <T>_{\nu} \beta^{-1} - p \ <V>_{\nu} \beta^{-1} = 0, \tag{6}$$

giving

$$2 \ <T>_{\nu} = p \ <V>_{\nu}, \tag{7}$$

the form of the virial theorem for power behaved potentials.

(*) This condition is fulfilled for (trial) wavefunctions of a power behaved potential (h. o. potential, for example).

From the very same condition (1), we still have, using (5) and (6),

$$\frac{d <E>_\nu}{d \mu} = \frac{\partial <E>_\nu}{\partial \mu} + \frac{\partial <E>_\nu}{\partial \beta_\nu} \frac{d \beta_\nu}{d \mu} = - \frac{<T>_\nu}{\mu} \, , \qquad (8)$$

a statement of the Hellman-Feynman theorem.

The argument is independent of p, although in practice the method is most suitable and easily applied to cases when p = n (integer), i. e., to polynomial potentials of the type $V(x) = \sum_{n \geq o} a_n x^n$ (n even) or $V(r) = \sum_{n \geq o} a_n r^n$.

We are still left with a large variety of possible trial functions. The 1-dimensional harmonic oscillator (h. o.) has the peculiarity that in this system the uncertainty relation for $\Delta p_x \cdot \Delta x$ is maximally realized; by this we mean that $\Delta p_x \cdot \Delta x = \hbar/2$ [6] ($\Delta p_x \cdot \Delta x = (n + 1/2) \hbar$ for $n > o$). Thus, its wavefunctions should be a good choice for variation calculations, either in 1- or in 3-dimensional problems, in agreement with ideas of Gersch and Braden and the interpretation of $\int pdq = n\,h$ (see ref [10]).

a) We start with a 1-dimensional system. In the spirit of the previous statements, the trial wavefunctions will be the h. o. wavefunctions

$$U_\nu = N_\nu \, H_\nu \left(\sqrt{\mu\omega}\, x \right) e^{-1/2 \mu\omega x^2} \, , \quad N_\nu = \left(\frac{\sqrt{\mu\omega}}{\sqrt{\pi}\, 2^\nu \nu!} \right)^{1/2} , \qquad (9)$$

where the integer ν gives the order of the level and H_ν are the Hermite polynomials; $\alpha = \sqrt{\mu\omega}$ is a strength parameter, ω the frequency of the oscillator and μ the reduced mass. We calculate equation (4) for $<E>_\nu$ and minimize the resulting equation with respect to ω (ω has dimensions of mass, but this is of no consequence here, as can be seen):

$$\partial <E>_\nu / \partial \omega = 0 \, . \qquad (10)$$

The key point is the application of (10) to each level separately.

As an exercise, we apply the procedure to the quartic oscilator: $V(x) = a\,x^4$, for which accurate approximate methods have been developed [1, 4]. Using $u_0(x) = (\alpha/\sqrt{\pi})^{1/2} \exp(-1/2\,\mu\omega x^2)$ we calculate $<ax^4>_0$ and $<T>_0 = <-1/2\,\mu\,.\,d^2/dx^2>$, corresponding to the ground-state:

$$<ax^4>_0 = 3/4\ a\,(\mu\omega)^{-2}\,,\quad <p^2/2\mu>_0 = \omega/4$$

Minimizing $<E>_0$, we find $\omega = (6a/\mu^2)^{1/3}$ and, as our best estimate for E_0:

$$<E>_0\ (a/\mu^2)^{-1/3} = 3/8\,.\,6^{1/3}\,. \tag{11}$$

Continuing for the excited states we construct Table I, where we compare our results with accurate numerical calculations [9]; we also quote Gersch and Braden [1] and the results of Hioie and Montroll [4] (taken from ref. [1]). Our results compare very

TABLE I — Approximate energy levels of $V = a\,x^4$

State	Our results $<E>_v / (a/\mu^2)^{1/3}$		Exact results (ref. 9)	Gersch, Braden (*) (ref. 1)	Hioie, Montroll (**) (ref. 4)
$v = 0$	$3/8.6^{1/3}$	$\simeq\ 0.6814$	0.6680	1.1906	0.5461
1	$9/8.10^{1/3}$	$\simeq\ 2.4237$	2.3936	3.0001	2.3627
2	$15/8.(78/5)^{1/3}$	$\simeq\ 4.6850$	4.6968	5.1514	4.6688
3	$21/8.(150/7)^{1/3}$	$\simeq\ 7.2911$	7.3367	7.5598	7.3121
4	$27/8.(83/3)^{1/3}$	$\simeq\ 10.167$	10.244	10.179	10.222
5	$33/8.(366/11)^{1/3}$	$\simeq\ 13.267$	13.379	12.980	13.358
6		16.565	16.712	15.943	16.692
7		20.037	20.221	19.050	20.201
8		23.668	23.890	22.289	23.869
9		27.446	27.706	25.651	27.685

(*) $<E>_v / (a/\mu^2)^{1/3} \simeq 1.1906\ n^{4/3}$ $(n = 1, 2, \dots\,;\ n = v+1)$

(**) $<E>_v / (a/\mu^2)^{1/3} \simeq 1.376\ (v+1/2)^{4/3}$ $(v = 0, 1, 2, \dots)$

Our results can be put into a form $\sim (v+1/2)^{4/3}$, except that the parameter in front of $(v+1/2)^{4/3}$ slightly decreases with increasing v.

well with the exact ones, the first level being much better than the values obtained in refs [1] and [4].

The case of several terms in V(x) is handled in exactly the same way. When V(x) has a part odd in x, an extension of the method is possible. In such cases the introduction of a second variation parameter is desirable in order to displace the origin of the variable ($x \rightarrow x - X_0$). For a complete treatment of the double-well potential and the anharmonic potential using the present method, the reader is advised to consult ref [5].

b) For three-dimensional potentials the method is a straight-forward generalization of the one-dimensional case. The wavefunctions of the three-dimensional h.o. are constructed from products of the one-dimensional wavefunctions

$$\psi_{\nu_1 \nu_2 \nu_3}(x, y, z) \propto e^{-1/2 \mu\omega r^2} H_{\nu_1}(\alpha x) H_{\nu_2}(\alpha y) H_{\nu_3}(\alpha z) \qquad (12)$$

with parity $(-1)^\nu$, $\nu = \nu_1 + \nu_2 + \nu_3$, and $r^2 = x^2 + y^2 + z^2$.

Taking linear combinations, we can form wavefunctions appropriate to levels with a given orbital angular momentum l and parity $(-1)^l$. As an example we quote for the first few levels:

State

(1S) $\nu = 0$ $\quad l = 0 \quad$ $(4(\mu\omega)^{3/2}/\sqrt{\pi})^{1/2} Y_{00}$

(1P) $\quad\quad 1$ $\quad\quad 1 \quad$ $(8(\mu\omega)^{5/2}/3\sqrt{\pi})^{1/2} r Y_{1m}$

(2S) $\quad\quad 2$ $\quad\quad 0 \quad$ $(2(\mu\omega)^{3/2}/3\sqrt{\pi})^{1/2} (2\mu\omega r^2 - 3) Y_{00}$

(2D) $\quad\quad 2$ $\quad\quad 2 \quad$ $(4(\mu\omega)^{7/2}/15\sqrt{\pi})^{1/2} r^2 Y_{2m}$

(3P) $\quad\quad 3$ $\quad\quad 1 \quad$ $(20(\mu\omega)^{7/2}/75\sqrt{\pi})^{1/2} (2\mu\omega r^3 - 5r) Y_{1m}$

$\quad\quad\quad l$ $\quad\quad\quad l \quad\quad\quad\quad\quad\quad \sim r^l Y_{lm}$, $\quad\quad\quad$ etc;

all expressions are to be multiplied by $\exp(-1/2 \mu\omega r^3)$ and the Y_{lm} refer to the spherical harmonics.

Let us calculate the energy levels of the linear potential $V(r) = ar$ which, as is well-known to particle physicists, has had a large application in quark models for mesons and baryons. To be definite, we assume two particles of mass m, bound by $V(r)$. Separating the centre-of-mass motion in the Schödinger equation, we are left with an equation in terms of the relative coordinates (r, θ, ϕ).

We find

$$<E>_{1S} = 3\omega/4 + 2a/\sqrt{\pi\mu\omega} \tag{13}$$

After minimization $(\partial <E>_{1S} / \partial \omega = 0)$, we get the best estimate for the ground-state: $<E>_{1S} = 9/4 (4a/3 \sqrt{\pi\mu})^{2/3}$. In Table II we compare our estimates for S-wave states with the

TABLE II — Linear Potential

$(M = <T> + <V> + 2m)$

State	Our results	Exact results ref. 6
1S	3.111	3.105 (input)
2S	3.695	3.695
3S	4.175	4.182
4S	4.599	4.609
5S	4.987	5.000
1P	3.456	
2P	3.966	

$(a = 0.211 \text{ GeV}^2, \quad m = 1.16 \text{ GeV})$

exact solutions of the Schrödinger equation, obtained from the poles of the Airy functions — ref [6]. This paper deals with a simple application of the linear potential to the charmonium system and the values quoted are very approximately the masses of the first few S-resonances: ψ, ψ', ψ'', etc. For completeness,

we show our results for the 1P and 2P-wave states. The results have an error smaller than 0.4 %.

How well behaves the method, with h. o. wavefunctions in the case of the Coulomb potential? The results are not as good as the previous ones and we can hint at that from the following detail: in a Coulomb potential there is a degeneracy between, for instance, levels 1P and 2S, 2P and 3S, etc. If we calculate $<E>$ with h. o. functions this degeneracy is artificially lifted, although by a small amount; the best approximation will be to take average values. In Table III we present the results for the first levels.

TABLE III — Coulomb Potential

(We take $m = 1$, $\alpha = 1$)

State		Our results		average	Exact results ($E_n = -1/4n^2$; $n = 1, ...$)
$\nu = 1,\ l = 0$		$-\dfrac{3}{4}\left(\dfrac{2\sqrt{2}}{3\sqrt{\pi}}\right)^2$	$\simeq -0.212$	-0.212	-0.250
2	0	$-\dfrac{7}{4}\left(\dfrac{5\sqrt{2}}{21\sqrt{\pi}}\right)^2$	$\simeq -0.06316$	-0.0599	-0.0625
1	1	$-\dfrac{5}{4}\left(\dfrac{4\sqrt{2}}{15\sqrt{\pi}}\right)^2$	$\simeq -0.05659$		
3	0	$-\dfrac{11}{4}\left(\dfrac{89\sqrt{2}}{660\sqrt{\pi}}\right)^2$	$\simeq -0.03184$	-0.0287	-0.0278
3	1	$-\dfrac{9}{4}\left(\dfrac{2\sqrt{2}}{15\sqrt{\pi}}\right)^2$	$\simeq -0.02547$		

One detail in the table is worth mentioning. We do not get upper bounds for the excited states when working with S-wave h. o. functions, but do get them using P-wave functions. This comes from the fact that the last functions are, due to their parity, orthogonal to the S-wave functions of the lower level.

The method should, nevertheless, still be reliable when the Coulomb interaction appears as a perturbation to the main potential: $V(r) = V_0 + V_{coul}$.

In the phenomenological models of particle physics, V_0 is often taken to be the linear potential. Such models do work very well, as far as mass spectroscopy is concerned, and work along these lines can be found in refs [3] and [8], which provide an intructive example of the influence, on the behaviour of the system, of the different terms of a potential.

III – CONCLUSIONS

We now put together those of the previous arguments which, in our view, justify the good results obtained with the method described.

In the first place, the application of the independent minimization procedure (1), with an appropriate choice of variation parameter, compels the expectation values of T and V to satisfy the virial theorem. There is an adaptation of the trial function to each state, in order to obtain the proper balance between the kinetic and potential energies of the state, as is required in spherically symmetric potentials. Certainly, both sides of the equality can still be wrong, differing from their exact values by the same amount, and we have to make sure that this difference is not large.

It is important, at this point, to understand the role of the uncertainty principle in reducing the possibility of a wrong estimate of the energy eigenvalues. Having used as trial wavefunctions solutions of the Schrödinger equation with harmonic oscillator potential, the constraint $<\Delta x> \cdot <\Delta p> = (<\Delta x> \cdot <\Delta p>)_{h.o.} \geq \hbar/2$ is naturally enforced. Intead of introducing an ad hoc, although quite reasonable, rule to fix $<\Delta x> \cdot <\Delta p>$, as in ref [1], we have in our case $<\Delta x> \cdot <\Delta p>$ given by the wavefunctions of the h. o. potential. As these trial wavefunctions are solutions of the Schrödinger equation they have the correct limiting behaviour as $x \to 0$ and $x \to \infty$ ($r \to 0$ and $r \to \infty$ in three dimensions) and the correct nodal structure for the various eigenstates. They look like as wavefunctions should look: $<\Delta x> \cdot <\Delta p>$ cannot come very

wrong. This provides an additional constraint that guarantees, with the viral theorem, that the energy levels are reasonably estimated.

However, one should not trust in detail these trial functions. In the virial theorem and in the uncertainty relations one only makes use of some of the lowest moments of the distribution $|\psi(x)|^2$. Whenever the detailed structure of the wavefunctions is required, as it may happen in transition matrix elements, the optimized wavefunctions, in particular for the excited states, may give a poor approximation. It is clear that the closer the potential being studied is to the potential used to extract the trial wavefunctions, the higher are the chances of the optimized wavefunctions to simulate accurately the real ones.

Finally, we would like to finish by expressing the hope that our simple procedure will be useful for first estimates of energy levels for a large class of potentials.

APPENDIX

Let us write the trial wavefunction ψ_n showing explicitly the parameter dependence:

$$\psi_n = \psi_n (x; \alpha_n, \beta_n, \dots). (*) \tag{A.1}$$

Recalling that $|\psi|^2$ has the meaning of a probability distribution, it is wise to choose the parameters $\{\alpha_n, \beta_n, \dots\}$ in connection with the moments of the distribution. For instances,

$$\alpha_n \sim <x>_n \tag{A.2}$$

being related to the mean and

$$\beta_n^{-1} \sim (<x^2>_n - <x>_n^2)^{1/2} \tag{A.3}$$

being related to the dispersion. We shall keep only these two parameters.

(*) True wavefunctions have no dependence of $\alpha, \beta, \dots$ on n. Such no dependence on n is equivalent to the orthogonality condition.

If the trial wavefunctions are solutions of the Schrödinger equation with a power behaved potentital, $V_0 = a(x-b)^r$, with r even, it can be easily shown, from scaling and translation invariance properties of the Schrödinger equation, that

$$\psi_n (x; \alpha_n, \beta_n) \equiv \sqrt{\beta_n} \; \phi(\xi), \qquad (A.4)$$

with $\xi \equiv \beta_n (x - \alpha_n)$ and

$$\int_{-\infty}^{+\infty} |\psi_n(x)|^2 \, dx = \int_{-\infty}^{+\infty} |\phi_n(\xi)|^2 \, d\xi = 1. \qquad (A.5)$$

The energy for the nth-level can be written

$$E_n = \frac{1}{2\mu} \beta_n^2 \int \overline{\phi}(\xi) \frac{d^2}{d\xi^2} \phi(\xi) \, d\xi + \int \overline{\phi}(\xi) \, V(\xi) \, \phi(\xi) \, d\xi \quad (A.6)$$

and the minimization conditions

$$\partial <\psi|H|\psi>_n / \partial \beta_n = 0 \quad \text{and} \quad \partial <\psi|H|\psi>_n / \partial \alpha_n = 0 \qquad (A.7)$$

become

$$\frac{\partial <\psi|H|\psi>_n}{\partial \beta_n} = -\frac{1}{\beta_n} \left[2 <T>_n - <x \frac{\partial V}{\partial x}>_n \right]$$

$$+ \frac{1}{\beta_n} \alpha_n \frac{\partial}{\partial \alpha_n} <V>_n = 0 \qquad (A.8)$$

and

$$\frac{\partial <\psi|H|\psi>_n}{\partial \alpha_n} = \frac{\partial}{\partial \alpha_n} <V>_n = 0. \qquad (A.9)$$

It is clear that (A.8), together with (A.9), implies the virial theorem.

An application of the two-parameter minimization procedure to the double-well problem is given in ref [5].

Portgal. Phys. — Vol. 16, fasc. 3-4, pp. 105-116, 1985

115

REFERENCES

[1] H. A. Gersch and C. H. Braden, *Am. J. Phys.*, **50** (1982), 53.

[2] See for ex. E. C. Kemble, *Fundamental Principles of Quantum Mechanics with Elementary Applications.*

[3] J. Dias de Deus, A. B. Henriques and J. R. Pulido, *Zeit Physik*, **C7** (1981), 157.

[4] F. T. Hioie and E. W. Montroll, *J. Math. Phys.*, **16** (1975), 1945 and references therein.

[5] J. Dias de Deus, *Phys. Rev.*, **D26** (1982), 2782.

[6] B. J. Harrington, S. Y. Park and A. Yildiz, *Phys. Rev. Lett.*, **34** (1975), 168.

[7] L. I. Schiff, *Quantum Mechanics,* McGraw-Hill, N. Y.

[8] A. B. Henriques, *Phys. Lett.*, **115 B** (1982), 317.

[9] I. Chan, D. Stelman and L. E. Thompson, *J. Chem. Phys.*, **41** (1964), 2828.

[10] Werner Heisenberg, *The Physical Principles of the Quantum Theory,* Dover Publications, Inc., chapter II, part 2.c) and comment after expressions (15).

MOLECULAR DYNAMICS IN A COLUMNAR
D_{ho} LIQUID CRYSTAL – NMR STUDY

A. C. RIBEIRO and A. F. MARTINS

Centro de Física da Matéria Condensada/INIC, Av. Prof. Gama Pinto 2, 1699 Lisboa Codex, Portugal

ABSTRACT — The proton spin-lattice relaxation time T_1 (T, ω) has been measured in the isotropic and columnar phases of hexaoctyloxytriphenilene (THE8). T_1 (T, ω) is continuous across the isotropic-columnar transition and is essentially due to the alkyl chain contribution. Data analysis suggests that the complexities of alkyl chain motions may be lumped into two simple mechanisms, namely «rigid body» chain reorientations and relatively faster internal motions. Chain motions corresponding to intercolumnar diffusion (permeation) are another effective mechanism of relaxation.

1 – INTRODUCTION

Since their discovery in 1977 [1], discotic liquid crystals have been a subject of growing interest and a large number of reports have been published on the properties of these materials [2]. Their molecular dynamics has been probed in two cases by proton spin relaxation techniques [3, 4]. We have used these techniques [3] to study the isotropic-columnar transition and the molecular dynamics in the isotropic phase of hexaoctyloxytriphenilene (THE8 for short). In this work we propose an interpretation of new and previous [3] data on the columnar phase of THE8, and revise briefly the interpretation previously given [3] to the data concerning the isotropic phase, with regard to some aspects on which an improvement is possible on the light of recently published data on some material properties.

2 – EXPERIMENTAL AND GENERAL REMARKS

The synthesis of THE8 was described in ref. [5]; it shows a single liquid crystalline phase of the columnar type D_{ho}, between 340 and 358.8 K. The molecules are regularly stacked in the columns with intermolecular distances of 3.6 Å, and the lattice arrangement of the columns is hexagonal with intercolumnar distance of 23.2 Å [6]. The sample (0.5 cm³) used in our NMR experiments was degassed and sealed under vacuum in a 10 mm diameter glass tube.

Measurements of the proton spin-lattice relaxation time T_1 were performed with a Bruker SXP/4-100 NMR spectrometer for twelve values of the Larmor frequency $\omega/2\pi$, between 4 and 90 MHz.

We have observed an apparent continuity of $T_1(T)$ through the isotropic to columnar transition at all working frequencies, and an apparently similar behaviour of $T_1(T, \omega)$ in both phases, including a strong frequency dependence of T_1 in the isotropic phase over the whole range of temperatures covered in our experiments (up to 90 K above the clearing point) [3]. We also have observed vanishing angular dependence of T_1 when the sample was rotated about an axis normal to the magnetic field.

In view of the following analysis we should also keep in mind that most of the protons in each molecule belong to the aliphatic chains and only 6/108 of them belong to the triphenilene core.

3 – DATA ANALYSIS

A significant portion of our experimental data on $T_1(\omega, T)$ for the columnar phase is displayed in Fig. 1 for T = 354 K. The curves were obtained from a computer analysis of the data, as explained below.

Four different types of molecular motions have been considered in our analysis of the data, as eventually effective mechanisms of spin-lattice relaxation:

(i) long-wavelength collective motions associated with bending fluctuations of the columns;

(ii) rotational diffusion of the molecules around the symmetry axes normal to the planes of their discs;

(iii)   intercolumnar translational self-diffusion of the molecules, with components along the columnar axis ($D_{||}^0$) and normal to it ($D_\perp^0$) due to the uncorrelated positions of adjacent columns;

(iv)   intramolecular motions such as conformational changes of the aliphatic chains, etc.

Mechanism (i) has been discarded on the basis of actual computations and the fact that no discontinuity of $T_1(T)$ is observed at the isotropic-columnar transition. Mechanism (ii) has been described by the following expression [7]:

$$(1/T_1)_R = B \left(\frac{\tau_R}{1 + \omega^2 \tau_R^2} + \frac{4\tau_R}{1 + 4\omega^2 \tau_R^2} \right). \tag{2}$$

and assumed to be independent of (iii); B has been treated as an adjustable parameter. To describe (iii), i. e., relaxation induced by molecular translational self-diffusion, the theoretical computations by Zumer and Vilfan [8] have been used. They give:

$$(1/T_1)_D = (9/8) \gamma^4 \hbar^2 (n\tau_D/d^3) R_c (l/d, D_\perp^0/D_{||}^0, \varepsilon, \Delta, \omega\tau_D) \tag{2}$$

where R_c is a dimensionless function such that expression (2) can be very well aproximated by:

$$(1/T_1)_D = C_1 \left(\frac{\tau_D}{1 + \omega^2 \tau_D^2} \right) \tag{3}$$

in the region of our measurements. The diffusion coefficients $D_\perp^0$ and $D_{||}^0$ are given by:

$$D_\perp^0 = <r_\perp^2>/4\tau_D \text{ and } D_{||}^0 = <r_{||}^2>/2\tau_D. \tag{4}$$

Finally, the motions included in (iv) have been assumed to be fast enough to contribute only with a constant term (C) to the relaxation rate.

The overall relaxation rate should then be given by the following expression:

$$\frac{1}{T_1} = B \left(\frac{\tau_R}{1 + \omega^2 \tau_R^2} + \frac{4\tau_R}{1 + 4\omega^2 \tau_R^2} \right) + C_1 \frac{\tau_D}{1 + \omega^2 \tau_D^2} + C \tag{5}$$

which was fitted to the experimental data in Fig. 1 (for T = 354 K) giving:

$$\tau_R = 1.5 \times 10^{-8}\,s \qquad B = 2.72 \times 10^7\,s^{-2} \qquad C = 2.58\,s^{-1}$$

$$\tau_D = 0.9 \times 10^{-8}\,s \qquad C_1 = 1.32 \times 10^9\,s^{-2}$$

Putting these values in expressions (1) to (3) and (5), curves for the overall relaxation rate $1/T_1$ and for its three components have been drawn as functions of $1/\sqrt{\omega}$, as represented in Fig. 1.
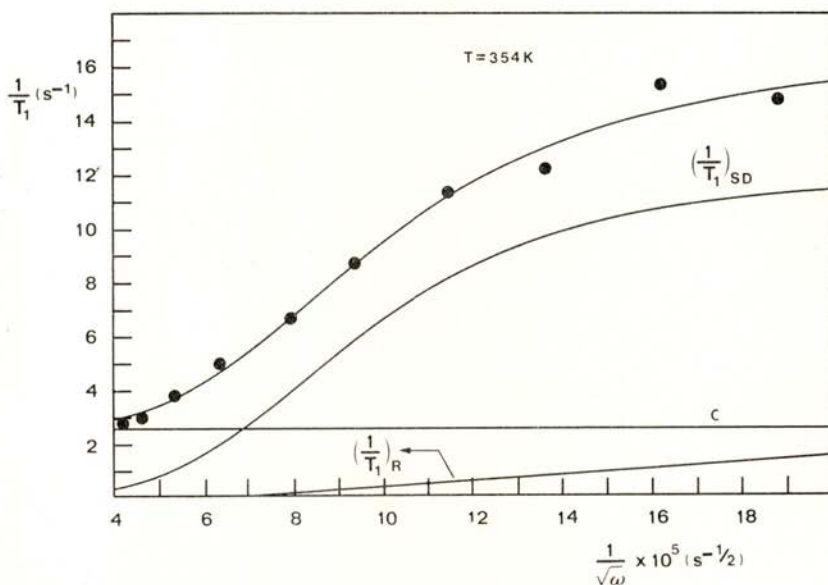

Fig. 1 — Frequency dependence of the overall and partial contributions to the relaxation rate, at T = 354 K, in the columnar phase.

4 — DISCUSSION

The value $\sim 10^{-8}\,s$ for the correlation times derived above is quite convincing in view of the apparent dispersion of $T_1(\omega)$ shown by Fig. 1 around the corresponding frequency.

The diffusion coefficients $D_\perp^0$ and $D_\parallel^0$ are another interesting output of this research, because they can be measured inde-

pendently, thus giving a check on our data analysis. Using expression (4) with the computed value of τ_D, and taking $<r^2>^{1/2} \leq L = 3.6$ Å, where L is the intermolecular distance within one column, and $<r_\perp^2>^{1/2} = d_1 = 23.2$ Å (intercolumnar distance [6]), we find, for T = 354 K:

$$D_\perp^0 = 1.5 \times 10^{-6} \text{ cm}^2 \text{ s}^{-1} \quad \text{and} \quad D_{||}^0 \leq 7.2 \times 10^{-8} \text{ cm}^2 \text{ s}^{-1}.$$

Dong et al. have recently measured the diffusion coefficient $D_\perp^0$ as a function of the temperature [9]. For T = 354 K we get, from their results, $D_\perp^0 = 0.6 \times 10^{-6}$ cm² s⁻¹; which has the order of magnitude of our result. The slight disagreement may be only apparent since Dong et al. [9] estimate that their absolute values of the D's may be off by as much as a factor two, due to experimental difficulties.

Small variations in the numerical values of the parameters given above do not change significantly the r. m. s. error of the fit in Fig. 1. We can, for instance, get smaller values of $D_\perp^0$ by increasing τ_D. This, however, leads to negative values of B in expression (5) (for $\tau_D \geq 10^{-8}$ s), which are unphysical. We remark that the contribution $(1/T_1)_R$ is relatively small in any case. On the other hand, $1/T_1$ as given by expression (5) may be viewed as a linear combination of three lorentzian contributions plus a constant term. We may ask whether a single lorentzian plus a constant term would reasonably fit the data. The answer is yes but if we associate that lorentzian contribution with translational diffusion we get $D_\perp^0 = 1.4 \times 10^{-6}$ cm² s⁻¹, i. e., nearly the same value as before.

Similar difficulties have arisen in a reanalysis [10] of our previous interpretation of the data about the isotropic phase [3]. The addition of new experimental data, now available in the low frequency region, changed significantly the outputs of the fitting procedure in [3], which was based on the well known Torrey's theory, and suggests the need for the introduction of a second relaxation mechanism. Such a need is more evident in the isotropic phase than in the columnar phase. Depending on the value assumed for $<r^2>^{1/2}$ (certainly greater than 3.6 Å), the value of the diffusion constant which comes out from the new analysis [10] of the data is of the order of 10^{-6} cm² s⁻¹ at T = 366 K, which is consistent with the value $D^0 = 1/3 \ (D_{||}^0 + 2D_\perp^0) = 1 \times 10^{-6}$ cm² s⁻¹, calcu-

lated from the results above for the columnar phase at $T = 354$ K (12 degrees below).

In the columnar phase the values of τ_D and τ_R are of the same order of magnitude. This suggests some coupling between molecular rotation and self-diffusion (this coupling was neglected in the analysis above). In the isotropic phase τ_D is an order of magnitude lower than τ_R [10]. The constant C is also an order of magnitude lower in the isotropic phase, thus suggesting an increased internal mobility of the alkyl chains in this phase. The correlation time for the internal motions in the isotropic phase is the order of 10^{-11} s (estimated with the interproton distance of -CH$_2$- groups).

5 – CONCLUSION

The proton spin-lattice relaxation rate in the columnar mesophase of hexaoctyloxytriphenilene in the 4-100 MHz region is dominated by the contribution of the protons in the alkyl chains. The data can be reasonably well rationalized on the basis of a simple model, in which the complexities of the alkyl chain motions are lumped into two main effects, namely global reorientations and relatively fast internal motions. In addition, the model considers molecular translational self-diffusion essentially as an inter-columnar permeation. A few puzzling problems arise, which suggest that more experimental studies are required, e. g. measurements at lower Larmor frequencies, to fully understand the relaxation mechanisms involved in the columnar and isotropic phases of discotic liquid crystals.

REFERENCES

[1] S. Chandrasekhar, B. K. Sadashiva and K. A. Suresh, *Pramana*, **9**, 471 (1977).
[2] See, e. g., the review by J. C. Dubois and J. Billard in *Liquid Crystals & Ordered Fluids»*, vol. 4, ed. by A. C. Griffin and J. F. Johnson, Plenum Press, N. Y., 1984.

[3] A. F. Martins and A. C. Ribeiro, *Port. Phys.*, **11**, 169 (1980).

[4] M. Vilfan, G. Lahajnar, V. Rutar, R. Blinc, B. Topic, A. Zann and J. C. Dubois, *J. Chem. Phys.*, **75**, 5250 (1981).

[5] J. Billard, J. C. Dubois, M. T. Nguyen and A. Zann, *Nouveaux J. de Chimie*, **2**, 535 (1978); C. Destrade, M. C. Mondon and J. Malthete, *J. Phys.* (Paris), **40**, C3-17 (1979).

[6] A. M. Levelut, Proceedings of the Int. Liq. Cryst. Conference, Bangalore (1979), Heyden and Son, London.

[7] A. Abragam, Les Principes du Magnetisme Nucléaire, Bibliotheque des Sciences et Techniques Nucléaires, Paris (1961).

[8] S. Zumer and M. Vilfan, *Mol. Cryst. Liq. Cryst.*, **70**, 39 (1981).

[9] R. Y. Dong, D. Goldfarb, M. E. Moseley, Z. Luz and H. Zimmermann, *J. Phys. Chem.*, **88**, 3148 (1984).

[10] A. C. Ribeiro and A. F. Martins, to be published.

TOWARDS AN EFFECTIVE INTERMOLECULAR POTENTIAL ENERGY FUNCTION FOR FLUID TETRAFLUOROMETHANE

Jorge C. G. Calado [1]

Complexo I, Instituto Superior Técnico, 1096 Lisboa, Portugal

Paulette Clancy

School of Chemical Engineering, 254 Olin Hall, Cornell University, Ithaca, N.Y. 14853, USA

ABSTRACT — The development of an intermolecular potential energy function for carbon tetrafluoride is outlined, which is able, when used in conjunction with a perturbation theory, to accurately predict a variety of PVT properties over wide ranges of temperature and pressure (120-400 K, 0-110 MPa). The importance of anisotropic forces in the dense fluid region for this molecule is clearly demonstrated, the most significant forces arising from the non-spherical shape of the molecule rather than its multipolar interactions.

1 – INTRODUCTION

The ability to predict P - V - T data over wide ranges of density and temperature is, perhaps, one of the strictest tests of intermolecular potentials. It is well-known [1] that second-virial coefficients do not generate a unique potential and recent potential-inversion techniques [2] for this property and transport properties can only generate gaseous potentials for spherical or quasi-spherical molecules. Transport properties, which are another source of potential functions, are difficult to measure accurately.

In perturbational and variational treatments, intermolecular potentials are usually developed by requiring agreement with experimental data along the saturation line (usually vapour pressures and liquid densities) often because accurate P - V - T data

---

[1] Author to whom correspondence should be addressed.

Portgal. Phys. — Vol. 16, fasc. 3-4, pp. 125-136, 1985

125

over extended pressure and temperature ranges are not available. However, as we have recently shown for ethylene [1], orthobaric data may not define the intermolecular potential in a unique way. That definition can only be reliably achieved by testing the potential against the whole phase surface of the substance. This supports the claim of Powles *et al.* [3] that there is an urgent need for configurational energy data over wide ranges of density and temperature, in order to properly test theories and improve intermolecular potential functions.

We have recently completed such a study for tetrafluoro-methane, CF_4 [4]. Thirty-three isotherms, covering the temperature range 95-413 K and pressures up to 110 MPa have been studied, resulting in over one thousand and five hundred data points. This amount of data should enable us to develop an effective and flexible intermolecular potential energy function for CF_4, which can then be applied to predict properties of systems of which CF_4 is a component.

Despite its apparent simplicity, tetrafluoromethane is an attractive substance from both the industrial and theoretical points of view. It has a low order of toxicity and a remarkable thermal stability. As Freon-14, it is widely used as a low-temperature refrigerator and sometimes as a gaseous insulator. On the other hand, CF_4 molecules display an interesting degree of anisotropy, as manifested in the intermolecular potential function, which any successful theory must be able to account. Whilst the gross features of the CF_4 molecules may be considered to be repre-sentable by a quasi-spherical or globular model, the thermodynamic behaviour of the substance, especially in mixtures, displays a non-ideality which is characteristic of the anisotropy present at the molecular level [5]. Even the existing low-density studies lead to contradictory conclusions about the intermolecular potential of CF_4. While some authors claim that a simple (12,6) Lennard-Jones potential

$$u(r) = 4\varepsilon [(r/\sigma)^{12} - (r/\sigma)^6] \tag{1}$$

is able to describe the second virial coefficient data [6], others have argued that a spherical-shell model is necessary [7]. Tetrafluoromethane is then an intermediate case between those of methane, CH_4 (which can roughly be treated as spherical) and of

tetrachloromethane, CCl$_4$ (which displays strong anisotropy and requires a spherical-shell or site-site model). The discriminating factor would appear to be the octopole moment (the first non-zero electric moment exhibited by a tetrahedral molecule) which is a measure of the electronic non-centrality of the molecule.

Strong orientational correlations, which seem to persist over several molecular diameters, have been found for tetrahedral molecules [8]. Interlocking effects have also been detected in CCl$_4$ molecules, using Brillouin scattering techniques [9]. In addition, calculations carried out using the site-site distribution function formulation show that the disagreement with results from computer simulation is much larger than for diatomic molecules [10]. All these facts seem to add up to the general conclusion that despite their apparent simplicity (small size, higher symmetry, non-polarity) CF$_4$ molecules offer enough problems to make a systematic study of its underlying potential worthwhile.

2 – THEORY AND PROPOSED MODELS

A spherical reference based perturbation theory approach due to Gubbins, Gray and co-workers [11-13] was used to evaluate the Helmholtz energy and hence all other thermodynamic properties of CF$_4$ from a knowledge of the dominant isotropic and anisotropic contributions to the intermolecular potential energy function, by the use of Statistical Mechanics techniques. The intermolecular pair potential $u(r\omega_1\omega_2)$ depends on the molecular orientations $\omega_i (= \theta_i \phi_i \chi_i$ for non-linear molecules) as well as the intermolecular separation, r. Such a potential may be separated into isotropic and anisotropic parts

$$u(r\omega_1\omega_2) = u_0(r) + u_a(r\omega_1\omega_2) \tag{2}$$

where u_0 is a reference pair potential of isotropic particles and u_a contains all the orientation-dependent terms. The reference potential is given by

$$u_0(r) = <u(r\omega_1\omega_2)>_{\omega_1\omega_2} \tag{3}$$

where $<...>$ denotes an unweighted average over orientations ω_i.

The Helmholtz energy, A, may be expanded in powers of the perturbing potential as

$$A_{total} = A_0 + A_1 + A_2 + A_3 + ... \tag{4}$$

With the choice of a reference potential given by Eq. (3), the first order term, A_1, vanishes. The series expansion is slowly convergent, but for moderately polar molecules its sum can be obtained from a Padé approximant

$$A_{total} = A_0 + A_2 (1 - A_3 / A_2)^{-1} \tag{5}$$

where A_i is the ith order term in the series. Detailed expressions relating A_i to the underlying intermolecular forces have been given previously (see, for example, ref. [11]) and will not be repeated here.

The major thrust of this paper lies in the development of the best possible effective intermolecular potential energy function for CF_4 which is able to give the closest prediction of experimentally determined thermodynamic properties over as wide a range of state conditions as possible, thus providing the most stringent test of the flexibility and dependability of the model potential. For CF_4, it will be interesting to try to ascertain whether a spherical, isotropic model for this molecule is indeed sufficient to reproduce the thermophysical properties of the fluid as has been suggested by some authors [6], to determine whether anisotropic forces contribute significantly to these properties and, if so, which anisotropic forces are the most important. Several candidates for orientation-dependent forces suggest themselves for this fluid. CF_4 is known to have a reasonably large octopole moment ($\Omega_{CF_4} = 4.8 \times 10^{-34}$ esu) and we might expect the spatial anisotropy of the molecule's electronic structure to cause charge overlap forces to be significant. In order to test the relative contributions of these terms we proposed four models, building on the isotropic potential model (which constitutes model A) in a stepwise fashion, thus:

Model A: $u = u_0^{(n, 6)}$

Model B: $u = u_0^{(n, 6)} + u_{\Omega\Omega} (336)$

Model C: $u = u_0^{(n, 6)} + u_{\Omega\Omega} (336) + u_{dis} (303 + 033)$

Model D: $u = u_0^{(n, 6)} + u_{\Omega\Omega} (336) + u_{dis} (303 + 033) + u_{ov} (303 + 033)$

where: u is the intermolecular potential energy; $u_0^{(n, 6)}$ is the contribution from the reference fluid, here a Lennard-Jones (n, 6) potential; $u_{\Omega\Omega}$ is the anisotropic octopole-octopole interaction; u_{dis} is that due to the anisotropic dispersion; and u_{ov} is that arising from anisotropic charge overlap forces. The figures in brackets refer to the leading term or terms in the spherical harmonic expansion of these interactions. Such a method of determining the quality of the proposed model was used recently for ethylene [1], with considerable success.

The thermodynamic properties of the reference fluid were obtained using a methane equation of state [14]. This has been shown previously [5] to provide a better reference system for CF_4 than the more commonly employed argon reference used, for example, in most of the proposed models for ethylene in reference [1]. The potential model for CF_4 used in reference [5] is that given as model D here, and we shall use exactly that potential (with accompanying potential parameters) as our model D to test its efficacy in predicting PVT and other thermophysical properties.

The adjustable potential parameters involved in each of the models (the Lennard-Jones parameters ε/k, σ and n for models A - D and the shape parameter δ_3 appearing in u_{ov} in model D) were obtained by fitting to the experimental saturation line values for ρ_{liq} and P_{liq} [15]. Experimental values for the octopole moment (Ω) and dispersion coefficient (β_7) were employed in each model where appropriate. For CF_4 it was found to be considerably more difficult than usual to determine an acceptably invariant set of parameters over the whole saturation curve. It was possible to obtain a similar quality of fit to the coexistence properties with each of the models tested, underlining once again that these properties do not provide a route to a unique potential model for any fluid. The potential parameters determined in this manner for each of the models are given in Table 1. Using these models, the PVT properties from 120-400 K and from 0-110 MPa were predicted with no further adjustment of parameters.

3 – RESULTS

Several key PVT properties were predicted using each of the potential models described in the preceding section, over as wide

a range of temperature and pressure as the theory (and the reference equation of state) would allow. The resulting theoretically predicted values were compared with recent, extensive experi-

TABLE 1 — Potential Parameters for CF_4 Models

Model	n	$(\varepsilon/k)/K$	σ/A	$\Omega \times 10^{34}/esu$	β_7	δ_3
A	20	232.7	4.255	—	—	—
B	18	221.2	4.260	4.8	—	—
C	20	231.7	4.230	4.8	-0.20	—
D	20	232.0	4.250	4.8	-0.20	0.10

mental data due to Rubio *et al.* [4]. Isotherms from 120-400 K and pressures from 0-110 MPa were investigated, excluding state points where the reduced density, $\rho\sigma^3$, exceeds 1.05 (the limit of the methane equation of state), and temperatures close to the critical region (210-240 K), where the theory is invalid.

TABLE 2 — Average Percentage Deviation Between Theory
and Experiment (120-210 K, 0-110 MPa)

Model	$|\Delta\rho|\%$	$|\Delta U^c|\%$	$|\Delta S^c|\%$
A	1.54	4.09	5.42
B	1.63	4.65	5.40
C	1.22	5.29	6.90
D	0.58	5.03	8.20

The most important property in this study is that of the density, due to its sensitivity to the intermolecular potential and its key value in industrial applications. Its prediction by each of the models is summarized in Table 2, where the average deviation

between theory and experiment is given covering the whole temperature and pressure ranges. This information is disseminated in Figure 1 to show the deviation between theory and experiment as a function of (sub-critical) temperature. It can be seen that the full anisotropic potential (model D) is clearly superior to that of a simple Lennard-Jones model (model A). It is interesting to note
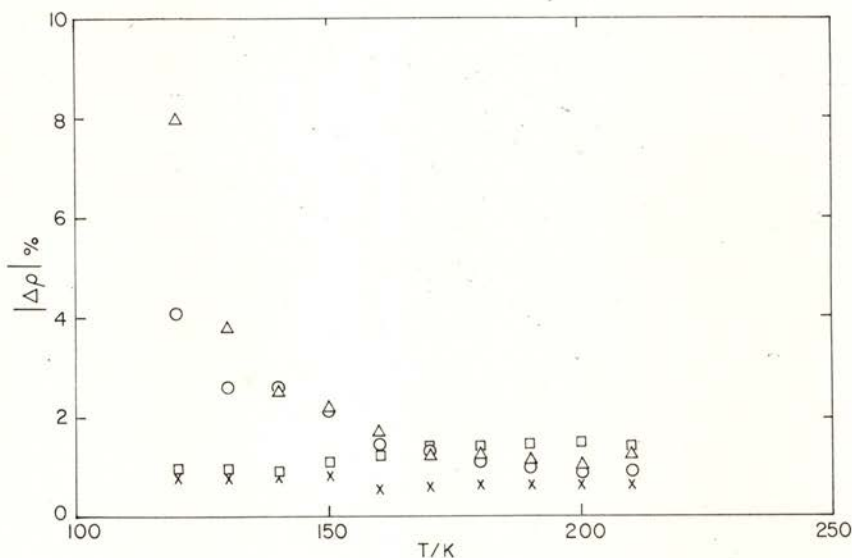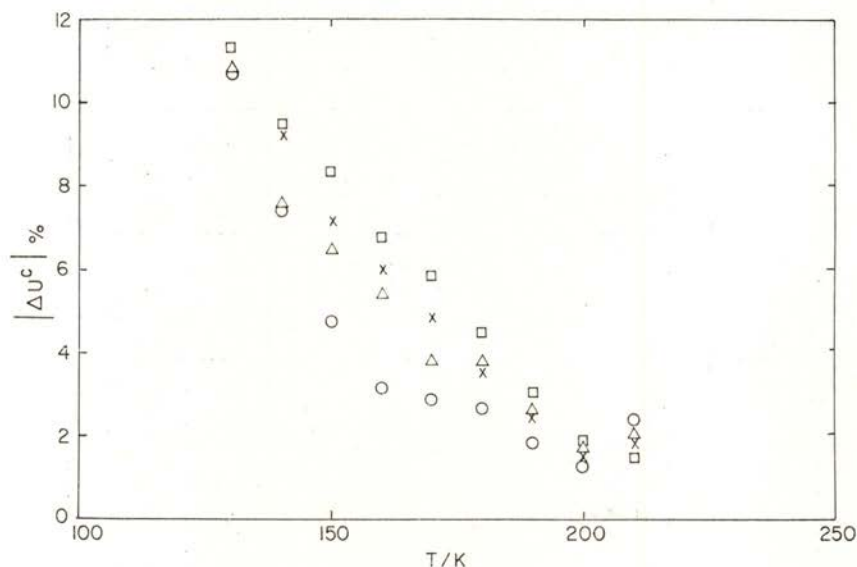

Fig. 1 — Deviation between theory and experiment for the density of CF_4 as a function of temperature: $\bigcirc$, model A; $\triangle$, model B; $\square$, model C; x, model D.

from this figure that the major improvement in predicting the density arises not from the addition of the octopolar forces (compare the results of models A and B), but from the addition of the shape forces (compare models C and D). The prediction of the density (and the other PVT properties) at supercritical temperatures is of much less interest. At high temperatures the effect of the anisotropy is 'washed out' by the higher kinetic energy of the molecules and any useful distinction between the potential models is precluded. The performance of the full anisotropic potential (model D) in predicting the density of CF_4

over wide density and temperature ranges can be fully appreciated in Figure 2, where the experimental results are compared with
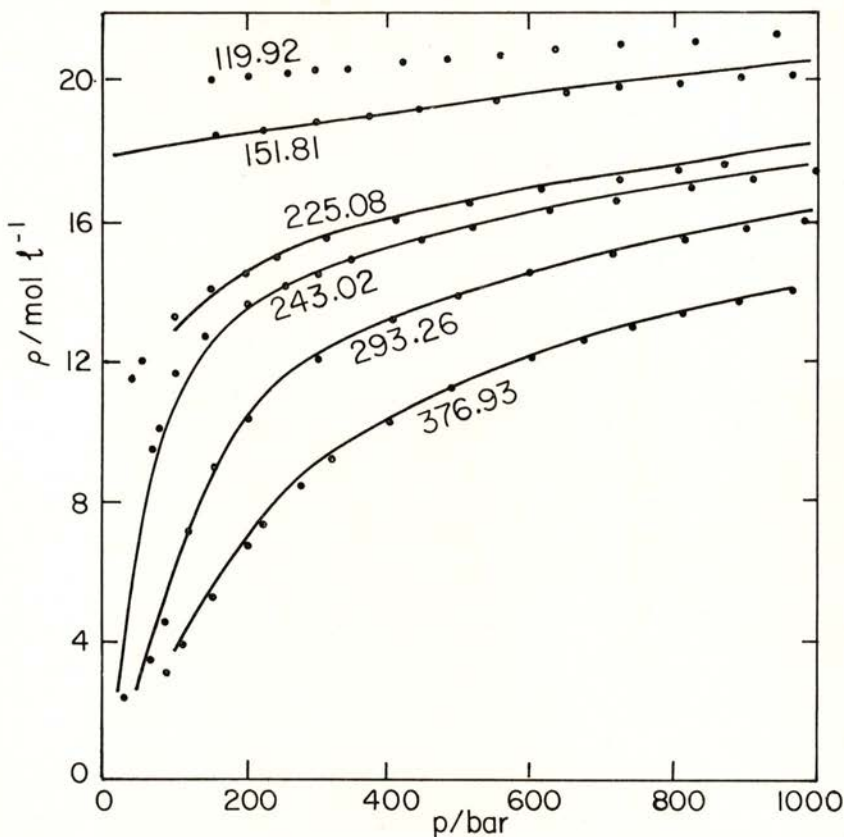
Fig. 2 — Comparison of experimental density values (•) with the predictions of perturbation theory using potential model D (—), as a function of pressure, for several isotherms.

those from perturbation theory. Table 3 lists both the experimental and calculated values of density at round values of temperature and pressure.

The prediction of the configurational internal energy, U^c, was also investigated; results for this are shown in Table 2 and

TABLE 3 — Comparison of Experimental Values and Theoretical Prediction of the Density of CF_4 from 120-200 K and 25-1100 bars

P/bar \\ T/K	120 Expt.	120 Theory*	140 Expt.	140 Theory*	160 Expt.	160 Theory*	180 Expt.	180 Theory*	200 Expt.	200 Theory*
25	19.790	19.760	18.659	18.553	17.438	17.448	16.058	16.116	14.332	14.073
50	19.852	19.824	18.745	18.635	17.565	17.566	16.260	16.311	14.716	14.641
100	19.970	19.950	18.908	18.795	17.796	17.787	16.606	16.646	15.287	15.297
200	20.188	20.218	19.198	19.095	18.190	18.180	17.152	17.185	16.069	16.111
300	20.385	20.434	19.454	19.376	18.521	18.526	17.583	17.626	16.632	16.687
400	20.567	20.895	19.684	19.642	18.810	18.838	17.943	18.005	17.081	17.151
500	20.735	21.086	19.893	19.898	19.067	19.123	18.256	18.340	17.458	17.548
600	20.892	21.609	20.085	20.152	19.299	19.387	18.533	18.642	17.785	17.897
700	21.039	—	20.264	20.266	19.512	19.634	18.783	18.918	18.074	18.209
800	21.179	—	20.431	20.469	19.709	19.867	19.011	19.173	18.336	18.495
900	21.311	—	20.588	20.943	19.892	20.088	19.221	19.411	18.574	18.757
1000	21.437	—	20.736	21.185	20.063	20.305	19.417	19.633	18.793	19.000
1100	21.557	—	20.877	21.297	20.225	20.518	19.599	19.844	18.997	19.228

* Theory results correspond to potential Model D.

Portgal. Phys. — Vol. 16, fasc. 3-4, pp. 125-136, 1985

133

Figures 3 and 4. This property is of somewhat less importance than the density, its experimental value being derived rather than

Fig. 3 — Deviation between theory and experiment for the configurational energy U^c of CF_4, as a function of temperature: ○, model A; △, model B; □, model C; x, model D.

fundamental and subject to more uncertainty (~5 %). The theoretically predicted values do not have the accuracy obtained for the density but give an adequately good description of the experimental values. Here, unlike for the density, no clear improvement is produced by adding anisotropic forces to the potential. The overall prediction of the internal energy for model D is numerically not quite as good as that of model A, but the difference is not particularly significant given the experimental uncertainly.

The results for the configurational entropy S^c in terms of the observed trends between models mirror those for U^c, although the prediction of this property is significantly poorer for all the models studied as can be seen in Table 2.
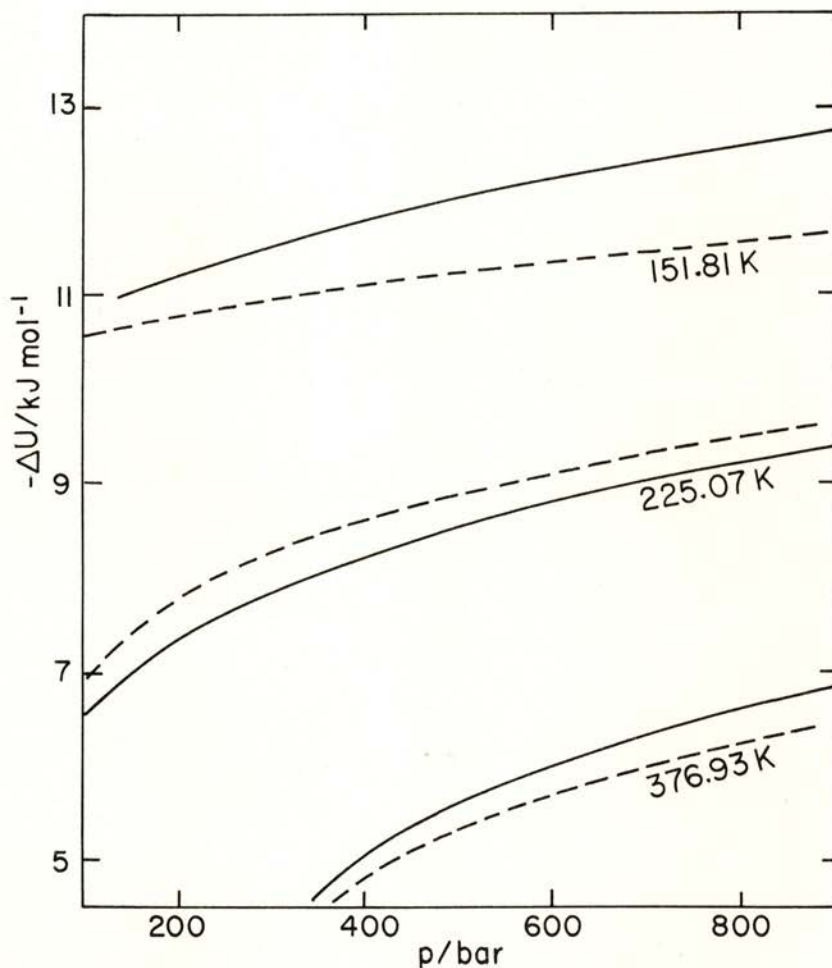
Fig. 4 — Comparison of "experimental" configurational energy, derived from the experimental values of density (——), and the predicted one by perturbation theory (— —), using potential model D.

4 — DISCUSSION

The development of an effective fluid potential for carbon tetrafluoride using a perturbation theory approach is clearly a difficult task; indeed it has been suggested [16] that this molecule is probably too far from sphericity to be adequately represented by such a procedure. It has already been noted that the deter-

mination of the potential parameters is particularly difficult for this fluid. Fortuitously, however, the prediction of the PVT properties appears to be relatively unaffected by this choice. The prediction of the most discerning property, the density, shows a clear distinction between the proposed models, with the importance of including the anisotropy of the molecule clearly demonstrated over a purely isotropic Lennard-Jones model. It was interesting and somewhat unexpected, to discover that it is the non-spherical shape of the fluid molecule which provides the most significant of the anisotropic forces, and not the octopolar forces. Whilst the preferred proposed model (D) clearly does not provide the definitive intermolecular potential for CF_4 , the stringent tests applied have demonstrated that for most practical purposes it may serve as a useful source of thermodynamic properties with acceptably good accuracy.

REFERENCES

[1] CALADO, J. C. G. and CLANCY, P., *Rev. Port. Quim,* 26, 85 (1984).

[2] MAITLAND, G. C., RIGBY, M., SMITH, E. B. and WAKEHAM, W. A., *Intermolecular Forces,* Clarendon Press, Oxford, 1981.

[3] POWLES, J. G., EVANS, W. A., McGRATH, E., GUBBINS, K. E. and MURAD, S., *Mol. Phys.,* 38, 893 (1979).

[4] RUBIO, R. G., CALADO, J. C. G., CLANCY, P. and STREETT, W. B., *J. Phys. Chem.,* 89, 4637 (1985).

[5] LOBO, L. Q., McCLURE, D. W., STAVELEY, L. A. K., CLANCY, P., GUBBINS, K. E. and GRAY, C. G., *J. Chem. Soc. Fara. Trans. II,* 77, 425 (1981).

[6] MacCORMACK, K. E. and SCHNEIDER, W. G., *J. Chem. Phys.,* 19, 849 (1951).

[7] DOUSLIN, D. R., HARRISON, R. H., MOORE, R. T. and McCULLOGH, J. P., *J. Chem. Phys.,* 35, 1357 (1961).

[8] MONTAGUE, D. G., CHOWDURY, M. R., DORE, J. C. and REED, J., *Mol. Phys.,* 50, 1 (1983).

[9] ASENBAUM, A. and WILHELM, E., *Adv. Mol. Relax. Int. Proc.,* 22, 187 (1982).

[10] MONSON, P. A., *Mol. Phys.,* 47, 435 (1982).

[11] GUBBINS, K. E. and TWU, C. H., *Chem. Eng. Sci.,* 33, 863; 879 (1978).

[12] GRAY, C. G., GUBBINS, K. E. and TWU, C. H., *J. Chem. Phys.,* 69, 182 (1978).

[13] CLANCY, P., GUBBINS, K. E. and GRAY, C. G., *Fara. Disc. Chem. Soc.,* 66, 116 (1978).

[14] ANGUS, S., ARMSTRONG, B. and DE REUCK, K. M., *International Thermodynamic Tables of the Fluid State - 5, Methane* (Pergamon, Oxford, 1977).

[15] LOBO, L. Q. and STAVELEY, L. A. K., *J. Chem. Eng. Data,* 26, 404 (1981).

[16] LUCAS, K., personal communication.

SURFACE AND EVAPORATION ENERGIES
OF MONOATOMIC CRYSTALS

J. Brito Correia and M. A. Fortes

Departamento de Engenharia de Materiais, Instituto Superior Técnico,
Av. Rovisco Pais, 1000 Lisboa, Portugal

ABSTRACT — Using a corrected version of the method first developed by Shuttleworth, very precise calculations of surface energies for a large number of orientations of the surface in a monoatomic f. c. c. crystal have been undertaken. The effect of the exponent of the repulsive and attractive terms in the Mye-type potential function was studied; the exponents used were combinations of 12, 9 and 6. The surface energies were corrected for the relaxation of the more exposed surface atoms to their equilibrium positions, using a method based on the TLK decomposition of the surface. The corrections never exceed 1 %. These calculations also allow the determination of (relaxed) evaporation energies of surface atoms, particularly atoms in surface terraces, ledges and kink sites and of ad-atoms. The energies (measured in terms of the cohesive energy) are little affected by the potentials studied.

1 – INTRODUCTION

In this paper we report on results of computer calculations of surface energies and evaporation energies, with emphasis on the anisotropy of these quantities and on the effect of the interatomic potential. The surface energies are calculated by the method first used by Shuttleworth [1], with a correction in the determination of the rests of the lattice sums, for a wide range of orientations of the surface. A pairwise interaction between the atoms is assumed, with a potential energy $\varepsilon(\rho)$. The actual calculations were made for f. c. c. crystals with Mye potentials $6\,|\,9$, $6\,|\,12$, and $9\,|\,12$. All surface and evaporation energies were corrected for the relaxation of the more exposed surface atoms.

Similar calculations of surface energies for a wide range of orientations were undertaken by Nicholas [2] using Mye and Morse potentials, but he did not consider the correction due to relaxation. Nicholas' calculations extend previous work [3] on the anisotropy of the surface energy of cubic crystals, based on the broken-bond model. Although the results of Nicholas [2] were obtained for various potentials, no general conclusions were drawn on the effects of the potential range on the anisotropy of surface energy. These effects were considered by Drechsler and Nicholas [4] in relation to the equilibrium shapes of crystals, but again with no correction for surface relaxation.

The use of pairwise potentials for calculating the energies of surfaces and other crystal defects can of course be criticized (e. g. [5]), in special because of the difficulty of developing good potentials (particularly for metals, e. g. [6]), but is still the more efficient method of studying the structure and properties of crystal defects. Linford and Mitchell [7] introduced interplanar potentials, instead of pairwise interatomic potentials, to calculate surface energies, but their method is of restricted application. Finally, a few attempts have been made to calculate surface free energies (e. g. [8], [9]) and predict the effect of temperature on the surface tension.

2 – LATTICE SUMS FOR SURFACE ENERGY

Consider a crystal with one atom per lattice point, in which the atoms interact by a pairwise potential $\varepsilon(\rho)$, where ρ is the distance between the two atoms. A suitable vector basis ($e_1 \, e_2 \, e_3$) is chosen in the crystal. The relative positions of the atoms are defined by vectors of the type

$$\mathbf{n} = \sum_i n_i \, \mathbf{e}_i \tag{1}$$

The permissible sets n_i have to be identified beforehand, for example, by relating the $\mathbf{e}_i$ to a lattice basis (if the $\mathbf{e}_i$ are a lattice vector basis, the n_i can take all integral values). The plane of the surface is defined by the Miller indices (p) = ($p_1 \, p_2 \, p_3$) relative to the vector basis chosen. The (unrelaxed) surface

energy $\gamma(p)$ is calculated from the potential energy, E, of inter-action between two half-crystals, C and C', separated by a plane (p), per unit area of this plane (Fig. 1). When relaxation
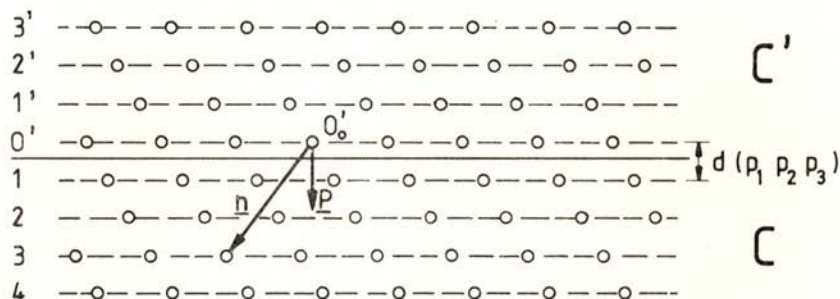
Fig. 1 — A crystal is divided into two half-crystals, C and C', by a plane $(p_1 p_2 p_3)$ of unit normal **P** and interplanar spacing d. When C and C' are separated, two (identical) surfaces are created.

of the atomic positions is neglected, the surface energy is simply given by

$$\gamma = -E/2 \qquad (2)$$

This follows directly from an energy balance and from the definition of surface energy as an excess energy, per unit area, relative to the perfect crystal.
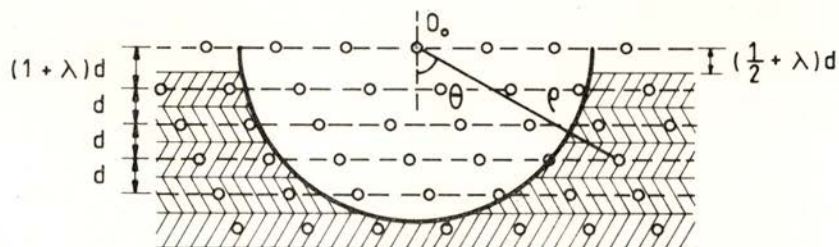
Fig. 2 — The topmost plane relaxes to a distance $(1 + \lambda)$ d. The dashed region is treated as a continuum for calculating the rest of the sums D_e (see Appendix).

The atoms in the surface region will relax to new equilibrium positions, and this reduces the surface energy calculated from eq. (2). Consider first the relaxation of the atoms in the topmost plane (Fig. 2). We assume that this relaxation occurs exclusively along the normal to the plane. The corresponding correction to the surface energy is obtained as follows (cf. ref. [1]). Let $E^*(\lambda)$ be the potential energy, per unit area of the topmost plane, in the field of the other planes, λ being a measure of the relaxation of that plane ($\lambda = 0$ for zero relaxation). The atoms are assumed to keep the same positions as in the perfect crystal, except, of course, for the change in the distance of the top plane to the following plane. The value, λ_e, of λ that minimizes E^* is calculated. If E_e^* is the corresponding energy and E_o^* is the energy for $\lambda = 0$, the corrected surface energy γ_c is

$$\gamma_c = \gamma + E_e^* - E_o^* \tag{3}$$

The energies per atom will be indicated by ε's and the energy correction per atom by $\Delta\varepsilon$ ($\Delta\varepsilon = \varepsilon_e^* - \varepsilon_o^*$).

In the calculation of E we use a generalized version of the method of Shuttleworth, with corrections in his procedure for calculating the lattice sums. In this method, the number of pairs of interacting atomic planes (p), one in half-crystal C, the other in C', is the relevant quantity.

Taking for origin an atom position $0'_o$ in the plane of order $0'$ of C', adjacent to the surface (Fig. 1), the positions of the atoms of crystal C are defined by all $\mathbf{n}$ such that

$$\frac{1}{d}(\mathbf{n} \cdot \mathbf{P}) = m \geqslant 1 \tag{4}$$

where d is the interplanar spacing and $\mathbf{P}$ is the unit normal to the surface plane. The number m is a (positive) integer that gives the order of the plane of C where the atom $\mathbf{n}$ is located (Fig. 1). For each $\mathbf{n}$, the number of pairs of planes, one in C the other in C', with a spacing equal to $m\,d$, is precisely m. The potential energy of C' in the field of C, per atom in the plane (p), can then be calculated from the potential energy $\varepsilon(n)$ of

an atom in the plane 0′, provided this energy is multiplied by m and then summed for all n satisfying eq. (4). Finally, if v is the volume per atom, the area per atom in the plane (p) is v/d and the unrelaxed surface energy is

$$\gamma = - \frac{d}{2v} \sum_n m \; \varepsilon(n) \; ; \qquad m = \frac{1}{d} \, (n \cdot P) \geqslant 1 \qquad (5)$$

which can be written as

$$\gamma(P) = - \frac{1}{2v} \sum_n (n \cdot P) \; \varepsilon(n) \; ; \qquad n \cdot P > 0 \qquad (6)$$

This form of $\gamma(P)$ was first presented by Herring [10] and used by Nicholas [2] in his calculations.

3 – CORRECTION TO SURFACE ENERGY

We now turn to the correcting terms E* due to relaxation of the top plane from its unrelaxed position at a distance d from the following plane (Fig. 2). The relaxed distance is $(1 + \lambda) d$, equivalent to a vector displacement $(-\lambda dP)$. The potential energy of the top plane, per unit area, is

$$E^*(P; \lambda) = \frac{d}{v} \sum_n \varepsilon(|n + \lambda \, dP|) = \frac{d}{v} \varepsilon^*(\lambda) \; ; \qquad n \cdot P > 0. \qquad (7)$$

The values $E_0^*(\lambda = 0)$ and $E_e^*(\lambda_e)$ at the minimum have to be determined to evaluate the correction to the surface energy (eq. 3) due to relaxation of the atoms in the top plane.

Except for the lower index planes, the relaxation of the atoms in planes following the topmost plane may give a non-negligible contribution to the correction. The method that we shall use to determine the correction to the surface energy in these cases is based on a description [11] of the surface in terms of terraces, ledges and kinks (TLK), such that the terraces and ledges are atomically compact, and the distances between ledges and between kinks are large compared to the interatomic spacing, as in the low atomic density surface of the two-dimensional crystal of Fig. 3.

In the companion paper we derive an equation (eq. 8 in ref. 11) for γ in terms of the contributions of terraces, ledges and kinks. From this equation we obtain for the correction $\Delta\gamma$ to the
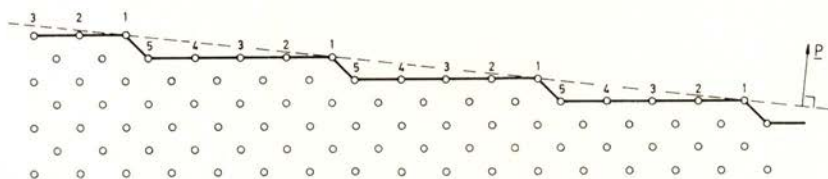
Fig. 3 — A two-dimensional crystal surface of orientation corresponding to the dashed line, showing terraces and ledges.

surface energy of a plane, with a particular decomposition TLK, the following result:

$$\Delta\gamma = \Delta\varepsilon_T \frac{d_T}{v} \cos \Theta_T + \frac{\Delta\varepsilon_L}{i_L d_T} \sin \Theta_T \cos \Theta_L + \frac{i_L}{v} \Delta\varepsilon_K \sin \Theta_T \sin \Theta_L$$

$$(8)$$

where $\Delta\varepsilon_T$, $\Delta\varepsilon_L$ and $\Delta\varepsilon_K$, respectively, are the corrections, per atom, for atoms in terraces, ledges and kink sites; d_T is the interplanar spacing of terraces, i_L the identity distance along ledges and v the volume per atom; Θ_T is the angle between the surface plane and the terraces and Θ_L the angle between the intersection of these planes with the direction of the ledges.

The total correction is then calculated by summing the corrections due to atoms in terraces, in ledges and in kinks. The latter is calculated from the correction for the topmost plane under consideration. The correction due to the terraces is directly obtained from the calculated $\varepsilon_e^* - \varepsilon_0^*$ for the plane of the terraces. Finally, the correction due to the ledges is obtained from that for a vicinal surface plane containing the same terraces and ledges (but no kinks) as the plane under consideration. In this method for obtaining the correction to the surface energy it is assumed that all atoms in terraces (e. g. atoms 2-5 in Fig. 3) and all atoms in ledges are equivalent. This is not strictly true: for example, the atoms in terraces near a ledge (e. g. atoms 2 or 5 in Fig. 3) are

not in positions equivalent to those in terraces far from ledges (atoms 3 and 4). The error in the calculated corrections should then decrease as the width of terraces and the inter-kink distance increases.

4 – LATTICE SUMS FOR EVAPORATION ENERGIES

The evaporation energy is the absolute value of the potential energy of a surface atom in the field of all other atoms. For an atom in the topmost plane, the (corrected) evaporation energy is given by

$$\varepsilon_{ev} = - (\varepsilon_e^* + \varepsilon_p^*) \tag{9}$$

where ε_e^* is the contribution of planes below the top plane and ε_p^* is the potential energy due to the other atoms in the top plane. ε_e^* is calculated as described above (eq. 7) and ε_p^* is obtained from

$$\varepsilon_p^* = \sum_n \varepsilon (n) ; \; n \cdot P = 0 ; \; n \neq 0 \tag{10}$$

Evaporation energies of atoms in the second and following planes may de comparable to ε_{ev} in the case of high index planes. By considering a TLK description of the surface, the evaporation energies of other surface atoms (in terraces and in ledges) can be obtained; the evaporation energy for the topmost plane corresponds to the kink site atoms (ledge atoms, if the surface has no kink sites).

5 – APPLICATION TO F. C. C. CRYSTALS

We take three orthonormal vectors ($e_1 \, e_2 \, e_3$) along the edges of the cube cell ($| e_i | = 1$). If a is the lattice parameter, the general form of n is

$$n = \frac{a}{2} \sum_i n_i \, e_i \quad \text{with} \quad \sum_i n_i = \text{even} \tag{11}$$

the n_i being integers such that their sum is even. The Miller

indices ($p_1\,p_2\,p_3$) will be taken as all odd (and coprime) or all even (g. c. d. $= 2$); then

$$d = \frac{a}{p} \;\; ; \;\; p^2 = \underset{i}{\Sigma}\, p_i^2 \;\; ; \;\; \mathbf{P} = \frac{1}{p} \underset{i}{\Sigma}\, p_i\, \mathbf{e}_i \tag{12}$$

The interatomic distance in the crystal is $r_0 = a/\sqrt{2}$ and the volume per atom is $a^3/4$. The e | e' Mye potential (namely 6 | 9, 6 | 12 and 9 | 12, see Fig. 4) will be used

$$\varepsilon\,(\rho) \,=\, \varepsilon_0 \left[\left(\frac{\sigma}{\rho}\right)^{e'} - \left(\frac{\sigma}{\rho}\right)^{e} \right] \; ; \; e' > e \tag{13}$$

where ε_0 and σ are constants that can be related respectively to the cohesive energy per atom, ε_c , and to the equilibrium separation, r_0 , in the crystal, by imposing that the potential energy of an atom is a minimum at the equilibrium separation. Table 1 gives
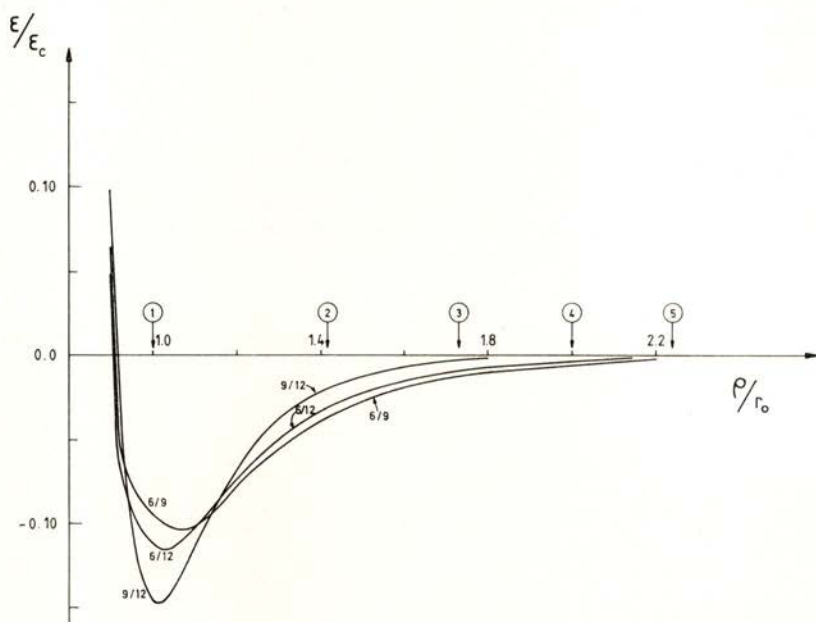
Fig. 4 — Plot of the potential functions $\varepsilon\,(\rho)$ used in the calculations. The energy is in ε_c units (cohesive energy in the crystal) and the distance in r_0 units (equilibrium 1st neighbour distance in the crystal). The distances to 2nd, 3rd, etc., neighbours are indicated.

values of σ/r_0 and $\varepsilon_0/\varepsilon_c$, obtained from very precise calculations of the lattice sums involved (cf. ref. [12]). Also indicated in Table 1 are the values of the equilibrium separation ρ_m and energy ε_m for an isolated pair of atoms. The fact that r_0/ρ_m is smaller than unity indicates that the near-neighbour interaction is repulsive for all potentials. This is in fact valid for any Mye potential [13].

TABLE 1 — Potential constants

	6 | 9 Potential	6 | 12 Potential	9 | 12 Potential
σ/r_0	0.91710	0.91729	0.91747
$\varepsilon_0/\varepsilon_c$	0.69769	0.46456	1.39026
r_0/ρ_m	0.95255	0.97123	0.99024
$-\varepsilon_m/\varepsilon_c$	0.10336	0.11614	0.14663

For the f. c. c. crystal with a potential $e \mid e'$, eq. 6 becomes

$$\gamma\,(\mathbf{P}\,;\,e\mid e'\,) = -\ \frac{\varepsilon_0}{r_0^2}\ (\,\sigma^{*e'}\ C_{e'} - \sigma^{*e}\ C_e\,) \tag{14}$$

where

$$\sigma^* = \sqrt{2}\ \sigma/r_0 \tag{15}$$

and

$$C_e = \underset{\mathbf{n}}{\Sigma}\ m'/n^e \tag{16a}$$

with

$$m' = \frac{1}{2p}\ \underset{i}{\Sigma}\ n_i\ p_i > 0\ ;\ \underset{i}{\Sigma}\ n_i = \text{even}\ ;\ n^2 = \underset{i}{\Sigma}\ n_i^2 \tag{16b}$$

The energy $E^*\,(\lambda\,)$ per unit area of the topmost plane, when its separation from the following plane is $(\,1 + \lambda\,)\,\mathbf{d}$, is obtained from eq. 7 noting that the displacement of the top plane is $-\lambda a p^{-2}\,(\underset{i}{\Sigma}\ p_i\ \mathbf{e}_i\,)$:

$$E^*\,(\lambda\,) = \frac{2}{p}\ \frac{\varepsilon_0}{r_0^2}\ (\,\sigma^{*e'}\ D_{e'} - \sigma^{*e}\ D_e\,) \tag{17}$$

where

$$D_e(\lambda) = \sum_n (n')^{-e} \tag{18a}$$

with

$$\frac{1}{2} \sum_i n_i \; p_i > 0 \; ; \; \sum_i n_i = \text{even} \; ; \; n'^2 = \sum_i n_i'^2 \; ; \; n_i' = n_i + 2\lambda p^{-2} \; p_i \tag{18b}$$

Finally, the potential energy of an atom in a plane (p) due to the other atoms in the plane is given by

$$\varepsilon_p^* = \varepsilon_0 \; (\sigma^{*e'} \; P_{e'} - \sigma^{*e} \; P_e) \tag{19}$$

where

$$P_e = \sum_{n \neq 0} n^{-e} \tag{20a}$$

with

$$\sum_i n_i \; p_i = 0 \; ; \; \sum_i n_i = \text{even} \; ; \; n^2 = \sum_i n_i^2 \tag{20b}$$

6 – RESULTS AND DISCUSSION

All lattice sums, C_e , D_e and P_e were calculated by the methods described in the Appendix, with $M = 10$. The number of terms (atoms) in the direct sums was approximately 1000 for the series C and D. The rest of the sum C_6 for (002) is 2.3 % of the value obtained in the direct sum. This figure is 0.35 % for D_6 (with $\lambda = 0$). The figures for C_9 and D_9 are respectively 3.7×10^{-3} % and 1.2×10^{-3} % and for C_{12} and D_{12} they are about 5.10^{-6} %. The precision in the values of γ is quite good. For example, the value of γ for the (002) plane obtained with $M = 20$ is between $(0.3\text{-}5) \times 10^{-5}$ different from the value for $M = 10$ for the three potentials. All calculated values will be written with at most four or five digits, according to the cases.

The determination of the equilibrium relaxation λ_e of the top plane was found by calculating $E^*(\lambda)$ with increments of 0.001 in λ, starting at $\lambda = 0$.

We shall consider separately the results for surface energies and for evaporation energies.

6a – SURFACE ENERGIES

Unrelaxed surface energies, γ, were calculated for a large number of planes and for the three potentials used (6 | 9, 6 | 12 and 9 | 12). In Table 2 are shown the values of γ for the more closely packed planes up to (135) and for a selected number of

TABLE 2 — Surface energies, γ (ε_c/r_o^2 units).

Plane	Potential		
	6 | 9	6 | 12	9 | 12
111	0.4831	0.4315	0.3283
002	0.4938	0.4480	0.3564
022	0.5137	0.4690	0.3798
113	0.5172	0.4717	0.3805
133	0.5181	0.4709	0.3763
024	0.5238	0.4811	0.3955
224	0.5172	0.4693	0.3735
115	0.5176	0.4717	0.3799
135	0.5259	0.4817	0.3933
100 100 102	0.4848	0.4333	0.3301
50 52 54	0.4890	0.4377	0.3350
500 502 520	0.4863	0.4348	0.3318
2 2 100	0.4980	0.4520	0.3601
2 100 100	0.5147	0.4699	0.3801
2 500 500	0.5139	0.4693	0.3798
0 2 40	0.5016	0.4559	0.3644
0 2 100	0.4971	0.4513	0.3597
0 30 38	0.5226	0.4784	0.3901
2 20 400	0.5017	0.4560	0.3645
1 15 19	0.5238	0.4794	0.3907
1 75 95	0.5229	0.4787	0.3903

Portgal. Phys. — Vol. 16, fasc. 3-4, pp. 137-160, 1985

147
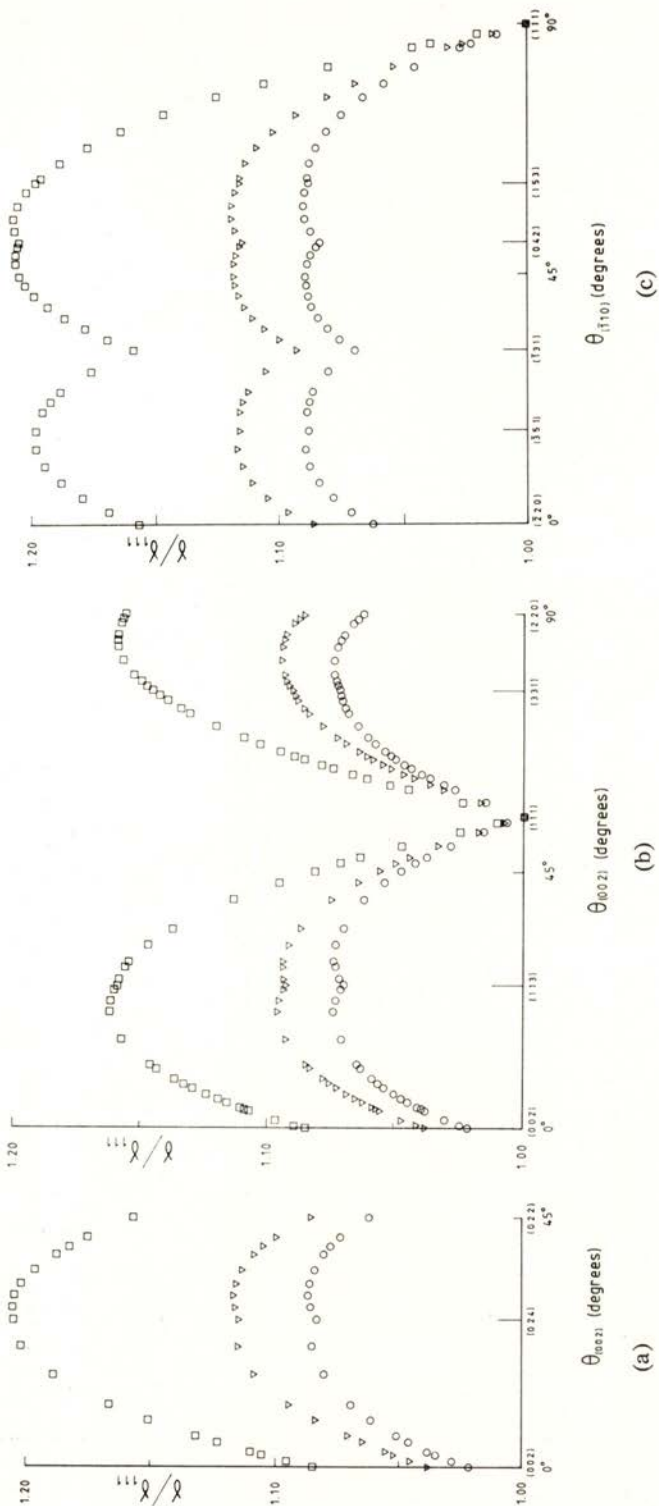
Fig. 5 —Variation of uncorrected surface energies along various crystallographic zones: a) [200] zone; b) [1Ī0] zone; c) [11Ī2] zone. Symbols for potentials: ○ - 6 | 9; ▽ - 6 | 12; □ - 9 | 12.

high index planes, most of which are vicinal to one of the lower index planes. From these data it is possible to calculate the contribution to the surface energy of edges and kinks in close packed planes. This will be discussed in detail in the companion paper. The γ values are expressed in units of ε_c/r_0^2, where ε_c is the cohesive energy per atom and r_0 is the interatomic distance. The values for the 6 | 12 potential are in excelent agreement with those that can be found in the work of Nicholas [2], but differ from those of Shuttleworth [1]. The 6 | 9 values are about 10 % larger than the 6 | 12 values and these are ~25 % larger than the 9 | 12 values, for the same surface planes. The data is conveniently displayed in γ-plots for individual zones, as shown in Figs. 5a-c respectively for the $<100>$, $<1\bar{1}0>$ and $<11\bar{2}>$ zones. The cusps at the lower index planes are clearly seen.

The fact that the relative values of γ for the three potentials are fairly independent of the surface orientation, suggests that if the γ values are expressed in another unit, characteristic of each potential, it might be possible to obtain values of γ fairly independent of the potential. Various attempts were made in this direction, using the data of Table 1, but without success. The energy depends on the interaction of a large number of atoms and it is not possible to write simple relations between the surface energy and properties of the interatomic potential.

The surface energy is least for (111) for all potentials. The largest γ found was for the plane (3 13 25) for the 6 | 9 and 6 | 12 potentials and for (1 7 13) for the 9 | 12 potential. These results on the maximum contrast with the conclusions drawn from a broken first-neighbour bond model [3, 4], according to which the maximum γ occurs for (024). The anisotropy, measured by the ratio of the two extreme γ's, is 1.207, 1.120 and 1.091 respectively for the 9 | 12, 6 | 12 and 6 | 9 potentials, in agreement with the general effect of the potential range on the anisotropy of γ [4].

Table 3 gives the equilibrium potential energy ε_e^* of an atom in a topmost plane, in the field of the atoms below that plane. The unit is ε_c. The values for each potential vary by a factor of ~1.6 between the maximum and minimum; they are slightly larger for the 6 | 9 potential and smaller for the 9 | 12 potential.

The calculated relaxations, expressed in r_0 units, vary between 1.2 and 2.5 % for the 6 | 9 potential, between 0.7 and 1.5 % for the 6 | 12 potential and between 0.2 and 0.5 % for the 9 | 12 poten-

Portgal. Phys. — Vol. 16, fasc. 3-4, pp. 137-160, 1985

149

tial. The smallest values are for (111), while (024) has values of the relaxation close to the maximum (which in fact occurs for a high index plane).

The corrections to the surface energy due to relaxation of the top plane, i. e. the values of $\varepsilon_o^* - \varepsilon_e^*$, are also indicated in Table 3. The values are per atom, in $_c$ units.

TABLE 3 — Energy of atoms in top plane, ε_e^*, and energy correction, $\varepsilon_e^* - \varepsilon_o^*$, per atom

Plane	$-\varepsilon_e^*$ (ε_c units)			$\varepsilon_o^* - \varepsilon_e^*$ (ε_c units) $\times 10^2$		
	6 | 9	6 | 12	9 | 12	6 | 9	6 | 12	9 | 12
111	0.6490	0.6143	0.5468	0.2672	0.1177	0.0086
002	0.7115	0.6940	0.6636	0.7535	0.3731	0.0634
022	0.8358	0.8302	0.8247	0.8843	0.4201	0.0602
113	0.8713	0.8607	0.8448	0.8104	0.3818	0.0515
133	0.8956	0.8797	0.8523	0.6892	0.3197	0.0391
024	0.9427	0.9501	0.9722	1.1403	0.5435	0.0822
224	0.8994	0.8825	0.8529	0.6417	0.2960	0.0354
115	0.9027	0.8845	0.8533	0.8329	0.3990	0.0587
135	0.9781	0.9807	0.9923	0.9872	0.4623	0.0634
100 100 102	0.9014	0.8846	0.8531	0.2875	0.1251	0.0094
50 52 54	0.9898	0.9912	0.9962	0.3234	0.1404	0.0115
500 502 520	1.0030	1.0013	1.0001	0.3030	0.1311	0.0100
2 2 100	0.9063	0.8872	0.8537	0.7756	0.3810	0.0633
2 100 100	0.9072	0.8875	0.8536	0.8681	0.4128	0.0589
2 500 500	0.9073	0.8875	0.8536	0.8760	0.4170	0.0599
0 2 40	0.9697	0.9714	0.9801	0.8398	0.4078	0.0668
0 2 100	0.9694	0.9713	0.9800	0.8072	0.3928	0.0650
0 30 38	0.9715	0.9721	0.9800	1.0140	0.4799	0.0691
2 20 400	1.0083	1.0040	1.0007	0.8331	0.4051	0.0660
1 15 19	1.0091	1.0042	1.0006	0.9870	0.4662	0.0657
1 75 95	1.0100	1.0047	1.0007	1.0043	0.4760	0.0680

TABLE 4 — Surface energy corrections using TLK decomposition (ε_c/r_o^2 units)

Plane	Terrace	Ledge	Vicinal plane for $\Delta\varepsilon_L$	$\Delta\gamma$ ($\times 10^2$)		
				6 | 9	6 | 12	9 | 12
111	111	—		0.3085	0.1359	0.0099
002	002	—		0.7535	0.3731	0.0634
022	022	—		0.6253	0.2971	0.0426
113	!13	—		0.4887	0.2302	0.0311
113	002	1$\bar{1}$0		1.1703	0.5677	0.0884
113	111	1$\bar{1}$0		0.7572	0.3485	0.0397
133	022	01$\bar{1}$		0.9248	0.4358	0.0594
133	111	01$\bar{1}$		0.6023	0.2727	0.0271
024	002	200		1.1839	0.5768	0.0935
024	022	200		1.1032	0.5249	0.0771
224	002	1$\bar{1}$0		1.1392	0.5463	0.0807
224	111	1$\bar{1}$0		0.5529	0.2490	0.0238
115	002	1$\bar{1}$0		1.0456	0.5126	0.0836
135	111	1$\bar{2}$1		0.6047	0.2757	0.0302
135	022	211		0.9316	0.4403	0.0621
100 100 102	111	1$\bar{1}$0		0.3118	0.1373	0.0100
50 52 54	111	1$\bar{2}$1		0.3156	0.1390	0.0102
500 502 520	111	1$\bar{1}$0	100 100 102	0.3154	0.1389	0.0102
2 2 100	002	1$\bar{1}$0		0.7842	0.3882	0.0659
2 100 100	022	01$\bar{1}$		0.6498	0.3087	0.0442
2 500 500	022	01$\bar{1}$		0.6302	0.2994	0.0429
0 2 40	002	200		0.7945	0.3930	0.0667
0 2 100	002	200		0.7695	0.3809	0.0647
0 30 38	022	200		0.7886	0.3743	0.0537
2 20 400	002	200	0 2 40	0.8028	0.3970	0.0673
1 15 19	022	21$\bar{1}$	1 3 5	0.8378	0.3969	0.0564
1 15 19	022	200	0 30 38	0.8694	0.4125	0.0591
1 75 95	022	200	0 30 38	0.8051	0.3822	0.0548

The smallest correction per atom is for (111) and the largest is for (024); these corrections differ by a factor of ~4 for the 6 | e' potentials and by a factor of ~8 for the 9 | 12 potential. The correction is very small for the 9 | 12 potential and largest for the 6 | 9 potential, but even for this potential does not exceed ~1 %.

Corrected surface energies were obtained with the values of Table 3, using eq. 8 and an appropriate TLK description of the

TABLE 5 — Corrected surface energies, γ_c (TLK corrections)

Plane	γ_c (ε_c/r_o^2 units)		
	6 | 9	6 | 12	9 | 12
111	0.4800	0.4301	0.3282
002	0.4863	0.4443	0.3558
022	0.5074	0.4660	0.3794
113	0.5096	0.4682	0.3801
133	0.5121	0.4682	0.3760
024	0.5128	0.4759	0.3947
244	0.5117	0.4668	0.3733
115	0.5071	0.4666	0.3791
135	0.5199	0.4789	0.3930
100 100 102	0.4817	0.4319	0.3300
50 52 54	0.4858	0.4363	0.3349
500 502 520	0.4831	0.4334	0.3317
2 2 100	0.4902	0.4481	0.3594
2 100 100	0.5082	0.4668	0.3797
2 500 500	0.5076	0.4663	0.3794
0 2 40	0.4937	0.4520	0.3637
0 2 100	0.4894	0.4475	0.3591
0 30 38	0.5147	0.4747	0.3896
2 20 400	0.4937	0.4520	0.3638
1 15 19	0.5151	0.4753	0.3901
1 75 95	0.5148	0.4749	0.3898

surface. The terraces were chosen among (111), (002) and (022) and the ledges among the directions [011], [002] and [112]. For each decomposition, the correction to the surface energy is given in Table 4 in ε_c/r_0^2 units. When the plane has no kinks, $\Theta_L = 0$, the correction $\Delta\varepsilon_L$ is the value found in Table 3 for that plane. If there are kinks, $\Delta\varepsilon_L$ is taken from Table 3 for a plane (indicated in Table 4) vicinal to the surface plane and with a TLK decomposition with no kinks; $\Delta\varepsilon_K$ is then the correction per atom for the surface plane.

Also included in Table 4 are the corrections to the four most close packed planes, calculated directly from the correction per atom for these planes, given in Table 3.

The corrected energies are given in Table 5 for the planes listed in Table 4. For planes with two TLK decompositions in Table 4, the correction corresponding to the decomposition with more close packed terraces (or ledges, in the case of (1 15 19)) was used. It is apparent that the correction slightly reduces the anisotropy of the surface energy (reduction of 1.5 % for the 6 | 9 potential). It also reduces the increase of γ for a given deviation away from a close packed orientation.

6b – EVAPORATION ENERGIES

The calculated potential energies ε_p^* of an atom in a crystal plane due to the other atoms in the plane are indicated in Table 6, in ε_c units. The values for the high index planes such as (2 100 100), (0 2 100) and (50 52 54) are very nearly those contributed by atoms in the lattice row, parallel to $<001>$, $<002>$ and $<112>$, respectively, where the reference atom is located. This is because in these planes, the rows indicated have inter-row spacings much larger than the repeat distance along the row. For similar reasons, the atoms in planes such as (1 75 95) are so far apart that the potential energy ε_p^* is negligible. Combining these results with the ε_e^* values of Table 3, corrected evaporation energies from the topmost planes can be calculated (eq. 8). The results are shown in Table 7.

As expected, the evaporation energy decreases as the compactness of the surface plane decreases, for the more close packed

TABLE 6 — Potential energy ε_p^*, per atom due to atoms in the same plane

Plane	$-\varepsilon_p^*$ (ε_c units)		
	6 | 9	6 | 12	9 | 12
111	0.7073	0.7737	0.9065
002	0.5919	0.6193	0.6741
022	0.3459	0.3479	0.3518
113	0.2734	0.2861	0.3114
133	0.2224	0.2470	0.2961
024	0.1374	0.1107	$0.5729.10^{-1}$
224	0.2140	0.2409	0.2948
115	0.2112	0.2390	0.2945
135	$0.6343.10^{-1}$	$0.4784.10^{-1}$	$0.1666.10^{-1}$
100 100 102	0.2029	0.2333	0.2940
50 52 54	$0.2671.10^{-1}$	$0.2040.10^{-1}$	$0.7790.10^{-2}$
2 2 100	0.2029	0.2333	0.2940
2 100 100	0.2029	0.2333	0.2940
2 500 500	0.2029	0.2333	0.2940
0 2 40	$0.7722.10^{-1}$	$0.6523.10^{-1}$	$0.4126.10^{-1}$
0 2 100	$0.7722.10^{-1}$	$0.6523.10^{-1}$	$0.4126.10^{-1}$
0 30 38	$0.7722.10^{-1}$	$0.6523.10^{-1}$	$0.4126.10^{-1}$
500 502 520	$0.1123.10^{-5}$	$0.7491.10^{-6}$	$0.1960.10^{-8}$
2 20 400	$0.2320.10^{-6}$	$0.1547.10^{-6}$	$0.1007.10^{-9}$
1 15 19	$0.1437.10^{-2}$	$0.9812.10^{-3}$	$0.6878.10^{-4}$
1 75 95	$0.2477.10^{-4}$	$0.1658.10^{-4}$	$0.1890.10^{-6}$

planes (from (111) to (135)). The (024) plane has a slightly lower value, which can be attributed to the low ε_p^* for this plane.

The evaporation energies for the following high index planes (from (100 100 102) to (0 30 38)) correspond to atoms which are located at atomic ledges separating low index terraces. The ledges are, depending on the cases, along $<110>$, $<200>$ and

TABLE 7 — Evaporation energies, ε_{ev}

Plane	ε_{ev} (ε_c units)		
	6 | 9	6 | 12	9 | 12
111	1.3563	1.3880	1.4534
002	1.3035	1.3134	1.3377
022	1.1818	1.1781	1.1765
113	1.1448	1.1468	1.1563
133	1.1181	1.1267	1.1485
024	1.0800	1.0608	1.0295
224	1.1134	1.1234	1.1478
115	1.1139	1.1235	1.1479
135	1.0415	1.0285	1.0090
100 100 102	1.1043	1.1179	1.1471
50 52 54	1.0166	1.0116	1.0040
2 2 100	1.1092	1.1204	1.1476
2 100 100	1.1101	1.1208	1.1476
2 500 500	1.1102	1.1208	1.1476
0 2 40	1.0470	1.0367	1.0213
0 2 100	1.0467	1.0365	1.0213
0 3 38	1.0487	1.0374	1.0213
500 502 520	1.0030	1.0013	1.0001
2 20 400	1.0083	1.0040	1.0007
1 15 19	1.0105	1.0051	1.0007
1 75 95	1.0100	1.0047	1.0007

<112> directions (see Table 4). It is noticeable that the evaporation energies of such ledge atoms are fairly constant, i. e., nearly independent of the low index terrace associated with the ledge, and decrease as the atomic density in the ledge decreases.

The evaporation energies per atom in top planes which do not contain close packed rows (the last four planes in Table 7) are

Portgal. Phys. — Vol. 16, fasc. 3-4, pp. 137-160, 1985

155

also fairly constant. They correspond to atoms at kink sites. It is interesting to note that the evaporation energies of such atoms can be as much as 1 % larger than the cohesive energy for the 9 | 6 potential.

It is apparent from the values of Table 7 that there is no systematic effect of the potential on the evaporation energies expressed in ε_c units. This contrasts with the marked effect on the γ values expressed in ε_c/r_0^2 units.

Finally, it is noted that the energies ε_e^* in Table 3 for the low index planes are the evaporation energies for isolated ad-atoms sitting on these planes. Such energies increase as the atomic density in the plane decreases.

APPENDIX — CALCULATION OF LATTICE SUMS

The sums C_e, D_e and P_e are calculated term by term up to a chosen value of $n = |\mathbf{n}|$:

$$n_1^2 + n_2^2 + n_3^2 \leqslant M^2$$

and the number, N, of terms in the sum, is counted. The region within which these atoms are located is then determined (e. g. a hemisphere or a circle). The rest of the series is calculated assuming that the remainder of crystal C is replaced by a continuum with the appropriate atomic density.

The correct assignment of the volume where the N atoms are located is crucial, if precise results are wanted. Shuttleworth assumed that this volume, in the case of the series C_e, is a hemisphere in crystal C of radius $R_0 a/2$, centred at atom $0'_0$ in the first plane $0'$ of C' (Fig. 6) and such that $(2\pi/3) R_0^3 = 2N$. Using this criterion we have obtained incoherent results: for example, the surface energy for (2 500 500) is smaller than that for (022). Since among the N atoms there are no atoms in the plane through $0'_0$, it is apparent that the volume in crystal C where the atoms are located is the volume of a hemisphere centred at $0'_0$, minus the volume of a layer adjacent to the plane through $0'_0$ and of thickness $d/2 = (a/2) \cdot (1/p)$ (see Fig. 6). This is consistent with the procedure that will be adopted to

evaluate the rest of the series. Therefore the radius $R_0 a/2$ of the sphere is given by

$$(2\pi/3) \; R_0^3 - \pi R_0^2 \; (1/p) = 2N$$

The difference between the R_0 determined by this equation and by Shuttleworth's equation tends to zero as the interplanar distance $d \to 0$, but for lower index planes the differences are significative leading to changes of about 0.2 % in the surface energy of (002), with the 6 | 12 potential. This results mostly from the change in C_6 which is the slowest convergent sum.
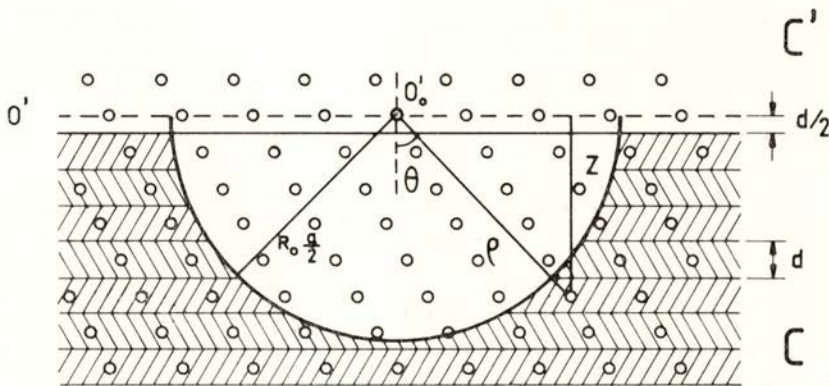
Fig. 6 — Illustration of the method used to obtain the rest of the lattice sums C_e (see Appendix). The half-crystal C is replaced by a continuum outside a hemisphere of radius $R_0 \; a/2$.

The atomic planes (p) outside the hemisphere are replaced by continuous lamella of thickness $d/2$ centred in each plane (Fig. 6). The integration domain for the integrals that give the rest of the series is the difference between the following two regions: i) the volume below plane 0' outside the hemisphere; ii) a lamella of thickness $d/2$ limited by that plane, outside the hemisphere. Shuttleworth wrongly assumed that region ii) was a lamella outside a cylinder of radius R_0.

Using spherical coordinates, (ρ, Θ, ϕ) and expressing all linear dimensions in units of a/2 (volume per atom = 2), we have (cf. eq. 16a)

$$m' = \rho \cos\Theta / d$$

and the integrals that have to be calculated are of the form

$$\iiint \rho^{3-e} \sin\Theta \cos\Theta \; d\rho \; d\Theta \; d\phi$$

For the integral over region (i) the integration limits are: ϕ (0 , 2π); Θ (0 , $\pi/2$); ρ (R_0 , ∞), with the result

$$C'_e = \frac{\pi}{e-4} \frac{p}{4} \frac{1}{R_0^{e-4}}$$

For the integral over region (ii) the integration limits are: ϕ (0 , 2π); ρ (R_0 , $\dfrac{1}{p \cos\Theta}$); Θ ($\cos^{-1} \dfrac{1}{R_0 p}$, $\pi/2$) with the result:

$$C''_e = \frac{\pi}{4p(e-2)} \frac{1}{R_0^{e-2}}$$

The series C_e is then calculated from

$$C_e = \sum_n \frac{m'}{n^e} + C'_e - C''_e \; ; \; n^2 = \sum_i n_i^2 \leqslant M^2$$

In the case of the series D_e the sum is calculated term by term up to

$$\sum_i n_i'^2 \leqslant M^2$$

The corresponding N atoms are within a hemisphere of radius R_0 a/2 centred at 0_0 with (Fig. 2).

$$(2\pi/3) \; R_0^3 - \pi R_0^2 \cdot (2\lambda + 1)/p = 2N$$

The second term in the left corresponds to a layer of thickness $d/2 + \lambda d$ where no atom centres lie. This integration volume

is again the difference between: i) the half-space below plane 0 outside the hemisphere; ii) a lamella of thickness $(1/2 + \lambda)\, d = (1 + 2\lambda)/p \cdot a/2$ outside the hemisphere and adjacent to plane 0. The integrals for the rest of the sum D_e are

$$\iiint \rho^{2-e} \sin\theta \; d\rho \; d\theta \; d\phi$$

For the integral over region (i): $\phi\,(0 , 2\pi)$; $\theta\,(0 , \pi/2)$, $\rho\,(R_0 , \infty)$ with the result

$$D'_e = \frac{\pi}{e-3} \; \frac{1}{R_0^{e-3}}$$

For the integral over region (ii): $\phi\,(0 , 2\pi)$; $\rho\,(R_0 , \frac{1 + 2\lambda}{p \cos\theta})$; $\theta\,(\cos^{-1} \frac{1 + 2\lambda}{p\, R_0} , \frac{\pi}{2})$ with the result

$$D''_e = \frac{2\pi}{p} \left(\frac{1}{2} + \lambda \right) \frac{1}{(e - 2)\, R_0^{e-2}}$$

The series D_e is then calculated from

$$D_e = \underset{n}{\Sigma} \frac{1}{n'^e} + D'_e - D''_e \quad n'^2 = \underset{i}{\Sigma} \, n'^2_i \leqslant M^2$$

Finally in the calculation of P_e the direct sum is determined for N atoms within a circle of radius $R_0\, a/2$ such that

$$\pi\, R_0^2 = Np$$

The atoms outside this circle are replaced by a continuum with atomic density $(p\, a^2/4)^{-1}$. The rest of the sum is

$$P'_e = \frac{1}{p} \int_{R_0}^{\infty} 2\pi \; \rho^{1-e} \; d\rho = \frac{2\pi}{p} \; \frac{1}{e-2} \; \frac{1}{R_0^{e-2}}$$

REFERENCES

[1] R. Shuttleworth, *Proc. Phys. Soc.*, **A62**, 167 (1949).

[2] J. F. Nicholas, *Aust. J. Phys.*, **21**, 21 (1968).

[3] J. K. Mackenzie, A. J. W. Moore and J. F. Nicholas, *J. Phys. Chem. Solids*, **23**, 186 (1962).

[4] M. Drechsler and J. F. Nicholas, *J. Phys. Chem. Sol.*, **28**, 2609 (1967).

[5] J. Th. M. de Hosson, in *Interatomic Potentials and Crystalline Defects*, ed. J. K. Lee, The Metallurgical Society of AIME, 1981.

[6] P. Wynblatt, *Surface Sci.*, **136**, L51 (1984).

[7] R. G. Linford and L. A. Mitchell, *Surface Sci.*, **27**, 142 (1971).

[8] V. O. Yesin, V. N. Porozkov and V. I. Danilyuk, *Phys. Met. Metall.*, **53**, 149 (1982); english translation of *Fiz. metal. metallowed.*, **53**, 361 (1982).

[9] J. Van Der Veen, *Z. Metalkde.*, **82**, 120 (1981).

[10] C. Herring, *Phys. Rev.*, **139**, A179 (1951).

[11] M. A. Fortes and J. Brito Correia, *Portgal. Phys.*, following paper in this issue.

[12] J. O. Hirschfelder, C. F. Curtis and R. B. Bird, in *Molecular Theory of Gases and Liquids* (Wiley, 1954) p. 1040.

[13] R. P. Gupta, *Phys. Rev. B*, **25**, 6265 (1981).

ENERGIES OF SURFACE LEDGES AND KINKS

M. A. FORTES and J. BRITO CORREIA

Departamento de Engenharia de Materiais, Instituto Superior Técnico,
Av. Rovisco Pais, 1000 Lisboa, Portugal

ABSTRACT — The description of the surface of a crystal in terms of terraces, ledges and kinks (TLK) is discussed , and equations are derived that determine the TLK content of the surface for any choice of terraces and ledges. The surface energy can be obtained as a sum of contributions of terraces, ledges and kinks. The form of the lattice sums that give these contributions in terms of a pairwise interaction potential is derived.

The accuracy of the TLK decomposition of surface energy is assessed by comparing the TLK energies with those calculated directly. Calculations were done for a f. c. c. crystal using three Mye potentials (6 | 9, 6 | 12 and 9 | 12) and limiting the choice of terraces and ledges to the more closely packed planes and directions, respectively. A very accurate method for calculating the lattice sums was developed, with which terrace, ledge and kink energies were determined. From these results it is concluded that the accuracy of the TLK decomposition of energy decreases as the range of the potential increases, but is never worse than one percent for the poten-tials used.

The analogy of the TLK description with the coincidence site lattice model of interfaces is emphasized.

1 – INTRODUCTION

At the atomic level, the simplest solid surfaces are those obtained in a monoatomic crystal by a cut parallel to a lattice plane, followed by removal of the atoms in one side of the cut. The atomic distribution of the atoms is then periodic in each of the planes parallel to the cut, even if relaxation of the atomic positions is taken into account. The surface atoms may be defined

as those with potential energies, ε (in the field of the other atoms), exceeding a specified value, for example $|\varepsilon| < 0.99\,\varepsilon_c$, where ε_c is the cohesive energy. If the plane of the surface is a low index, high atomic density plane, the surface atoms will be, if the interaction is of short enough range, only those in the topmost plane. In this case, there is only one type of surface site (see example in Fig. 1a). However, for high index surfaces (Fig. 1b), the surface atoms will belong to a number of planes parallel to the topmost plane, although the thickness of the surface region should be comparable in both cases. For a high index surface, the properties (e. g. the energy) of the atoms vary slightly from plane to plane, in the surface region, so that, strictly, there are as many types of surface sites as parallel planes in the surface region. However, the change in energy from plane to plane is not in general uniform (broken bond model!), and it is formally convenient to group the atoms with similar properties in the same class. This then leads to the terrace-ledge-kink (TLK) description of the surface [1], which essentially recognizes only three types of surface atom sites (marked 1, 2 and 3 in Fig. 2a). The terraces are low energy, high atomic density planes. The ledges (or steps) are parallel to close packed directions and uniformly spaced; they can be regarded as monoatomic steps from one terrace to the next. The kinks are arranged in a planar lattice (that of the surface plane) and can be described as steps in the ledges. The energy of the surface atoms increases in the order terrace sites, ledge sites, kink sites.

This is the essence of the TLK model of a crystal surface, which has proved very useful in discussing properties such as surface and evaporation energies [2-4] and phenomena such as adsorption, surface diffusion and crystal growth [5]. Real surfaces do contain ledges and kinks, but not regularly distributed, and in general other types of atom sites will be found in them. In this paper, we shall consider only regular ideal surfaces obtained by a cut through a lattice plane, for which the TLK decomposition is periodic.

Formally, the TLK description can be applied to any orientation of the surface and to any choice of the plane of the terraces
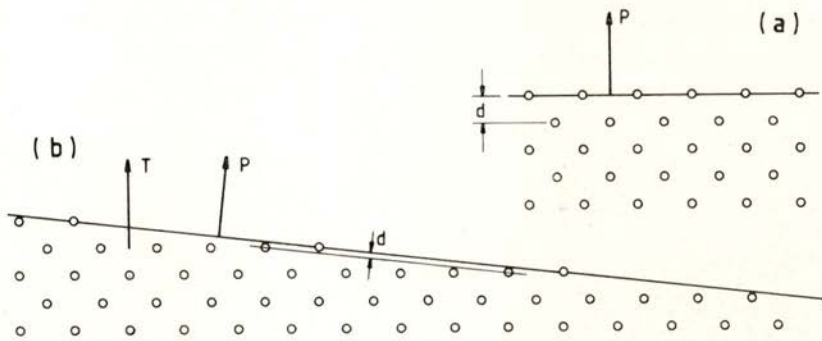
Fig. 1 — Different orientations of the surface "plane" **P** in a two-dimensional crystal: (a) low index, high atomic density; (b) high index, low atomic density. The interplanar spacings are indicated.
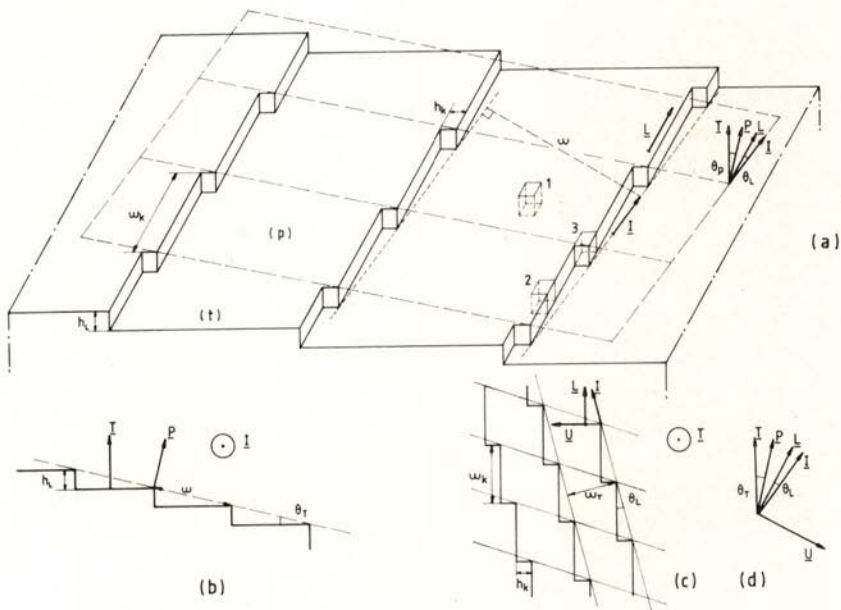
Fig. 2 — An arbitrary surface orientation (p) showing a TLK decomposition. The unit vectors normal to the surface plane (**P**) and to the terraces (**T**) are shown. **L** is a unit vector along the ledges and **I** a unit vector parallel to the intersection of planes **P** and **T**. Atoms 1, 2 and 3 are respectively at terrace, ledge and kink sites. Diagrams (b) and (c) are sections of (a) through planes perpendicular to **I** and **T**, respectively. Diagram (d) shows the vectors used in the text; **U**, **L**, **T** define a triorthogonal direct reference system.

and of the direction of the ledges. The spacing between ledges and that between kinks is then determined to give the specified orientation of the surface plane. However, as the orientation of the surface deviates more and more from that of the chosen terraces, the density of ledges and kinks increases so that their interaction becomes strong [6] and their individuality may become questionable. On the other hand, if the terraces are taken as high index planes, it is no longer legitimate to consider only one type of surface sites in the terraces. These limitations to the applicability of the TLK model will have a repercussion when one attempts to calculate overall surface properties, e. g. the surface energy, in terms of contributions due to terraces, ledges and kinks.

The present paper concentrates on this topic and contains a detailed study of the surface energy decomposition in terms of TLK, from which conclusions on the applicability of the TLK model can be drawn. We first write down the equations that give the TLK content of an arbitrary surface and for arbitrary orientations of the terraces and ledges. We then derive the lattice sums that give the contributions to the surface energy of ledges and kinks, assuming a pairwise interaction between the atoms. The properties of the sums are discussed and their actual calculation is done for a f. c. c. crystal using three potentials of the Lennard-Jones type (Mye potentials). The results are used to calculate surface energies of various planes from their TLK content. These surface energies are then compared with those obtained by a direct method [7], in order to assess the range of applicability of the TLK decomposition from the point of view of surface energy. No corrections associated with relaxation of the atoms to their equilibrium positions have been included in our calculations. As shown in the preceding paper, these corrections are always very small for the potentials that will be used here. A recent example of calculations of relaxed ledge energies in ionic crystals can be found in ref. 8.

The problems that we discuss are formally similar to those found in the coincidence site lattice (c. s. l.) model of grain boundaries [e.g. 9, 10]. In this model, the concept of special (or favoured) c. s. l. boundaries is the equivalent to low index surfaces, and the grain boundary dislocations are the equivalent to surface ledges and kinks, which can, in fact, be regarded as surface

defects. On the other hand, the range of applicability of the c. s. l. model is limited by similar questions and can be assessed in similar grounds.

2 – DETERMINATION OF THE TLK DECOMPOSITION

Consider a surface in a crystal with one atom per lattice point, parallel to an arbitrary crystallographic plane with Miller indices $(p) \equiv (p_1 p_2 p_3)$ referred to a vector basis $e_1 e_2 e_3$ (not necessarily a lattice basis). The unit normal to the plane is P and the interplanar spacing is d (Figs. 1 and 2).

The plane of the terraces is $(t) = (t_1 t_2 t_3)$ with unit normal T. The ledges are parallel to the crystal direction $[l] = [l_1 l_2 l_3]$ with unit vector L. The height h_L of the ledges is the interplanar spacing d_T of (t)

$$h_L = d_T \tag{1}$$

and the height h_K of the kinks is the distance between adjacent rows $[1]$ in the plane (t). Let i_L be the repeat distance along the ledges and v the volume per lattice point (atom). Then

$$h_K = \frac{v}{d_T \, i_L} \tag{2}$$

The angle $\Theta_T \, (0 \leqslant \Theta_T < \pi/2)$ between the plane of the surface (p) and the plane of the terraces (t) is given by

$$\cos \Theta_T = P \cdot T \tag{3}$$

The intersection of these two planes is a crystal direction $[i]$ of unit vector I at an angle Θ_L with the direction of the ledges $(0 \leqslant \Theta_L < \pi/2)$:

$$\cos \Theta_L = I \cdot L \; ; \quad I \cdot P = I \cdot T = 0 \tag{4}$$

The spacing between ledges, measured in the direction perpendicular to I in the plane (p) is $w = h_L/\sin \Theta_T$. The width w_T of the terraces (distance between ledges measured in the plane (t)) can be related to h_L (Fig. 2c):

$$w_T = h_L \cot g \, \Theta_T \cos \Theta_L \tag{5}$$

The distance between adjacent kinks in the same ledge, w_K, is measured along the ledge and is given by

$$w_K = h_K \cotg \Theta_L \tag{6}$$

All the quantities defined above are indicated in Fig. 2.

If **P** defines a lattice plane, as we are assuming, the distribution of ledges and kinks is periodic. The period corresponds to a unit cell in the plane (p), defined by the kink sites. The area of this unit cell is $ww_K/\cos \Theta_L$. The corresponding area of terrace is obtained by multiplying by $\cos \Theta_T$. The length of ledges in the period is w_K and there is one kink per period. Let γ be the surface energy of (p), γ_T the surface energy of the terraces (both per unit area), $_L$ the ledge energy per unit length and ε_K the energy of a kink. Then

$$\gamma \frac{ww_K}{\cos \Theta_L} = \gamma_T \frac{ww_K}{\cos \Theta_L} \cos \Theta_T + \varepsilon_L w_K + \varepsilon_K \tag{7}$$

Using eqs. 5 and 6 we finally obtain

$$\gamma = \gamma_T \cos \Theta_T + \frac{\varepsilon_L}{h_L} \sin \Theta_T \cos \Theta_L + \frac{\varepsilon_K}{h_L h_K} \sin \Theta_T \sin \Theta_L \tag{8}$$

with h_L and h_K given by eqs. 1 and 2, respectively.

In this approach, ledges and kinks are treated as line and point features on the surface, respectively. The surface itself is treated as a geometric surface. The approach is macroscopic in this respect. For example, the specific surface energy, γ_T, should be regarded as an average surface energy of the actual terraces, and possibly affected by their width. The TLK decomposition of the energy is acceptable for those planes such that the terrace and ledge energy is negligibly different from that of a wide terrace or of a ledge with no kinks, respectively.

We will now show how these limitations to eq. 8 can be put in more precise terms. This will be done by using an atomic approach to the surface energy, through which we are able to obtain the lattice sums with which terrace, ledge and kink energies can be calculated.

3 — LATTICE SUMS FOR LEDGE AND KINK ENERGIES

The derivation of the lattice sums for γ_T, ε_L and ε_K is based on the equation for the energy of a surface of arbitrary orientation in terms of the pairwise interaction between the atoms. For a potential $\varepsilon(\rho)$, where ρ is the distance between two atoms, the surface energy γ for the orientation defined by a plane ($p_1 p_2 p_3$) of unit normal $\mathbf{P}$, is [7]

$$\gamma = -\frac{1}{2v} \sum_n (\mathbf{n} \cdot \mathbf{P}) \, \varepsilon(\mathbf{n}) \; ; \; \mathbf{n} \cdot \mathbf{P} > 0 \tag{9}$$

where v is the volume per atom and $\mathbf{n}$ defines the positions of the atoms relative to a reference atom; the sum is for all $\mathbf{n}$ such that $\mathbf{n} \cdot \mathbf{P} > 0$.

We define a unit vector $\mathbf{U}$ by the vector product

$$\mathbf{U} = \mathbf{L} \times \mathbf{T} \tag{10}$$

$\mathbf{L}$, $\mathbf{T}$ and $\mathbf{U}$ define a triorthogonal direct reference system (Fig. 2d). The vector $\mathbf{P}$ makes an angle Θ_T with $\mathbf{T}$ and its projection in the plane of $\mathbf{U}$ and $\mathbf{L}$ makes an angle with $\mathbf{U}$ which is equal to the angle Θ_L, between $\mathbf{I}$ and $\mathbf{L}$. Therefore

$$\mathbf{P} = \mathbf{T} \cos \Theta_T + \mathbf{U} \sin \Theta_T \cos \Theta_L + \mathbf{L} \sin \Theta_T \sin \Theta_L \tag{11}$$

with both Θ_T and Θ_L in the interval $(0, \pi/2)$. Combining eqs. 9 and 11 yields

$$\gamma = -\frac{1}{2v} [\cos \Theta_T \sum_n (\mathbf{n} \cdot \mathbf{T}) \, \varepsilon(n) + \sin \Theta_T \cos \Theta_L \sum_n (\mathbf{n} \cdot \mathbf{U}) \, \varepsilon(n)$$

$$+ \sin \Theta_T \sin \Theta_L \sum_n (\mathbf{n} \cdot \mathbf{L}) \, \varepsilon(n)] \; ; \; \mathbf{n} \cdot \mathbf{P} > 0 \tag{12}$$

The sums in eq. 12 are for all $\mathbf{n}$ such that $\mathbf{n} \cdot \mathbf{P} > 0$. When Θ_T and Θ_L tend to zero (the density of ledges and kinks tends to zero), the condition $\mathbf{n} \cdot \mathbf{P} > 0$ is equivalent to the following three alternative conditions: (i) $\mathbf{n} \cdot \mathbf{T} > 0$; (ii) $\mathbf{n} \cdot \mathbf{T} = 0$ and $\mathbf{n} \cdot \mathbf{U} > 0$; (iii) $\mathbf{n} \cdot \mathbf{T} = \mathbf{n} \cdot \mathbf{U} = 0$ and $\mathbf{n} \cdot \mathbf{L} > 0$. In this limit,

the sucessive sums in eq. 12 are calculated for the **n** that satisfy the sucessive conditions (i) to (iii). Comparing eq. 8 with eq. 12 we obtained the lattice sums for γ_T, ε_L and ε_K. The first has the expected form, analogous to eq. 9:

$$\gamma_T = -\frac{1}{2v} \sum_n (n \cdot T)\, \varepsilon(n)\,;\ n \cdot T > 0 \tag{13}$$

The ledge energy is given by

$$\varepsilon_L = -h_L/(2v)\sum_n (n \cdot U)\, \varepsilon(n)\,;\ n \cdot U > 0,\ n \cdot T = 0 \tag{14}$$

and the kink energy by

$$\varepsilon_K = -h_L h_K/(2v)\sum_n (n \cdot L)\, \varepsilon(n)\,;\ n \cdot L > 0,\ n \cdot T = 0,\ n \cdot U = 0 \tag{15}$$

The series for ε_L is a double sum (two subscripts) and that for ε_K is a simple sum (one subscript). Eqs. 14 and 15 give the energy of isolated ledges and kinks, respectively. Eq. 15 shows that the energy of a kink depends on the ledge where the kink is located, but not on the associated terrace.

A simple interpretation can be given to these equations. Eq. 14 is the expression that one would write to calculate the energy, per unit length, of a "surface" created in a crystal plane (t), of normal **T**, by a cut along a direction **L**. This energy is, apart from the sign, one half the potential energy of one half-plane in the field of the other half-plane, the two half-planes being separated along a direction **L**. Calculating this energy by a process similar to that used to obtain surface energies, Eq. 14 would result, since the repeat distance along **L** multiplied by the inter-**L** direction spacing is v/h_L. Similarly, Eq. 15 gives the "surface" energy per atom of a row **L**, the "surface" being created by separating the row into two halves. These interpretations of ε_L and ε_K could have been used to derive Eqs. 14 and 15. For example, two isolated parallel ledges can be created on the surface by separating the topmost plane into two half-planes, while keeping the half-planes at the same distance from the next plane. Eq. 14 would then result for the energy of an isolated ledge, per unit length. It is then apparent that the energies γ_T, ε_L and ε_K obtained from

Eqs. 13-15 are exact for the isolated or "pure" terraces, ledges and kinks, respectively. If those energy values are used to calculate energies of surfaces of any orientation, an error will result, which increases as the density of ledges and kinks increases, and, as will be shown below, as the atomic density in terraces and ledges decreases. An evaluation of these errors will be described in the following sections.

4 – APPLICATION TO F. C. C. CRYSTALS, MYE POTENTIALS

Taking a orthormal basis e_1, e_2, e_3, with $|e_i| = 1$, parallel to the cube edges of a f. c. c. cell, the general form of n is

$$n = \frac{a}{2} \sum_i n_i \, e_i \; ; \quad \sum_i n_i = \text{even integer} \tag{16}$$

where the n_i are integers with an even sum and a is the lattice parameter. For a plane with Miller indices $(p_1 \, p_2 \, p_3) = (p)$ we have

$$d = \frac{a}{p} \; ; \quad P = \frac{1}{p} \sum_i p_i \, e_i \; ; \quad p^2 = \sum_i p_i^2 \tag{17}$$

provided the p_i are chosen as all odd (coprime) integers or all even integers (g. c. d. equal to 2). The indices $[l_1 \, l_2 \, l_3]$ of a lattice direction are chosen such that their sum is even; the repeat distance i_L along the direction is given by

$$i_L = \frac{a}{2} \, l \qquad l^2 = \sum_i l_i^2 \tag{18}$$

The interaction energy between two atoms will be described by a Mye potential $e \,|\, e'$:

$$\varepsilon (\rho) = \varepsilon_0 \left[\left(\frac{\sigma}{\rho} \right)^{e'} - \left(\frac{\sigma}{\rho} \right)^{e} \right] \, , \; e < e' \tag{19}$$

with e, e′ = 6, 9 and 12; ε_0 can be related to the cohesive energy per atom in the crystal, ε_c, and σ to the near-neighbour distance, r_0 (see Table 1 in ref. 7). Eqs. 9 and 13 for the surface energies take the form that has been derived in ref. 7.

The ledge energy (eq. 14) becomes

$$\varepsilon_L = \frac{\sqrt{2}}{t\,u}\,\frac{\varepsilon_0}{r_0}\,(\,\sigma^{*e'}\,\Delta_{e'} - \sigma^{*e}\,\Delta_e\,) \tag{20a}$$

where

$$\sigma^* = \sqrt{2}\,\frac{\sigma}{r_0}\;;\quad u^2 = \sum_i u_i^2\;;\quad t^2 = \sum_i t_i^2 \tag{20b}$$

and

$$\Delta_e = \sum_n \frac{m}{n^e} \tag{20c}$$

with

$$m = 1/2 \sum_i n_i\,u_i > 0\;;\quad \sum_i n_i\,t_i = 0\;;\quad n^2 = \sum_i n_i^2 \tag{20d}$$

The u_i are the indices of the lattice direction parallel to **U**.

For the energy of a kink we obtain from eq. 15

$$\varepsilon_K = \frac{\varepsilon_0}{l^2}\,(\,\sigma^{*e'}\,\Psi_{e'} - \sigma^{*e}\,\Psi_e\,)\;;\quad l^2 = \sum_i l_i^2 \tag{21a}$$

where

$$\Psi_e = \sum_n \frac{m'}{n^e} \tag{21b}$$

with

$$m' = 1/2 \sum_i n_i\,l_i > 0\;;\quad \sum_i n_i\,t_i = \sum_i n_i\,u_i = 0\;;\quad n^2 = \sum_i n_i^2 \tag{21c}$$

l_i are the indices of the direction of the ledges. The sum Ψ_e can be written in a simpler form. Since n is parallel to **L** and $n \cdot \mathbf{L} > 0$ we write

$$n_i = k l_i \qquad k \geqslant 1$$

where k is an integer. This leads to

$$\Psi_e = 1/2\,l^{2-e}\,\sum_{k \geqslant 1} \frac{1}{k^{e-1}} = 1/2\,l^{2-e}\,\phi_e \tag{22}$$

The actual calculation of the lattice sums Δ_e and Ψ_e is discussed in the Appendix.

5 — RESULTS

5.1 — *Ledge and Kink Energies*

Ledge and kink energies were calculated for f. c. c. Lennard-Jones crystals (potentials 6 | 9, 6 | 12 and 9 | 12) by the method described in the Appendix with M = 10 and k_0 = 10, respectively. Values of the calculated ledge energies are indicated in Table 1,

TABLE 1 — Ledge energies (ε_c / r_0 units)

Terrace	Ledge	Ledge energy		
		6 | 9	6 | 12	9 | 12
(111)	[1$\bar{1}$0]	0.1467	0.1500	0.1566
	[11$\bar{2}$]	0.1594	0.1658	0.1785
(002)	[110]	0.1075	0.1038	0.0962
	[200]	0.1179	0.1188	0.1207
	[130]	0.1208	0.1202	0.1192
(022)	[01$\bar{1}$]	0.0376	0.0299	0.0145
	[200]	0.0526	0.0536	0.0555
	[21$\bar{1}$]	0.0548	0.0537	0.0513
	[22$\bar{2}$]	0.0531	0.0494	0.0421
(113)	[1$\bar{1}$0]	0.0184	0.0138	0.0044
	[12$\bar{1}$]	0.0397	0.0413	0.0443
	[03$\bar{1}$]	0.0371	0.0368	0.0361

in ε_c/r_0 units. The values are fairly similar for the three potentials. These data also show the effect of the associated terraces on the ledge energy. The ledge energy tends to decrease as the atomic density in the associated terrace decreases.

Table 2 gives the energy of kinks located in the more close packed ledges, in ε_c units. The energies are again not too different for the three potentials used and decrease as the atomic density in the ledge decreases.

TABLE 2 — Kink energies (ε_c units)

Ledge	Kink energy × 10		
	6 | 9	6 | 12	9 | 12
[011]	0.5447	0.6101	0.7409
[002]	0.1980	0.1665	0.1034
[112]	0.0683	0.0520	0.0195
[013]	0.0161	0.0114	0.0021
[222]	0.0095	0.0066	0.0010

Surface energies, γ, including terraces energies, γ_T, were calculated in the preceding paper [7]; they are shown in Table 2 of that paper.

The method that we use to calculate the lattice sums is quite accurate. It is described in the Appendix. For example, when the number of terms in the direct sums is increased by changing M from 10 to 15 (respectively $\sim 10^3$ and $\sim 15^3$ terms in the direct sums), the resulting relative change in ε_L is at most 10^{-3} for the 6 | 9 and 6 | 12 potentials and at most 10^{-4} for the 9 | 12 potential. A similar precision can be obtained for ε_K and γ_T (cf. ref. 7).

5.2 – Applicability of the TLK Decomposition

From a purely geometrical point of view, the TLK decomposition can be applied to any orientation of the surface and for any choice of the terraces and ledges. However, the surface energy calculated from eq. 8 using the energies of "pure" terraces and ledges of the same crystallography as that of the actual terraces and ledges, may deviate more or less from the true surface energy.

This is because, as the ledges become closer or the kink spacing decreases, the actual contribution of ledges and kinks to the surface energy will change, since they will interact with each other.

A first method for assessing the accuracy of the TLK decomposition is to compare the actual surface energies (see ref. 7) with those calculated by the TLK equation (eq. 8). Examples are given in Table 3 for planes vicinal to (002) and containing [1$\bar{1}$0]

TABLE 3 — Surface energies by TLK and by direct sum of planes
with (002) terraces

Plane	Surface energies (ε_c / r_0^2 units) *					
	6 | 9		6 | 12		9 | 12	
113 [a]	0.5115	*0.5172*	0.4678	*0.4717*	0.3803	*0.3805*
024 [b]	0.5163	*0.5238*	0.4758	*0.4811*	0.3951	*0.3955*
115 [a]	0.5166	*0.5176*	0.4710	*0.4717*	0.3799	*0.3799*
2 2 50 [a]	0.5016	*0.5025*	0.4556	*0.4563*	0.3635	*0.3640*
2 2 100 [a]	0.4979	*0.4980*	0.4520	*0.4520*	0.3601	*0.3601*
0 2 40 [b]	0.5015	*0.5016*	0.4558	*0.4559*	0.3644	*0.3644*
0 2 100 [b]	0.4971	*0.4971*	0.4513	*0.4513*	0.3597	*0.3597*
2 4 50 [a]	0.5069	*0.5069*	0.4611	*0.4611*	0.3694	*0.3694*
4 6 50 [a]	0.5122	*0.5123*	0.4664	*0.4665*	0.3747	*0.3747*
2 6 50 [b]	0.5113	*0.5115*	0.4658	*0.4659*	0.3747	*0.3747*
4 6 20 [a]	0.5202	*0.5231*	0.4760	*0.4779*	0.3874	*0.3875*

* The values in italic were obtained by direct sum.

a — [1$\bar{1}$0] ledges; b — [200] ledges.

or [200] ledges. The TLK values are calculated from eq. 8 using the energy contributions of ledges and kinks given in Tables 1 and 2 and the values of γ_T obtained in the preceding paper for (002). The correct values are written in italic; they are always larger than the TLK values. The agreement is excellent, even for planes deviating as much as ~25° from (002), for which the ledge separation is of the order of r_0 .

Table 4 refers to the errors in different TLK decompositions of the (6 8 10) plane, which makes similar angles with (002), (022) and (111). The smallest error among the various decompositions is always smaller than 1 %. Of course better descriptions, leading to smaller errors, would be possible for the (6 8 10) plane, including one in terms of (6 8 10) terraces for which the error would be zero.

TABLE 4 — Effect of the TLK decomposition on calculated surface energy of (6 8 10) plane

Terrace	Ledge	Θ_T (degrees)	Θ_L (degrees)	γ (ε_c / r_0^2 units)		
				6 | 9	6 | 12	9 | 12
(111)	[1$\bar{1}$0]	28.61	7.59	0.5139	0.4712	0.3856
(002)	[1$\bar{1}$0]	26.57	8.13	0.5143	0.4715	0.3859
(022)	[200]	27.69	35.26	0.5058	0.4652	0.3839
(022)	[21$\bar{1}$]	27.69	0	0.5054	0.4649	0.3839
(6 8 10)*	—	0	—	0.5222	0.4769	0.3862

* Direct sum.

An alternative method of showing the accuracy of the TLK values consists of plotting the correct surface energies of a family of planes containing (only) ledges of a given type and terraces of a given type, as a function of the angle between the plane and the terraces, Θ_T. From eq. 8 (with $\Theta_L = 0$)

$$\frac{\gamma}{\cos \Theta_T} = \gamma_T + \frac{\varepsilon_L}{h_L} \, tg \, \Theta_T \tag{23}$$

Fig. 3a shows a plot $\gamma/\cos \Theta_T$ as a function of $tg \, \Theta_T$ for planes vicinal to (002) and containing [110] ledges. Similarly, Fig. 3b applies to (002) terraces and [200] ledges. The curves are very nearly linear, deviating from linearity only at large angles. For (113) with $\Theta_T \simeq 25°$, the difference between the two terms of eq. 23 is at most 1 % (for the 6 | 9 potential).

A direct calculation of the error in the TLK equation is also possible. The method consists of comparing the correct eq. 12 with the TLK equation (eq. 8), in which the energies γ_T, ε_L, ε_K are calculated from eqs. 13-15. Consider, for example, the terrace term in the two equations. The difference results from the fact that in
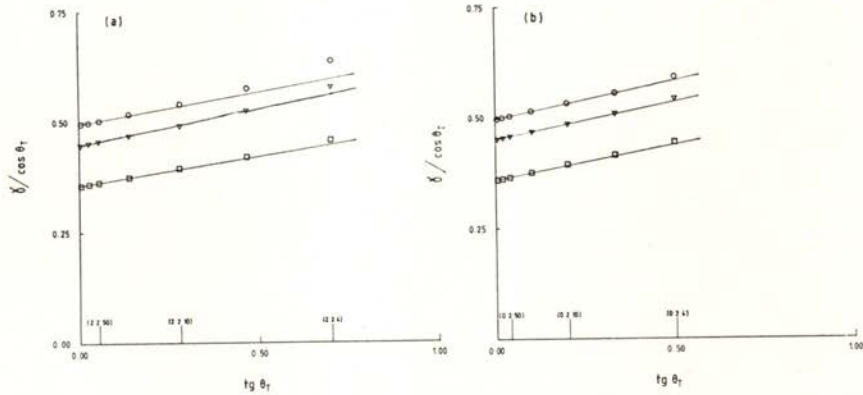
Fig. 3 — Variation of surface energy with orientation (Θ_T) for planes vicinal to (002): (a) in the [1$\bar{1}$0] zone, [1$\bar{1}$0] ledges; (b) in the [200] zone, [200] ledges. The surface energy is in $_c/r_0^2$ units. Potentials: $\bigcirc$ - 6 | 9; $\triangledown$ - 6 | 12; $\square$ - 9 | 12.

the TLK equation the atoms that enter in the lattice sum are those with $\mathbf{n} \cdot \mathbf{T} > 0$, whereas in the correct equation all atoms with $\mathbf{n} \cdot \mathbf{P} > 0$ are considered. The following result for the difference between the two sums is easily obtained, noting that for any atom $\mathbf{n}$ there is an atom $-\mathbf{n}$:

$$\sum_{\mathbf{n} \cdot \mathbf{T} > 0} (\mathbf{n} \cdot \mathbf{T})\, \varepsilon\,(\mathbf{n}) - \sum_{\mathbf{n} \cdot \mathbf{P} > 0} (\mathbf{n} \cdot \mathbf{P})\, \varepsilon\,(\mathbf{n}) = 2 \sum_{\substack{\mathbf{n} \cdot \mathbf{T} > 0 \\ \mathbf{n} \cdot \mathbf{P} < 0}} (\mathbf{n} \cdot \mathbf{T})\, \varepsilon\,(\mathbf{n}) +$$

$$\sum_{\substack{\mathbf{n} \cdot \mathbf{T} > 0 \\ \mathbf{n} \cdot \mathbf{P} = 0}} (\mathbf{n} \cdot \mathbf{T})\, \varepsilon\,(\mathbf{n}) \qquad (24)$$

The first sum in the right-hand side is for all atoms in a wedge formed by the two planes $\mathbf{P}$ and $\mathbf{I}$: this term has a factor 2. The other sum is for atoms in the plane $\mathbf{P}$ to one side of its inter-

section with T. The difference (24) is expected to be always negative thus explaining why the TLK surface energies are always smaller than those obtained by direct sum. The error in the other terms can be obtained by similar equations.

6 — DISCUSSION

The fundamental equations derived in this paper are the equation for the surface energy in terms of contributions of the energies of terraces, ledges and kinks, and the lattice sums that give the specific energies of terraces, ledges and kinks.

As already noted, from a purely geometrical point of view, any TLK decomposition of a surface of arbitrary orientation is legitimate. From the point of view of energy, however, the TLK decomposition leads to an error which, in broad terms, increases as the spacing of ledges and the spacing of kinks decreases, and, on the other hand, as the atomic densities in terraces and ledges decrease.

The energy per unit area of a surface obtained from eq. 8 is always larger than the terrace specific energy. This points to the conclusion that the terraces should be chosen as planes for which pointed cusps occur in the γ-plots. These are in fact the more closed packed planes. In the f. c. c. crystals studied (Mye potentials) these planes are (111), (002) and (022). For similar reasons the ledges should be taken along directions, in each of these planes, corresponding to cusps in the ε_L-plot for that plane. Calculations show that these cusps occur in $<1\bar{1}0>$ and $<1\bar{1}2>$ directions in the (111) plane, in $<1\bar{1}0>$ and $<200>$ directions in the (002) planes and in $<01\bar{1}>$ and $<200>$ directions in (022) planes. Decompositions using such terraces and ledges are therefore those compatible with the observed cusps in the γ-and ε_L-plots.

A problem that can be raised concerns the range of applicability of the TLK decomposition using these low index terraces and ledges, and more generally any other set of terraces and ledges. The problem can be solved by finding the region in the stereographic triangle corresponding to planes for which the error in the TLK equation is smaller than a given amount, e. g. 1 %. Our calculations show that for the three more close packed terraces

and for the two more close packed ledges in each of these planes, the error for the best TLK decomposition is at most ~1 %.

Clearly, the accuracy of the TLK decomposition of energy depends on the type of potential, particularly on its range. As the results (of Table 3, for example) show, the accuracy decreases as the ranges of the attractive and repulsive terms in the potential increase.

The analogy with the coincidence site lattice (c. s. l.) model of grain boundaries is worth a few comments. Formally any grain boundary can be described in terms of a reference c. s. l. boundary where a certain distribution of grain boundary dislocations is introduced. The good descriptions are those for which the dislocations are widely spaced, although a more sound test would be in terms of an energy criterion. For example, one could decompose the energy per unit area of any grain boundary as a sum of the energy of the c. s. l. boundary with terms due to the families of grain boundary dislocations [9]. The energy so calculated could be compared with that obtained directly, e. g. by computer calculations, and the error used as a test to the applicability of the model. Unfortunately, it is not easy to obtain the energy terms associated to the dislocations, and the range of applicability of the c. s. l. model has so far been evaluated simply from the spacing of the dislocations [e. g. 10].

APPENDIX — CALCULATION OF LATTICE SUMS FOR LEDGE AND KINK ENERGIES

The sum Δ_e (eq. 20c) is calculated term by term up to

$$n_1^2 + n_2^2 + n_3^2 \leqslant M^2$$

and the number, N, of atoms (terms) in the sum is counted. These atoms are within a half-circle in the plane (t), limited by a row [l] and centred in an atom 0_0 in that row (see Fig. 6 of preceding paper). The half-circle is in the half-plane C and its radius $R_0 a/2$ is given by

$$\frac{\pi}{2} R_0^2 - \frac{t}{2 l} R_0 = N t$$

since the area per atom in (t) is ($a^2/4$) t. The subtractive term corresponds to a rectangular region adjacent to the diameter through 0_0 , of thickness equal to one-half of the interrow spacing, which is ($a/2$)·(t/l); no atom centres occur in this region. The rows [l] in C, outside the semi-circle, are replaced by continuous layers of thickness equal to the interrow spacing and centred in each row, and with an atomic density equal to $4/(a^2t)$. The region outside the half-circle is the difference between: (i) the area of the half-plane C outside the circle; (ii) a layer of thickness ($a/4$) (t/l) adjacent to the diameter of the semi-circle and outside it.

The integrals that give the rest of the sum Δ_e are calculated in polar coordinates: ρ (in $a/2$ units), Θ. They have the form

$$\frac{1}{t} \frac{t}{l} \iint \frac{\rho \cos \Theta}{\rho^e} \rho\, d\Theta\, d\rho$$

since the number of rows m is

$$m = \rho \frac{t}{l} \cos \Theta$$

For the integral over region (i) defined above, the integration limits are: ρ (R_0 , ∞), Θ (0 , $\pi/2$) leading to

$$\Delta'_e = [\, l\, (e - 3)\, R_0^{e-3}\,]^{-1}$$

For the integral over region (ii), the integration limits are: ρ (R_0 , $t/(2l\cos \Theta)$), Θ ($\cos^{-1} t/(2lR_0)$, $\pi/2$). Using the approximation $\cos \Theta \simeq \pi/2 - \Theta$, we obtain

$$\Delta''_e = \frac{t^2}{l^3} \frac{1}{8\, (e - 1)} \frac{1}{R_0^{e-1}}$$

The value of Δ_e is

$$\Delta_e = \sum_{n \leq M} \frac{m}{n} + \Delta'_e - \Delta''_e$$

178

Portgal. Phys. — Vol. 16, fasc. 3-4, pp. 161-179, 1985

The series ϕ_e (eq. 22) is calculated directly up to $k = k_0$. The rest of the sum is

$$\phi'_e = \int_{k_0+1/2}^{\infty} \frac{dk}{k^{e-1}} = [\,(e-2)\,(k_0+1/2)^{e-2}\,]^{-1}$$

REFERENCES

[1] W. KOSSEL, *Nachr. Ges. Wiss. Göttingen*, 135 (1927).

[2] O. KNACKE and I. N. STANSKI, *Progr. in Met. Phys.*, 6, 181 (1956).

[3] J. P. HIRTH and G. M. POUND, *J. Chem. Phys.*, 26, 1216 (1957).

[4] T. SUREK, G. M. POUND and J. P. HIRTH, *J. Chem. Phys.*, 55, 5157 (1971).

[5] W. K. BURTON, N. CABRERA and F. C. FRANK, *Phil. Trans. Roy. Soc. London*, A243, 299 (1950).

[6] P. WYNBLATT, in *Interatomic Potentials and Simulation of Lattice Defects*, eds. P. C. Gehlen, J. R. Beeler and R. I. Jaffee (Plenum, New York, 1972), p. 633.

[7] J. BRITO CORREIA and M. A. FORTES, *Portgal. Phys.*, preceding paper.

[8] P. W. TASKER and D. M. DUFFY, *Surface Sci.*, 137, 91 (1984).

[9] R. W. BALLUFFI, A. BROKMAN and A. H. KING, *Acta Metall.*, 30, 1453 (1982).

[10] M. A. FORTES, *Portgal. Phys.*, 15, 143 (1984).

CHARGE DENSITY STUDY OF V F$_2$

M. J. M. DE ALMEIDA and M. M. R. COSTA

Centro FCI, INIC, Departamento de Física, Univ. de Coimbra, 3000 Coimbra, Portugal

ABSTRACT — X-ray diffraction data from two single crystals of VF$_2$, obtained with two different wavelength radiations, Ag-Kα and Mo-Kγ, are compared in this paper.

The corrections applied to the observed data and the reproducibility of the results are analysed. The main features of the electron density in this compound are discussed in terms of Fourier difference maps.

1 – INTRODUCTION

The study of rutile type structures has been undertaken in our Laboratory in order to investigate the main features of the electron density of these compounds.

Previous results of X-ray diffraction from a single crystal of VF$_2$ (crystal I) at room temperature have already been reported [1]. These were based on intensity data collected on a CAD4 diffractomer at the Enraf-Nonius, Delft, using Mo-Kα radiation. In order to test the reproducibility of these results, the data collection was repeated in our Laboratory under identical conditions, using the same crystal and the same type of radiation.

The corrections applied to the observed data were those described in reference [1]. Position and temperature parameters (Table 1) were refined from a set of 190 independent reflection intensities, using a least-squares technique. Comparison with similar parameters obtained from the previous data set showed that:

i) the position of the fluorine atom agrees within the experimental error;

ii) the anisotropic temperature parameters agree within 2 standard deviations;

iii) difference Fourier maps, $(\rho_{obs} - \rho_{calc})$, evidence similar features.

Similar experiments were carried out on a second crystal (II) with different dimensions; in this case, two wavelengths were used, in order to investigate the extinction effects, as will be discussed.

2 – DATA COLLECTION

A single crystal of VF$_2$ (cristal II) with prismatic shape and approximate dimensions (0.06 × 0.07 × 0.12) mm^3 was selected from a large single crystal (from which specimen I had been cut) and used in the present work.

The lattice parameters were determined using the standard technique developped for X-ray diffractometry, as:

$$a = b = (4.806 \pm 0.010) \text{ Å} , \; c = (3.237 \pm 0.007) \text{ Å} .$$

Two independent experiments (A and B) were performed on a CAD4 four-circle diffractometer using Ag-Kα and Mo-Kα radiations, respectively. This was suggested by a comparison of data obtained from crystals I and II: no evidence for extinction was found when Ag-Kα radiation was diffracted by crystal II; however, when crystal I, which is significantly smaller [1], was irradiated with a longer wavelength radiation (Mo-Kα), some degree of extinction was detected as will be mentioned later.

Experiment B (Mo-Kα) was hence carried out as an attempt to decide whether this effect should be attributed to the difference in wavelength of the incident beam or to a distinct mosaic spread in crystals I and II.

---

[1] The volume ratio for both crystals is $V_{II} / V_I = 2.5$.

Integrated intensities of reflections out to $(\sin \Theta)/\lambda = 1.02$ Å⁻¹ in experiment A and $(\sin \Theta)/\lambda = 1.08$ Å⁻¹ in experiment B were measured in $\omega - 2\Theta$ scans. Each reflection hkl was considered to be "observed" only if the corresponding integrated intensity, I_{hkl}, was such that $I_{hkl} > 3 \sigma_{hkl}$, σ_{hkl} being the standard deviation of I_{hkl}.

For each hkl, up to 16 symmetry-equivalent reflections were measured in order to correct for absorption of the beam inside the crystal.

A set of 1361 reflections were observed in experiment A and 1895 in experiment B. These will be referred to as sets A and B, respectively.

A few reflection intensities (five in experiment A and eight in B) were periodically measured and used as a standard against which all the other intensities were checked.

A plot of the standard intensities against time of measurement showed that their variation was in all cases smaller than 0.03 %.

3 – DATA ANALYSIS

Integrated intensities in sets A and B were corrected in the usual way for Lorentz and polarization effects [1]. Two different absorption corrections were calculated:

i)   one which is based on the observed shape of the crystal from which the pathlengths of the incident and diffracted beams inside the crystal are derived;

ii) an empirical correction suggested by North et al. [2], which is based on the intensity variation for a few reflections occurring at high χ-angles ($70° < \chi < 90°$) when the crystal is rotated around the scattering vector.

The latter method was found to yield the best agreement between the intensities of equivalent reflections; hence, the empirical absorption correction was applied to the data in both sets.

Least squares refinements including the 143 independent reflections of set A and 212 of set B were carried out. A plot

of the calculated structure factors against the observed ones placed on the same scale (Fig. 1 a)) showed that a few reflections

Fig. 1 a) — Plot of SF$_0$ against F$_c$ for crystal II (Mo-Kα radiation)

- • before the extinction correction
- * when an extinction correction is applied (only reflections significantly affected by extinction are represented)

of data set B were affected by extinction; this is indicated by the deviation of the curve from a straight line.

No evidence for extinction was found in data set A (Fig. 1 b)). An extinction parameter was hence included in the refinement carried out for set B and the corresponding correction applied to these data.
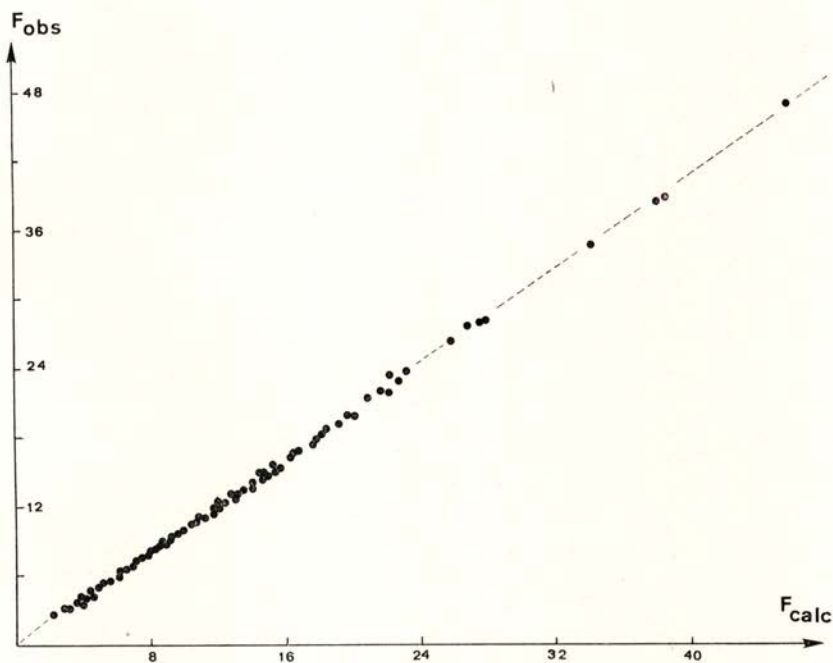
Fig. 1 b) — Plot of SF$_o$ against F$_c$ for crystal II (Ag-Kα radiation)

According to Stevens and Coppens [3] a refinement based on high order reflection data should yield a more reliable value for the scale factor, S. In fact the low angle reflections are the most likely to be affected by extinction and asphericity in the electron distribution; therefore, their inclusion in a refinement is liable to mask the results.

Hence, a second refinement was carried out, based on reflections with (sin Θ)/λ > 0.6 Å^{-1}, already corrected for extinction. The results are shown in Table 1; the scale factors can be compared

with those obtained from a refinement including all the reflections, namely:

$$S_I \, (\text{Mo-K}\alpha) = 0.1924(7) \, , \quad S_{II} \, (\text{Ag-K}\alpha) = 0.2124(8) \, ,$$
$$S_{II} \, (\text{Mo-K}\alpha) = 0.1007(7)$$

TABLE 1

Parameter	Crystal I (Mo-Kα)	Crystal II (Mo-Kα)	Crystal II (Ag-Kα)
Atom: V			
$\beta_{11} = \beta_{22}$	0.00549 (3)	0.00528 (2)	0.00565 (4)
β_{33}	0.01073 (11)	0.01001 (10)	0.01037 (17)
β_{12}	−0.00005 (4)	−0.00065 (12)	−0.00076 (28)
Atom: F			
x	0.30509 (15)	0.30533 (10)	0.30536 (20)
$\beta_{11} = \beta_{22}$	0.01054 (14)	0.01038 (9)	0.01088 (16)
β_{33}	0.01609 (48)	0.01522 (32)	0.01397 (46)
β_{12}	−0.00993 (44)	−0.00961 (38)	−0.00965 (59)
g	$(1.12 \pm 1.05) \times 10^{-5}$	$(0.955 \pm 0.144) \times 10^{-6}$	
S	0.1936 (7)	0.0998 (5)	0.2174 (10)
R	0.014	0.007	0.017
R_w	0.015	0.012	0.023

An attempt was also made to measure the absolute scale experimentally. It is well known that the integrated intensity of any reflection (E ω) is related to the absolute value of the corresponding structure factor, F_{abs} :

$$(E \, \omega) = S \, | F_{abs} |^2$$

where

$$S = I_0 \, N^2 \, \lambda^3 \left(\frac{e^2}{mc^z} \right)^2 V_c$$

where I_0 is the intensity of the primary beam, N the number of unit cells per unit volume, λ the wavelength of the incident radiation, V_c the volume of the crystal used in the experiment and the remaining symbols have their usual meaning.

The measurement of I_0 was carried out using a method developped in our Laboratory [4] in which the use of absorbers is avoided; the dead time of the detector was measured and the corresponding correction applied to I_0.

Values of 0.2310 and 0.09675 were obtained for sets A and B, respectively. The estimated accuracy in S is of the order of 4 %; the main source of error (which may have been overestimated) is the determination of the crystal volume, V_c. This was calculated by careful observation of its shape and measurement of the length of its edges under a powerful microscope. The origin of the error in I_0 (~ 1 %) is the unhomogeneity of the beam in the region occupied by the crystal; the dead time of the counter was measured with a precision better than 2 %.

In either case the experimental value of S was found to be closer to the value obtained from refinement of high order data.

Final structure factors (F_{calc}) were calculated for reflections in sets A and B, using the parameters obtained from the latter refinement and assuming spherical distributions of the atomic electrons.

4 – FOURIER DIFFERENCE MAPS

Fourier analysis of the differences ($S F_{obs} - F_{calc}$) enabled difference density maps to be drawn for two sections of the unit cell, namely [001] and [1$\bar{1}$0]. These are shown on Figs. 2 a), b) and 4 a), b) for crystal II and on Figs. 6 a), b) for crystal I. The results of Fourier syntheses of the corresponding standard deviations can be seen in Figs. 3, 5 and 7, which show that the error is only significant at or near the atomic sites. On each map one curve corresponds to $0.17 \, e/Å^3$.

A few significant features can be observed in all maps:

  i) a positive density near the vanadium sites along the directions joining two vanadium atoms (which are second nearest neighbours) on the z = 0 plane;
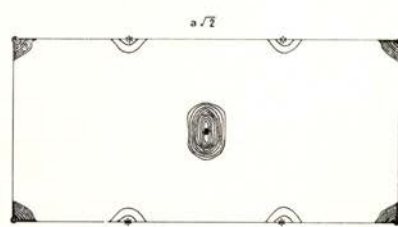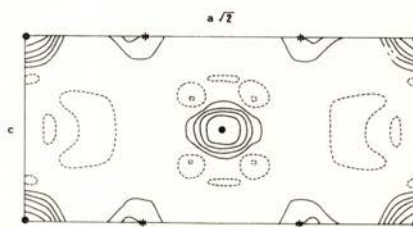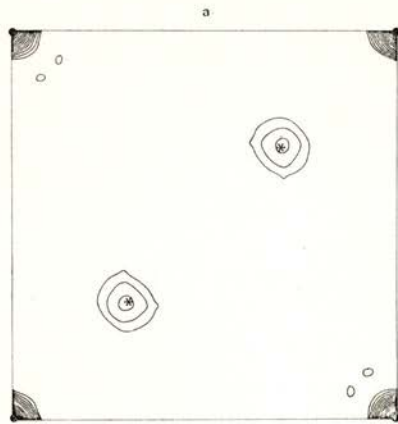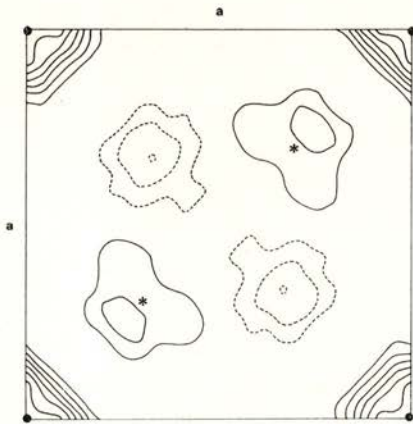
Fig. 2 a) e b)

Fig. 3 a) e b)
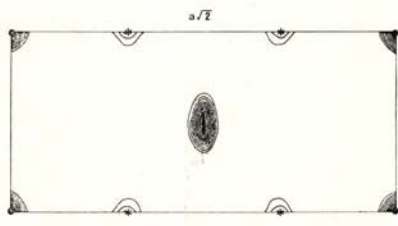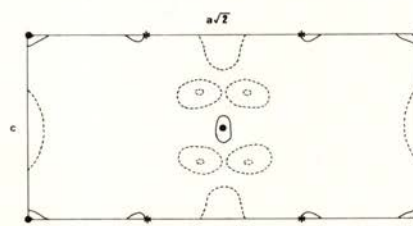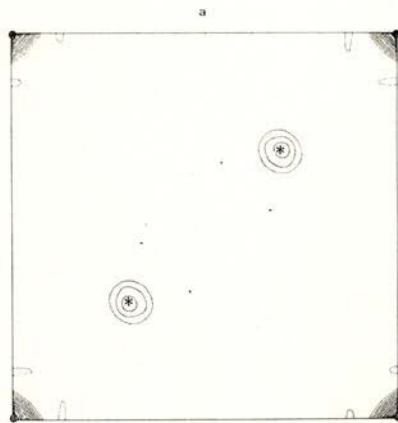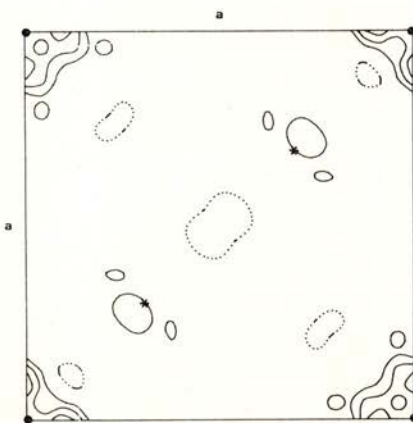
Fig. 4 a) e b)

Fig. 5 a) e b)
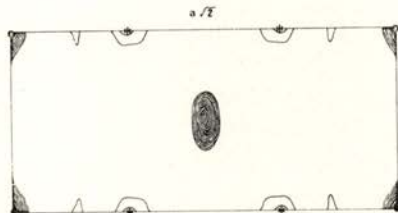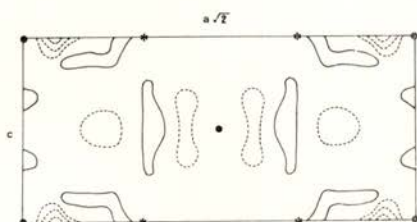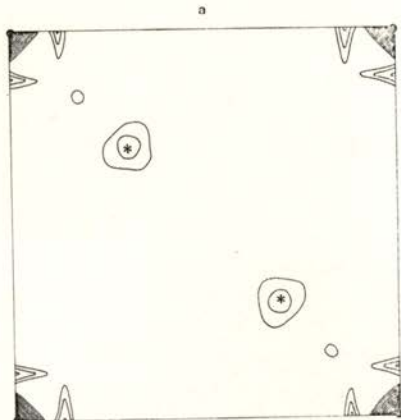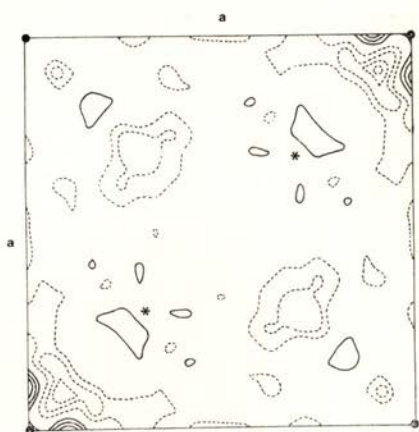
Fig. 6 a) e b)

Fig. 7 a) e b)

Fig. 2 — Fourier difference maps, SF_o-F_c, for crystal II (Ag-Kα radiation). Contour levels at 0.17 e/Å^3. Broken lines represent negative contours.
● : position of V atoms; * : position of F atoms
a) Section [001] of the unit cell; b) Section [1$\bar{1}$0] of the unit cell

Fig. 3 — Fourier maps representing the distribution of errors, for crystal II (Ag-Kα radiation). Contour levels at 0.17 e/Å^3.
a) Section [001] of the unit cell; b) Section [1$\bar{1}$0] of the unit cell

Fig. 4 — Fourier difference maps, SF_o-F_c, for crystal II (Mo-Kα radiation). Contour levels at 0.17 e/Å^3.
● : position of V atoms; * : position of F atoms
a) Section [001] of the unit cell; b) Section [1$\bar{1}$0] of the unit cell

Fig. 5 — Fourier maps representing the distribution of errors, for crystal II (Mo-Kα radiation). Contour levels at 0.17 e/Å^3.
a) Section [001] of the unit cell; b) Section [1$\bar{1}$0] of the unit cell

Fig. 6 — Fourier difference maps, SF_o-F_c, for crystal I (Mo-Kα radiation). Contour levels at 0.17 e/Å^3.
● : position of V atoms; * : position of F atoms
a) Section [001] of the unit cell; b) Section [1$\bar{1}$0] of the unit cell

Fig. 7 — Fourier maps representing the distribution of errors, for crystal I (Mo-Kα radiation). Contour levels at 0.17 e/Å^3.
a) Section [001] of the unit cell; b) Section [1$\bar{1}$0] of the unit cell

ii) a positive density near the fluorine sites delocalised towards the vanadium atom;

iii) a negative density across the line joining the vanadium atom at the center of the unit cell and the fluorine atoms on the XY planes above and below.

Assuming that only the 3 d electrons of the transition element contribute to the observed difference densities, $\rho_{obs} - \rho_{calc}$, an attempt will be made to deduce from these the degree of asphericity in the distribution of such electrons.

REFERENCES

[1] COSTA, M. M. R. and DE ALMEIDA, M. J. M., *Portgal. Phys.*, 14, 71 (1983).

[2] NORTH, A. C. T., PHILLIPS, D. C. and MATHEWS, F. S., *Acta Cryst.* A 24, 351 (1968).

[3] STEVENS, E. D. and COPPENS, P., *Acta Cryst.* A 31, 612 (1975).

[4] ANDRADE, L. C. R., COSTA, M. M. R. and DE ALMEIDA, M. J. M., Proceedings of "I Simpósio Ibérico de Física da Matéria Condensada", Lisboa, 1983.

MAGNETORESISTIVITY IN MAGNETIC METALS
Theoretical principles and a high accuracy method

J. B. Sousa, J. M. Moreira

Centro de Física da Universidade do Porto, 4000 Porto, Portugal

ABSTRACT — The paper reviews basic physical mechanisms underlying magnetoresistivity in normal and magnetic metals. It describes an experimental high accuracy system implemented in our laboratory and discusses some typical results of magnetoresistivy measurements in magnetic metals; brief comments on their interpretation are also presented.

1 – INTRODUCTION

When a magnetic field **H** is applied to a metal, small changes occur in the value of the electrical resistivity, originating the so called magnetoresistivity coefficient at temperature T,

$$\Delta\rho/\rho = [\,\rho\,(\,T\,,\,H\,) - \rho\,(\,T\,,\,0\,)\,]\,/\,\rho\,(\,T\,,\,0\,) \qquad (1)$$

In a non-magnetic metal the change in resistivity is caused essentially by the curvature of the electron trajectories produced by the magnetic field (Lorentz force) [1-3]. The magnetoresistance then increases with the sample purity (larger electron mean free paths), as confirmed by experiment.

In a magnetic metal, besides the curvature effect (normal magnetoresistivity), two extra contributions are usually observed in $\Delta\rho/\rho$.

Taking a simple ferromagnetic metal with localized magnetic moments m_i below the Curie point ($T < T_c$), the first extra contribution arises from an *orientational* effect of **H** in the spontaneous magnetization (M_s), as the scattering of an electron (wavevector **k**) with a magnetic ionic moment m_i usually depends on the angle between **k** and m_i [4, 5]. Since the thermal average $< m_i >$ has a definite direction in each magnetic domain, the

Portgal. Phys. — Vol. 16, fasc. 3-4, pp. 191-220, 1985

191

change of such directions produced by the applied field slightly modifies the intrinsic electric resistivity of each domain, therefore the sample resistivity. This effect is easy to observe in soft magnetic metals, for which M_s rotates easily under the application of H (low magnetic anisotropy).

Besides this orientational effect, the field H also reduces the (thermal) spin fluctuations in the system. The resulting increase in the magnetic order usually produces a decrease in the electrical resistivity (fluctuation effect) (*). This magnetoresistivity should be bigger in the vicinity of a magnetic transition point, where the spin fluctuations dominate [5, 6].

Magnetoresistance data can be usually related to fundamental aspects of the electronic and/or magnetic structure of the metal under investigation.

In normal metals, direct information can be obtained on the Fermi surface structure (open and closed electron orbits; shape and connectivity) when the measurements are performed at low temperatures and in high purity samples [2, 7, 8].

In magnetic metals, magnetoresistivity measurements enable the study of fairly diverse problems, ranging from magnetic anisotropy constants [11] and spin reorientation transitions [12], to critical phenomena and corresponding exponents near the Curie or Néel transition points [13]; when magnetic interactions compete, magnetoresistance studies may give fairly detailed information on the succession of different magnetic structures under the application of an increasing magnetic field [14, 15].

The magnetoresistivity effects are usually fairly small, both in normal and magnetic metals, corresponding to variations in the electrical resistivity of the order of $10^{-10} - 10^{-11}$ Ω.m per 10^6 Am^{-1} applied field (corresponding to B ~ 1 Tesla). The smallness of the effect puts stringent conditions on the experimental technique, and corresponding accuracy, particularly for detailed studies of the structure of $\Delta\rho/\rho$ curves, either as a function of H or temperature.

In section 2 of this paper a brief account is presented on the basic physical mechanisms underlying the behaviour of the magnetoresistivity in normal and magnetic metals. In section 3

(*) In ferromagnetic metals with large conduction electron wavelengths, the increase in magnetic order may produce an *increase* in ρ, due to coherence effects in the electron scattering by different magnetic moments [9, 10].

we describe in detail an experimental system implemented to measure $\Delta\rho/\rho$ with great accuracy, with an automatic recording unit. In section 4 we present various applications of the magnetoresistivity measurements in magnetic metals, making brief comments on the physical information provided in each case.

2 — PHYSICAL ORIGIN OF THE MAGNETORESISTIVITY

2.1 — *Phenomenological equations*

Normal metals

In general, the electrical fields causing transport phenomena are sufficiently weak to be valid a linear approximation,

$$E_i = \rho_{ik} \, j_k \tag{2}$$

between the components E_i of the electrical field (**E**) and the components j_k of the electrical current density (**j**). The quantities ρ_{ik} define the generalized electrical resistivity tensor for the material under consideration. Isothermic conditions are assumed here and repetition of the k-index indicates a sum over the values (1, 2, 3). In the presence of an internal magnetic induction (**B**) caused by the applied magnetic field (**H**), the resistivity tensor obeys the Onsager relations $\rho_{ik} (\mathbf{B}) = \rho_{ki} (-\mathbf{B})$.

Separating ρ_{ik} into a symmetrical and an antisymmetrical part (in **B**), and having in mind that the effect of a magnetic field is usually fairly small, we can expand the resistivity tensor components in power of B_i, obtaining, to second order in **B**, the result [16, 17],

$$\rho_{ik} (T , \mathbf{B}) = \rho_{ik} (T , 0) + \varepsilon_{ikl} \, \alpha_{lm} (T) B_m + \beta_{iklm} (T) B_l B_m \tag{3}$$

where $\varepsilon_{ikl} = + 1$ for $i, k, l = 1, 2, 3$ (or any even permutation), $\varepsilon_{ikl} = - 1$ for odd permutations, and zero otherwise.

In a standard measurement of the electrical resistivity one determines the electrical field component along the current direction (say **n**), i. e.

$$\mathbf{E} \cdot \mathbf{n} = E_i \, n_i = \rho_{ik} \, n_i \, j_k \tag{4}$$

with $j = j\,n$, $|n| = 1$. We then have for the electrical resistivity measured at temperature T, in the n-direction and under a magnetic induction **B** :

$$\rho\,(\,T\,,\;\mathbf{n}\,,\;\mathbf{B}\,) = (\,\mathbf{E}\cdot\mathbf{n}\,)\,/\,j = \rho_{ik}\;n_i\;n_k \qquad (5)$$

Introducing ρ_{ik} given by eq. (3), we obtain:

$$\rho\,(\,T\,,\;\mathbf{n}\,,\;\mathbf{B}\,) = \rho_{ik}\,(\,T\,,\;0\,)\,n_i\,n_k + [\,\varepsilon_{ikl}\,n_i\,n_k\,]\,\alpha_{lm}\,(\,T\,)\,B_m$$

$$+[\,\beta_{iklm}\,(\,T\,)\,n_i\,n_k\,]\,B_l\,B_m = \rho\,(\,T\,,\;\mathbf{n}\,,\;0\,) + \lambda_{lm}\,(\,T\,,\;\mathbf{n}\,)\,B_l\,B_m \qquad (6)$$

where $\lambda_{lm}\,(\,T,n\,) = \beta_{iklm}\,(\,T\,)\;n_i\,n_k$, and the first order terms in **B** do not contribute to the electrical resistivity ($\varepsilon_{ikl}\,n_i\,n_k = 0$).

We can then define a magnetoresistivity coeficient (eq. 1) corresponding to an electrical current along **n** and a magnetic induction along $\hat{\mathbf{b}}$ ($\mathbf{B} = B\,\hat{\mathbf{b}}$, $|\hat{\mathbf{b}}| = 1$) :

$$(\,\Delta\rho\,/\,\rho\,)_{\mathbf{n},\,\hat{\mathbf{b}}} = [\,\rho\,(\,T\,,\;\mathbf{n}\,,\;\mathbf{B}\,) - \rho\,(\,T\,,\;\mathbf{n}\,,\;0\,)\,]\,/\,\rho\,(\,T\,,\;\mathbf{n}\,,\;0\,)$$

$$= [\,\lambda_{lm}\,(\,T\,,\;\mathbf{n}\,)\,/\,\rho\,(\,T\,,\;\mathbf{n}\,,\;0\,)\,]\,B_l\,B_m = [\,\gamma_{lm}\,(\,T\,,\;\mathbf{n}\,)\,\beta_l\,\beta_m\,]\,B^2 \qquad (7)$$

where

$$\gamma_{lm}\,(\,T\,,\;\mathbf{n}\,) \equiv \lambda_{lm}\,(\,T\,,\;\mathbf{n}\,)\,/\,\rho\,(\,T\,,\;\mathbf{n}\,,\;0\,).$$

The quadratic field dependence of the magnetoresistivity, obtained at the present level of approximation, is well reproduced by the experimental result in most metallic systems investigated [1-3].

Magnetic metals

In this case, because of the existence of magnetic moments m_i, the curvature effect associated with the Lorentz force is enhanced, due to the increase of the internal magnetic induction:

$$\mathbf{B} = \mu_0\,(\,\mathbf{H} + \mathbf{M} + \mathbf{H}_d\,) \qquad (8)$$

M is the *technical* magnetization produced in the sample by the applied magnetic filed, $\mathbf{M} = \Sigma_i < \mathbf{m}_i > /\,\Omega$ (Ω is the sample volume), and $\mathbf{H}_d$ is the demagnetizing field, $\mathbf{H}_d = -\,D\mathbf{M}$ (D = demagnetizing factor; we assume, for simplicity, an ellipsoidal sample) [5, 18].

Besides the curvature effect, we must also consider carefully the scattering between the conduction electrons and the magnetic moments m_i. The corresponding contribution to the electrical resistivity depends on the degree of magnetic order present in the sample, i. e. on the value of the spontaneous magnetization at each temperature, $M_s(T)$ (mean field effect), and on the magnetic moment correlations e. g. $< m_i \cdot m_j >$, particularly near the critical points (fluctuation effects) [19].

Furthermore, since each electron collision with a magnetic moment is in general anisotropic (angle k, m_i), the electrical resistivity also depends on the angle θ between the electrical current and the technical magnetization M (or, equivalently, of the applied field H) [5].

Putting these effects together (curvature, degree of magnetic order and scattering anisotropy) we can write:

$$\rho_{ik}(T, H) = \rho_{ik}^o(T, B) + \rho_{ik}^m(T, M_s, \theta, < m_\alpha \cdot m_\beta >) \qquad (9)$$

where ρ_{ik}^o contains the normal magnetoresistivity effect (with the trivial inclusion of M effects in B, eq. 8) and ρ_{ik}^m represents the new magnetic contributions, associated with magnetic order (M_s + correlations between fluctuations) and with the electron scattering anisotropy (angle θ).

In the following section we focus attention on some basic microscopic mechanisms which can contribute to the magneto-resistivity term ρ_{ik}^m. Within the scope of this paper, such treatment will be mainly illustrative rather than exhaustive.

2.2 — Thermal disorder and fluctuation effects. Microscopic mechanisms in magnetic metals

a) Zero field case ($H = 0$)

In a perfect crystal with the moments m_i fully ordered at $T = 0K$, the conduction electrons travel through a periodic potential (electrostatic + magnetic), with no damping in the corresponding wavepackets; we then have $\rho = 0$ (*). In a simple

---

(*) In an *ideally pure* crystal, no d. c. conductivity exists at $T = 0$ K; the conduction electrons simply oscillate under the action of a d. c. electrical field, due to the caracteristic periodicity of the energy bands [20].

approximation the motion of a conduction electron through the lattice can be described by the Hamiltonian:

$$\mathcal{H} = -\hbar^2/(2m) \, \nabla^2 + \sum_{i=1}^{N} v(r-R_i) + \sum_{i=1}^{N} G(r-R_i) \, s \cdot J_i \quad (10)$$

where the first term represents the electron kinetic energy, the second term the electrostatic electron-lattice interaction (R_i refers to the i ion in the lattice and r to the electron position), and the third one gives the magnetic interaction between the electron spin s and the ionic magnetic moment $m_i = (g_J - 1) \, \mu_B J_i$ (g_J is the Landé factor and μ_B is the Bohr magneton); J_i is the total angular momentum of the ion i and $G(r-R_i)$ measures the strength of the magnetic interaction.

At finite temperatures and below the Curie point (assuming, for simplicity, a ferromagnet), thermal disorder breaks the periodicities of the last term in eq. 10, with the consequent appearance of a magnetic resistivity contribution. Standard transport theory leads to the following expression for the magnetic resistivity measured along the i crystal direction [21, 22]:

$$\rho_m^{(i)}(T) / \rho_{m\infty}^{(i)} = \sum_{j=0}^{N} \Gamma(R_j, T) \, \phi^{(i)}(R_j) \quad (11)$$

where $\rho_{m\infty}$ is the saturation value of the magnetic resistivity ($T \gg T_c$), $\Gamma(R_j, T)$ is the correlation function between ionic moments at distance R_j,

$$\Gamma(R_j, T) = \langle J_0 \cdot J_j \rangle / [J(J+1)] \quad (12)$$

and $\phi^{(i)}(R_j)$ is the interference function for the electron scattering from different ions, which has the electron wavelength λ_F as a characteristic parameter for each metal. For an arbitrary crystal lattice, $\phi^{(i)}(R_j)$ is generally anisotropic, always satisfying the two conditions:

$$\sum_{j=0}^{N} \phi^{(i)}(R_j) = 0 , \quad \phi^{(i)}(0) = 1 \quad (13)$$

Notice also that $\Gamma(0, T) = 1$.

Introducing these conditions in eq. 11 we obtain:

$$\frac{\rho_m^{(i)}(T)}{\rho_{m\infty}^{(i)}} = 1 + \sum_{j=0}^{N} \frac{\langle J_i \cdot J_j \rangle}{J(J+1)} \, \phi^{(i)}(R_j) \quad (14)$$

196

Portgal. Phys. — Vol. 16, fasc. 3-4, pp. 191-220, 1985

Using the angular momentum thermal averages $<J_i>$, $<J_j>$ and the thermal fluctuations δJ_i, δJ_j we can write:

$$J_i = <J_i> + \delta J_i, \quad J_j = <J_j> + \delta J_j \tag{15}$$

and thus

$$<J_i \cdot J_j> = <J_i> \cdot <J_j> + <\delta J_i \cdot \delta J_j> \tag{16}$$

In a single domain ferromagnet, $<J_i> = <J_j> = <J^z> \hat{z}$ and $<J^z> = J \sigma(T)$, where $\sigma(T)$ is the reduced spontaneous magnetization at temperature T, $\sigma(T) = M_s(T)/M_s(0)$; we then have

$$<J_i \cdot J_j> = J^2 [\sigma(T)]^2 + <\delta J_i \cdot \delta J_j> \tag{17}$$

Introducing these results in eq. 14, and using the properties of $\phi^{(i)}(R_j)$, we obtain:

$$\frac{\rho_m^{(i)}(T)}{\rho_{m\,\infty}} = 1 - \frac{J}{J+1} [\sigma(T)]^2 + \frac{1}{J(J+1)} \sum_{j \neq 0}^{N} <\delta J_i \cdot \delta J_j> \phi^{(i)}(R_j) \tag{18}$$

The $[\sigma(T)]^2$ term represents the mean field effect on $\rho_m^{(i)}$, associated with the temperature variation of the spontaneous magnetization. The last term gives the effect of the *correlations* between the thermal fluctuations in different ions.

If the system is not too close to the Curie point, the fluctuations δJ_i and δJ_j are usually fairly small and $\rho_m^{(i)}(T)$ is dominated by the mean field term. Close to the Curie point $\sigma(T) \to 0$, the thermal fluctuations grow very rapidly, and the last term in eq. 18 may become important (*). The correlations between the thermal fluctuations (δJ_i and δJ_j) therefore determine the critical behaviour of the electrical resistivity near T_c.

For temperatures not in the immediate vicinity of T_c, the correlations between fluctuations can be described in terms of a mean field treatment (Landau type [16]; $|(T-T_c)/T_c| > \varepsilon_G$ where ε_G is the so called reduced Ginzburg temperature [23], usually of the order of 10^{-2} for many magnetic metals).

_____

(*) The fluctuations may be large, but if they are *uncorrelated*, the corresponding term $<\delta J_i \cdot \delta J_j>$ could still be neglected.

For temperatures in the range $|(T-T_c)/T_c| < \varepsilon_G$, a full treatment of the fluctuations is necessary, within the context of the modern theories of critical phenomena [24], namely renormalization group treatments [25, 26]. Inside such critical region, scaling laws apply, and the critical exponents depend only on the lattice dimensionality (d) and on the number of components (n) of the order parameter; in particular, they are independent of the symmetry of the crystal lattice and of the direction in which the electrical resistivity is measured [27].

b) Magnetic field effects

When a magnetic field (**H**) is applied, two distinct effects arise, in connection with the terms discussed in eq. 18. First, the progressive alignment of the magnetic moments $\mathbf{m}_i$ produced by **H** increases the value of the sample magnetization, reducing therefore $\rho_m(T)$ (negative magnetoresistance arising from the mean field term in eq. 18). Second, the field **H** modifies the correlations between the different magnetic moments (i , j), an effect which becomes increasingly important as T approaches T_c. This leads to characteristic critical features in the magnetoresistance near T_c, both in terms of the temperature and of the magnetic field. The sign of the corresponding magnetoresistance depends on the particular system under study, through the interplay between $\phi^{(i)}(\mathbf{R}_j; \lambda_F)$ and $< \delta\mathbf{J}_i \cdot \delta\mathbf{J}_j >$, in the lattice sum of eq. 18.

An extended summary of such effects of **H** (on thermal disorder and fluctuations) has been given recently in the literature [13], including the critical indices theoretically expected for the magnetoresistivity in the vicinity of the Curie point, within different temperature and magnetic field ranges [6, 28, 29].

2.3 – Anisotropy of ρ_m versus $\mathbf{M}_s$ (H = 0)

2.3.1 – Phenomenological approach

a) Single domain ferromagnetic crystal

Quite generally [30], the electrical resistivity of a single domain monocrystalline ferromagnetic metal, besides the dependence on the temperature due to spin disorder (section 2.2), also

198

Portgal. Phys. — Vol. 16, fasc. 3-4, pp. 191-220, 1985

depends on the direction of the electrical current I with respect to the crystal axes c_i (lattice anisotropy, e. g. due to different dynamical properties of the conduction electrons travelling along different crystal directions) and on the angle between I and the spontaneous magnetization M_s (magnetic anisotropy, e. g. due to spin-orbit effects on the scattering of the electrons by the ionic magnetic moments). Normally we can write [31]:

$$\rho(\hat{a}, \hat{b}) = F(\alpha_i, \beta_i, T) \tag{19}$$

where α_i and β_i are the cosines of the angles (M_s, c_i) and $(I \quad c_i)$ respectively (*); $\hat{a}, \hat{b}$ are the corresponding unit vectors.

The general form of F depends on the symmetry of the crystal under consideration, as it must be invariant with respect to all its symmetry operations. For example, in the case of hexagonal symmetry and to a fourth order approximation, one can show, in analogy with similar formulae for the magnetostriction [32] (a physical property with the same tensorial character as the electrical resistivity):

$$\rho(\hat{a}, \hat{b}) = a_0 + k_1(\beta_3^2 - 1/3) + k_2(\alpha_3^2 - 1/3) + k_3(\beta_3^2 - 1/3)(\alpha_3^2 - 1/3)$$
$$+ k_4[(\alpha_1^2 - \alpha_2^2)(\beta_1^2 - \beta_2^2) + 4\alpha_1\alpha_2\beta_1\beta_2] + k_5(\alpha_1\beta_1 + \alpha_2\beta_2)\alpha_3\beta_3 \tag{20}$$

where a_0 is the non-orientational contribution to the resistivity (given in 2.2) and k_i are the anisotropy constants for the *electrical resistivity*.

b) Multidomain ferromagnetic crystal

The direction of the current with respect to the crystal axes continues to have a single value $\hat{b}$. However, because of the domain magnetic structure, the direction of M_s with respect to the crystal axes changes from one domain to the next. In each domain M_s selects *one* of the (n) easy directions in the crystal, which we characterize by the unit vector $\hat{a}_l$ ($l = 1, 2, \ldots n$).

Since the orientational anisotropy of the resistivity is fairly small, the ρ-differences between different domains are small

---

(*) We include explicitly the angles between M_s and the crystal axes, since the crystal anisotropy is always operative, and may distinguish different directions of M_s with respect to c_i, e. g. through magnetoelastic effects.

compared with the domain resistivities ρ ($\hat{a}_l$, $\hat{b}$). The effective resistivity of such multidomain structure can then be approximated by [33],

$$\rho_{ef} (\hat{b}) \simeq \{ \rho (\hat{a}_l, \hat{b}) \} \tag{21}$$

where $\{...\}$ means a spatial average over the sample, and a fine domain structure is assumed. We then write:

$$\rho_{ef} (\hat{b}) \simeq (1 / \Omega) \sum_{l=1}^{n} \sum_{r=1}^{N_d} c_{rl} \rho (\hat{a}_l, \hat{b}) \omega_d^{(r)} \tag{22}$$

where Ω is the sample volume, $\omega_d^{(r)}$ is the volume of the r magnetic domain ($r = 1, 2, ... N_d$), and c_{rl} are occupation numbers: $c_{rl} = 1$ if the domain r has M_s along the l easy crystal direction, and $c_{rl} = 0$ otherwise. A complete description of the domain structure means therefore the knowledge of all the individual domain volumes $\omega_d^{(r)}$ *and* of the corresponding easy direction (c_{rl} coefficients).

Performing first the r sum we get,

$$\rho_{ef} (\hat{b}) = (1 / \Omega) \sum_{l=1}^{n} \rho (\hat{a}_l, \hat{b}) \sum_{r=1}^{N_d} c_{rl} \omega_d^{(r)} \tag{23}$$

Notice that $\sum_{r=1}^{N_d} c_{rl} \omega_d^{(r)}$ gives the total domain volume corresponding to the l orientation, which we call $\omega_d (l)$; we then have

$$\rho_{ef} (\hat{b}) = (1 / \Omega) \sum_{l=1}^{n} \rho (\hat{a}_l, \hat{b}) \omega_d (l) \tag{24}$$

If the magnetic domains are equally distributed over the easy directions, $\omega_d^{(l)} = \Omega/n$; and the simple result appears:

$$\rho_{ef} (\hat{b}) = (1 / n) \sum_{l=1}^{n} \rho (\hat{a}_l, \hat{b}) \tag{25}$$

c) Multidomain polycrystalline ferromagnet

We assume the sample as an assembly of N_c crystallites oriented at random, each one numbered by an index j, with volume Ω_j, and with its own magnetic domain structure. Due to the polycrystalline structure, the current I makes in general different angles (I, $c_i^{(j)}$) with the crystal axes of the different

crystallites, $c_i^{(j)}$. The direction of I inside each crystallite can then be associated with a corresponding unit vector $\hat{b}^{(j)}$. Due to the domain structure, we can first calculate the effective resistivity of each crystallite, using eq. 24:

$$\rho_{ef}(\hat{b}^{(j)}) = (1/\Omega_j) \sum_{l=1}^{n} \rho(\hat{a}_l, \hat{b}^{(j)}) \omega_d^{(j)}(l) \qquad (26)$$

The spatial average over the crystallites can now be written:

$$\rho_{ef}(\text{sample}) = (1/\Omega) \sum_{j=1}^{N_c} \rho_{ef}(\hat{b}^{(j)}) \Omega_j \qquad (27)$$

Introducing the explicit form of $\rho_{ef}(\hat{b}^{(j)})$, eq. 26, we obtain:

$$\rho_{ef}(\text{sample}) = (1/\Omega) \sum_{j=1}^{N_c} \sum_{l=1}^{n} \rho(\hat{a}_l, \hat{b}^{(j)}) \omega_d^{(j)}(l) \qquad (28)$$

If we assume that the crystallites have similar volumes ($\Omega_j \simeq \Omega/N_c$) and that M_s is equally distributed over the n easy directions, we then get the simple result:

$$\rho_{ef}(\text{sample}) = 1/(N_c n) \cdot \sum_{j=1}^{N_c} \sum_{l=1}^{n} \rho(\hat{a}_l, \hat{b}^{(j)}) \qquad (29)$$

2.3.2 — Microscopic approach

Physical origin of the (I, M_s) anisotropy; Smit mechanism.

Experiment shows that the anisotropy of the electrical resistivity with respect to the direction of the spontaneous magnetization, M_s, is present in most magnetic metals, ranging from heavy rare earths [12, 34] to 3d transition elements [5] (localized, quasi-localized or itinerant magnetism), either isolated or in the form of alloys, compounds or pseudocompound systems. Furthermore, the anisotropy is present even in the cases when the crystal lattice has cubic symmetry. This shows that the observed anisotropy has a magnetic origin, and must be a consequence of an anisotropic scattering mechanism. In the case of cubic crystals, the anisotropy could result from some lower-than-cubic-symmetry scattering potential (e. g. magnons) with cubic-symmetry initial and final states, or from an isotropic scattering potential with lower-than-cubic-

symmetry wavefunctions [30, 35, 36, 37]. The latter mechanism is generally considered the more likely one in the case of 3d transition metals, and was successfully applied, for the first time, by Smit [4] to discuss the intriguing resistivity anisotropy in cubic transition metal ferromagnets. To illustrate the subtle mechanisms underlying the magnetic anisotropy, we will concentrate here only on the Smit mechanism, following closely the review of McGuire and Potter [30], which assumes an isotropic scattering potential V(r).

As observed by Smit, in 3d cubic crystals the symmetry of the electronic wavefunctions associated with each lattice ion can be lowered by the spin-orbit interaction,

$$H_{so} = k \mathbf{L} \cdot \mathbf{S} \qquad (30)$$

provided the electrostatic potential is radial; $\mathbf{L}$ and $\mathbf{S}$ are the ion total orbital momentum and total spin, respectively, whereas k measures the strength of the spin-orbit coupling.

In the absence of such interaction, the five 3d atomic orbitals are degenerate ($\varphi_1 = xzf(r)$, $\varphi_2 = yzf(r)$, $\varphi_3 = xyf(r)$, $\varphi_4 = (x^2 - y^2)f(r)/2$, $\varphi_5 = (r^2 - 3z^2)f(r)/(2\sqrt{3})$), and such degeneracy remains even when we switch the (cubic symetry) crystal field interaction. Recalling that in transition metals the main resistivity mechanism results from the transitions of electrons from the s-conduction band ($\psi_s \sim e^{i\mathbf{k} \cdot \mathbf{r}}$; high mobility; low effective mass) to the d-band (Φ_i wavefunctions; appropriate linear combinations of φ_i functions, with the crystal field (cubic) symmetry; low mobility; high effective mass), no anisotropy exists in the absence of spin-orbit coupling (within the model under discussion).

The spin-orbit interaction makes a contribution to the energy of the d-states that depends on spin or magnetization direction, making it favourable for $\mathbf{M}_s$ to point along certain crystallographic directions. Thus the d-electron spin is coupled to its orbital motion, which in turn is coupled to the lattice by the crystal field. In the presence of H_{so}, the degeneracy in the Φ_i functions is lifted, and new wavefunctions $\Phi_i^{(1)}$ then result, associated with each 3d ion. Due to the direction effect of $\mathbf{M}_s$, the functions $\Phi_i^{(1)}$ exhibit symmetry lower than cubic and are not eigenfunctions of S_z because H_{so} mixes states of opposite spin.

Because the levels associated with different $\Phi_i^{(1)}$ functions have not all the same energy, a particular combination of φ_i functions is therefore energetically favoured. If some functions φ_i predomi-

202

Portgal. Phys. — Vol. 16, fasc. 3-4, pp. 191-220, 1985

nate over the others in such particular combination, the resistivity anisotropy immediately results. To illustrate this in simple terms, let us choose an extreme case in which the spin-orbit interaction selects, as dominant, the function $\varphi_3 = xyf(r)$ (in this case, $\mathbf{M}_s$ points along OZ, by symmetry).

The transition probability of a conduction electron ($\mathbf{k}$ vector, $\psi_k \sim e^{i\mathbf{k}\cdot\mathbf{r}}$) to the 3d band (φ_3 state), produced by the scattering potential $V(r)$, is proportional to the usual Born approximation factor,

$$P_{sd}(\psi_k \to \varphi_3) \propto \left| \int e^{-i\,\mathbf{k}\cdot\mathbf{r}} V(r)\, \varphi_3\, d^3\mathbf{r} \right|^2 \qquad (31)$$

Since $k_F \simeq a^{-1}$ (a = atomic spacing) and φ_3 is localized in the vicinity of the scattering ion, the dominant contributions to the integral correspond to $|\mathbf{k}\cdot\mathbf{r}| \ll 1$, which justifies a series development of the exponential. We then have, after trivial calculations,

$$P_{sd}(\psi_k \to \varphi_3) \propto k_x^2 k_y^2 \left| \int (xy)^2 V(r) f(r)\, d^3\mathbf{r} \right|^2 \qquad (32)$$

The s-d transition probability is in this case highly anisotropic, $P_{sd} \propto k_x^2 k_y^2$, depending on the particular direction of the electron ($\mathbf{k}$). For example, for an electron moving along OX or OY ($k_y = 0$, $k_x = 0$, respectively) no scattering occurs, whereas collisions occur when both k_x *and* k_y are different from zero. We recall that the reference axes have been imposed by the $\mathbf{M}_s$ direction, along OZ in the particular case just discussed. Therefore, the anisotropy with respect to the crystal axes is primarily due to the anisotropy with respect to $\mathbf{M}_s$.

2.4 – *Anisotropy of* ρ_m *v. technical magnetization* $\mathbf{M}$ (H $\neq$ 0)

2.4.1 – General expressions

For the general case of a polycrystalline (N_c crystallites) multidomain ferromagnet we have seen that the zero field electrical resistivity is given by the expression,

$$\rho_{ef}(T, 0) = (1/\Omega) \sum_{j=1}^{N_c} \sum_{l=1}^{n} \rho(\hat{\mathbf{a}}_l, \hat{\mathbf{b}}^{(j)})\, \omega_d^{(j)}(l, 0) \qquad (33)$$

Portgal. Phys. — Vol. 16, fasc. 3-4, pp. 191-220, 1985

203

where $\omega_d^{(j)}$ (l, 0) represents the total volume of the domains in crystallite j orientated along the l-easy direction (for $\mathbf{H} = 0$).

When a magnetic field is applied, the first effect is a redistribution of the domain pattern, through domain wall motion, so as to increase the domains oriented in favourable directions (with respect to $\mathbf{H}$) at the expense of the domains oriented in unfavourable directions. Provided no magnetic domain is extinct in such initial process, the sum over l is still complete, and the only field effect will be the change in the individual magnetic domains. We can then write for the corresponding magnetoresistivity:

$$\left(\frac{\Delta\rho}{\rho} \right)_{\text{wall motion}} = \frac{1}{\rho\,(\mathrm{T},\,0)} \cdot \frac{1}{\Omega} \sum_{j=1}^{N_c} \sum_{l=1}^{n} \rho\,(\,\hat{\mathbf{a}}_l,\,\hat{\mathbf{b}}^{(j)}\,)\,\Delta\omega_d^{(j)}\,(\,l,\,\mathbf{H}\,) \quad (34)$$

where $\Delta\omega_d^{(j)}\,(\,l,\,\mathbf{H}\,) = \omega_d^{(j)}\,(\,l,\,\mathbf{H}\,) - \omega_d^{(j)}\,(\,l,\,0\,)$.

When some of the easy directions cease to be represented by magnetic domains, the sum over l is progressively restricted. Ultimately, at higher fields, only a single easy direction survives in each crystallite (monodomain situation), not necessarily the same for all crystallites. Representing such particular crystallite easy direction by a unit vector $\hat{\mathbf{a}}_{lj}$, we then have:

$$\rho_{\text{ef}}\,(\mathrm{T},\,\mathbf{H}) = \frac{1}{\Omega} \sum_{j=1}^{N_c} \sum_{l=1}^{n} \rho\,(\,\mathbf{a}_l,\,\mathbf{b}^{(j)}\,)\,\omega_d^{(j)}\,(\,l,\,\mathbf{H}\,)\,\delta_{l,\,l_j} \quad (35)$$

When the field produces this situation, no further domain wall motion exists inside each crystallite, and the magnetization process can only proceed through *rotation* of the spontaneous magnetization inside each crystallite, towards progressive alignment with the magnetic field $\mathbf{H}$.

The above expressions, although physically adequate to identify the various effects associated with the magnetoresistive process, are not in a simple form appropriate to analyze the experimental results. Such formulae can be obtained through an adequate averaging process over the sample, restricted to the case of saturation resistivity, i.e. $\Delta\rho$ is calculated between an initial demagnetized state (random domain distribution) and a final state where $\mathbf{M}_s$ is everywhere aligned with $\mathbf{H}$.

As shown in next section, the following general expression is obtained for the orientational dependence of the magnetoresistivity,

$$(\Delta\rho / \rho)_{sat} = A (T) + B (T) \cos^2 \theta \qquad (36)$$

where θ is the angle between the electric current and H, and A, B are temperature dependent quantities, which can be related with the magnetoresistivity anisotropy coefficients k_i (defined in 2.3.1.a)).

2.4.2 — Averaging processes

(i) *Single crystal samples*

To illustrate this averaging process, let us take a hexagonal single crystal, with the electric current flowing along $\hat{b}$.

When the applied field H (along an $\hat{u}$ direction) produces magnetic saturation, we have $M_s \| H$ everywhere in the sample, i. e. $\hat{a} = \hat{u}$. We can then calculate the saturation resistivity, ρ_{sat}, using eq. 20 for single crystals,

$$\rho_{sat}=\rho (\hat{u} , \hat{b})=a_0+k_1 (\beta_3^2-1/3)+k_2 (u_3^2-1/3)+k_3 (\beta_3^2-1/3) (u_3^2-1/3)$$
$$+k_4 [(u_1^2-u_2^2) (\beta_1^2-\beta_2^2)+ 4 u_1 u_2 \beta_1 \beta_2]+ k_5 (u_1 \beta_1+u_2 \beta_2) u_3 \beta_3 \quad (37)$$

When $H = 0$, we assume the sample to be fully demagnetized, with the magnetic domains equally distributed over the easy directions. The result of the necessary averaging process depends on the particular easy directions imposed by the magnetic anisotropy of the sample. For example, if we have a basal plane ferromagnet, the easy directions lie entirely in this plane and we can take $\alpha_1 , \alpha_2 \neq 0 , \alpha_3 = 0$ (taking the c-axis along Ox_3). For this case we have the following zero field *domain* resistivity,

$$\rho (\hat{a} , \hat{b}) = (a_0 - k_2/3) + k_1 (\beta_3^2 - 1/3) - 1/3 k_3 (\beta_3^2 - 1/3)$$
$$+ k_4 [(\alpha_1^2 - \alpha_2^2) (\beta_1^2 - \beta_2^2) + 4 \alpha_1 \alpha_2 \beta_1 \beta_2] \qquad (38)$$

Because the domains are assumed equally distributed in the basal plane easy directions, when we average ρ over such directions we obtain a simple result (using $< \alpha_1^2 > = < \alpha_2^2 >, < \alpha_1 \alpha_2 > = 0$):

$$< \rho (\hat{a} , \hat{b}) >_{H=0} = (a_0 - k_2/3) + (k_1 - k_3/3) (\beta_3^2-1/3) \quad (39)$$

The non-normalized saturation magnetoresistivity is then given by,

$$\Delta\rho_{sat}(\mathbf{H}\|\mathbf{u}) = \rho_{sat} - <\rho(\hat{\mathbf{a}}, \hat{\mathbf{b}})>_0 = k_2 u_3^2 + k_3(\beta_3^2 - 1/3)u_3^2$$
$$+ k_4[(u_1^2 - u_2^2)(\beta_1^2 - \beta_2^2) + 4u_1 u_2 \beta_1 \beta_2] + k_5(u_1 \beta_1 + u_2 \beta_2)u_3 \beta_3 \tag{40}$$

If **H** is applied along the c-axis ($u_1 = u_2 = 0$, $u_3 = 1$) we obtain:

$$\Delta\rho_{sat}(\mathbf{H}\|\mathbf{c}) = (k_2 - k_3/3) + k_3 \beta_3^2 \tag{41}$$

Noticing that β_3 is, in this case, the cosine of the angle (θ) between **I** and **H**, we arrive at eq. 36, in the explicit form:

$$\Delta\rho_{sat}(\mathbf{H}\|\mathbf{c}) = (k_2 - k_3/3) + k_3 \cos^2 \theta \tag{42}$$

(ii) *Polycrystalline samples*

For this case we have to calculate an average of $\rho(\hat{\mathbf{a}}, \hat{\mathbf{b}})$ over a large number of randomly oriented crystallites. Following McGuire and Potter [30], the polycrystalline average can be performed by choosing $\hat{\mathbf{a}}$ to lie within a cone about an arbitrary current direction $\hat{\mathbf{b}}$, with $\hat{\mathbf{a}} \cdot \hat{\mathbf{b}} = \cos\Theta$, and evaluating

$$\rho_{poly} = (8\pi^2)^{-1} \int_0^{2\pi} d\psi \int_0^{\pi} d\gamma \int_0^{2\pi} \rho(\hat{\mathbf{a}}, \hat{\mathbf{b}}) d\phi \tag{43}$$

where ψ is an angle that locates $\hat{\mathbf{a}}$ within the cone as shown in Fig. 1. The final result gives again an expression with a $\cos^2 \theta$ dependence for the magnetoresistivity (eq. 36).

3 — HIGH ACCURACY METHOD FOR MAGNETORESISTANCE MEASUREMENTS

3.1 — *Requirements on the experimental resolution*

As referred in 1, the magnetoresistive effects are fairly small, the relative change $\Delta\rho/\rho$ under an applied magnetic field rarely attaining a value of 10^{-2} at saturation. If we want to measure such magnetoresistivity with a relative error of 1 %, one should have

$$\frac{\delta(\Delta\rho/\rho)}{\Delta\rho/\rho} = \frac{\delta(\Delta\rho)}{\Delta\rho} = \frac{\delta\rho}{\Delta\rho} = 10^{-2} \tag{44}$$

where δ stands for the *absolute* errors. Putting $\Delta\rho = 10^{-2}\rho$, we obtain the following requirement on the *relative* accuracy for resistivity measurements,

$$\delta\rho/\rho = 10^{-4} \qquad (45)$$

This estimate refers to the (favourable) measurement of $\Delta\rho$ at the maximum field. If we want to study in detail the structure of
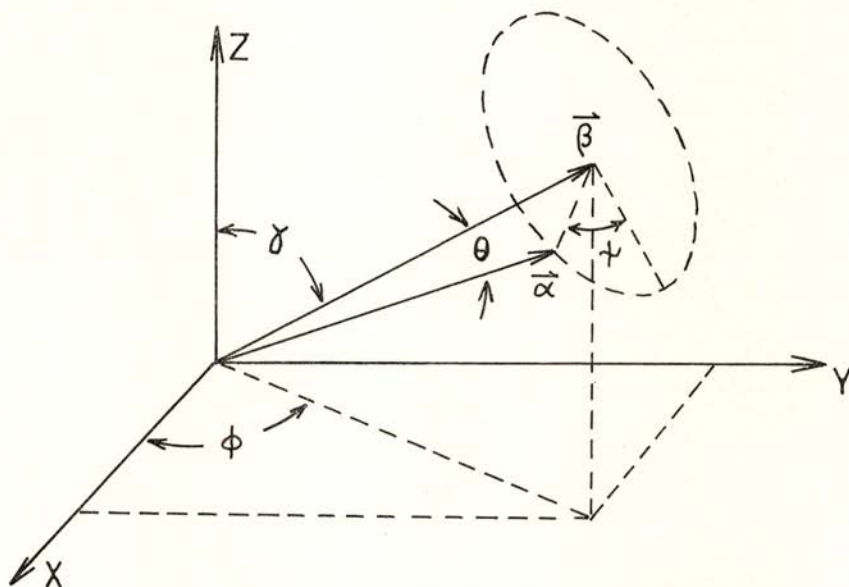
Fig. 1 — Geometry and notation used to calculate the polycrystalline average of the magnetoresistivity (eq. 43).

the magnetoresistivity curves (at field values from 0 to H_m) one should measure the resistivity with higher resolution, at least one or two orders of magnitude better. We then conclude that high accuracy magnetoresistivity measurements require an experimental set-up which ensures, with confidence, $1/10^5 - 1/10^6$ relative resolution in resistivity. The method here described fulfills this requirement.

3.2 — *Experimental technique*

The electrical resistivity, thus the magnetoresistivity, was measured with a four-wire potentiometric method, using a highly

stabilized dc current (0 - 1 A; $1/10^6$ stability per hour), the sample voltage (V) being measured with a few nV resolution ($V \sim 10^3 \, \mu V$).

The sample resistivity (ρ) is given by the usual expression,

$$\rho = f \cdot (V/I) \tag{46}$$

where f is a constant geometric factor.

Under *strictly isothermal* conditions, we then have the following limit for the relative error in ρ :

$$| \delta\rho/\rho | \leqslant | \delta V/V | + | \delta I/I | \tag{47}$$

From the figures quoted above for $\delta V/V$ and $\delta I/I$, we just obtain the appropriate resolution in the ρ measurements.

In practice the temperature is not strictly constant in the course of the measurement, when the field is gradually swept from 0 to H_m ; usually a complete measuring cycle lasts for about 2 - 3 min. One should then ensure that the change in resistivity ($\delta\rho_T$) due to a change in temperature during the measurement (δT) is kept within the required limits. If one recalls that in most metals the relative changes in ρ, per degree change of temperature, are of the order of 10^{-3} (or below), we can write

$$\delta\rho_T / \rho \approx 10^{-3} \, \delta T \tag{48}$$

which restricts the allowed temperature variation during the measuring process to a maximum value $\delta T_{max} \approx 1$ mK, for $\delta \rho_T / \rho \approx 10^{-6}$. One then concludes that, in order to measure accurately the magnetoresistivity, it is crucial to implement an efficient temperature controller; such unit was projected and implemented in the course of our studies, and will be described in 3.3.

Fig. 2 shows the block diagram of the experimental set-up constructed to measure the magnetoresistivity.

The temperature was measured using a copper-constantan thermocouple, the corresponding emf being measured to within a few nV.

The low magnetic fields were obtained with a copper wire solenoid locally constructed [38] ($0 \leqslant H \leqslant 1$ kOe ; $1:10^4$ homogeneity over 10 cm axial length), powered from a stabilized dc current supply ($1:10^4$ stability). The solenoid calibration is

263 Oe/A . The solenoid is refrigerated with a water cooled coil, the ensemble being immersed in a large capacity oil bath.

The high fields (up to 10 kOe) are obtained with a commercial iron core electromagnet with an adjustable gap. The current is provided by a stabilized power supply (0-30 A) with $1:10^5$ stability.

In each case the field was automatically increased from 0 to H_m by means of a ramp sweep unit, which controlled the output of the magnet current supply (rising times adjustable between 10 s and 80 h; usually we adopted about 2 min).
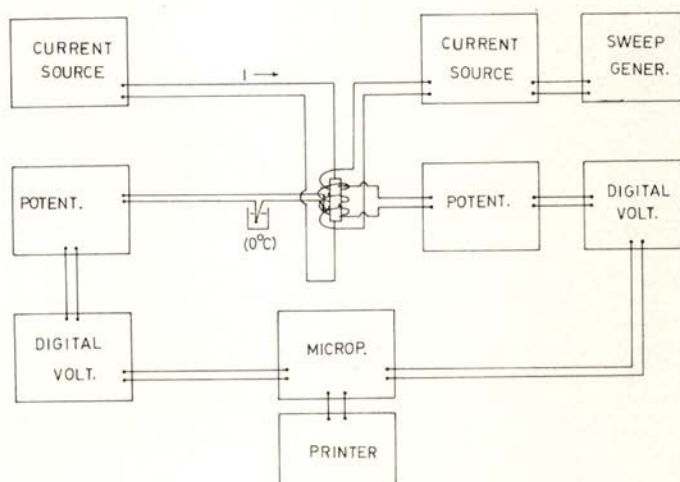
Fig. 2 — Block diagram of the experimental unit for magnetoresistivity measurements.

Automatic data acquisition was obtained with a microprocessor unit locally constructed [39], which prints the relevant data (ρ, H, T) every 2 seconds, if necessary.

3.3 — *Temperature controller*

In order to ensure the necessary stability in temperature, an automatic temperature controller was designed, using a high precision digital lock'in phase sensitive detecter. Fig. 3 shows the block diagram of such temperature controller.

The lock'in internal oscillator provides, besides the internal reference signal, the excitation voltage for the Wheatstone bridge. In two adjacent arms we use fixed resistances of 200 Ω, whereas in the other arms we put the controller resistance thermometer (thin copper coil; r ≃ 200 Ω at room temperature, about 60 Ω at nitrogen temperatures) and a 4 decade resistance box with 0.1 Ω resolution.
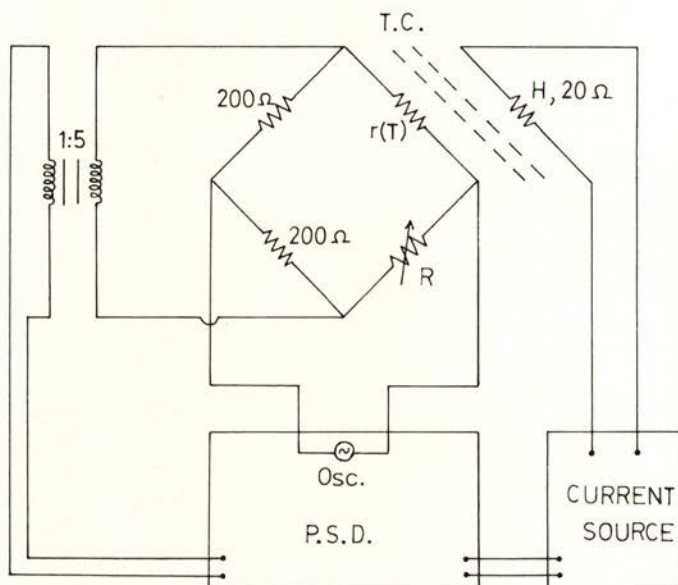
Fig. 3 — Block diagram of the temperature controller for magnetoresistivity measurements.

The unbalance signal from the bridge is accurately detected by the lock'in detector and, after suitable internal amplification, is used as the input of an unidirectional power supply. This source provides the current for the controlling heater of the experimental chamber (R ≃ 20 Ω ; 5 W maximum heating power).

This temperature controller enables quick temperature adjustments (e. g. a 10 K variation in the setting point can be achieved in 5 min), with a guaranteed subsequent stability better than 1 mK/min. In order to ensure such degree of efficiency,

adequate attention has been paid to the design of the experimental chamber and the sample holder, as we describe next.
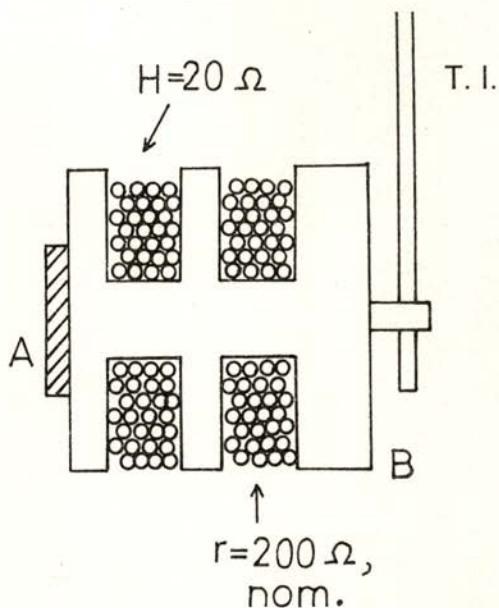
Fig. 4 — Details of the sample holder: A-sample, B-copper basis, H-heater, r-resistance thermometer, T. I.-inox tube.

3.4 — Sample holder (and controller basis)

In order to optimize all the thermal links in the system "sample-controller thermometer-heating coil", a special design was adopted for the supporting copper basis, as shown in Fig. 4. The coils of the controller copper thermometer and of the heater (constantan) are wound in narrow flat grooves in the immediate vicinity of the copper basis where the sample is attached with low temperature, thermal conducting, GE varnish. The ensemble is suspended inside the experimental chamber by two thin wall inox tubes, in order to increase the thermal resistance between the controlling copper basis and the external environment.

A limited account of the method described in this section has been given elsewhere [40].

4 – ILLUSTRATIVE EXPERIMENTAL RESULTS

Experimentally, two distinct field orientations are usually adopted in magnetoresistivity measurements, either with the magnetic field perpendicular to the electrical current (Fig. 5a),

$$\Delta\rho_\perp / \rho = [\rho_\perp (T, H) - \rho(T, 0)] / \rho(T, 0) \qquad (49)$$

or with **H** parallel to **I** (Fig. 5b),

$$\Delta\rho_{||} / \rho = [\rho_{||} (T, H) - \rho(T, 0)] / \rho(T, 0) \qquad (50)$$

Here $\rho(T, 0)$ is the sample resistivity in zero field.
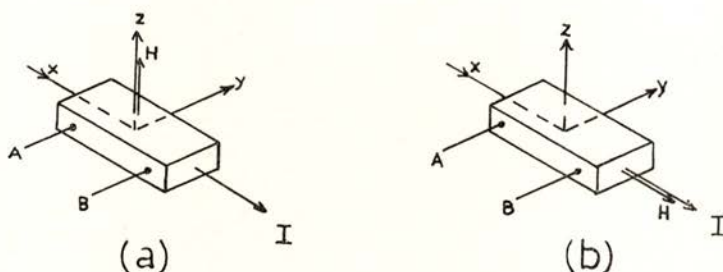
Fig. 5 — Distinct field orientations used for magnetoresistivity measurements: a) Transverse $\Delta\rho_\perp / \rho$, b) longitudinal $\Delta\rho_{||} / \rho$

In order to eliminate from $\Delta\rho/\rho$ spurious odd effects in **H**, we should always take the average, for each T, of the results obtained with the two opposite directions of the field ($\pm$ **H**).

The results shown below illustrate some of the potentialities of the experimental method described in 3 and, at the same time, constitute selected examples of the behaviour of the magnetoresistivity contributions theoretically described in section 2.

4.1 – *Critical phenomena* (ferro-paramagnetic transition in $Tb_{68} - Gd_{32}$ single crystal).

Fig. 6 shows the temperature dependence of the longitudinal magnetoresistivity of an hcp single crystal $Tb_{68} - Gd_{32}$ (current **I** in the basal plane) in the vicinity of the Curie point, $T_c = 253$ K, and at a constant applied field H = 526 Oe.

A pronounced negative dip occurs in $\Delta\rho_{||}/\rho$ just at the Curie point, which we associate with the characteristic strong reduction (by the field) of the spin fluctuations near a ferro-paramagnetic transition, as discussed in 2.2. Notice that both sides of the $\Delta\rho_{||}/\rho$ curve exhibit critical behaviour near T_c; a full analysis of such behaviour, with the estimation of the corresponding critical exponents, will be done in due course.
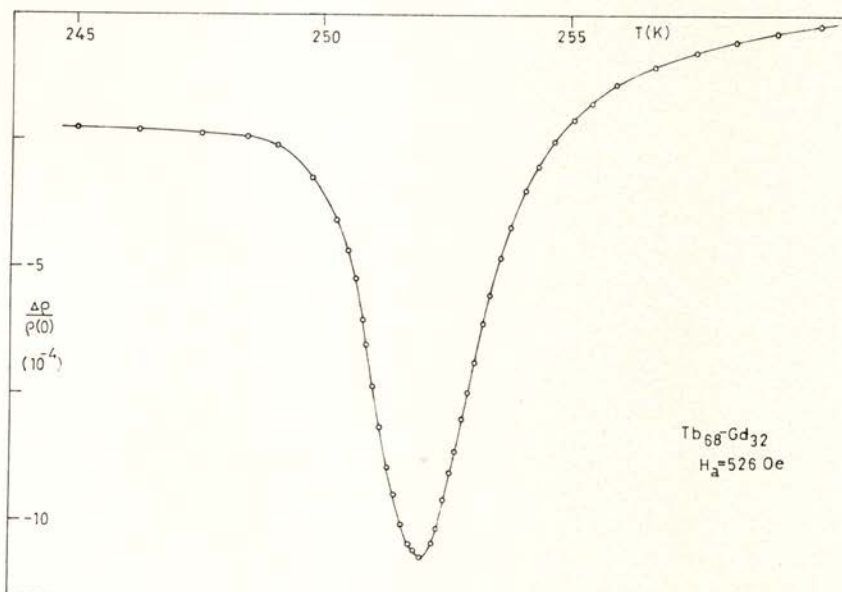
Fig. 6 — Temperature dependence of the longitudinal magnetoresistivity in a Tb_{68} - Gd_{32} single crystal.

Notice also that sufficiently above T_c (when the correlations between fluctuations are virtually absent), the magnetoresistivity is fairly small, attributable to just the non-magnetic (normal) magnetoresistivity.

On the other hand, for temperatures sufficiently below T_c the magnetoresistivity exhibits an almost constant negative value. Since fluctuations are then drastically damped, such result is attributed to an oriental effect of **H** on the basal plane spontaneous magnetization, for which the low magnetic anisotropy readily enables directional changes in $\mathbf{M_s}$.

4.2 — *Orientational effects* (Pr_2 ($Co_{1-x}Fe_x$)$_{17}$ intermetallic
    compounds)

Fig. 7 shows the field dependence of the longitudinal magneto-resistivity ($H = 0 - 9.7$ kOe) for a Pr_2 ($Co_{0.8}Fe_{0.2}$)$_{17}$ polycristalline sample (Th_2Ni_{17} hexagonal structure), at different values of the
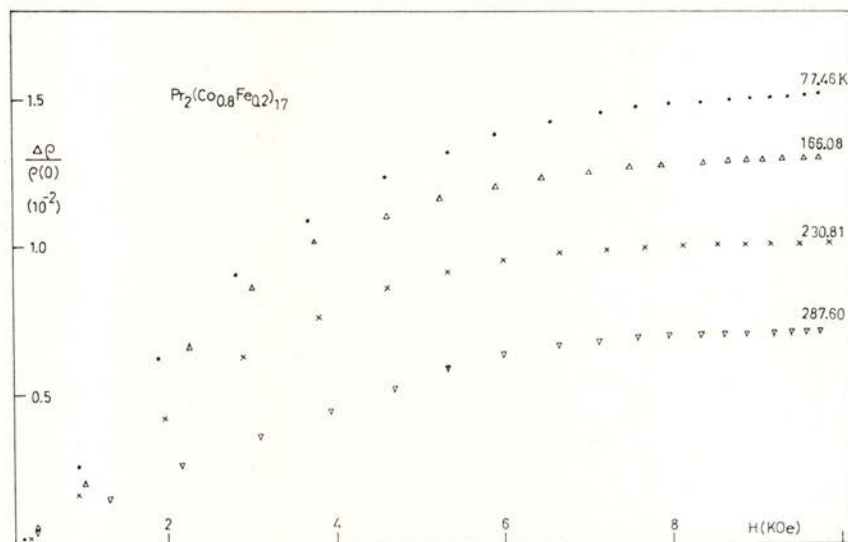
Fig. 7 — Field dependence of the longitudinal magnetoresistivity of a $Pr_2(Co_{0.8}Fe_{0.2})_{17}$ polycrystalline sample, at several constant temperatures.

measuring temperature, with the sample always in the ferromagnetic phase ($T \ll T_c$). The magnetoresistance is now positive, and entirely attributed to an orientational effect (Smit mechanism [5, 36, 37]; see 2.3.2).

In all the isothermal $\Delta\rho_{\parallel}/\rho$ curves shown in Fig. 7, we distinguish three distinct regions, underlying characteristic dominant effects. In the first portion, at low fields, the curvature is positive and is associated with the growth of domains in favourable directions, at the expense of decreasing domains in unfavourable directions (wall domain motion). The second portion of the curve, with a noticeable negative curvature, is associated with the rotation of the magnetic domains inside the sample (towards the direction of **H**), a process which is particularly difficult for those crystallites

where H points in hard magnetic directions. Finally, a third region, at high fields (where saturation is almost achieved in $\Delta \rho_{\parallel} / \rho$), is the final aligment stage of M_s with H (*).

4.3 – *Field effects on helimagnetic structures* (Gd_{1-x} - Y_x single crystal)

Fig. 8 shows the field dependence of the longitudinal magnetoresistivity (H = 0-520 Oe) for a hcp $Gd_{0.68}$ - $Y_{0.32}$ single crystal (I // c axis) at several measuring temperatures, corresponding either to the ferro or to the helimagnetic phase, in zero field.

The crystal under investigation is ferromagnetic just above $T_c^* = 208.15$ K, with M_s along the c-axis, and helimagnetic just below this temperature. In the latter phase the magnetic moments lie in the basal plane (ferromagnetically ordered), exhibiting however an helical modulation along the c-axis, associated to a characteristic q vector [42, 43].

(i) Let us start with the curve taken with the sample initially in the ferromagnetic phase (T = 208.55 K).

At low fields (H ≤ 50 Oe), no measurable change is detected in ρ, a fact which we associate with the absence of field penetration in the sample. This is achieved by domain motion (**), so as to produce a technical magnetization $M = H / D$ in the sample, which ensures a zero value for the internal magnetic field, $H_i = H - DM$. An estimate of the maximum value of H compatible with the absence of field penetration, $H_{max} = DM_s(T)$ (using information on $M_s(T)$ and D for our sample) confirms the explanation referred above.

At higher fields we observe a progressive reduction of the electrical resistivity, up to the maximum field used. This is attributed to the gradual suppression of the spin fluctuations, since the measuring temperature is only about 2 K below the Curie point of this crystal.

(*) In practice, the *total* alignment of the magnetic moments with H is not exactly achieved under finite fields, except for the principal symmetry directions in the crystal [41].

(**) In uniaxial ferromagnets, the growth of domains of one type (+ z), at the expenses of the other type (- z), does not change ρ (even function of $\cos \theta$).

(ii)   For the other curves, obtained with the crystal initially in the helimagnetic phase, the field penetration occurs immediately
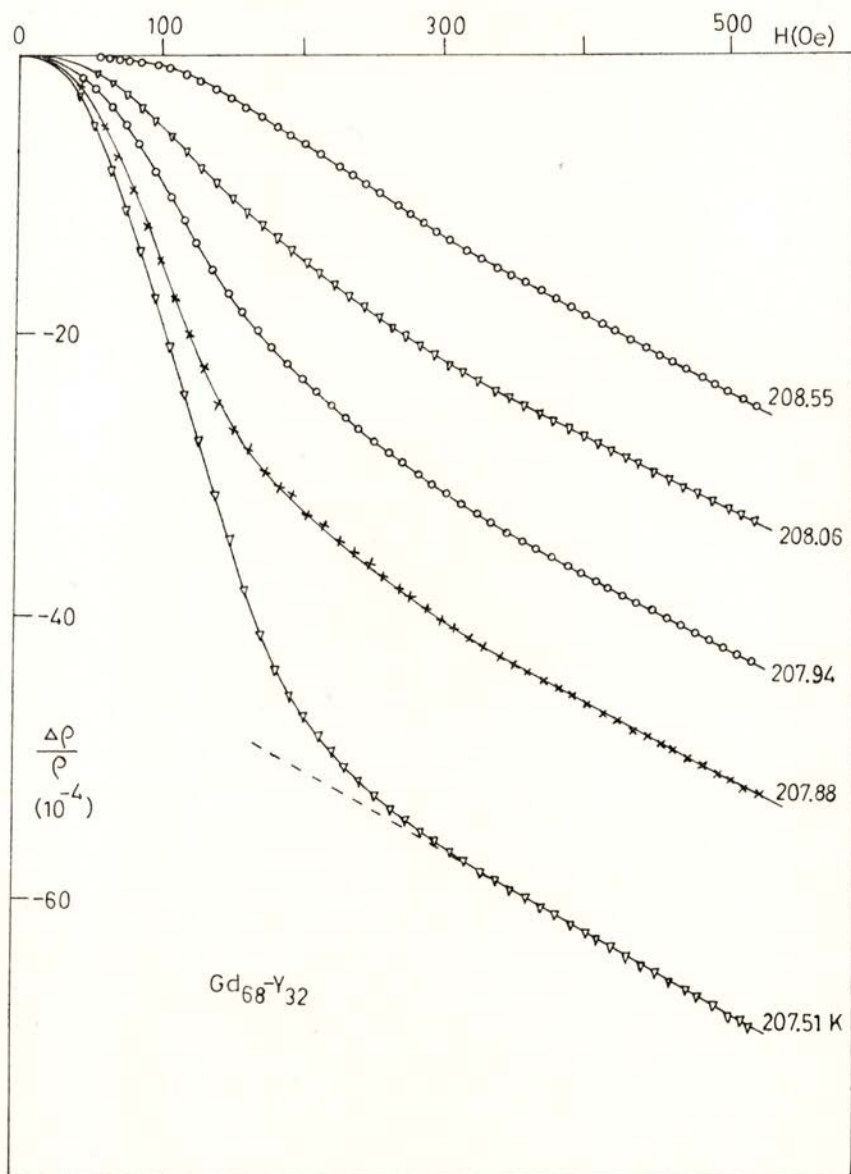
Fig. 8 — Field dependence of the longiutdinal magnetoresistivity of a $Gd_{0.68}$ - $Y_{0.32}$ single crystal, with $I \| c$ axis, at several constant temperatures.

at low fields, as expected for an antiferromagnetic structure [44].

A pronounced negative magnetoresistance is first observed in the $\Delta\rho_{\parallel}/\rho$ curve, as a result of the gradual distortion of the
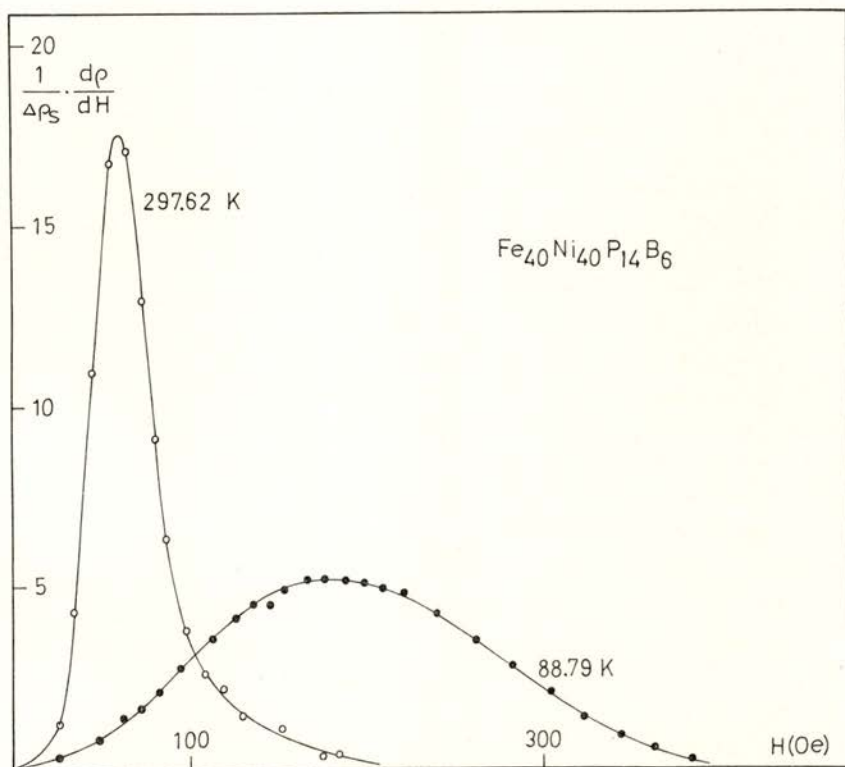
Fig. 9 — Normalized field derivative $(1/\Delta\rho_s) \cdot (d\rho/dH)$, as a function of the applied magnetic field (**H**), for a $Fe_{40}Ni_{40}P_{14}B_6$ amorphous sample (**I** $\parallel$ **H**), at two distinct temperatures.

helimagnetic phase (*). The final extinction of the helimagnetic structure is clearly associated with the kinks observed in our experimental curves, marking the onset of the ferromagnetic phase.

_____

(*) When the helimagnetic order exists, the associated magnetic periodicity (modulation vector **q**; period generally different from the lattice one) originates new energy gaps (less conduction electrons), thus higher electrical resistivity.

The subsequent increase of H only originates a small enhancement of the negative magnetoresistivity, due to the gradual suppression of the spin fluctuations in the system. One should notice the almost perfect parallelism between these $\Delta \rho_{||} / \rho$ curves at high fields and the one described in (i) (corresponding to an intrinsically ferromagnetic situation).

4.4 — *Magnetoresistance of amorphous metals* ($Fe_{40}Ni_{40}P_{14}B_6$)

Although we did not consider this case in the previous sections, the magnetoresistance measurements can be very informative in the study of amorphous metals.

Fig. 9 shows the normalized field derivative $(1/\Delta \rho_s) \cdot (d\rho /dH)$ as a function of **H**, at two distinct temperatures well below the Curie point; $\Delta \rho_s$ is the saturation value of $\Delta \rho$ in high fields [45].

The pronounced differences between the two experimental curves have been associated with important changes (with temperature) of the direction of the easy magnetization in the amorphous metallic ribbon. This assumption is compatible with the recent interpretation of Mössbauer data in $Fe_{40}Ni_{40}P_{14}B_6$ amorphous samples [46], assuming that the easy magnetic direction changes from the ribbon plane ($T \gtrsim 220\,K$) towards a tilted configuration with respect to the ribbon plane (about 20°; $T \lesssim 220\,K$).

REFERENCES

[1] A. H. Wilson, *The Theory of Metals*, Cambridge Univ. Press, London (1953).

[2] J. L. Olsen, *Electron Transport in Metals*, Interscience Publishers, N. Y. (1962).

[3] H. M. Rosenberg, *Low Temperature Solid State Physics*, Oxford Univ. Press (1965).

[4] J. Smit, *Physica*, **16**, 612 (1951).

[5] R. M. Bozorth, *Ferromagnetism*, D. Van Nostrand (1951).

[6] Y. Yamada, S. Takada, *J. Phys. Soc. Japan*, **34**, 51 (1973).

[7] C. M. Hurd, *Advances in Physics*, **23**, 315 (1974).

[8] N. W. Ashcroft, N. D. Mermin, *Solid State Physics*, Holt, Rinehart and Winston (1976).

[9] J. S. Dugdale, *The Electrical Properties of Metals and Alloys*, Edward Arnold, London (1977).

[10] J. B. Sousa, M. M. Amado, M. E. Braga, R. S. Pinto, J. M. Moreira, *Commun. on Physics*, **2**, 95 (1977).

[11] T. Hiraoka, M. Suzuki, *J. Phys. Soc. Japan*, **31**, 1361 (1971).

[12] D. S. Simons, M. S. Salomon, *Phys. Rev.*, **B10**, 4680 (1974).

[13] P. P. Freitas, J. B. Sousa, *J. Phys. F: Metal Physics*, **13**, 1245 (1983).

[14] J. M. Moreira, *Ph. D. Thesis*, Univ. Porto (1985).

[15] J. M. Moreira, J. B. Sousa, J. D. Montenegro, M. E. Braga, D. Melville, *Physica*, **130 B**, 88 (1985).

[16] L. D. Landau, E. M. Lifshitz, *Statistical Physics*, Pergamon Press, vol. V Course on Theoretical Physics (1958).

[17] J. B. Sousa, J. M. Moreira, *Portugaliae Physica*, **13**, 137 (1982).

[18] R. I. Joseph, E. Schlömann, *J. Appl. Phys.*, **36**, 1579 (1965).

[19] S. Alexander, J. S. Helman, I. Balberg, *Phys. Rev.*, **B13**, 304 (1976).

[20] H. Clark, *Solid State Physics*, MacMillan (1968).

[21] T. G. Richard, D. J. W. Geldart, *Phys. Rev. Lett.*, **30**, 290 (1973).

[22] M. E. Fisher, J. S. Langer, *Phys. Rev. Lett.*, **20**, 665 (1968).

[23] V. L. Ginzburg, *Sov. Physics, Solid State*, **2**, 1824 (1960).

[24] H. E. Stanley, *Introduction to Phase Transitions and Critical Phenomena*, Oxford Univ. Press (1971).

[25] G. Toulouse, P. Pfeuty, *Introduction au Groupe de Renormalisation et à ses Applications*, Presses Univ. Grenoble (1975).

[26] S. K. Ma, *Modern Theory of Critical Phenomena*, W. A. Benjamin Inc. (1976).

[27] N. Boccara, *Symétries Brisées*, Hermann (1976).

[28] H. Yamada, S. Takada, *Prog. Theor. Phys.*, **48**, 1828 (1972).

[29] I. Balberg, J. S. Helman, *Phys. Rev.*, **B18**, 303 (1978).

[30] T. R. McGuire, R. I. Potter, *Trans. Magnetics*, **MAG-11**, 1018 (1975).

[31] J. B. Sousa, J. F. D. Montenegro, J. M. Moreira, M. E. Braga, *J. Phys. F: Metal Physics*, **12**, 351 (1982).

[32] E. du Trémolet de Lacheisserie, *Ann. Phys.*, Paris, **5**, 267 (1970).

[33] C. Herring, *J. Appl. Physics*, **35**, 1939 (1960).

[34] J. B. Sousa, M. M. Amado, R. P. Pinto, M. F. Pinheiro, J. M. Moreira, M. E. Braga, M. Ausloos, P. Clippe, D. Hukin, G. Garton, P. Walker, *Advances in Condensed Matter Physics*, ed J. T. Devreese, Plenum Press N. Y., vol. 4, 115 (1981).

[35] L. Berger, *Physica*, **30**, 1141 (1964).

[36]   J. Smit, *Physica, 21*, 877 (1955).

[37]   J. Smit, *Physica, 24*, 39 (1958).

[38]   J. Sant'Ovaia, J. B. Sousa, Seminário, Lab. Física do Porto (1981).

[39]   A. Lage, A. Gomes, Fac. Engenharia do Porto (1979).

[40]   J. B. Sousa, J. M. Moreira, P. P. Freitas, *Proceedings Portuguese Physics Conference 84,* Évora, page 346 (1984).

[41]   S. Chikazumi, *Physics of Magnetism,* John Wiley, N. Y. (1966).

[42]   T. Ito, S. Legvold, B. J. Beaudry, *Phys. Rev.,* **B23**, 3409 (1981).

[43]   J. B. Sousa, J. M. Moreira, M. E. Braga, S. B. Palmer, S. Bates, B. J. Beaudry, *J. Phys. F.,* **16**, 1171 (1985).

[44]   D. H. Martin, *Magnetism in Solids,* Iliffe Books, London (1967).

[45]   J. M. Moreira, J. B. Sousa, J. D. Montenegro, M. E. Braga, *Proceedings of Portuguese Physics Conference 84,* Évora, page 312 (1984).

[46]   C. L. Chien, R. Hasegawa, *J. Appl. Phys.,* **47**, 2234 (1978).

ANALYSIS OF ARCHAEOLOGICAL SAMPLES USING ENERGY DISPERSIVE X-RAY FLUORESCENCE METHOD

N. Venkateswara Rao, S. Bhuloka Reddy, G. Satyanarayana
and D. L. Sastry

Jnanananda Laboratories for Nuclear Research, Andhra University,
Visakhapatnam - 530 003, (India)

ABSTRACT — A study of pottery samples belonging to different periods is undertaken employing an energy dispersive high resolution X-ray fluorescence spectrometer and 30 mCi ^{238}Pu source. The ratios of Manganese to Cobalt and Iron to the 17.28 keV coherent line intensity are found to vary from period to period. It is found that these ratios are high for the present pottery samples when compared to the earlier periods.

1 – INTRODUCTION

A study of archaeological samples is of interest from the view point of the advancement of civilization and technology adopted during different periods of history. There are several analytical methods employed in this direction. Radio-active carbon dating, thermoluminescence [1] and X-ray fluorescence method (XRF) [2], [3] are a few popular techniques to carry out these studies. Each method is being used with varying degrees of success. The energy dispersive X-ray fluorescence method (ENDXRF) [4], [5] is non-destructive, fast and permits a simultaneous multielement analysis. In recent years, it has become a useful tool for approximate dating of archaeological samples [6]. It makes possible the analysis of rock paintings, glazed surfaces, the determination of elemental concentrations and elemental ratios. It also helps distinguish between genuine and fake samples. There are three

types of X-ray fluorescence methods [7], namely, 1) Radioisotope excitation 2) X-ray tube excitation and 3) particle induced X-ray fluorescence (PIXE). The first two methods are referred to as photon induced excitation. The sensitivity limits depend on the mode of excitation used in the analysis of archaeological samples. Several studies [2], [3], [8] on archaeological samples have been carried out employing radioisotopes like Cd-109 and Am-241. The radioisotope excitation method is cheap and the system convenient to handle . However, with this method the sensitivity limits are low when compared to tube excitation. The PIXE method is very expensive and really not necessary for the analysis of archaeo-logical samples inasmuch as the concentration levels of different elements are high and can be easily detected using the first two methods. The present work concerns analysis of archaeological samples belonging to Telangana region of Andhra Pradesh, India and periods ranging from 2500 BC to 600 AD. We have used a 30 mCi ^{238}Pu radioisotope sample as source of exciting radiation and a high resolution XRF spectrometer for the detection and measurement of X-rays. The relative ratios of Mn/Co and Fe/coherent scattered peak intensity, are reported in this paper and the results are discussed.

2 – XRF METHOD

For the present studies, a high resolution XRF spectrometer was used. The spectrometer comprises a 30 mm^2 Si (Li) detector coupled to a low noise FET type preamplifier kept at liquid nitrogen temperature and a 4096 channel analyser with a computer facility. The computer allows data storage and analysis of X-ray spectra.

The block diagram of the XRF system used for the present studies is shown in Fig. 1. The energy resolution (full width at half maximum) is found to be 160 eV at an energy of 5.89 keV — the K-line of ^{55}Mn. The energy standardisation was accomplished by using standard lines from different sources as shown in Fig. 2. The energy calibration plot helps identification of different elements present in any sample. The intensity of a particular X-ray line is measured in terms of the X-ray counts (area under the X-ray peak distribution), the two words being used synony-
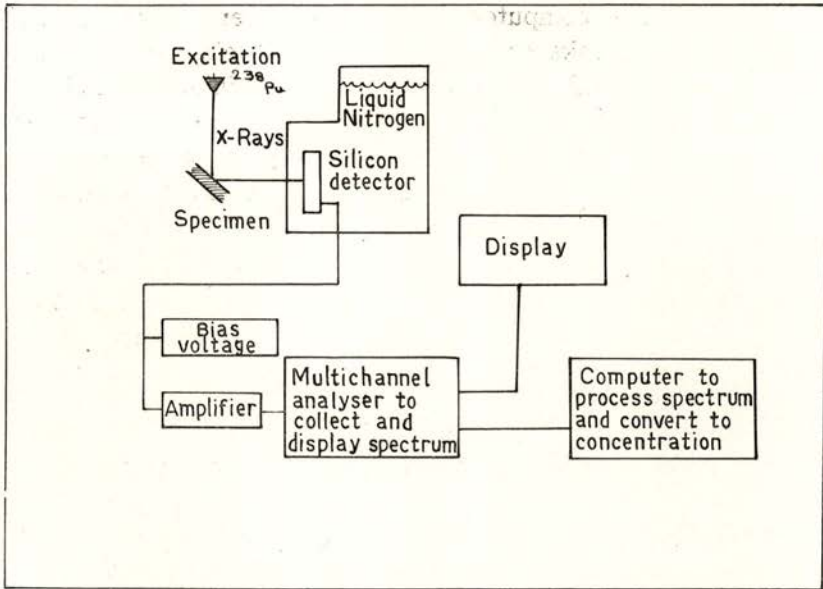
Fig. 1 — Block diagram of the experimental set-up.
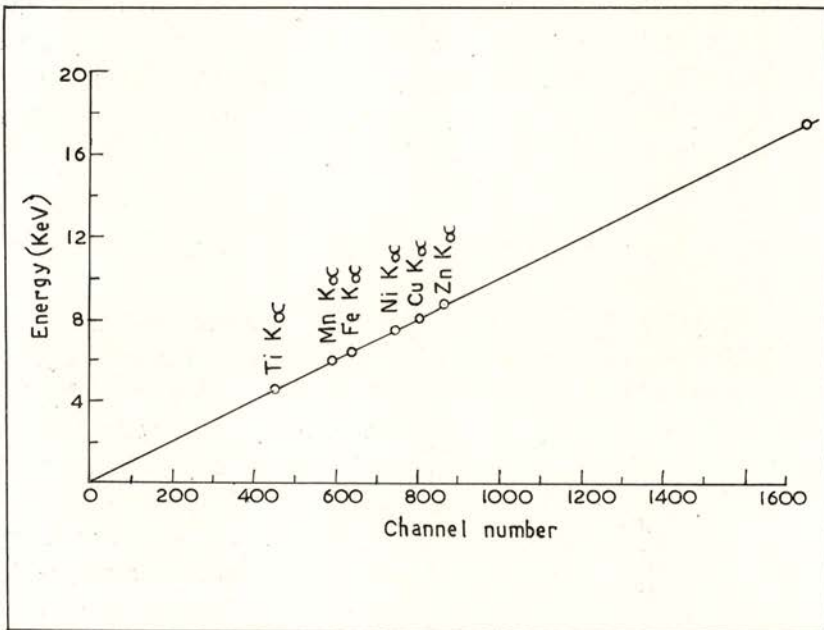
Fig. 2 — Energy linearity characteristic of the system.

mously. Suitable computer programmes were used for the identification of peaks and the corresponding elements, spectrum stripping, backround correction and for obtaining the net peak intensities. Having obtained the individual elemental intensities, the ratios Mn/Co and Fe/17.28 keV intensity can be obtained in a straightforward way. The parameters Mn/Co an Fe/Coherent peak intensity typically label the pottery samples of different ages inasmuch as they decide the colour of the sample and iron is one of the major components of any sample. Also, when one considers ratios, the matrix effects tend to cancel for similar types of samples.

3 – COLLECTION OF ARCHAEOLOGICAL SAMPLES

A total number of about 25 archaeological samples belonging to the Telangana region of Andhra Pradesh were provided by the Department of Archaeology, Government of Andhra Pradesh, India for the present studies. They are pottery samples, have different shapes and surface texture, belong to early historic times and are of neolithic and megalithic types. The depths at which they were collected range from 0.25 meters to 1.7 meters. The samples were used as they were, without any further preparation, for collecting the experimental data, using the XRF system.

4 – RESULTS AND DISCUSSION

Two typical XRF spectra, one from neolithic and one from megalithic samples, are shown in Figs. 3 and 4, respectively. In these figures, the X-ray peaks are identified and labelled by the elements to which they belong. The primary ^{238}Pu source emits X-ray lines ranging from 13 to 17 keV. When X-rays interact with matter, they get scattered by the sample and show up in the XRF spectrum as coherent and incoherent peaks. In the case of coherent peaks, the incident and scattered peak energies are the same, while in the case of incoherent peaks, energies of incident and scattered peaks will be different. For the present purpose the coherent peaks are used in the analysis and the corresponding lines in the

XRF spectrum are labelled by the energies 13.6 and 17.28 keV. The ratio of Fe/coherent peak intensity using the 17.28 keV line was determined for each sample. To look for the matrix effects three pottery samples of different shapes and sizes belonging to the same period were studied. It was found that the Mn/Co and Fe/17.28 keV line ratios were consistent within experimental errors. This suggests saturation of matrix effects for thick samples.
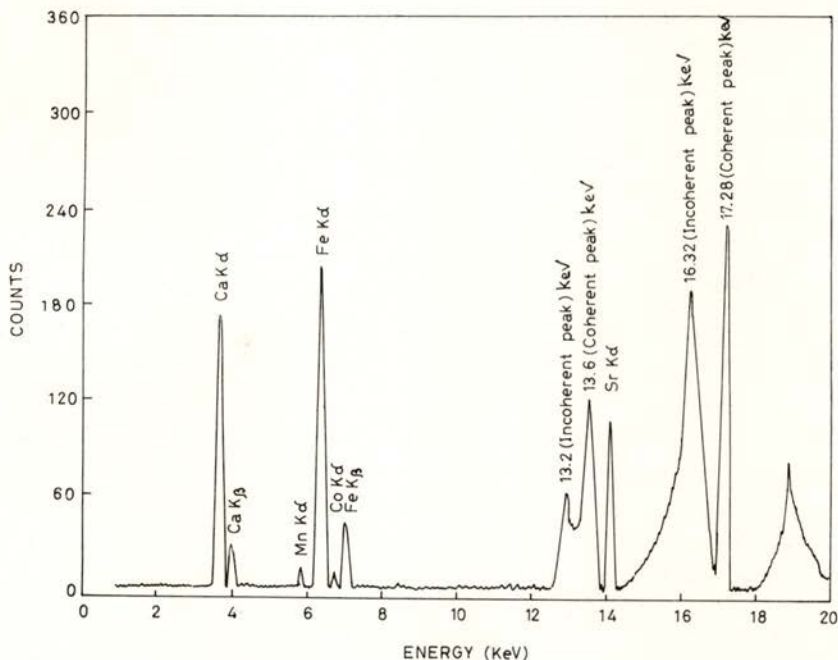
Fig. 3 — A typical X. R. F. spectrum from a Neolithic sample
(Period 2500-1000 B. C.).

The results on the Mn/Co and Fe/coherent peak intensity ratios for the different periods characterising the pottery samples are summarized in Table 1. It can be seen, from table 1, that the Mn/Co ratio is very high for present pottery samples as compared to the earlier ones; that being also the case with the Fe/coherent peak intensively ratio. The figures reported in table 1 help to

distinguish between present and ancient pottery samples. Table 1 also helps to distinguish between neolithic and megalithic samples.
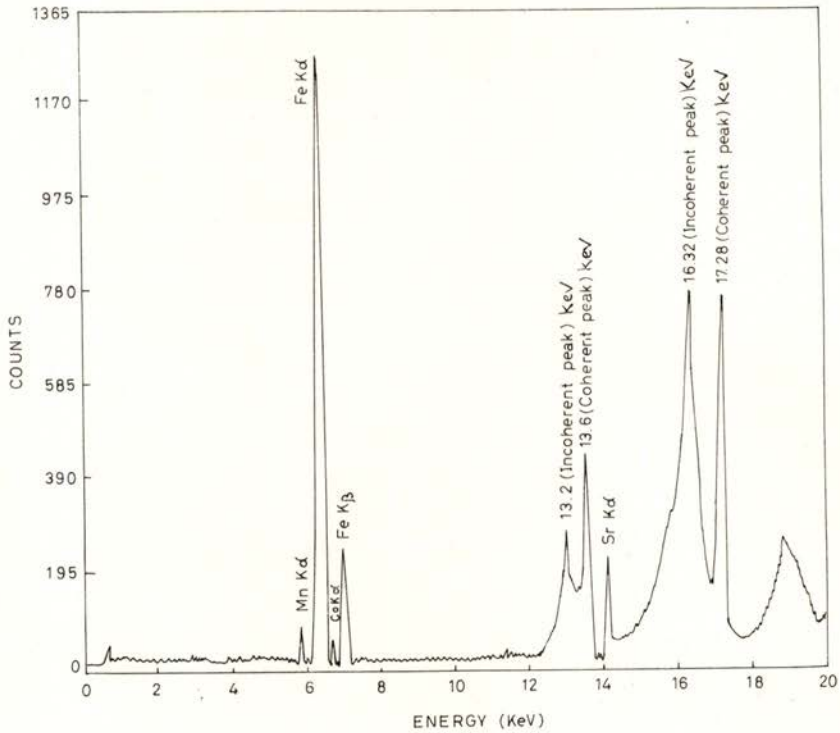
Fig. 4 — A typical X. R. F. spectrum from a Megalithic sample (Period 1000-300 B. C.).

TABLE 1 — Mn/Co and Fe/17.28 (Coh.) Intensity Ratios

No. of Samples	Period	Type	Mn/Co	Fe/17.28 keV
8	2500-1000 B. C.	Neolithic	0.584-0.793	0.906-0.914
8	1000- 300 B. C.	Megalithic	0.385-0.475	1.379-1.407
9	300- 600 A. D.	Historical (Vishnukundan)	0.351-0.405	1.292-1.318
10	Present	—	0.905-1.290	1.688-1.722

5 — CONCLUSION

It is thus illustrated that the energy dispersive X-ray fluorescence method offers a good tool to label pottery samples belonging to different periods.

REFERENCES

[1] MICHELS, J. W., *Dating methods in Archaeology,* Seminor press, New York and London, 1973.

[2] YAP, C. T. and TANG, S. M., X-ray fluorescence analysis of modern and recent Chinese porcelains, *Archaeometry,* **26**, 78-81, 1984.

[3] YAP, C. T. and TANG, S. M., X-ray fluorescence analysis of Chinese porcelains from K'ang Hsi to modern times using Cd-109 source, *Appl. Spectroscopy,* **38**, 527-529, 1984.

[4] GOULDING, F. S. and JAKLEVIC, J. M., Photon excited energy dispersive X-ray fluorescence analysis for trace elements, *Ann. Rev. Nucl. Sci.,* **23**, 45-73, 1973.

[5] Technical Report Series No. 115, *Radio-isotope X-ray fluorescence Spectrometry,* International Atomic Energy Agency, Vienna, 1970.

[6] BANKS, M. S. and MERRICK, J. M., Further analysis of Chinese blue--and-white, *Archaeometry,* **10**, 101-103, 1967.

[7] BERTIN, E. P., *Introduction to X-ray spectrometry analysis,* Plenum Press, New York, 1978.

[8] YAP, C. T. and TANG, S. M., Energy dispersive X-ray fluorescence analysis of Chinese porcelains using Am-241, *Archaeometry,* **27**, 1-3, 1985.

CONTENTS

FASCÍCULO 1-2

CONTENTS

FASCÍCULO 3-4

AUTHOR INDEX

PORTUGALIAE PHYSICA

VOL. 16 · NUMB 3/4 · 1985

CONTENTS

PORTUGALIAE PHYSICA publishes articles or research notes with original results in theoretical, experimental or applied physics; invited review articles may also be included.

Manuscripts, with an abstract, may be written in English or French; they should be typewritten with two spaces and in duplicate. Figures or photographs must be presented in separate sheets and be suitable for reproduction with eventual reduction in size; captions should make the figures intelligible without reference to the text. Authors are requested to comply with the accepted codes concerning references.

There is no page charge. Author(s) will get 50 free reprints (without covers); these are to be shared among all the authors of the article. Authors interested in more reprints should say so when sending their manuscripts; quotations shall be sent with the proofs.

Subscription rates for volume 16:

4.200 Escudos (US$24) — individuals
10.500 Escudos (US$60) — libraries

PORTUGALIAE PHYSICA may also be sent on an exchange basis; we wellcome all suggestions to such effect.

All mail to be addressed to

PORTUGALIAE PHYSICA

C/O LABORATÓRIO DE FÍSICA, FACULDADE DE CIÊNCIAS
PRAÇA GOMES TEIXEIRA
4000 PORTO PORTUGAL